3D Optical flow analysis of a pulsed contrast agent in the bloodstream. Application to virtual angiography and Magnetic Particle Imaging

Romain Lacroix

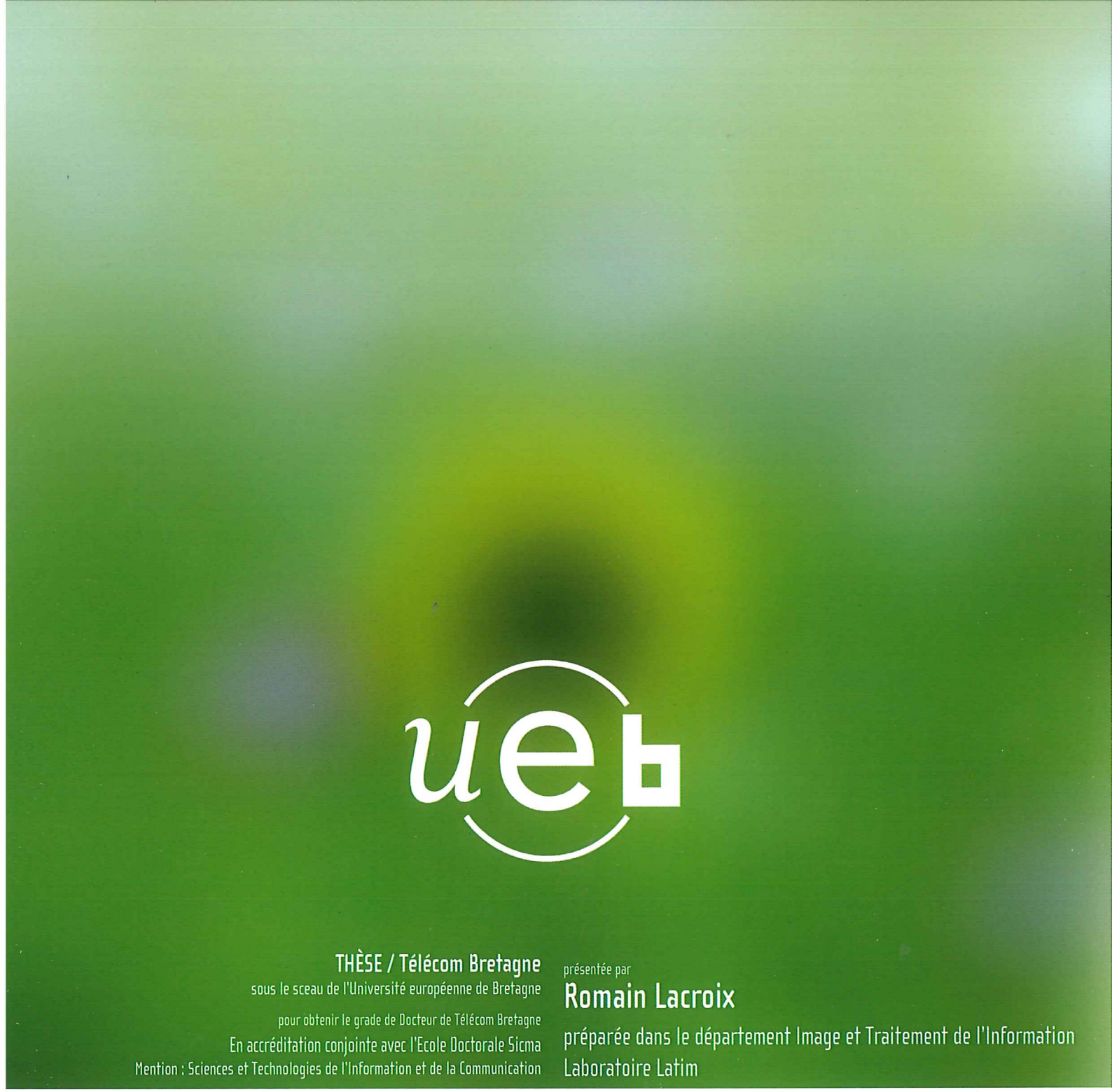

THÈSE / Télécom Bretagne
sous le sceau de l'Université européenne de Bretagne

pour obtenir le grade de Docteur de Télécom Bretagne
En accréditation conjointe avec l'Ecole Doctorale Sicma
Mention : Sciences et Technologies de l'Information et de la Communication

présentée par
Romain Lacroix
préparée dans le département Image et Traitement de l'Information
Laboratoire Latim

3D Optical flow analysis of a pulsed contrast agent in the bloodstream. Application to virtual angiography and Magnetic Particle Imaging

Thèse soutenue le 14 décembre 2015
Devant le jury composé de :

Douraeid Ben Salem
Professeur, CHU de Brest et Université de Bretagne Occidentale / président

Thorsten M. Buzug
Professeur, Université de Lubeck / rapporteur

Jean-Frédéric Gerbeau
Directeur de recherche, INRIA / rapporteur

Philippe Douek
Professeur, Hôpital Louis Pradel - Bron / examinateur

Marcel Breeuwer
Professeur, Université d'Eindhoven/ examinateur

Valérie Burdin
Professeure, Télécom Bretagne / directrice de thèse

Christian Roux
Professeur, Institut Mines-Télécom – Paris / invité

Sherif Ebeid Makram
Docteur, Makram Ebeid Consulting – Suresnes / invité

N d'ordre : 2015telb0364

Sous le sceau de l'Université européenne de Bretagne

Télécom Bretagne

En accréditation conjointe avec l'Ecole Doctorale Sicma

3D optical flow analysis of a pulsed contrast agent in the bloodstream - Applications to virtual angiography and Magnetic Particle Imaging

---

Thèse de Doctorat

Mention : Sciences et Technologies de l'Information et de la Communication (STIC)

Présentée par **Romain Lacroix**

Département Image et Traitement de l'Information

Laboratoire de Traitement de l'Information Médicale - INSERM UMR 1101

Philips Medisys Paris

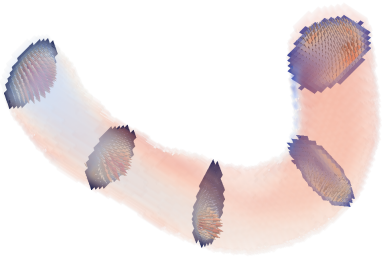

Co-directrice de thèse : Professeure Valérie Burdin - Télécom Bretagne
Co-directeur : Professeur Christian Roux - Institut Mines-Télécom
Encadrant : Dr. Sherif Makram-Ebeid - Philips Medisys

THÈSE DE DOCTORAT

Département **Image et Traitement de l'information**

Présentée par **Romain Lacroix**

Laboratoire de Traitement de l'Information Médicale - INSERM UMR 1101

Philips Medisys Paris

3D optical flow analysis of a pulsed contrast agent in the bloodstream - Applications to virtual angiography and Magnetic Particle Imaging

Analyse de flux optique 3D d'un produit de contraste pulsé dans la circulation sanguine - Application à l'angiographie virtuelle et à l'Imagerie à Particules Magnétiques

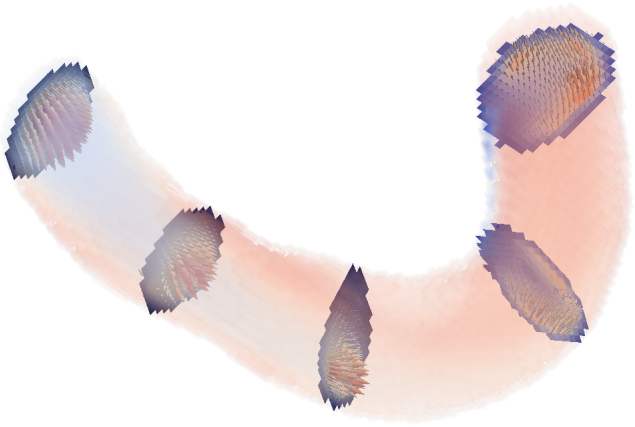

Résumé

De nos jours, les maladies cardiovasculaires restent un sujet de préoccupation majeur pour la santé et une charge économique importante dans les pays développés. Avec les progrès de la médecine, les systèmes d'imagerie médicale ont permis la détection des pathologies cardiovasculaires à un stade précoce, et la surveillance de leur évolution à travers des outils d'analyse de données avancés. La mesure du débit sanguin, en particulier, est une information précieuse pour le médecin. Aujourd'hui, de nombreuses techniques d'acquisition du flux sanguin ont été développées et appliquées dans les routines cliniques et la recherche médicale. L'une d'entre elles recourt à l'injection d'un produit de contraste dans le sang artériel. La propagation du traceur dans la circulation sanguine et sa modulation spatiotemporelle délivre l'information des motifs du flux sanguin dans des séquences d'images 2D. Cependant, les systèmes d'imagerie de contraste 3D+T n'ont pas encore atteint un stade clinique. Le but de cette thèse est d'apporter un cadre général de l'estimation de flux sanguin pour les futurs systèmes d'imagerie de contraste 3D+T.
Une formulation variationnelle du flot optique est présentée, incluant diverses connaissances a priori sur la concentration du produit de contraste, et les propriétés du flux sanguin inspirées de la mécanique des fluides. Par la suite, le potentiel de l'algorithme d'estimation de flot optique est évalué sur de l'angiographie virtuelle par CFD, avec une analyse de l'influence du débit sanguin et des paramètres de l'algorithme. Enfin, une version simplifiée de l'approche de flot optique est testée sur les toutes premières données MPI 3D+T. Dans un premier temps, une expérience de flux in vitro est proposée à l'intérieur d'un fantôme avec une injection de contraste modulé, dans un second temps une analyse du flux sanguin est démontrée sur des données in vivo.
Dans son ensemble, cette thèse investigue le sujet original de l'estimation de flux sanguin et l'analyse de ses motifs en 3D. La contribution technique consiste en la création d'un nouvel algorithme de flot optique dédié à de l'information de contraste temporellement résolue dans le système cardiovasculaire. La contribution clinique sous-jacente consiste en un pipeline complet pour l'estimation du flux sanguin, en partant de la procédure d'acquisition par modulation de contraste, jusqu'au calcul du flot optique et à sa validation in silico.

Mots-clés: Imagerie médicale, angiographie, flux sanguin, produit de contraste, flot optique, méthodes variationnelles, CFD, MPI.

Abstract

Nowadays, cardiovascular diseases remain a subject of major concern for healthcare and an important economic burden in developed countries. With the progress of medicine, medical imaging systems have allowed to detect cardiovascular pathologies at an early stage, and to monitor their evolution through advanced data analysis tools. The measurement of blood flow, in particular, is a precious information for a physician. Today, numerous blood flow estimation techniques have been developed and applied in clinical routines and medical research. One of them resorts to the injection of a contrast product in the arterial blood. The propagation of tracer throughout the bloodstream and its spatiotemporal modulation delivers the information of blood flow patterns in 2D image sequences. However, 3D+T contrast systems have not reached a clinical stage yet. The goal of this thesis is to provide the future 3D+T contrast systems with a general framework of blood flow estimation.

A variational formulation of optical flow is presented, including different prior knowledge concerning the contrast concentration, and blood flow properties inspired from fluid mechanics. Subsequently, the fruitfulness of the optical flow estimation algorithm is evaluated on CFD based virtual angiography, with a sensitivity analysis on flow rate and algorithm parameters. Finally, a simplified version of the optical flow approach is tested on 3D+T early MPI evaluation. First, an in vitro flow experiment is proposed with a modulated contrast injection and secondly a blood flow analysis on in vivo data is demonstrated.

All in all, this thesis investigates the original subject of blood flow estimation and the analysis of 3D blood flow patterns. The technical contribution consists in the creation of a new optical flow algorithm dedicated to time-resolved contrast information in the cardiovascular system. The underlying clinical contribution is a full pipeline for blood flow estimation, starting from the acquisition procedure with contrast modulation, to the optical flow computation, and the in silico validation.

Keywords: medical imaging, angiography, blood flow, contrast agent, optical flow, variational methods, CFD, MPI.

Remerciements

Cette thèse n'est pas seulement le fruit d'une aventure personnelle, elle est aussi l'aboutissement du travail, de la réflexion, mais aussi de l'aide et du soutien de plusieurs personnes que je souhaite remercier ici.

Mes premiers remerciements vont à mes collaborateurs de Philips Hambourg, en particulier à Michael Kuhn, qui a permis l'initiation de ce sujet de thèse audacieux et avant-gardiste sur une toute nouvelle modalité d'imagerie médicale Philips. Je remercie Jürgen Rahmer, pour m'avoir accueilli dans son équipe de recherche, pour sa disponibilité lors des multiples téléconférences et pour m'avoir permis d'expérimenter et d'utiliser le prototype MPI du laboratoire de Hambourg. Je remercie également Oliver Weber et Nils Notnagel pour leur aide précieuse au cours des acquisitions de données MPI in vitro.

Je tiens à remercier mes directeurs de thèse académique: Christian Roux dans un premier temps pour avoir permis cette collaboration avec Télécom Bretagne, puis Valérie Burdin dans un deuxième temps pour m'avoir encadré pendant mes séjours à Brest, pour ses corrections du manuscrit et enfin pour sa généreuse invitation à l'école d'été EMBS en juin 2012.

Je suis profondément reconnaissant envers mon responsable de Philips Sherif Makram-Ebeid pour m'avoir communiqué sa passion de la recherche et son expérience, pour son optimisme inébranlable, ses encouragements malgré les obstacles rencontrés, et enfin pour ses innombrables conseils et leçons de mathématiques sans lesquelles je n'aurais pas pu progresser aussi loin dans cette thèse.

Je voudrais remercier mon jury de thèse pour me faire l'honneur de leur présence, en particulier Thorsten Buzug et Jean-Frédéric Gerbeau d'avoir accepté d'être rapporteurs de ce manuscrit. Je remercie aussi vivement Marcel Breeuwer, Philippe Douek et Douraied Ben Salem de me donner de leur temps pour assister à ma soutenance.

Je remercie Nicolas Villain, directeur de Medisys, pour m'avoir donné l'opportunité d'effectuer cette thèse dans un cadre aussi agréable et accueillant. Grâce à lui, il m'a été possible de découvrir les premiers pôles d'activité du MPI en Allemagne comme en Californie lors des conférences dédiées. J'aimerais remercier Nathalie pour son accompagnement administratif, mais surtout pour sa bienveillance et sa gentillesse.

Je tiens à remercier chaleureusement mes collègues de Medisys pour leur bonne humeur et leur disponibilité. J'aimerais exprimer mon immense gratitude à Hernán, mon 'grand frère scientifique', non seulement pour avoir apporté son expertise en simu-

lations numérique lorsque les données MPI venaient à manquer, mais pour son soutien inconditionnel, ses conseils expérimentés et son amitié qui m'ont aidé à traverser les derniers mois de thèse.

Je remercie également Odile Bonnefous et Mathieu De Craene pour leur expérience, leurs conseils et autres discussions qui m'ont aidé à affiner la compréhension de mon sujet. Un grand merci à Raoul pour son aide, sa générosité et son efficacité lors du dépôt de mon second brevet, celui-ci me permet de valoriser une partie importante de ma thèse. Merci aussi à Hector Recoules pour sa contribution au dépôt de l'invention.

Je voudrais remercier tous mes co-bureaux, du début à la fin de ma thèse, incluant Raphaël, Blandine, Romane et Yitian pour l'ambiance agréable et propice au bon déroulement de ma thèse. Des clins d'œil amicaux à Antoine et Thomas pour nos sorties intra et extra Philips qui m'ont permis d'oublier temporairement ma rédaction. Quelques pensées nostalgiques à certains stagiaires qui ont croisé ma route pendant ces 3 ans, tels que Nicolas, Hakim, Alix, Marina, Matias et Youssef, et qui ont apporté détente et rires à mon quotidien chez Philips. Je remercie l'équipe du LaTIM pour leur acceuil lors de mes quelques passages à Brest, mais surtout à Awen et Katia, mes camarades d'école et amis pour leur hospitalité, leurs sorties rafraîchissantes le long de la côte bretonne, et leur talent certain pour la cuisine.

Je remercie plus généralement tous mes copains d'école avec qui j'ai passé de formidables années à Strasbourg, ainsi que de très sympathiques weekends et vacances pendant ma thèse. Marcounet, Blaisou, Romain le vrai, et Awen l'elfe breton, j'espère continuer à vous voir aussi souvent que possible malgré l'éloignement, et peut-être un jour aurons nous le courage de monter la start-up de nos rêves! Une petite pensée à Maxime également, Alexandre et d'autres amis que j'espère revoir plus souvent après la thèse.

Je termine par des remerciements plus personnels qui vont à ma famille. Merci à mes parents tout d'abord pour leur soutien et leurs encouragements qui m'ont permis d'aller aussi loin dans mes études, c'est grâce à vous que je peux aujourd'hui évoluer dans un métier qui me passionne. Merci à mes grands parents, pour leur générosité et leur gentillesse depuis le début, merci aussi d'avoir fait l'effort de vous intéresser plusieurs fois à mon sujet de thèse. Merci à ma sœur, mon frère, mes cousins et ma cousine, mes oncles et tantes pour les bons moments que l'on continue à partager en famille, malgré le temps qui nous fait évoluer dans des directions différentes. Enfin, je voudrais remercier Lucie, qui a supporté mes humeurs pendant mes longs mois de rédaction, qui m'a donné le courage d'avancer dans mes instants de relâchement, et qui m'apporte chaleur et bien être depuis presque 4 ans.

Contents

Acronyms

2D	Two dimensional
3DRA	Three dimensional rotational angiography
3D	Three dimensional
CA	Contrast Agent
CFD	Computational Fluid Dynamic
CG(M)	Conjugate Gradient (Method)
CT	Computed Tomography
CVD	Cardiovascular Diseases
DC	Direct Current (constant component)
DSA	Digital Subtraction Angiography
FFP	Field Free Point
FMG	Full MultiGrid
FWHM	Full Width at Half Maximum
FoV	Field of View
LMSE	Least Mean Square Error
MPI	Magnetic Particle Imaging
MRI	Magnetic Resonance Imaging
NMR	Nuclear Magnetic Resonance
OFM	Optical Flow Method
PBOF	Phase Based Optical Flow
PET	Positron Emission Tomography
PSF	Point Spread Function
ROI	Region Of Interest
SNR	Signal-to-Noise Ratio
SPIO	SuperParamagnetic Iron Oxyde
SSD	Sum of Squared Difference
TIC	Time Intensity Curve
US	UltraSounds
WSS	Wall Shear Stress

Notation

$\mathbb{R}$	Set of real numbers
N	Number of spatial dimensions of the medical image
Ω	Image domain, open subset of $\mathbb{R}^N$
$\mathbf{x}$	N-D coordinate of the spatial domain, with $\mathbf{x} \in \Omega$
t	Time of the image sequence, with $t \in \mathbb{R}^+$
$I(\mathbf{x}, t)$	Image sequence, integrable in $[\Omega \quad \mathbb{R}^+]$
$\tilde{I}(\mathbf{x}, f)$	*Fourier* transform of I in the temporal domain
$\hat{I}(\mathbf{x}, t)$	Analytic signal of I
$S(\mathbf{x}, t)$	Bandpass signal of the temporal sequence I
$Q(\mathbf{x}, t)$	Quadrature signal of S, computed from the *Hilbert* transform $Q(t) = \int_{v.p} \frac{S(t)}{\pi t} dt$
C^*	Conjuguate of the complex number C
$\phi(\mathbf{x}, t)$	Temporal phase of the bandpass signal S, with $\phi(\mathbf{x}, t) = \arctan(\frac{Q(\mathbf{x},t)}{S(\mathbf{x},t)})$
$f \star g$	Convolution product, *i.e.* $[f \star g](t) = \int_\Omega f(t)g(t-\tau)d\tau$
$\mathbf{v}(\mathbf{x}, t)$	N-dimensional velocity field sequence of the tracer in I, $\mathbf{v} : [\Omega \quad \mathbb{R}^+] \longrightarrow \mathbb{R}^N$
$\mathbf{a} \cdot \mathbf{b}$	Scalar product between two column vectors in $\mathbb{R}^N \times \mathbb{R}^N$
$\mathcal{L}$	Vessel lumen, subset of Ω such that $\mathcal{L} \subset \Omega$
$\mathcal{B}$	Vessel boundaries, subset of $\mathcal{L}$ such that $\mathcal{B} \subset \mathcal{L}$
$\mathbf{n}(\mathbf{x})$	Outward pointing unit normal field of the lumen boundary $\mathcal{B}$
∇	Gradient operator in $\mathbb{R}^N$
Δ	Laplacian operator in $\mathbb{R}^N$

List of Figures

List of Tables

Introduction abrégée

English speakers are invited to go directly to the extended and translated version of this introduction.

Au cours de ces dernières décennies, une large variété de systèmes d'imagerie médicale a émergé des progrès de la médecine, de la physique, et de l'informatique. Parmi les plus connus apparaissent chronologiquement les rayons X en 1895, les ultrasons (US) à la fin des années 1940, la tomographie par émission de positrons (TEP) et l'endoscopie optique dans les années 1950, le scanner par tomographie dans les années 1960, et l'imagerie par résonnance magnétique (IRM) en 1977. Chacune de ces modalités utilise un principe physique différent et répond à un besoin clinique différent. Par exemple, les structures anatomiques peuvent être efficacement imagées aujourd'hui avec les rayons X, le scanner, l'IRM, les ultrasons, et l'endoscopie, alors que les informations fonctionnelles sur les structures physiologiques et leurs métabolismes peuvent être obtenues à partir de la médecine nucléaire (TEP), les ultrasons, la fluorescence, et quelques variantes de l'IRM (IRM fonctionnelle, IRM de diffusion).

Ces nouveaux outils d'imagerie ont permis aux médecins d'explorer plus profondément le corps humain et ont surtout apporté une meilleure compréhension de maladies graves telles que le cancer, l'insuffisance cardiaque, les tumeurs cérébrales, et les maladies cognitives. L'acquisition d'images multidimensionnelles hautement résolues d'organes complexes a considérablement révolutioné la médecine. Les diagnostics assistés par ordinateur, l'évaluation des traitements, et les interventions guidées par ordinateur sont les avancées majeures qui ont profondément transformé les pratiques médicales.

En parallèle, les images médicales et l'extraction d'informations cliniques a donné lieu à une nouvelle branche de l'imagerie médicale, appelée **traitement d'image médical**. Ce champ de recherche très actif a pour but d'extraire d'images brutes (l'intensité de l'image originale) une connaissance implicite concernant les organes étudiés: la forme des organes, la taille d'une tumeur, la longueur d'un os, le débit sanguin, la fraction d'éjection ventriculaire, par exemple, ou n'importe quelle autre information présentant un intérêt clinique. Bien sûr, les images originales peuvent être directement interprétées par un clinicien, mais le traitement et l'analyse d'image lui procure une meilleure interprétation et une évaluation plus riche du tableau clinique. En outre, la quantité toujours croissante des données cliniques à analyser freine

aujourd'hui les médecins dans leurs examens. Des outils de traitement d'image automatiques représentent donc un gain de temps précieux. Le traitement d'image médical joue un important rôle dans un diagnostic, les propriétés requises pour un logiciel de traitement d'image sont principalement:

- La précision
- La robustesse
- La reproducibilité
- L'invariance
- L'automaticité (si possible)

L'intérêt croissant pour les techniques d'imagerie médicales et de traitement d'image a permis de décupler les possibilités de diagnostic et d'intervention clinique. Aujourd'hui, quasiment tous les systèmes d'imagerie médicale sont pourvus de logiciels de visualisation et d'analyse de données. Cette thèse s'intéresse à une application particulière du traitement d'image médical: **l'estimation du flux sanguin**.

L'estimation du flot optique pour le flux sanguin

La mesure du débit sanguin présente très souvent un intérêt clinique majeur dans le diagnostic de **maladies cardiovasculaires**. Elle permet d'indiquer la perfusion des organes, telle que celle des viscères ou du myocarde, mais peut aussi fournir la résistance vasculaire pendant un effort, ou après. Les anciens dispositifs ultrasonores ont été intensivement utilisés jusqu'ici dans les examens cardiovasculaires, pour leur capacité à évaluer le débit sanguin de façon instantanée. Avec le temps et les progrès de l'imagerie médicale, une exploration plus précise du comportement du flux sanguin dans les artères est devenue possible. Le débit étant une information limitée pour décrire le flot sanguin, la visualisation des **motifs de flux** devient prédominante pour l'analyse du mouvement dans les cavités cardiaques, les artères tortueuses, les bifurcations, et les anévrismes. Les améliorations récentes des systèmes d'acquisitions et de leur logiciels de traitement de données ont permis l'acquisition de motifs de flux sanguin:

- **Les systèmes ultrasons 3D** utilisent deux sondes ou plus pour reconstruire des champs de vitesses 3D [Evans et al., 2011, Gómez, 2013].
- **L'angiographie par soustraction digitale (ASD)** recourt à un agent de contrast radio-opaque injecté dans la circulation sanguine. Celui-ci délivre des informations de flux par l'irradiation de rayons X et leur absorbtion par le traceur [Shpilfoygel et al., 2000, Bonnefous et al., 2012]. Les systèmes d'angiographie rotationnelle 3D n'ont pas encore été utilisé pour l'analyse de flux, ainsi seules des estimations en 2D peuvent être actuellement effectuées.

- **L'imagerie par résonance magnétique** possède un mode d'acquisition spécifique (le **flow MRI**) qui exploite la sensibilité au mouvement pour encoder des champs de vitesse 3D [Wigström et al., 1996, Markl et al., 2007].

Dernièrement, Philips Research a mis au point une technologie nommée **l'Imageur à Particules Magnetiques** (MPI en anglais) [Gleich and Weizenecker, 2005]. Ce système d'imagerie exploite les propriétés de saturation de particules ferromagnétiques en réponses à un champ magnétique excitateur. Cette modalité 3D+T délivre des informations quantitatives sur la concentration des particles suite à leur injection dans la circulation sanguine. Le MPI présente divers avantages comparés aux autres modalités de flux, telles que l'acquisition 3D temps réel et la non toxicité du traceur, mais également un défi majeur: la taille réduite du champs de vue. A l'instar des autres modalités de contraste (l'ASD et l'angiographie rotationnelle), le MPI possède un potentiel certain pour l'évaluation du flux sanguin. A partir d'une séquence d'image, le champ de déplacement du produit de contraste, aussi appelé **flot optique** [Beauchemin and Barron, 1995], peut être estimé.

Ce travail de recherche entreprends tout d'abord d'estimer le **potentiel du MPI dans l'analyse du flux sanguin**, puis traite plus généralement du problème de **l'estimation de flux sanguin 3D à partir d'un produit de contrast**. Les avantages et les inconvénients du MPI nous mènent aux interrogations suivantes:

- Quel est le potentiel du MPI pour l'estimation de flux sanguin ?
- Peut on exploiter la pulsatilité du sang pour l'estimation de flux ?
- Quel algorithme de flux optique utiliser pour l'estimation de flux sanguin 3D ?
- Comment évaluer et valider l'algorithme de flux optique ?
- Quelles informations peut-on extraire à partir d'un champ de vitesse ?

Cette thèse se donne pour but de répondre à ces cinq questions. La structure de ce manuscrit est brièvement exposée ci-après.

Plan du manuscrit

Ce manuscrit s'organise en cinq chapitres indépendants, chacun traitant d'un sujet différent.

Le **chapitre 1** présente le contexte clinique de cette thèse. La mesure du débit sanguin a été longtemps utilisée en imagerie médicale, mais l'acquisition des champs de vitesse est très récente. De nouvelles possibilités de diagnostic ont vu le jour, ainsi que

de nouveaux besoins cliniques. Dans un premier temps, les **maladies cardiovasculaires** sont présentées. L'utilité de la mesure de **champs de vitesse** pour le diagnostic et l'étude des pathologies telles que l'athérosclérose et les anévrismes est démontrée. Ensuite, les différentes modalités d'imagerie médicale permettant l'acquisition du flux sanguin sont présentées avec leurs avantages et inconvénients. Les **modalités à produit de contraste** sont particulièrement mises en avant, et une discussion physique et mathématique montre comment une carte de vitesse peut être obtenue à partir d'une séquence d'image angiographique.

Le **chapitre 2** introduit le cadre général de l'analyse des séquences d'images, avec un description rigoureuse du flot optique et son principal inconvénient le **problème d'ouverture**. Ensuite, les techniques les plus utilisées pour l'estimation du flot optique, telles que les approches variationnelles, sont décrites. Elles comportent deux classes différentes: les méthodes locales et les méthodes globales, avec ou sans terme de régularisation. Dans un deuxième temps sont énumerés quelques problèmes classiques survenant en estimation de flux: les grands déplacements, le repliement temporel et les changements d'illumination de la scène. Pour chacun d'entre eux sont présentées les solutions classiques retrouvées dans l'état de l'art. Enfin, d'autres méthodes d'estimation du flot optique n'utilisant pas de cadre variationnel sont décrites.

Le **chapitre 3** propose une méthode pour l'estimation du flux sanguin en 3D. Après une courte revue des techniques existantes, une **nouvelle approche de flot optique** dédiée à l'angiographie 3D est détaillée. L'algorithme de flot optique se base sur plusieurs a priori concernant la concentration du produit de contraste et le flot sanguin. En s'inspirant de l'état de l'art (chapitre 2), une **approche variationnelle** utilisant une énergie de flot optique E et des **termes de régularisation** est proposée. Le premier a priori est sur la **pulsatilité** que le contraste subit lors de sa propagation dans le sang. Dans des modalités telles que l'angiographie par soustraction numérique, l'intensité de la séquence d'image présente de forte oscillations correspondant à la fréquence cardiaque, et se traduit dans l'espace de *Fourier* par la présence de pics en plusieurs harmoniques. Un traitement du signal temporel est proposé pour modéliser cette propriété et simplifier la formulation du flot optique.
Dans une deuxième étape, quelques **propriétés du flux sanguin** sont injectées dans l'énergie E au moyen de termes de régularisation (viscosité, incompressibilité, conditions aux limites au niveau des parois du vaisseau). Un algorithme d'optimisation usuel est décrit pour la minimisation de l'énergie E et la résolution du champ de vitesse $\mathbf{v}$, puis étendu à des techniques **multi-grilles**. Cette contribution peut se résumer en une régularisation sur le temps pour le contraste, suivie d'une régularisation spatiale pour le flux sanguin.

Le **chapitre 4** est une application du chapitre 3 in silico à l'aide de **l'angiographie virtuelle**. Tout d'abord, les logiciels de simulations appelés MFN (Mécanique des Fluides Numériques, ou CFD en anglais) sont présentés. La simulation de séquences

d'images de contraste est expliquée, en partant de l'extraction de paramètres physiologiques pour les conditions aux limites, jusqu'à l'obtention par le calcul des cartes de contraste et des champs de vitesses. Par la suite, **l'algorithme de flot optique est testé sur les données d'angiographie virtuelle**, et les résultats sont comparés à la vérité terrain. Finalement, les résultats sont analysés et le rôle des paramètres de l'algorithme est mis en évidence.

Le **chapitre 5** est une application du chapitre 3 in vitro et in vivo sur des données MPI. Ce chapitre résume le **travail préliminaire** de cette thèse, qui se vouait initialement à l'étude de données MPI. Un travail exploratoire est presenté, révèlant le potentiel du MPI en estimation de flux. Une expérience in vitro originale est décrite, et présentée comme prometteuse pour **l'estimation du flux sanguin en MPI**. Pour finir, un traitement du signal est proposé sur une acquisition MPI in vivo d'une souris, avec la possibilité d'extraire les **lignes de courant du flux sanguin dans les chambres cardiaques**.

Le dernier chapitre conclut le manuscrit et apporte une synthèse des contributions techniques et cliniques, et discute de futures approches.

General Introduction

Medical imaging and medical image processing

Over the last decades, a wide variety of medical imaging systems have emerged from the progress of medicine, physics, and computer science. Amongst the most famous stand chronologically X-Rays in 1895, ultrasounds (US) in late 1940s, positron emission tomography (PET) in 1950s, optical endoscopy in the same decade, computed tomography (CT) in 1960s, and magnetic resonance imaging (MRI) in 1977. Each of these modalities relies on a different physical principle and addresses a different clinical need. For instance, anatomical structures can be effectively imaged today with X-Ray, CT, MRI, US, and optical imaging methods, while functional information about physiological structures and their metabolism can be obtained through nuclear medicine (PET), US, optical fluorescence, and some variations of MRI (fMRI, diffusion-tensor MRI).

Those new imaging tools have allowed physicians to deeply explore the internal human body and more importantly brought a better understanding of critical diseases such as cancer, cardiac failures, brain tumors, and cognitive disorders. The acquisition of highly resolved multidimensional images of complex organs have considerably revolutionized healthcare. Computer-assisted diagnosis, treatment evaluation, and guided interventions are the main advances that have tremendously changed the daily practice of physicians.

In parallel, medical images and image-based clinical knowledge gave rise to a new branch of medical imaging, called **medical image processing** [AP Dhawan, 2008]. This very active field of research aims to extract from untreated images (i.e raw signal intensity) implicit knowledge about the organs of interest: organ shape, tumor size, bone length, blood flow, ventricular ejection fraction for example, or any other quantified information having a clinical relevance. Indeed, the acquired images can be directly interpreted by a clinician, but the image processing and analysis provides him with a better interpretation and a richer analysis of the clinical picture. On top

of that, the increasing amount of clinical data to be analyzed today slows down the physicians in their routine so that automated image analysis tools are a precious save of time. Medical image processing plays an important role in diagnosis, the important properties required for medical processing software are:

- Accuracy
- Robustness
- Reproducibility
- Invariance
- Automatic (when possible)

General overview of medical image processing applications

Within the very extended field of medical image processing, several different classes of algorithms can be distinguished. For each of those, researchers strive for reaching the best accuracy and the best efficiency in extracting the information of interest. We can list those categories as follows:

- **Image reconstruction:** This class of methods aims to recover the full dimensionality of an object when not directly acquired. For instance in three-dimensional rotational angiography (3DRA), CT or PET imaging, where native data consists in few one-dimensional (1D) or two-dimensional (2D) image projections. Reconstruction algorithms transform the sparse and undersampled 1D or 2D data into the original 2D or 3D object.
- **Registration:** Registration methods wish to align two images from different modalities or from different patients. It is always of great help for physicians to have several information fused in the same view (for example PET scan and MRI), or to have intra-patient and inter-patient follow up merged.
- **Image enhancement:** These image processing techniques attempt to improve the image quality, especially by removing the noise, optimizing the contrast, and attenuating the artifacts. It helps the clinician to better interpret the medical image.
- **Segmentation:** This image processing task takes aim at labeling the medical image into several regions. It is particularly employed to locate regions of interest such as organs, blood vessels or tumors. It is very often a prior step before further statistical analysis.

- **Classification:** Classification is one of the foremost goals in medical imaging. Its purpose is to assign to each element a meaning that eases the image interpretation. For example healthy tissues can be distinguished from tumorous tissues by highlighting their location with different colors.

- **Feature extraction:** Feature extraction consists in computing low-level image characteristics (such as local statistics on the intensity information) or high-level features (such as shapes and textures) in order to analyze and classify the information represented in the image. It is often used as a first step in classification algorithms.

- **Motion analysis:** This class of image processing method undertakes to estimate the displacement or the velocity of an object in a temporal image sequence. Currently, these methods prove very useful in the blood flow estimation, the analysis of wall motion, the image stabilization during breathing or heartbeat, and the localization of surgical tools such as catheter tips and pacemakers.

The growing interest in those imaging techniques has boosted the possibilities of diagnostics and clinical practices. Today, almost every medical imaging system is fitted with those tools of visualization and analysis. **In this thesis, we investigate blood flow estimation, which is of major clinical importance in cardiovascular diagnosis.**

Blood flow and optical flow estimation

Blood flow is a crucial element of a cardiovascular diagnosis, it can indicate the perfusion of organs, such as viscera or heart muscle, but can also be exploited to derive the vascular resistance during an exercise, or after an exercise. Ancient US devices knew some glorious years in cardiovascular routines (late 1960s), with their ability to measure the instantaneous blood flow rate with the *Doppler effect*. Over time, the progress of medical imaging allowed a deeper exploration and a more precise vision of how blood flow behaved inside the arteries. The interpretation of blood flow as a **global flow rate** was no more sufficient. The studying of blood flow in cardiac cavities, tortuous arteries, bifurcations, and aneurysms was undoubtedly more appropriate by the visualization of **flow patterns**. With the latest improvements of both medical imaging hardware and software, it recently became possible to acquire flow patterns in the bloodstream:

- **3D ultrasounds** systems make use of two or more probes to reconstruct 2D or 3D flow vector fields [Evans et al., 2011, Gómez, 2013].

- **Digital Subtraction Angiography (DSA)** employs a radio-opaque contrast agent (CA) injected in the bloodstream, which provides blood flow information

through X-Ray irradiation [Shpilfoygel et al., 2000, Bonnefous et al., 2012]. 3D rotational angiography systems (3DRA) have not been investigated yet for flow purpose, therefore only 2D flow fields can be estimated at this stage.

- **Magnetic Resonance Imaging** has a specific imaging mode known as **flow MRI** that makes benefit of motion sensitivity to encode 3D flow fields [Wigström et al., 1996, Markl et al., 2007]. This imaging mode is up to now the most accurate in term of resolution and provides the highest quantity of information: time resolved streamlines, pathlines and degree of turbulence in the blood can be assessed [Dyverfeldt, 2010].

Lately, Philips Research developed a new medical imaging technology called **Magnetic Particle Imaging (MPI)** [Gleich and Weizenecker, 2005]. This imaging system uses the interesting saturation property of superparamagnetic iron oxyde (SPIO) nanoparticles when stimulated by oscillating magnetic fields. This tracer modality provides 3D+T quantitative information about the nanoparticle concentration after injection in the bloodstream, with early in vivo successes [Weizenecker et al., 2009, Rahmer et al., 2013]. MPI presents different advantages compared to the other flow modalities, such as **3D real time acquisition with kidney safe CA**, but also one main challenge: the **limited Field of View** (FoV). As with other contrast modalities like DSA and 3DRA, MPI is thought to be a good candidate for blood flow evaluation. This medical imaging system acquires an image sequence $I(\mathbf{x}, t)$ describing the propagation of the CA through the bloodstream. From the image sequence, the displacement field $\mathbf{v}(\mathbf{x}, t)$ of the CA called **optical flow** [Beauchemin and Barron, 1995] can be estimated.

This research work first undertakes to unveil **the potential of MPI regarding blood flow analysis**, but then more generally tackles the problem of **3D blood flow estimation based on a CA propagation**. From both the potential and the challenges of MPI, few questions arise:

- Is MPI a good candidate for flow imaging?
- Can we benefit from the blood flow pulsatility to achieve blood flow estimation?
- What is the best choice of optical flow algorithm to assess 3D contrast based flow imaging?
- How can we evaluate and validate the optical flow algorithm?
- What information can we derive from a blood flow field?

This manuscript basically tries to answer the five aforementioned questions.

Outline

The manuscript is organized in five chapters, each can be read independently and focuses on a different subject.

Chapter 1 brings the clinical background of this thesis. The measurement of blood flow has been used for decades in medical imaging, but the assessment of blood flow patterns is rather new. The emerging technologies acquiring flow patterns created new possibilities of diagnosis and new clinical needs. In a first place, several **cardiovascular diseases** (CVD) are presented, and how some of them as atherosclerosis and aneurysms can be detected and studied with **flow patterns**. Afterward, the different medical imaging tool allowing to resolve flow patterns are introduced, with their advantages and drawbacks. A particular emphasis on **contrast modalities** is made, and a physical and mathematical digression finally proves how a velocity map can be derived from a contrast sequence.

Chapter 2 presents the general framework of image sequence analysis. It provides an in-depth description of the **optical flow formulation** and its principal pitfall the **aperture problem**. Then, the most popular techniques for optical flow estimation as variational approaches are described. They include local or global miminization scheme with or without regularization terms. Secondly, several quandaries often arising in motion estimation are enumerated, among which are large displacements, temporal aliasing, and illumination changes. Different state of the art approaches are explained for each of them. Finally, miscellaneous approaches other than variational techniques are presented.

Chapter 3 describes a methodology for three dimensional blood flow estimation. After a short overview of the already existing techniques, a **new optical flow approach** addressing 3D angiography is developed. The optical flow algorithm is based on several physical priors concerning the contrast concentration and the blood flow. Based on the state of the art review described in the previous chapter, a **variational approach** using optical flow energy E and **regularization term** is proposed.
The first prior is the **pulsatility** that contrast undergoes when propagating through the bloodstream. In contrast modalities such as DSA, the intensity of the image sequence exhibits strong oscillations corresponding to the heart frequency, and resulting in sharp harmonic peaks in the *Fourier* domain. A specific time processing approach is proposed to model this property and simplify the optical flow formulation.
In a second phase, **blood flow properties** are modeled through several regularization terms, including incompressibility, smoothness and boundary conditions on vessel walls. A typical optimization scheme is detailed in order to minimize the energy E, solve the blood flow field $\mathbf{v}$, and is later extended to **multigrid techniques**. This scheme makes use of a temporal regularization on contrast followed by a spatial regularization on blood flow.

Chapter 4 is an in silico application of chapter 3 on **virtual angiography**. First, a simulation software is presented, and the generation of simulated contrast image sequence is explained. This simulation makes use of physiologically relevant boundary conditions for the computation of contrast image and blood flow field. Afterward, **the optical flow algorithm is tested on a set of virtual angiography data**, and results are compared to ground truths. Finally, results are discussed and the role of algorithm parameters is highlighted.

Chapter 5 presents an in vitro and in vivo application of the chapter 3 on MPI data. This chapter portrays the **preliminary work** of this thesis that originally focused on MPI. An early work is proposed, revealing the future MPI potential. The originality of the in vitro experiment is pointed out, and presented as a promising method for blood flow estimation in MPI. Finally, in vivo MPI evaluation of a mouse is showed with early time processing approaches for the extraction of **blood flow streamlines in heart chambers**.

The last chapter eventually concludes the manuscript with a synthesis of its technical and clinical contributions, before discussing on potential future work.

The overall structure of this thesis is summarized in figure 1.

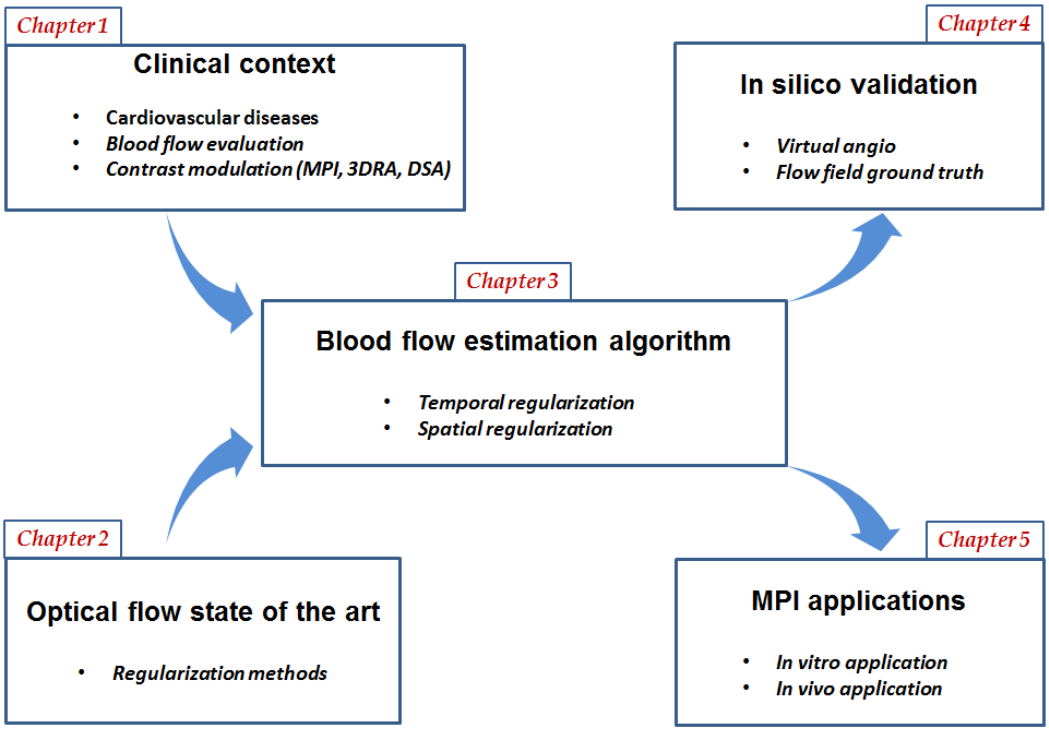

Figure 1: *Organization of the manuscript according to the different chapters.*

Chapter 1

The clinical context

Contents

Abstract

This chapter presents the basic motivation of this thesis, which stands at a crossroad of healthcare, computer science, physics and applied mathematics. The clinical background will be first put forward, introducing different diseases in the cardiovascular system, their strong relationship with blood flow, and how we can study them with flow imaging. Several medical imaging systems will be introduced, with their advantages and drawbacks, and a particular emphasis on contrast modalities. Finally, the possibility to capture blood flow with equations of contrast propagation will be demonstrated. General considerations about hemodynamics and contrast dynamics will be brought up as theoretical support for the next chapter.

Résumé

Ce chapitre présente la motivation principale de cette thèse, située à la frontière entre la médecine, l'informatique, la physique et les mathématiques appliquées. Le contexte clinique sera tout d'abord exposé, en décrivant les différentes maladies du système cardiovasculaire, leur lien étroit avec le flot sanguin, et les différentes modalités d'imagerie permettant de les étudier. Plusieurs systèmes d'imagerie médicale seront par la suite présentés, avec leurs avantages et inconvénients, ainsi qu'un accent particulier sur les modalités à produit de contraste. Finalement, la possibilité d'extraire le flot sanguin à partir des équations de propagation du contraste sera démontrée. Des considérations générales sur la dynamique du sang et du produit de contraste permettront d'apporter un support théorique utile pour les futurs chapitres.

1.1 Cardiovascular diseases

According to the World Health Organization, cardiovascular diseases (CVDs) are the leading cause of mortality in the world, outclassing all the other causes of death put together [WHO, 2015]. It is estimated that around 17.5 million people died in 2012 because of cardiovascular accidents, which represents 31% of the global mortality, and occurs at 75% in developing countries. Some of CVDs can be dealt with or controlled by addressing the behavioral causes (smoking, unhealthy diets, settled way of life, alcoholism, stress...), but some other kinds of CVDs are more difficult to avoid when arising from genetic conditions, bacterial infections, or traumatic injuries. Among the CVDs, several groups of disorders can be identified, whether they can be attributed to arteries, veins, or heart function [WHO, 2015]:

- Coronary heart diseases (vessels supplying the heart muscle)
- Cerebrovascular diseases (vessels supplying the brain)
- Peripheral arterial diseases (vessels supplying the limbs)
- Vein thrombosis and pulmonary embolism (blood clots in the leg veins, which can dislodge and move to the heart and lungs)
- Rheumatic heart diseases (damages to heart muscle and valves during a rheumatic fever, caused by a streptococcal bacteria)
- Congenital heart diseases (malformation existing at birth)

CVDs often manifest themselves by the corruption of the cardiovascular morphology, which disturbs the blood flow transport. In the case of blood vessel deformation - the four first aforementioned diseases - the vessel lumen is either narrowed (stenosis), or dilated (aneurysm). Theses two abnormalities are at the core of this thesis. They can be explained by a physiological mechanism known as **atherosclerosis** but more importantly by **hemodynamic factors**. After a short presentation of atherosclerosis and aneurysms, both impairments of the blood vessel function, the principal hemodynamic causes will be discussed.

1.1.1 Atherosclerosis

One of the main reason for the development of a CVD is the **atherosclerosis**. Atherosclerosis, or hardening of the arteries, is a condition in which plaques build-up in the arteries [AHA, 2014]. The rupture of the arterial plaques stimulates a thrombosis process, which often results in the formation of clots. This mechanism eventually leads to a complete blockage of blood flow supply to heart or brain tissues, thereby causing

a heart attack, or a stroke. Plaques can manifest themselves on angiographies as a reduction or an occlusion of the vessel, also called **stenosis** (see figure 1.1).

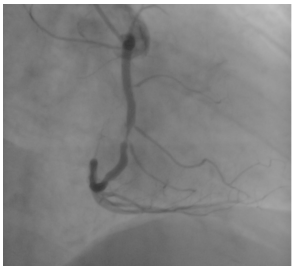

Figure 1.1: *Stenosis in the right coronary artery. This angiogram is reproduced from a Philips X-Ray database.*

How are arterial plaques generated ?

What is exactly the origin of atherosclerosis is still unclear today. Nevertheless, many scientists as Wootton et. al [Wootton and Ku, 1999a] believe that the formation of arterial plaques might arise from the damage of **endothelium** due to the blood flow. The endothelium is a very thin layer of squamous cells interfacing the bloodstream with the arterial wall. When this thin barrier is damaged, arterial wall is weakened, allowing lipids and toxins to penetrate the smooth muscle layer, known as **media**. This triggers an inflammation and oxidative cascade in the media, where fat and cellular wastes accumulate: a plaque is created [Cito et al., 2013]. Eventually, the plaque begins to calcify and, over time, becomes prone to rupture.

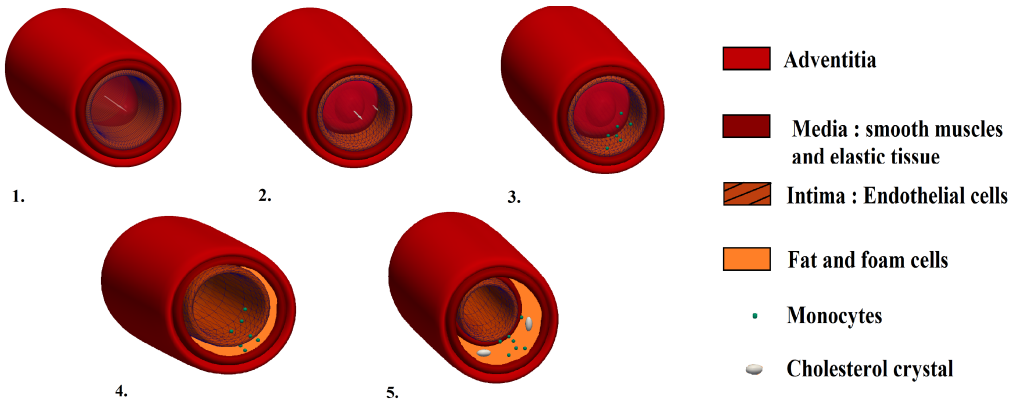

Figure 1.2: **Schema of atherosclerosis:** *1. Healthy artery with a laminar parabolic flow profile: endothelial cells are elongated in the direction of flow 2. Flow turbulence occurs and damages the intima: endothelial cells get destructured 3. Monocytes are recruited to the inflammation site 4. Fatty streak and foam cells penetrate the media through weakened endothelium: atherosclerosis begins 5. Fat and cholesterol accumulate over time and create an arterial plaque.*

1.1.2 Aneurysms

Another common CVD is the formation of **aneurysms**. Aneurysms are balloon-like, blood filled bulges localized in the wall of a blood vessel. Common locations for aneurysms in the human vascular system include the circle of Willis in the brain, the thoracic aorta, the abdominal aorta, or even heart itself. It has been established that around 2% of the population harbors cerebral aneurysms [Rinkel et al., 1998], but fortunately most of them remains asymptomatic and harmless (between 50% and 80% never rupture [Brisman et al., 2006]). As an aneurysm increases in size, the risk of rupture also increases. The consequence of rupture is an extensive bleeding, a hypovolemic shock and death if not treated within a short time. Aneurysms are a result of a weakened blood vessel wall, caused by a hereditary condition, an acquired disease or hemodynamic factors.

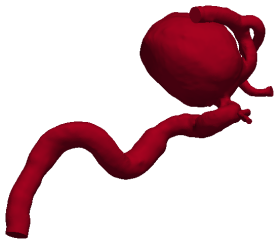

Figure 1.3: *Example of saccular-type cerebral aneurysm (courtesy of Dr. Morales, Philips Research Paris- Medisys Research Lab).*

1.1.3 Dissections

A dissection is a tear within the wall of a blood vessel. Usually a layer of the intima or media ruptures, creating a separation between two wall layers. The blood infiltrates in this passage and digs a second vessel lumen (see figure 1.4). Dissections often lead to two different outcomes: ischemic complications, by the reduction of the native lumen (stenotic configuration), or by the dilation of the 'false lumen' created by the new space within the wall of the artery (aneurysmal configuration). From a hemodynamic point of view, the two above configurations boil down to either the case of a stenosis or the case of an aneurysm. Dissection are mainly located in the aorta, the coronary arteries, the vertebral artery, and the carotid artery.

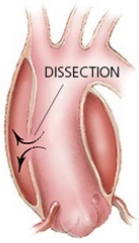

Figure 1.4: *Artery dissection*

1.1.4 Hemodynamic factors in cardiovascular diseases

The hemodynamic conditions are fundamental to understand what is health and what is illness in the circulatory system. Recently, medical literature started to unveil the strong relationships between hemodynamics, endothelial function and CVDs [Wootton and Ku, 1999a,Reneman et al., 2006,Malek, 1999,Dolan et al., 2011,Dolan et al., 2012]. Endothelium is suspected to react to local hemodynamics, especially to **wall shear stress** (WSS) alongside the arterial walls. It has the ability to sense and mechanically transduce the mechanical stress of blood flow into a biological signal [Traub and Berk, 1998, Ishida et al., 1997]. Thus, feedback and regulation of the circulatory system can be achieved by optimally adapting the arterial diameter to the required flow rate.

However, when endothelium gets damaged by blood flow forces, the flow regulation of endothelial cells gets disrupted and the arterial wall starts to behave improperly [Malek, 1999, Raj, 2013, Moore et al., 1994]. Indeed, the endothelium is supposed to maintain the arterial function only within a physiological WSS range, outside which homeostasis cannot be guaranteed. For instance, low oscillating WSS that occurs in flow recirculation area promotes the formation of arterial plaques by destructuring the endothelial cells [Dolan et al., 2012]. High WSS in stenotic arteries stimulates a so-called **arterial remodeling** process [Girerd et al., 1996, Zarins et al., 1987], often increasing the risk of plaque rupture. WSS is therefore a crucial indicator of atherogenesis, arterial remodeling, and plaque rupture.

Additionally, hemodynamics is very important for the assessment of aneurysm rupture and treatment success. Strong correlations between hemodynamics and aneurysm initiation, growth and rupture have been reported [Gao et al., 2008,Cebral et al., 2011]. In [Meng et al., 2014], it is shown that both high and low WSS can expose arterial wall to aneurysm initiation, while the **impingement jet** and **flow stability** are associated with aneurysm rupture [Cebral et al., 2009].

In that respect, **computational fluid dynamics** (CFD) software have been used to study and to predict hemodynamic conditions in abnormal vasculatures of the cardiovascular system. For instance, CFD has allowed to better understand the origins of aneurysm rupture, and to simulate the possible outcome of a surgical intervention [Morales, 2012]. Even though CFD is not integrated in clinical routines yet, it lets us envision a significant improvement in the clinical management of CVDs, including unruptured aneurysms [Singh et al., 2009]. The spreading use of CFD attests to actual importance of hemodynamics in the genesis and growth of CVDs, while allowing a completely non-invasive analysis of the cardiovascular system. For further information about CFD, the reader is invited to go directly to chapter 4.

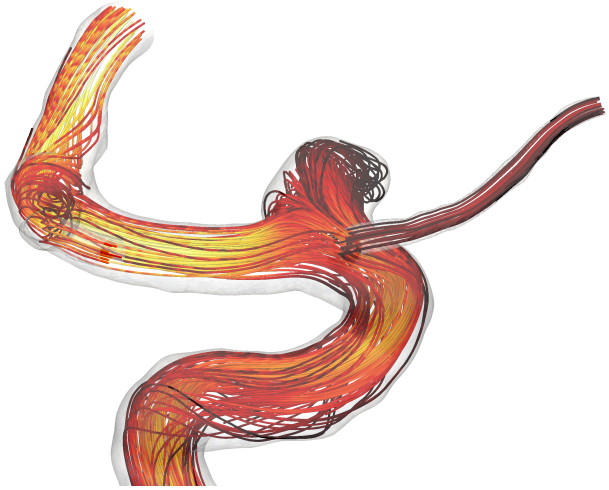

Figure 1.5: *Examples of CFD simulation for arterial flow with aneurysm (the streamlines corresponding to bloodflow are color-coded with the velocity magnitude: yellow for high velocity and red for low velocity).*

All the above information about hemodynamic features (WSS and jet among others) prove very valuable for the clinical assessment of CVDs, from the prediction and detection of the disease, to the evaluation of its severity and the need to resort to surgery. However, further studies about the dysfunction of cardiovascular system and particularly about the influence of blood flow still need to be conducted. The current knowledge about the hemodynamic factors on CVDs is still incomplete. In order to broaden our understanding of the CVDs pathogenesis and evolution, medical imaging systems dedicated to the in-vivo assessment of blood flow had to be developed. Hence, the next section will describe the medical imaging devices allowing blood flow analysis.

1.2 Blood flow assessment in medical imaging

Nowadays, cardiovascular diseases can be efficiently imaged with the advances of medical imaging. Medical devices such as US, CT, or MRI are perfectly capable of detecting a cardiovascular condition. Typically, angiography enables the visualization of stenosis, aneurysms, and bloodflow malfunctions, while cardiac imaging allows to temporally resolve heartbeats and study wall and valves motion.

In this section, we will present the different medical imaging modalities that are employed to capture the blood flow in medical imaging:

- **Doppler Ultrasonography** (Doppler US) is the gold-standard flow modality and also the most commonly used in clinical routines.
- **Digital Subtraction Angiography** (DSA) which takes benefit from a radio-opaque contrast agent to image the propagation of blood flow under X-Rays irradiation.
- **Flow MRI** which is an emerging MRI acquisition mode that makes possible the visualization of complex flow patterns inside cardiovascular organs.
- **Magnetic Particle Imaging** (MPI) which is a totally new medical image modality with high potential in angiography and blood flow assessment, albeit not fully developed at this time.

1.2.1 Doppler US

Doppler ultrasonography has been a long-standing and reliable tool for the studying of blood flow in medical imaging. It takes advantage of the well-known **Doppler effect** that describes the frequency shift that occurs when a wave source is moving away from an observer [Kremkau, 1990]. Hence, the velocity component of blood flow in the direction of the US beam can be computed, using the frequency change of reflected ultrasounds. This technique has proven very useful for more than 30 years, with the advantage of providing a real time blood flow estimation and also to require simple and low cost electronics.

Several acquisition protocols actually exist for the assessment of bloodflow in US: the continuous wave system, the pulsed wave system, the spectral analysis, the color flow imaging, and tissue doppler imaging. They usually provide the time variation of the blood velocity within a single range gate in the form of an audio signal corresponding to the evolution of the Doppler frequency shifts. If we produce an ultrasound beam of frequency f_0 toward the moving blood of velocity v, the ultrasound wave will be contracted twice: the first time when blood receives the signal at velocity $c - v$ and the second time when backscattering the wave to the probe at $c + v$, c being the speed of sound. The return frequency f_r therefore reads [Bonnefous, 2001]:

$$f_r = f_0 \frac{c+v}{c-v} \approx f_0(1+2\frac{v}{c}) \tag{1.1}$$

As a consequence, blood velocity can be related to the **frequency shift** f_D by:

$$f_D = f_r - f_0 = 2f_0\frac{v}{c} \tag{1.2}$$

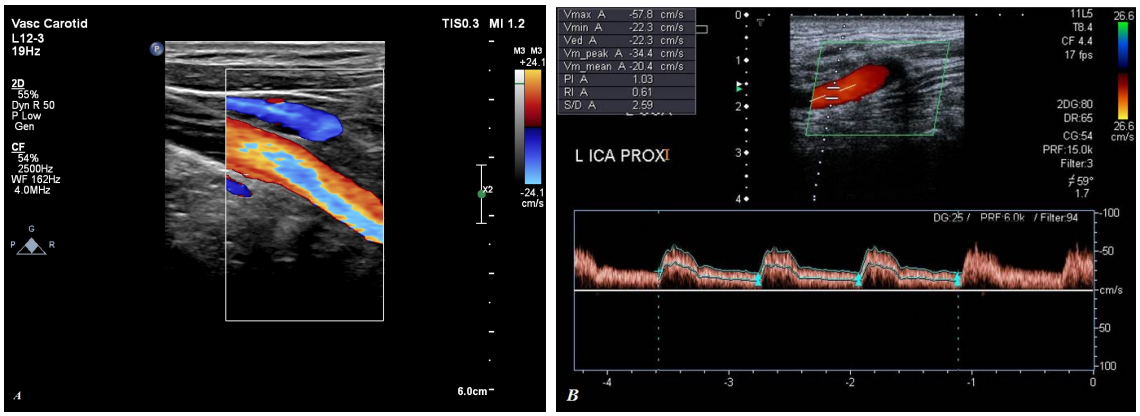

Figure 1.6: *Color flow imaging of the carotid artery, using Doppler on a Philips US device. In A., two colors are displayed: the red shows the blood particles moving away from the probe, while the blue shows the ones getting closer to the probe. In B. is displayed a velocity spectrogram measured inside a local window of the US image. The time axis is represented horizontally, and for each time sample is color coded a velocity distribution of the window of interest. From this spectrogram can be derived the time evolution of both maximum and mean velocity.*

Yet, the ultrasound waves are limited in their penetration depth, and are strongly reflected by bones (skull, ribs...). This reduces the applications of color flow imaging to accessible parts of the body. The color flow imaging has also the main drawback that it only yields the velocity component of the blood flow in the beam axis. The angle from which the transducer generates ultrasounds is therefore paramount for the observation of a blood vessel, especially when the latter harbors curved or tortuous shapes. Nevertheless, new acquisitions and reconstruction methods using two or more probes allow to extend color flow imaging to 3D images, with 2 or 3 components of the velocity vectors [Evans et al., 2011, Gómez, 2013]. The portability and the low cost of US together with the recent advances of flow acquisition protocols ought to enable US to stay one of the gold standard modality for blood flow estimation.

1.2.2 X-Ray DSA

X-Rays devices have been the first medical imaging system invented, after the discovery of Röntgen in 1895. They make use of the penetrating X-Ray electromagnetic waves to image the absorption rate of human tissues. Since the first radiographs were obtained on photographic plates, the acquisition method of X-Rays evolved with the advent of electronic sensors into modern digital radiography, fluorography, mammography, angiography, and their 3D derived rotational angiography and CT scanners [AP Dhawan, 2008].

The basic principle is that the X-Ray attenuation provides information about variations in the tissue density. The output intensity of a radiation beam parallel to a x-direction for a y-coordinate location in a z-axial planar cross-section $I_{out}(y; x, z)$ would be given by:

$$I_{out}(y; x, z) = I_{in}(y; x, z)e^{-\int \mu(x,y;z)dx} \tag{1.3}$$

where $\mu(x, y, z)$ is the attenuation coefficient to the transmitted X-Ray energy.

X-Ray devices produce images with morphological information at high spatial resolution, which often proves useful for both interventional and diagnostic purpose. Generally CT is used to acquire an accurate 3D volume of the patient with anatomical landmarks, to ease a diagnosis or to complement the functional information of other modalities like PET-scans. Other X-Ray systems as 3DRA or DSA are fitted with rotating C-arms (see figure 1.7) that make possible the access to patient acquisitions during the intervention.

Figure 1.7: *Philips C-arm BV-Vectra with its monitor.* *(available on http://www.healthcare.philips.com)*

In the domain of **angiography**, 3DRA and DSA outperform all other modalities in term of spatial and temporal resolution. **DSA** is a 2D X-Ray imaging mode that generates cone beam projections of the vasculature of interest under a controllable angulation. A radio-opaque tracer is injected in the bloodstream, which creates a strong contrast between the background and the blood vessels. Fast image sequence can be achieved with a frame rate of 60 Hz and a sub-millimetric resolution. **3DRA** basically uses the same acquisition protocol, but adds an extra-dimension by taking benefit from multiple angulations acquired during a single acquisition. As a result, 3D

volume reconstruction becomes possible, but at the cost of temporal resolution (figure 1.8). Although these image modalities provide valuable information regarding vascular morphology [Conti et al., 2011], it is still uneasy to extract functional information, such as blood flow.

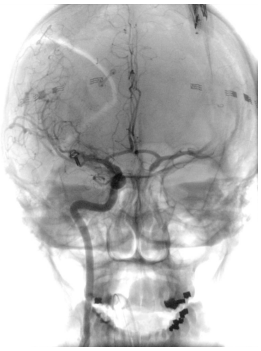

Figure 1.8: *3DRA of brain arteries.*

Recently, quantitative assessment of hemodynamics has been investigated by detecting the displacement of the radio-opaque contrast material through the vascular system in DSA sequences. This concept has been studied since the 1960s, and an extensive review has been published recently [Shpilfoygel et al., 2000], where different classes of flow estimation methods are shown. Some techniques are based on physical models, like advection, to compute a realistic flow [Sarry et al., 2002], while other approaches only rely on the image intensity information [Bogunović and Loncarić, 2006, Rhode et al., 2005].

Especially **optical flow methods** (OFM) have been employed to estimate locally the velocity of blood flow in the arteries. For example, [Bonnefous et al., 2012] estimate the flow inside arteries, exploiting both spatial and time derivatives of the contrast product on 2D DSA sequences. This technique was validated later by comparing the flow estimation with Doppler US measurement in the internal carotid artery (ICA) [Pereira et al., 2014]. The method estimates **flow patterns** with pixelwise-2D velocities. For instance, flow patterns in cerebral aneurysms were studied before and after flow-diverter stenting [Pereira et al., 2013]. OFMs in DSA have a considerable advantage compared to 2D Doppler US since it provide an additional component of the blood velocity (see figure 1.9).

However, one should note that the propagation of the CA cannot be observed when its concentration gets homogeneous in the arteries. Indeed, if the CA has been diluted over time inside the circulatory system, the blood motion is not visible through the angiogram and the flow cannot be captured. That is why 3DRA or CT cannot be used for flow estimation: they require the injection of a long contrast product bolus. The CA saturates the vessel lumen so that contrast density fluctuations cannot be observed. Whereas, lower contrast loads are used in DSA. The mixability of contrast with arterial blood produces a **spatio-temporal modulation** of the CA. This modulation originates from the sharp and periodic pulsation that blood flow undergoes with heart

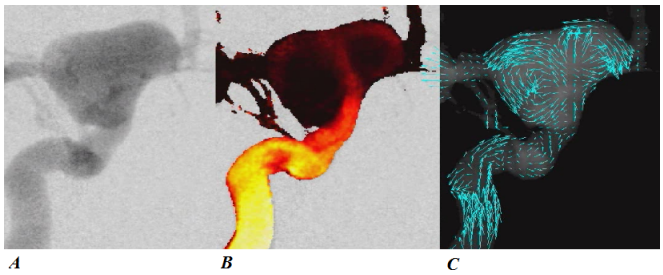

Figure 1.9: *DSA depicting an aneurysm. A: Original image sequence. B: The contrast was enhanced with post-processing. C: Vector field depicting the velocities of the contrast product estimated from an OFM.*

pumping (see section 1.3). This phenomenon can be observed several centimeters away from the injection point, were the CA starts to form a stable mixture [Lieber et al., 2009]. Also, the diffusion process tends to homogenize contrast after a long time, which explain why contrast has to be injected during the DSA examination.

DSA might stay the modality of choice for angiography and flow analysis, by benefiting from a high spatio-temporal resolution, by being minimal-invasive for the patient and by allowing cerebral imaging. The emission of ionizing radiations is nevertheless an inherent drawback to X-Rays, even with low dose utilization and image intensifiers. Furthermore, the functional flow evaluation in DSA is currently limited by the projective 2D geometry, which not only misses one dimension, but brings perspective complications with overlapped structures and **foreshortening** effect (X-Ray beams get even more absorbed when penetrating a vessel longitudinally, thereby skewing the contrast information).

1.2.3 Flow MRI

MRI techniques provide non-invasive, highly accurate anatomic depictions of the heart and vessels. The intrinsic motion sensitivity of MRI can be used to image vessels with phase contrast (PC) MR-angiography, or to quantify blood flow [Firmin et al., ,Dumoulin, 1995,Bock et al., 2010]. After 2D encoding techniques were invented [Pelc et al., 1991], the advent of 3D spatial encoding offered the ability to measure **3D time-resolved flow patterns** in vascular regions (aorta, cranial arteries, carotid arteries,...), making 4D flow MRI the modality with the richest amount of flow information ever acquired [Wigström et al., 1996, Markl et al., 2007].

Its potential is such that flow MRI becomes central in the analysis of complex flow pattern, associated with healthy and pathologic hemodynamics [Wetzel et al., 2007, Harloff et al., 2009,Uribe et al., 2009,Hope et al., 2010]. The possibility to determine the degree of blood turbulence with high order statistics of intra-voxel velocity distribution has been proven as a precious asset [Dyverfeldt, 2010].

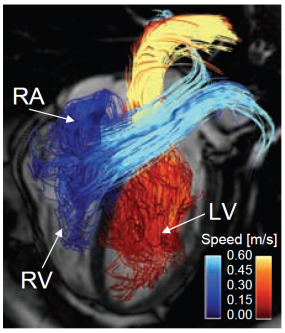

Figure 1.10: *Pathlines visualization of PC-MRI data in the heart. Blue pathlines show the flow in the right side of the heart while red ones show those in the left side. RA: Right atrium. RV: Right ventricle. LV: Left ventricle. This picture was reproduced from [Dyverfeldt, 2010], with the courtesy of Dr. Petter Dyverfeldt (Linköping University).*

The relatively long scan time of 3D flow MRI (several minutes) is today the only obstacle to its eligibility in clinical applications and large scale studies. Notwithstanding, several improvements can be expected on the acquisition time by using spatiotemporal correlation techniques in the dynamic data [Tsao et al., 2003], or optimizing the encoding mode from Cartesian approach to echo-planar imaging, or non-Cartesian k-space trajectories for example.

1.2.4 MPI

Magnetic particle imaging is a new imaging system invented in 2001 by *Gleich* and *Weizenecker* and presented for the first time in 2005 in Nature [Gleich and Weizenecker, 2005]. This **tracer imaging modality** uses the non-linear magnetization property of superparamagnetic iron oxide (**SPIO**) nano-particles. Similarly to its elder cousin MRI, MPI acquires images with the magnetic relaxation of particles in answer to a magnetic excitation. However, MPI does not use anatomic tissues to generate a signal, but the more powerful answer of an injected ferromagnetic contrast agent. The different **saturation behavior** of the ferro-particles allows to isolate their magnetization signal from that of other tissues. This new imaging concept gave rise to a totally new research field of medical imaging. Few years after being designed in Philips facilities, MPI is now at an exciting stage of development. This stage is similar to where MRI was in the early 1980s, when commercial MRI scanners and contrast agents were just being developed. Although a few handful preclinical prototype scanners have been constructed worldwide, there is a significant interest in this new imaging modality, especially from nuclear magnetic resonance (NMR) and MRI researchers.

MPI offers **quantitative 3D real-time** imaging at spatial resolutions comparable to other established modalities. One of its greatest advantage, compared to any other modality, lies in its ability to perform **background free** measurements. Because tissues are transparent to the excitation field (they contain no ferromagnetic components),

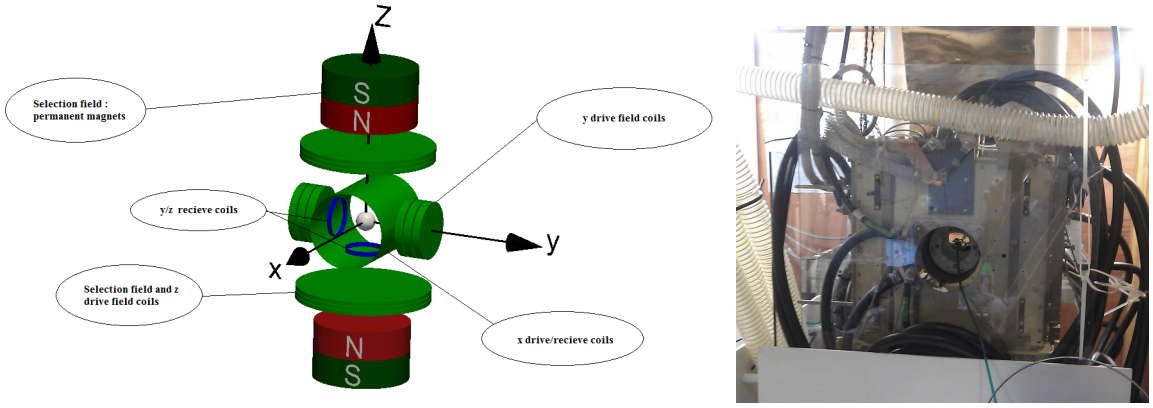

Figure 1.11: *On the left, a rough representation of an MPI device. It contains several sets of magnets and coils for the control of magnetic field during the acquisition procedure. The 3 directions are encoded, and some coils are used in both excitating the sample, and receiving the induced signal. On the right, a photo of the unique 3D MPI prototype in a laboratory of Philips Hamburg.*

we only detect the SPIO nanoparticles injected into the body.

The first in-vivo acquisitions were recently demonstrated on living mice [Weizenecker et al., 2009], where heartbeat and motion of vascular structures were imaged (see figure 1.12). A bolus of SPIOs was injected into the tail vein of the animal, and revealed the propagation of the magnetic tracer into the bloodstream. The background free and high sensitive signal of the nanoparticles image very clearly the shape of the heart chambers, and the wall motion during the cardiac cycles. From that start, several potential applications were envisioned, among which stand human angiography, cancer imaging, in vivo-cell tracking, and inflammation imaging.

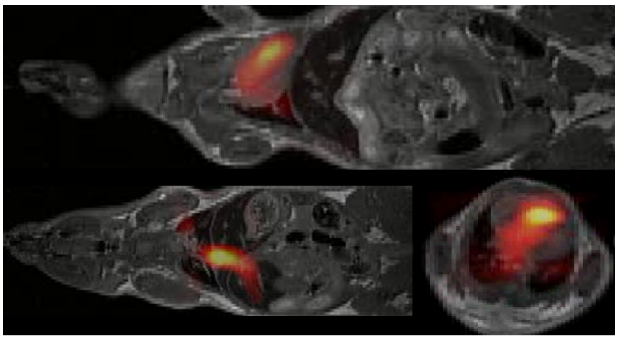

Figure 1.12: *Three orthogonal slices of a fused MRI-MPI mouse scan. The grey scale intensity corresponds to MRI acquisition, while the jet color code depicts the MPI signal intensity (i.e magnetic nanoparticles concentration).*

The potential of MPI

MPI could become the modality of choice for diagnoses requiring a fast blood flow estimation, namely the artery diseases (stenosis, aneurysms) and heart malfunctions. Its high 3D acquisition speed and fine data resolution are serious assets for quantitative analysis of **contrast propagation** in arteries. For the moment, the MPI system is not fully developed and human acquisitions are still not available. Technical improvements in MPI hardware have to be addressed, which will favor new image acquisitions with higher resolution in large animals. Nevertheless, it can be expected in the upcoming years that this totally new tomographic device will challenge gold-standard cardiovascular modality (Doppler US, DSA or flow MRI) in the diagnostic of cardiac diseases and the use in interventional procedures [Duschka et al., 2013].

Compared to today's standards in medical imaging such as CT, MRI and PET, this new modality combines several advantages of each of them. MPI offers the potential of achieving a higher sensitivity in detection of tracers, compared to the detection of contrast agents in MRI or CT with a good spatial as well as high temporal resolution [Buzug et al., 2012]. While the current setting of SPIOs and hardware allows a **1 millimeter** spatial resolution scale, in theory even a resolution of 250 micrometer and a sensitivity of 20 nanomolar appears feasible [Goodwill et al., 2012]. Acquisition rates of over **40 volumes per second** have already been demonstrated [Weizenecker et al., 2009]. Another benefit arises from using magnetic fields instead of ionizing radiation. Human tissue is diamagnetic [John, 1996] and thus is not expected to generate any MPI signal. As a consequence no anatomical background is picked up by the system and interferes with the structures of interest, resulting in an excellent contrast. Furthermore, SPIOs generate a signal that is proportional to the amount of particles in the FoV, thus allowing a true **quantitative** analysis. Currently the main drawback is the small FoV, which does not exceed **several centimeters** per dimension.

Considering this unique combination of characteristics, MPI is a method with great promise for a number of applications, including cardiovascular imaging or even cardiovascular interventions.

1.3 Contrast modulation in arteries: the fingerprint of blood propagation

This section will prepare the ground for the main chapter and contribution of my thesis: the blood flow estimation in tracer modalities. Without ignoring all the potential of flow MRI and Doppler US in blood flow analysis, we chose to focus exclusively on **DSA** and **MPI** images, which both have in common to provide time-resolved contrast information.

1.3.1 Blood flow in arteries

The primary purpose of the circulatory system is to drive, control, and efficiently maintain the blood flow in vessels, so as to continuously supply organs with oxygen and nutrients. A healthy artery is relatively free of turbulence, it efficiently transports blood components in a laminar flow with few resistance. Researchers created a science specific to hydrodynamics of cardiovascular system called **hemodynamics**. The way blood propagates into arteries can be modeled by few mechanical laws, including:

- The mass conservation equation:

$$\frac{\partial \rho}{\partial t} + \nabla \cdot (\rho \mathbf{v}) = 0 \tag{1.4}$$

- The momentum conservation equation:

$$\rho(\frac{\partial \mathbf{v}}{\partial t} + \mathbf{v} \cdot \nabla \mathbf{v}) = -\nabla p + \mu \nabla \mathbf{v} \tag{1.5}$$

With ρ being the blood density, μ the dynamic blood viscosity, p the local blood pressure, and $\mathbf{v}$ the blood velocity. The density $\rho \simeq 1060 kg/m^3$ can be considered as constant, which yields the **incompressibility** equation:

$$\nabla \cdot \mathbf{v} = 0 \tag{1.6}$$

The blood viscosity however, varies within a range between 4.10^{-3} Pa.s and 25.10^{-3} Pa.s, with an average of 6.10^{-3}Pa.s. Blood can be categorized as a **non-Newtonian fluid**: its viscosity depends on the applied shear rate.

The **flow rate** Q is the quantity of fluid matter flowing during a time unit. It can also be defined as the net flux of fluid displacement vectors $\mathbf{v}$ through a tube cross section $\mathcal{C}$:

$$Q = \iint_{\mathcal{C}} \mathbf{v} \cdot \mathbf{dS} \tag{1.7}$$

An important property of the flow rate is that it must be kept constant along the flow conduct. The divergence equation (1.6) together with *Green-Ostrogradski* divergence theorem gives:

$$\iiint_{cylinder} (\nabla.v)d\tau = 0 \tag{1.8}$$

$$\oiint_{cylinder} \mathbf{v} \cdot \mathbf{dS} = 0 \tag{1.9}$$

$$\iint_{inlet} \mathbf{v} \cdot \mathbf{dS_{inlet}} + \iint_{wall} \mathbf{v} \cdot \mathbf{dS_{wall}} + \iint_{outlet} \mathbf{v} \cdot \mathbf{dS_{outlet}} = 0 \tag{1.10}$$

$$Q_{inlet} = Q_{outlet} \tag{1.11}$$

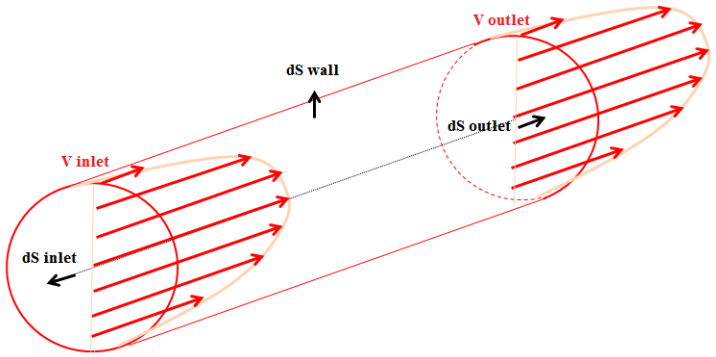

Figure 1.13: *Cylindrical artery with conservation of flow rate.*

As a result, the flow rate constancy between inlet and outlet is verified, provided that there are no leaks along the arterial wall, i.e:

$$\mathbf{v_{wall}} \cdot \mathbf{dS_{wall}} = 0 \tag{1.12}$$

The flow rate conservation should be respected in every segment of the arterial network, at any time. It is a strong indicator of the flow reliability to fluid mechanics. As will be seen in later chapters, there are substantial numerical difficulties to capture complex velocity patterns that satisfy flow rate conservation.

Poiseuille flow

The simplest example of flow in the cardiovascular system would be a long and straight tube, undergoing no pulsatility nor turbulence, with a steady flow rate. Such a flow is well-known to be modeled by the *Poiseuille equation* (1.13), which states that the pressure drop Δp along the tube is directly proportional to the length l of the tube, the flow rate Q,the viscosity μ, and inversely proportional to the fourth power of the internal radius r [Ku, 1997]:

$$\Delta p = \frac{8\mu l}{\pi r^4} Q \tag{1.13}$$

with $R = \frac{8\mu l}{\pi r^4}$ the flow resistance.

This formula shows the strong dependency of flow resistance to the radius of artery. This is particularly true in stenotic artery portions, where the small lumen radius increases flow resistance, thereby provoking a higher harmful pressure drop Δp between the inlet and the outlet.

A simple implementation of the **first Newton's law** on viscous and pressure forces inside the artery (figure 1.13) yields the well-known parabolic velocity profile:

$$\boxed{v(r) = v_0(1 - \frac{r^2}{R^2})} \tag{1.14}$$

Where r stands for the coordinate along the tube radius, R is the tube radius, and v_0 is the maximum velocity on the tube center.

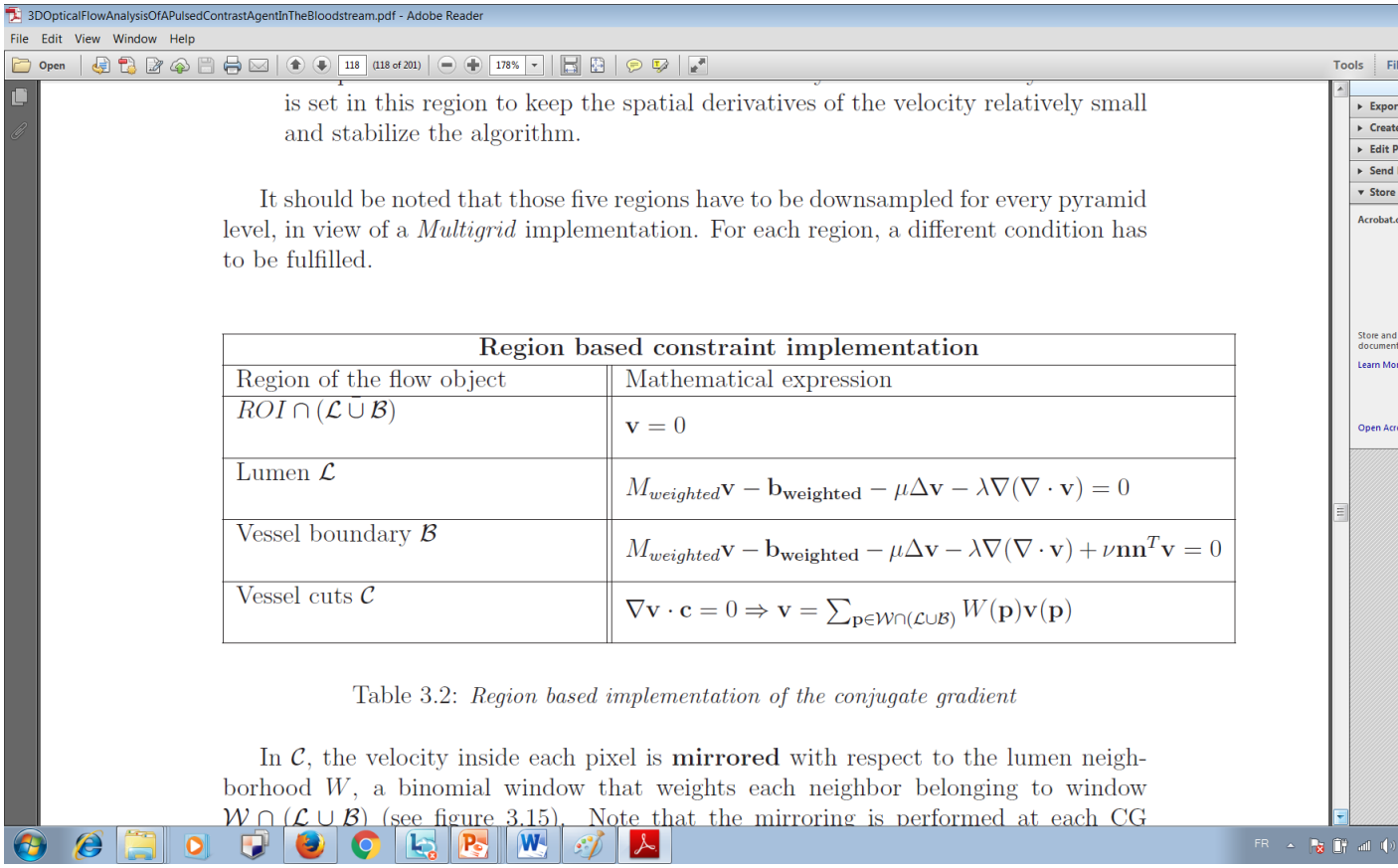

Figure 1.14: *Slice of the artery (figure 1.13) where the velocity follows a parabolic profile depending on the lumen radius.*

The flow profile in arteries approximately respects this law for long and straight vessel portions, with very few pulsatility. Indeed, this is only a simple approximation of flow behavior since pulsatility causes the flow profile to drift from *Poiseuille* profile. Flow particles slow down due to the boundary layer and by assumption that there is no slippery between wall and particles:

$$v(R) = 0 \tag{1.15}$$

Flow regime and pulsatility

In the limit layer, the viscous forces dominate the flow inertia, eliminating the small-scales turbulence. Whereas, flow generally tends to be more turbulent away from this layer. The number that quantifies the flow regime is referred to as the dimensionless **Reynolds number**, it measures the ratio between inertia forces and viscous dissipation forces:

$$Re = \frac{\rho v D}{\mu} \tag{1.16}$$

With D being the characteristic linear dimension of the flow, here the vessel diameter. This number characterizes the **global flow regime** of the conduct, as opposed to local. In the cardiovascular system, the range of Re stands between 1 for the small arterioles and 4000 for the great arteries as aorta [Ku, 1997]. However, this number generally stays within laminar range ($Re < 2000$), with 150 for right coronary artery, 220 for internal carotid, 240 for left main coronary, 280 for femoral artery, and 330 in the common carotid [Wootton and Ku, 1999b].

Another typical characteristic of arterial flow is **pulsatility**. The heart pumping causes the blood flow velocity to oscillate as the valves intermittently close and open with each beat of the heart. In most parts of the arterial network, the blood undergoes a sharp pulsation, wherein velocity profiles are distorted and strongly drifted from parabolas such as in equation (1.14). Instead, more complex pattern can be oberved [Ku, 1997], including several crests with reversed parabola, or also flat profiles. The **Womersley** number α especially quantifies pulsatile flows with:

$$\alpha = R(\frac{\omega\rho}{\mu})^{1/2} \tag{1.17}$$

with ω the pulsation frequency.

This dimensionless number α is important in describing the pulsatile flows, since it gives an idea of the ratio between pulsation frequency and viscous effects, irrespective of the flow geometry.

Among the general properties of blood flow described above, pulsatility is the most interesting for the study of the propagation of a CA. The next section describes how blood pulsatility can help solving the equations of contrast propagation and eventually retrieve blood flow information.

1.3.2 Contrast behavior in arteries

Because the blood flow information is not directly accessible to DSA and MPI devices, one has to use the CA as a marker, or a **fingerprint of the bloodflow propagation**. A CA dragged by the blood flow can be approximated by the **scalar transport equation**, whose expression reads:

$$\frac{\partial c}{\partial t} = \nabla \cdot (D \nabla c) - \nabla \cdot (c\mathbf{v}) + R \tag{1.18}$$

with c the CA concentration, D the diffusion coefficient of the said contrast in blood, and R describing 'sinks' or 'source' contrast quantities.

This equation can be highly simplified, considering the very weak diffusivity of contrast into blood ($D \simeq 0$), and also the absence of contrast sources and sinks ($R = 0$), excepted at injection point. The scalar transport equation is then:

$$\frac{\partial c}{\partial t} + \nabla \cdot (cv) = 0 \tag{1.19}$$

By bringing the incompressibility equation (1.6) into (1.19), we obtain the **simplified scalar transport equation** that relates the contrast concentration c with the blood velocity $\mathbf{v}$:

$$\boxed{\frac{\partial c}{\partial t} + v \cdot \nabla c = 0} \tag{1.20}$$

A model for constrast injection

When injecting the CA within an artery, blood and contrast material mix. The contrast flow rate Q_c is added to blood flow rate Q_b. The tracer concentration $c_{injected}$ is diluted in the total flow $Q = Q_b + Q_c$:

$$c = \frac{Q_c}{Q_b + Q_c} c_{injected} \tag{1.21}$$

In arteries, blood flow Q_b can be split into two components: a constant component Q_0 and a pulsatile component $Q_p(t)$: $Q_b(t) = Q_0 + Q_p(t)$.

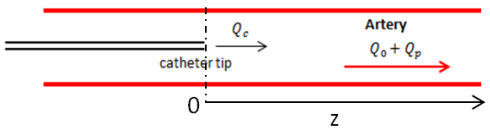

Figure 1.15: *Catheter tip injecting the contrast flow rate Q_c inside the arterial lumen wherein blood flow rate is the superposition of a constant flow Q_0 and a pulsatile flow Q_p.*

During the end diastole, the flow rate is the lowest and the pulsatile component is nearly 0: $Q_p(t) \simeq 0$. The contrast concentration is at its highest:

$$c_{max} = \frac{Q_c}{Q_c + Q_0} c_{injected} \tag{1.22}$$

Whereas during systole, $Q_p(t)$ increases, and the contrast is diluted according to:

$$c(t) = \frac{Q_c}{Q_c + Q_0 + Q_p(t)} c_{injected} \tag{1.23}$$

The concentration variation $\delta c(t)$ during a cardiac cycle is then:

$$\delta c(t) = c_{max} - c(t) \tag{1.24}$$

Under the assumption that the contrast flow rate Q_c can be neglected compared to blood flow, it comes:

$$\boxed{\delta c(t) \simeq \frac{Q_c Q_p(t)}{(Q_c + Q_0)^2} c_{injected}} \tag{1.25}$$

As $Q_p(t)$ is pulsatile, this proves that the concentration $c(t)$ is made up of a constant component c_{max} and a **pulsatile component** $\delta c(t)$. Thanks to the natural blood flow modulation, a **temporal modulation of CA density** can be achieved at the injection point.

A model for contrast propagation and modulation

After injection, the contrast patterns are dragged by the bloodstream within the arterial network. Unfortunately, the transformation the CA undergoes with blood pulsatility is not linear. Contrast information far from the injection point does not follow velocity variations. However, in order to evaluate the flow far from the injection point, one can rely on the **local scalar transport equation** (1.20). For the sake of simplification, let us consider a flow inside a straight artery of longitudinal axis z. At the injection point $z = 0$, the concentration function $c_0(t) = c(0, t)$ is periodic with the cardiac period T. At a sufficiently small distance z from the injection point, such that the time of flight of a fluid particle is very small compared to the heart period T, the contrast $c(z, t)$ in adequation with the transport equation verifies:

$$c(z, t) = c_0(t - \frac{z}{v(t)}) \tag{1.26}$$

where $v(t)$ is the flow velocity.

Given the periodicity of $c_0(t)$ and $v(t)$, we can deduce the periodicity of $c(z, t)$ with the same cardiac period T:

$$c(z, t + T) = c_0(t + T - \frac{z}{v(t + T)}) = c_0(t - \frac{z}{v(t)}) = c(z, t) \tag{1.27}$$

This reasoning can be further extended to the transport between z and $2z$, $2z$ and $3z$, and so on. Hence, the temporal periodicity can be asserted for the whole arterial mesh.

On top of that, a pseudo **spatial modulation** can be noticed. Indeed, if we choose to neglect the pulsatile velocity component with respect to average velocity $\hat{v}$, we can approximate on the first order:

$$c(z + \hat{v}T, t) \simeq c_z(t - T - \frac{z}{\hat{v}}) \simeq c_z(t - \frac{z}{\hat{v}}) = c(z, t) \tag{1.28}$$

Indeed, this equation is inexact, especially for large waves. With a heart frequency of $1.2Hz$ and an average velocity of $20cm.s^{-1}$, we get a spatial wavelength $L = 16cm$, which is way sufficient for the wave to undergo distortion. Since the velocity is not steady during the contrast transport, and might also be subject to spatial variations, the **contrast wave** is non linearly propagated by blood flow.

Nevertheless, the time **periodicity** of contrast concentration with a heart period T can be used to decompose $c_0(t)$, the contrast at the injection point, as a *Fourier* serie:

$$\boxed{\hat{c}_0(t) = \sum_{n=-\infty}^{+\infty} C_n e^{j2\pi n f_c t}} \tag{1.29}$$

with $f_c = \frac{1}{T}$ the cardiac frequency, approximated as constant during the injection, C_n the complex *Fourier* coefficients of the contrast density, and n the n-th harmonic of the cardiac frequency.

At a small distance z from the injection, the local transport equation is:

$$\hat{c}(z, t) = \sum_{n=-\infty}^{+\infty} C_{n,z} e^{jn\omega_c(t-z/v)} = \sum_{n=-\infty}^{+\infty} C_{n,z} e^{jn(\omega_c t - k_c z)} \tag{1.30}$$

where $\omega_c = 2\pi f_c$ is the angular cardiac pulsation and $k_c = \frac{\omega_c}{v}$ is the **wavenumber** or fundamental spatial frequency of the wave. Now consider the local scalar transport equation (1.20) along z axis, the $1D$ equation is:

$$\frac{\partial \hat{c}}{\partial t} + v\frac{\partial \hat{c}}{\partial z} = 0 \tag{1.31}$$

The scalar transport equation is actually what allows to estimate the blood flow v, based on the contrast concentration c. However, if the spatial derivative $\frac{\partial \hat{c}}{\partial z}$ vanishes, the velocity gets undefined and the above equation is not possible to solve. This pitfall will be better investigated in chapter 2. Developing the spatial gradient from equation (1.30) yields:

$$\|\frac{\partial \hat{c}}{\partial z}\| = k_c \| \sum_{n=-\infty}^{+\infty} n C_n e^{jn(\omega_c t - k_c z)} \| \tag{1.32}$$

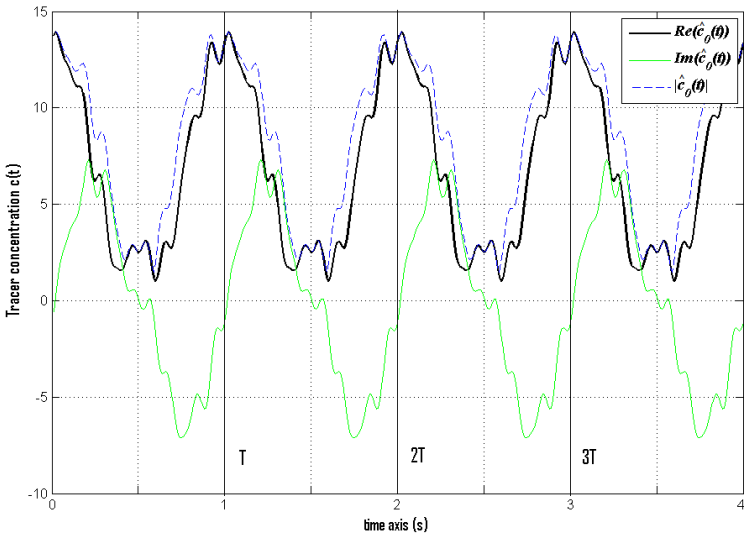

Figure 1.16: *Example of concentration-time curve at the injection point. The concentration is periodic with period T. The real part of Fourier signal is displayed as the black curve, the imaginary part corresponds to the green curve and the dashed blue line to the instantaneous modulus.*

where $k_c > 0$.

The modulus of the complex derivative signal should not cancel. Since the real part and the imaginary part are in quadrature, they cannot nullify at the same time. At least one frequency component $C_1 \neq 0$, so the term in equation(1.32) should not cancel out. If no pulsatility was present in the CA signal, the concentration would be homogeneous and the blood flow invisible on the image sequence. Thanks to the fundamental periodicity of the CA density, the modulus of the complex concentration gradient is always carrying information. We could argue indeed that the real part of contrast serie (1.30) can exhibit some spatial extrema, but the information of the imaginary part can be used to overcome this issue, as described later in section 3.2.2. Another complication could arise from infinite velocity v, which would cancel k_c and bring down the possibility to capture a gradient information. This very situation is not met in reality, but can bring numerical issues when velocity is large compared to the field of view. This problem will be also discussed in the next chapter.

The above simplified equations show that contrast modulation is paramount in blood flow assessment. It can be exploited to solve the scalar transport equation (1.20) and finally estimate blood velocity. Without modulation, the contrast tends to get homogeneous over time. Typically, this natural phenomenon allows researchers to track the propagation of CA in DSA sequences.

*

* *

In this chapter, we evoked the damages of CVDs and the burden it represents for global healthcare today. The main responsible for these is the corruption of vessel morphology as encountered in stenosis and aneurysms. Evidences have shown that hemodynamics play a role in the initiation and evolution of a cardiovascular pathology. To further understand the pathogenesis of CVDs, and to improve both diagnostics and treatments, medical flow imaging was developed. MRI flow and Doppler US have pioneered this field with great promises, but are still not able to combine both accuracy and real-time. On the other hand, the DSA and the emerging MPI feature as good candidates in the extraction on flow information, with high speed/accuracy compromise. The main information on which they rely is the contrast displacement and modulation inside the arterial flow. As a reminder of the thesis, the chapter 2 will present the main state-of-the art techniques about **optical flow estimation**, and chapter 3 will detail the image processing method developed during this thesis to assess blood flow estimation. The following chapters 4 and 5 will present different applications of the optical flow techniques, based on *in-silico*, *in-vitro* and *in-vivo* evaluations.

Chapter 2

State of the art on optical flow

Contents

Abstract

The previous chapter outlined advantages of contrast modalities providing images of the tracer displacement at a very good temporal resolution. Nowadays, numerous image processing techniques have been developed in order to estimate motion inside image sequences. Since the *Lucas-Kanade* algorithm was proposed in 1981 [Lucas and Kanade, 1981], the approach became a widely used technique for providing a solution to the computer vision optical flow problem. The information of **optical flow**, which forms the basis of this manuscript, is central in the analysis of image sequences, and particularly in medical imaging. After a short definition of optical flow, the main difficulties related to flow estimation, such as the aperture problem, the large displacement, the occlusions, and the spatial and temporal aliasing will be discussed. Numerous authors try to overcome these issues by employing regularization schemes. The main state of the art techniques will then be presented as a technical background for the next chapters. Finally, the downsides and advantages of each method will be summarized, and will contribute to find the best suited technique for the blood flow estimation problem.

Résumé

Dans le chapitre précédent, l'avantage des modalités à contraste imageant le déplacement du traceur avec une fine résolution temporelle a été mis en avant. Aujourd'hui, de nombreuses techniques de traitement d'image ont été développées afin d'estimer le mouvement dans les séquences d'images. Depuis que l'algorithme de *Lucas-Kanade* a été proposé en 1981 [Lucas and Kanade, 1981], leur méthode différentielle est largement utilisée pour résoudre des problèmes de flot optique en vision par ordinateur. L'information du **flot optique**, qui forme la base de ce manuscrit, est centrale dans l'analyse des séquences d'images, et particulièrement en imagerie médicale. Après une brève définition du flot optique, les difficultés principales liées à l'estimation de flux, telles que le problème de l'ouverture, les grand déplacements, les occlusions, et le repliement spatiotemporel seront abordées. De nombreux auteurs tentent de surmonter ces problèmes en employant des méthodes de régularisation. L'état de l'art portant sur ces méthodes sera presenté de façon à fournir une base théorique pour le prochain chapitre. Enfin, les avantages et inconvénients de chaque méthode seront résumés, ce qui contribuera au choix d'une technique adaptée au problème d'estimation du flux sanguin.

2.1 Optical flow principle

Optical flow refers to the apparent motion of objects, surfaces and edges in a visual scene caused by the relative motion between an observer (eye or camera) and a scene. The term has been proposed by roboticists to describe image processing techniques related to motion detection, object segmentation, time-to-contact information, motion compensation, and stereo disparity measurement [Aires et al., 2008, Beauchemin and Barron, 1995]. Industrial applications of optical flow are countless. They range from defense (vision in rocket science), meteorology (turbulence studying in weather radar images), cinema post-production (image stabilization and blurring), fluid mechanics (flow analysis), computer hardware (optical mice sensors) to medical imaging (breathing stabilization, surgical tools tracking, myocardium tracking, flow estimation).

Basically, a 3D moving object is recorded by means of a camera or another video acquisition system. The resulting 2D or 3D image sequence, in which intensity changes occur, allows to derive the movement of pixels in the image, i.e the optical flow.

First, let us define an image I as a function of time and space:

$$I : \begin{cases} \mathbb{R}^N \times \mathbb{R}^+ \longrightarrow \mathbb{R} \\ (\mathbf{x}, t) \longmapsto I(\mathbf{x}, t) \end{cases}$$

$\mathbf{x}$ is the *N-dimensional* vector at which image I is evaluated, and t corresponds to the time of the image sequence. Generally, N ranges between 1 and 3. The most common is the case of images (N=2) where $\mathbf{x}$ refers to a pixel (or '**pict**ure **el**ement'). In medical imaging, 3D volumes (N=3) are also studied and described by voxels (**vo**lumetric pi**xel**s). In some rare cases, one can also choose to study changes of intensity along a line (N=1), which is the simplest.

When a small displacement $d\mathbf{x}$ occurs in the image sequence, the assumption of **brightness constancy** between point $\mathbf{x}$ at time t and $\mathbf{x} + d\mathbf{x}$ at time $t + dt$ yields:

$$\boxed{I(\mathbf{x} + d\mathbf{x}, t + dt) = I(\mathbf{x}, t)} \tag{2.1}$$

Developing the left hand side term of the equation (2.1) for infinitely small time step dt results in:

$$I(\mathbf{x} + d\mathbf{x}, t + dt) = I(\mathbf{x}, t) + \nabla I \cdot d\mathbf{x} + \frac{\partial I}{\partial t} dt \tag{2.2}$$

$$\Longrightarrow \nabla I \cdot d\mathbf{x} + \frac{\partial I}{\partial t} dt = 0 \tag{2.3}$$

Finally, dividing both sides by dt yields:

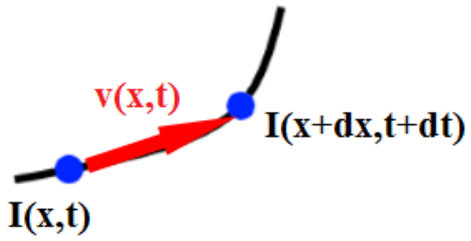

Figure 2.1: *Brightness constancy of the object during motion.*

$$\boxed{\nabla I \cdot \mathbf{v} + \frac{\partial I}{\partial t} = 0} \tag{2.4}$$

where $\mathbf{v} = \frac{d\mathbf{x}}{dt}$ is the instantaneous velocity of the moving object.

This is the general **optical flow equation** that allows to relate image intensity to the motions occurring inside the sequence. It can be strongly compared with the scalar transport equation (1.20) obtained in section 1.3.2 when assuming pure convection. Indeed, in the case of DSA or MPI, the intensity I captured by the imaging system is proportional to the tracer concentration c, both corresponding to the same information. The scalar transport equation being linear turns to the optical flow equation, and contrast can be regarded as the image intensity.

Yet if we consider digital image sequence, $\mathbf{x}$ and t take discrete values. We do not rely on infinitesimal values but on the inter-frame difference (two consecutive time samples $\Delta t = t_2 - t_1$) and the displacement vector $\Delta\mathbf{x}$ between two frames. As a consequence, the brightness constancy equation (2.1) is not exactly true. Instead, we have to resort to a *Taylor-Lagrange* expansion, reading:

$$I(\mathbf{x}+\Delta\mathbf{x}, t+\Delta t) = I(\mathbf{x},t) + \nabla I \cdot \Delta\mathbf{x} + \frac{1}{\Delta t}(I(\mathbf{x},t+\Delta t) - I(\mathbf{x},t)) + \frac{1}{2}\Delta\mathbf{x}^T H \Delta\mathbf{x} + h.o.t \tag{2.5}$$

Here the serie is expanded to the 2nd order ($H = \frac{\partial I}{\partial x_i x_j}$ is the Hessian matrix), while for more accuracy, one should use higher-order terms (h.o.t). In practice, we can assume that the **displacement $\Delta\mathbf{x}$ is small**, so that 1st order approximation is reasonably accurate. By using the constancy of intensity (equation (2.1)), we obtain the discretized version of optical flow constrain (2.4):

$$\nabla I(\mathbf{x},t) \cdot \Delta\mathbf{x} + \frac{1}{\Delta t}(I(\mathbf{x}, t+\Delta t) - I(\mathbf{x},t)) \simeq 0 \tag{2.6}$$

The difference of this equation lies in the nature of the solution that describe a **displacement vector**, and not an instantaneous velocity. Moreover, the equation is only an **approximation** at the first order of the true displacement, meaning that the solution can be inaccurate especially for large displacements. This leads to numerous numerical problems that will be tackled in section 2.4.

2.2 The aperture problem

The optical flow recovery is an inverse problem that wishes to retrieve the flow vectors from image intensity information. However, as many inverse problems, optical flow is **ill-posed**. In the sense of *Hadamard* ([Hadamard, 1902]), an ill-posed problem is met when small perturbations of the initial data (i.e the optical flow) create large fluctuations in derivative of the solution (i.e the image derivatives) [Poggio and Yuille, 1986]. Here, the ill-posedness manifests itself in the nonuniqueness due to the aperture problem [Bertero et al., 1988]. The optical flow equation generally include 2 or 3 unknown components of the velocity $\mathbf{v}$, while the constraint consist of only one equation (2.4). As a result, the velocity vector cannot be solved straightforwardly. Instead, one can only compute the optical flow component aligned with image gradient:

$$v_{\parallel} = \frac{-\frac{\partial I}{\partial t}}{\|\nabla I\|} \tag{2.7}$$

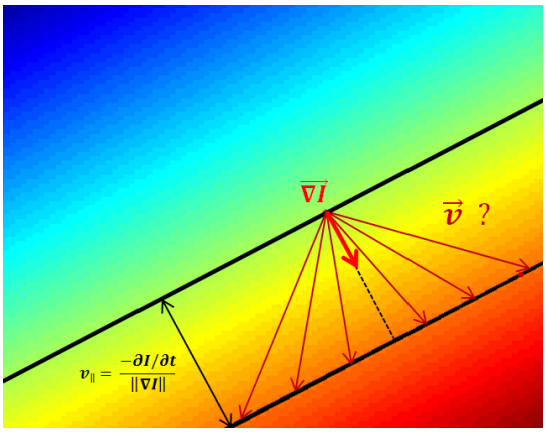

Figure 2.2: *Aperture problem in optical flow: the points described by the black line have moved downward the image. The displacement component $v_{\parallel}$ parallel to the image gradient ∇I is known, while the perpendicular component $v_{\perp}$ is undefined, allowing infinite number of solutions.*

Because velocity $\mathbf{v}$ is projected onto the gradient vector ∇I, the normal component to the image gradient $v_{\perp}$ is irrelevant in equation (2.4). Any value will verify the optical flow equation, as illustrated in figure 2.2.

As a result, the optical flow constraint lacks one information about the **velocity component normal to the image gradient**. Only a basic assumption about flow being parallel to the gradient can provide a solution, which is seldom true in a real image sequence.

2.3 Regularization of the optical flow

In order to solve the optical flow problem, other additional constraints need to be introduced. Basically the idea is to remove the underdetermination of equation (2.4) by adding regularization terms and to impose the solution uniqueness. The solving of the optical flow equation will then be achieved by the convex optimization of an optical flow energy E. The general formulation of a regularized optical flow solution could be written as follows:

$$\boxed{\begin{aligned} &\mathbf{v}^\star = \ argmin_{\mathbf{v}} E(\mathbf{v}) \\ &E(\mathbf{v}) = \ (\nabla I \cdot \mathbf{v} + \frac{\partial I}{\partial t})^2 + \mathcal{R}(\mathbf{v}, \partial\mathbf{v}, ..., \partial^n\mathbf{v}) \end{aligned}} \tag{2.8}$$

where $\mathbf{v}^\star$ is the solution vector and $\mathcal{R}$ is a **convex** quadratic function to insure the convergency and the uniqueness of $\mathbf{v}^\star$.

Numerous algorithm have been proposed and a wide variety of extensions have been made to the original formulation. In a survey, [Beauchemin and Barron, 1995] mentioned six classes of methods. However, a simpler classification can be made by considering **local** and **global** strategies. Local methods use the **spatial constancy** assumptions of the optical flow in a small neighborhood surrounding the pixels. They offer relatively **high robustness under noise**, but do not give dense flow fields. Global methods, on the other hand, yield flow fields with **100% density**, but are experimentally known to be more sensitive to noise [Barron et al., 1994, Galvin et al., 1998]. A typical way to overcome the ill-posedness problems in global methods consists in making use of smoothing techniques and **smoothness assumptions**. The most famous global method is the one of *Horn and Schunck* that attempts to minimize the gradient of the flow field [Horn and Schunck, 1981]. Both local and global approaches are described hereinafter.

2.3.1 Local Optical flow methods

Examples of the first category include the *Lucas-Kanade* method [Lucas and Kanade, 1981] and the structure tensor approaches of *Bigün* [Bigun and Granlund, 1988, Bigun et al., 1991]. The most widespread technique is the one of *Lucas- Kanade*. It assumes that inside a small window of the image $\mathcal{W}$ surrounding the pixel at $\mathbf{x}$, the velocity $\mathbf{v}$ is constant. It basically uses a weighted least squares method to approximate the

optical flow at a specific location. This approach is local since the energy corresponds to only one pixel $\mathbf{x}$:

$$E_{\mathbf{v}}(\mathbf{x}) = \sum_{\mathbf{p}\in\mathcal{W}} W(\mathbf{p}) \left[\nabla I(\mathbf{p}) \cdot \mathbf{v} + I_t(\mathbf{p})\right]^2 \tag{2.9}$$

where I_t is the interframe difference and W represents a weighting function inside the window $\mathcal{W}$. This weighting should favor pixels in the center of the window so as to enhance local fidelity, and should sum up to 1 in the window. W is often chosen as *Gaussian* since the scale of the movement can be easily adapted according to the **standard deviation** of the gaussian function.

The energy E is minimized for each pixel independently, assuming one unknown vector $\mathbf{v}$. It represents the sum of quadratic errors between the regressed velocity and the individual data fidelities of the window. The above *least mean square error* (LMSE) (2.9) minimization:

$$\frac{\partial E_{\mathbf{v}}(\mathbf{x})}{\partial \mathbf{v}} = 0 \tag{2.10}$$

leads to following system:

$$M\mathbf{v} = \mathbf{b} \tag{2.11}$$

where $M = \sum_{\mathcal{W}} W \nabla I \nabla I^T$ is the **gradient tensor** averaged and weighted in the neighborhood of $\mathbf{x}$ and $b = \sum_{\mathcal{W}} -W^2 I_t \nabla I$ is the right hand side vector term containing temporal information. For instance in 2D images, the matrix M can be further written as follows:

$$M = \begin{pmatrix} \sum W I_x^2 & \sum W I_x I_y \\ \sum W I_y I_x & \sum W I_y^2 \end{pmatrix} \tag{2.12}$$

The system (2.11) is solved in each point $\mathbf{x}$ by inverting the inertia tensor M. As any symmetric real matrix, M can be diagonalized and decomposed in a new coordinate system defined by **eigenvectors $\mathbf{e_1}$** and **$\mathbf{e_2}$**. These vectors define the axis along which the data are scattered inside $\mathcal{W}$, and the **eigenvalues** roughly describe the average gradient components on these axis. The key idea is that inside a local image window, one should collect a sufficient number of gradient samples so that the average gradient information does not cancel out in any direction and the aperture is dealt with. For the system to be safely inverted, the matrix M needs to be **well-conditioned**, i.e to have a low **condition number**. The condition number can be defined as:

$$C(M) = \frac{\lambda_{max}(M)}{\lambda_{min}(M)} \tag{2.13}$$

where $\lambda_i (i \in [1\, N])$ represents the eigenvalues of M. If the conditioning number is close to 1, the matrix is well-conditioned, and can be inverted properly. In our case, this

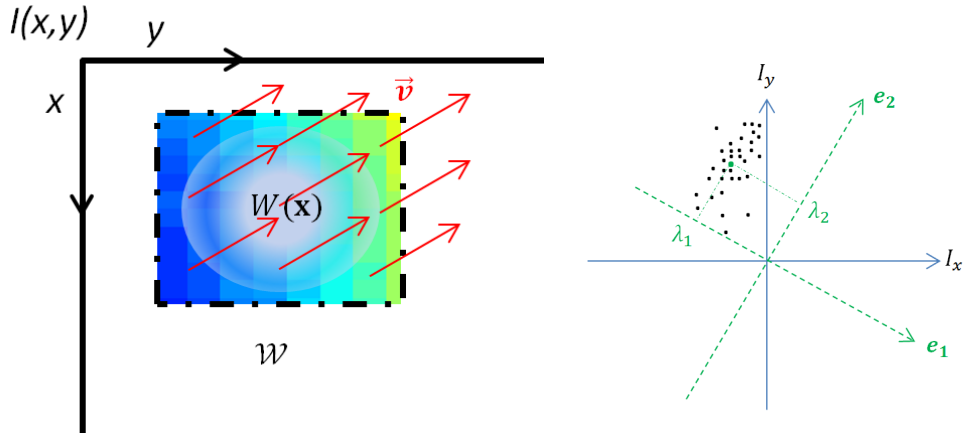

Figure 2.3: *Left: Least mean square estimation of the constant optical flow vector* $\mathbf{v}$ *in the window* $\mathcal{W}$*. Right: gradient components* I_x *and* I_y *inside* $\mathcal{W}$*, with direction of eigenvectors* e_1 *and* e_2*, the main axis of data scattering. The eigenvalues* λ_1 *and* λ_2 *are related to the average gradient vector.*

means that average gradient components are evenly distributed along each eigenvectors, or that gradient information is strong enough in each axis to provide a reliable flow vector. If the condition number is very large ($C > 1000$), at least one component of the gradient information is missing and the system will be badly inverted. The inversion will be very sensitive to small variations of vector $\mathbf{v}$ and the flow recovery will be highly unstable and inaccurate. The ratio between eigenvalues, i.e the conditioning can be visually understood by looking at the local contrast information around a questioned pixel:

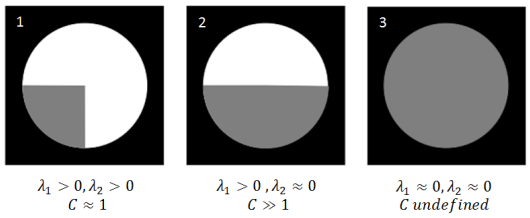

Figure 2.4: *Eigenvalues of 2D tensor matrices for different cases of gradient information. In 1., two eigenvalues are strictly positives, which happen in the case of corners or points with high curvature. The window collects all information needed to assess a 2D flow vector. In 2., one eigenvalue vanishes resulting in ill-conditioning and bad system inversion. Edges with low curvature are typical of this problem since they cannot provide information about the velocity component parallel to the edge (aperture problem met in section 2.2). 3. exhibits a constant intensity information, which brings down the possibility of flow recovery. Well conditioning can be obtained indeed if both eigenvectors are very close to each other, but the vanishing gradient information will be present in both* M *and* $\mathbf{b}$*, leading to a singularity and an unpredictable solution.*

Here we see that the conditioning of M is paramount in the achievement of accurate flow estimation. According to the scale of the regression window, more or less information can be captured. Nevertheless it happens in some locations that the scale of the aperture effect is greater than the window size, and well-conditioning cannot be obtained. In this case, we generally resort to a *Thikonov* regularizer [Tikhonov, 1943]:

$$E_{\mathbf{v}}(\mathbf{x}) = \sum_{\mathbf{p}\in\mathcal{W}} W(\mathbf{p}) \left[\nabla I(\mathbf{p}) \cdot \mathbf{v} + I_t(\mathbf{p})\right]^2 + \|\Gamma\mathbf{v}\|^2 \tag{2.14}$$

Penalizing the l_2-norm of $\mathbf{v}$ allows to control the instabilities that ill-conditioning entails. In general $\Gamma = \alpha I$ is used were $\alpha \neq 0$ is the regularization factor, and matrix (2.12) turns to:

$$M = \begin{pmatrix} \sum W I_x + \alpha^2 & \sum W I_x I_y \\ \sum W I_y I_x & \sum W I_y^2 + \alpha^2 \end{pmatrix} \tag{2.15}$$

This amounts to load the diagonal of M, thereby boosting its eigenvalues and avoiding the ill-conditioning. This approach is employed to prevent the solution vector $\mathbf{v}$ to exceed a certain threshold. Unfortunately this threshold cannot be determined automatically and is highly dependent on the alpha parameter. Instead, experimental evaluation of the optimal factor α is generally achieved.

Local methods such as the one of *Lucas-Kanade* are well-known to be very robust to noise, since they make the local assumption of velocity constancy. However, in situations where aperture is dominant, it usually fails to provide a reliable flow estimation.

2.3.2 Global Optical flow methods

The category of global optical flow methods is represented by the classic *Horn and Schunck* [Horn and Schunck, 1981] method, and its numerous discontinuity-preserving variants [Alvarez et al., 1999, Aubert et al., 1999, Black and Anandan, 1991, Cohen, 1993, Heitz and Bouthemy, 1993, Kumar et al., 1996, Nagel, 1983, Proesmans et al., 1994, Schnorr, 1994, Shulman and Herve, 1989, Wei, 2001]. These methods mainly use the assumption on the **smoothness** of the flow field, meaning that the flow field should not exhibit sharp spatial variations of the velocity vectors. The global approaches undertake to minimize a **global energy**, corresponding to the whole flow field, and not only to one pixel (previous section). Therefore, only one energy $E(\mathbf{v})$ is being minimized and a **unique flow field solution** $\mathbf{v}^\star(\mathbf{x}, t)$ has to be obtained:

$$\boxed{\begin{aligned} &\mathbf{v}^\star(\mathbf{x}, t) = \ argmin_{\mathbf{v}} E \\ &E(\mathbf{v}(\mathbf{x}, t)) = \int_\Omega \left[(\nabla I \cdot \mathbf{v} + \frac{\partial I}{\partial t})^2 + \mathcal{R}(\mathbf{v}, \partial\mathbf{v}, ..., \partial^n\mathbf{v}) \right] d\Omega \end{aligned}} \tag{2.16}$$

where Ω is the whole spatial domain.

In the case of *Horn and Schunk* method the regularization term is:

$$\mathcal{R} = \alpha^2 \|\nabla \mathbf{v}\|_F^2 \tag{2.17}$$

where $\|.\|_F$ is the *Frobenius* norm given for every vector gradient $\nabla \mathbf{v}$ by:

$$\|\nabla \mathbf{v}\|_F^2 = \sum_{i,j} (\frac{\partial \mathbf{v}_i}{\partial x_j})^2$$

Working the *Euler-Lagrange* equation on the above energy yields:

$$\begin{aligned} &\frac{\partial E}{\partial \mathbf{v}} = 0 \\ \Longrightarrow &M\mathbf{v} - \alpha^2 \Delta \mathbf{v} = b \end{aligned} \tag{2.18}$$

The size of this system is huge, vector $\mathbf{v}$ is not a local vector but a flow field with $N \times Card(\Omega)$ elements, N being the number of image dimensions and $Card(\Omega)$ the total number of pixels. Likewise, M and b are not local quantities anymore, but a global matrix of size $(N \times Card(\Omega))^2$ and b a vector field of size $N \times Card(\Omega)$. M is very sparse, since only its diagonal is filled with blocks of $N \times N$ local matrices $M_{\mathbf{x}}$. Each block would represent the individual matrix tensor with $M_{\mathbf{x}} = \nabla I(\mathbf{x}) \nabla I(\mathbf{x})^T$, while the vector field b would be the concatenation of every $b_{\mathbf{x}} = -I_t(\mathbf{x}) \nabla I(\mathbf{x})$. Overall, the shape of the system will look like:

$$\left[\begin{pmatrix} M_{\mathbf{x}_1} & & & \\ & M_{\mathbf{x}_2} & 0 & \\ & \dots & \dots & \\ & 0 & & M_{\mathbf{x}_{Card(\Omega)}} \end{pmatrix} - \alpha^2 \mathcal{L} \right] \begin{pmatrix} \mathbf{v}(\mathbf{x}_1) \\ \mathbf{v}(\mathbf{x}_2) \\ \dots \\ \dots \\ \mathbf{v}(\mathbf{x}_{Card(\Omega)}) \end{pmatrix} = \begin{pmatrix} b_{\mathbf{x}_1} \\ b_{\mathbf{x}_2} \\ \dots \\ \dots \\ b_{\mathbf{x}_{Card(\Omega)}} \end{pmatrix}$$

where $\mathcal{L}$ is a symetric matrix that spreads the discrete laplacian terms of the flow field $\mathbf{v}(\mathbf{x})$ all over the system matrix.

The inversion of this massive system cannot be considered. *Horn and Schunk* prefers to use an iterative technique based on estimating the velocity from the spatial average of the last iteration. Given $\Delta \mathbf{v} \simeq \bar{\mathbf{v}} - \mathbf{v}$, the discrete approximation of velocity laplacian, the idea is to relax independently each row of the above system by the following iterations:

$$\mathbf{v}(\mathbf{x_i})^{n+1} = \bar{\mathbf{v}}(\mathbf{x_i})^n - \nabla I \frac{(\nabla I \cdot \bar{\mathbf{v}}(\mathbf{x_i})^n + I_t)}{\alpha^2 + \|\nabla I\|^2} \tag{2.19}$$

where n is the number of iterations.

The main effect of this approach is that vectors will propagate and fill in empty regions where information of image gradient is missing. As the iterations run on, the reliable gradient information will diffuse in the surrounding, this without violating the optical flow constraint. The regions with aperture problems will then be supported by their neighbor carrying high fidelity and will overcome their ill-conditioning. The factor α controls the **diffusion range**. The higher α, the more important the smoothing effect. According to the sparsity of the gradient information in the image, one should use a more or less important regularization weight.

The main asset of global techniques such as *Horn and Schunk* is their ability to get rid of the aperture by diffusing gradient information in locations with homogeneous intensity. However the assumption of flow field smoothness has a downside: it fails in predicting flow field discontinuities. In particular, this method needs to be substantially modified to deal with fluid flow that only occurs within well defined lumen regions. These phenomenons are very common in image sequences as moving objects are occluded by other objects in a foreground. The diffusion of flow field in object interfaces will create erratic estimation of optical flow. Furthermore, the small motion patterns will be smoothed out when using too much regularization, for the benefit of large scale motions. These issues can be dealt with using discontinuity constraints but global methods most often suits for the assessment of **smooth flow fields**.

Finally, one should not that local and global methods are not incompatible. *Bruhn et al.* [Bruhn et al., 2005] combine *Lucas-Kanade* and *Horn and Schunk*'s approaches with great performances, and further extend their work to non-linear and multi-resolution techniques. The local and variational methods actually complement each other by providing both smoothness and robustness against noise.

2.4 Iterative warpings in optical flow

In the section 2.1, we alluded to the approximated nature of discrete optical flow equation. Under the assumption of a **small displacement v** between time t_1 and t_2, the 1st order Taylor expansion is accurate enough:

$$\nabla I(\mathbf{x}, t_1) \cdot \mathbf{v} + I(\mathbf{x}, t_2) - I(\mathbf{x}, t_1) \simeq 0 \tag{2.20}$$

This equation can be understood in a $1D$ example, where the brightness constancy assumption (2.1) ($I(x, t_1) = I(x + v, t_2)$) together with equation (2.20) gives:

$$I(x + v, t_2) = I(x, t_2) + \nabla I(x, t_1) \cdot \mathbf{v} \tag{2.21}$$

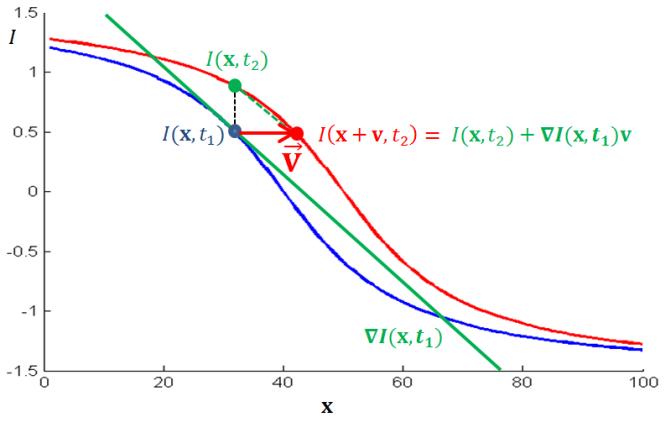

Figure 2.5: *1D optical flow with first order approximation. The blue curve represents the profile of image intensity at time t_1, while the red curve describe that at a small time step later t_2. The horizontal difference is the displacement magnitude v, while the vertical difference is the discrete time derivative $I(x, t_2) - I(x, t_1)$.*

The time difference of I at a position x is **proportional** to the displacement v, with $-\nabla I$ being the linear factor. This is simply what means a 1st order approximation of the intensity with respect to v (see figure 2.5).

Now, if v becomes larger, the 1st order expansion is not sufficient. Higher order terms are needed, as described in equation (2.5). Unfortunately, higher orders of v will make the optical flow constraint more complex, and will compromise the chances of flow recovery. On the other hand, keeping the 1st order approximation leaves the equation (2.20) with a residue ϵ:

$$\nabla I(x, t_1) \cdot \mathbf{v} + I(x, t_2) - I(x, t_1) = \epsilon \tag{2.22}$$

In other words, the brightness assumption is violated with an error of ϵ:

$$I(x + v, t_2) - I(x, t_1) = \epsilon \tag{2.23}$$

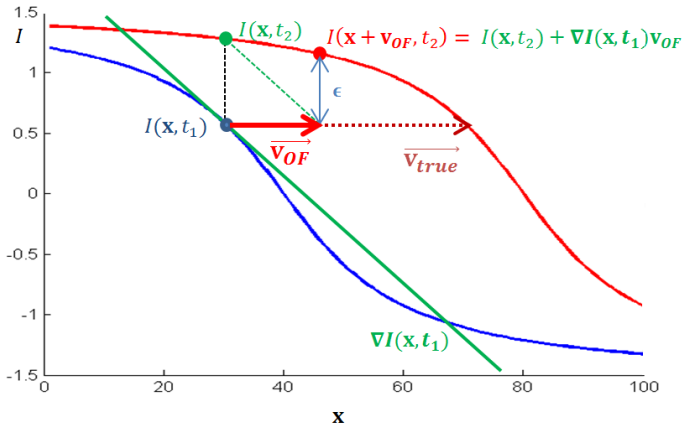

Figure 2.6: *1D optical flow with large displacement and optical flow residue ϵ. The gradient information $\nabla I(x, t_1)$ drifts from that of $I(x, t_2)$. As a result, the optical flow estimation v_{OF} is underestimated compared to the actual value v_{true}. The evaluation of $I(x + v_{OF}, t_2)$ does not yield the expected $I(x, t_1)$. The difference between the two supposedly equals quantities is the optical flow residue ϵ.*

To overcome the limitation of 1st order approximation, and bring the residue ϵ to 0, iterative warping approaches are usually considered. First, let us define a warping transformation $\mathcal{T}$:

$$\mathcal{T} : \begin{cases} \mathbb{R}^N \longrightarrow \mathbb{R}^N \\ I \longmapsto \mathcal{T}(I) \end{cases}$$

After a first rough estimation of the optical flow, the image $I(\mathbf{x}, t_1)$ is **warped** with a transformation $\mathcal{T}_0$ that corresponds to the flow field $\mathbf{u}_0(\mathbf{x}, t_1)$, such that the output is closer to the solution image $I(\mathbf{x}, t_2)$: $\mathcal{T}_0(I(\mathbf{x}, t_1)) = I(\mathbf{x}+\mathbf{u}_0(\mathbf{x}), t_1)$. If the residue ϵ_1 is still too large, a new optical flow estimation is performed and the process is reiterated with a new transformation $\mathcal{T}_1$. For each iteration i, an increment $\mathbf{u}_i$ is estimated from the warped image $\mathcal{T}_{i-1}(I(\mathbf{x}, t_1))$:

$$\forall\, \mathbf{x} \in \Omega, \quad \mathcal{T}_i(I(\mathbf{x}, t_1)) = I(\mathbf{x} + \mathbf{v}_i(\mathbf{x}, t_1)) \tag{2.24}$$

with:

$$\mathcal{T}_i = \mathcal{T}_{i-1} \circ \mathcal{T}_{i-2} \circ \cdots \circ \mathcal{T}_0 \tag{2.25}$$

$$\mathbf{v}_i(\mathbf{x}, t_1) = \sum_{k=0}^{i} \mathbf{u}_k(\mathbf{x}, t_1) \tag{2.26}$$

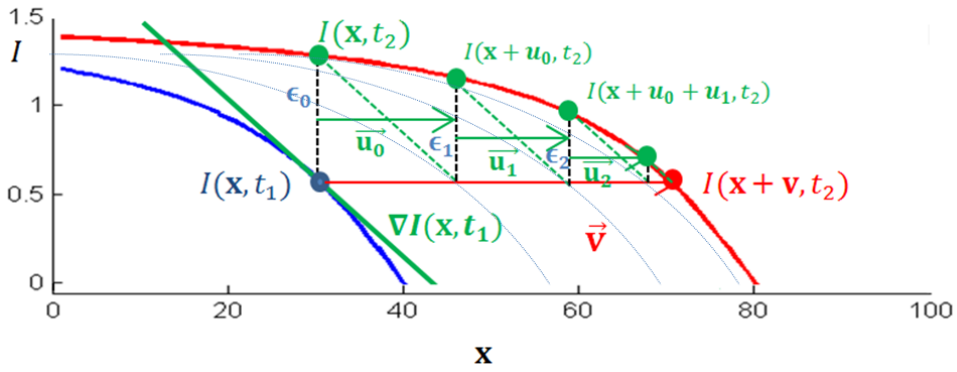

Figure 2.7: *Iterative warping of the 1D image $I(x,t_1)$ toward target image $I(x,t_2)$. The same gradient information $\nabla I(x+v_i,t_1)$ is evaluated at each iteration (dashed green line) and the linear approximation is repeated. As a result, the warped point (in green) is moved toward the solution point (in red). The iterations end when the optical flow increment satisfy the brightness constancy equation.*

The implementation of the iterative warping techniques can be performed with both local or global approaches detailed in section 2.3. Let us define M the local or global system matrix and $\mathbf{b}$ the local or global right hand side vector. Without loss of generality, the corresponding pseudo-code for solving optical flow is:

Algorithm 1 Calculate the optical flow solution $\mathbf{v}^\star$ with iterative warping

Define $thresh > 0$, i_{max}
Initialize $\mathbf{v}_0 = 0, i = 0, \hat{\epsilon_0} = \sum_{\mathbf{x}\in\Omega} \frac{|I2(\mathbf{x})-I1(\mathbf{x})|}{I2(\mathbf{x})}$
while $\epsilon_i > thresh$ **or** $i \leq i_{max}$ **do**
  Solve $M(\mathbf{v}_i + \mathbf{u}_i) = \mathbf{b}$ for $\mathbf{u}_i$
  $I1(\mathbf{x}+\mathbf{v}_i+\mathbf{u}_i) = \mathcal{T}_{\mathbf{u}_i}(I1(\mathbf{x}+\mathbf{v}_i))$
  $\mathbf{v}_{i+1} = \mathbf{v}_i + \mathbf{u}_i$
  $\hat{\epsilon_i} = \sum_{\mathbf{x}\in\Omega} |\frac{I2(\mathbf{x})-I1(\mathbf{x}+\mathbf{v}_{i+1})}{I2(\mathbf{x})}|$
  $i = i + 1$
end while

The normalized residue $\hat{\epsilon}$ will decrease until a tolerance threshold is satisfied. The final optical flow solution will read:

$$\mathbf{v}^\star(\mathbf{x},t_1) = \sum_{k=0}^{i_{max}} \mathbf{u}_k(\mathbf{x},t_1) \tag{2.27}$$

Iterative warping are efficient when larger motion occurs in image sequences. However, the warping process is computationally expensive, especially in the case of 3D images. It is desirable for the reference image $I(x,t_1)$ and target image $I(x,t_2)$ not to be too far from each other, so that few warping steps are required.

2.5 Multi-resolution in optical flow

When dealing with large displacements, a good alternative is also the multi-resolution approach. In the literature, *Anandan* [Anandan, 1989, Black and Anandan, 1996],and *Mémin and Perez* [Memin and Perez, 1998, Mémin and Pérez, 2002] incrementally compute the optical flow field based on a sophisticated **coarse-to-fine** strategy. A *Gaussian* pyramid is generally built from the original pair of images $I1$ and $I2$. For instance, an image $I1_n$ at level n will be **downsampled** to achieve a coarser level $n+1$ by a *restriction* operator:

$$I1_{n+1} = I1_n \downarrow \tag{2.28}$$

where I_{n+1} is decimated each time by a factor of 2, with respect to:

$$\mathbf{x}_n = \frac{1}{2^n}\mathbf{x}_0 \tag{2.29}$$

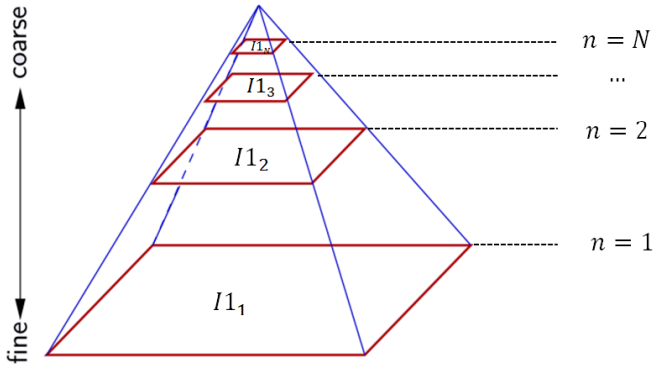

Figure 2.8: *Pyramidal approach in optical flow. The image is downsampled $N-1$ times, until the coarsest grid is obtained. Each grid processes a different scale of optical flow, and inherits the displacement of coarser scale.*

Large motions get much smaller in coarser grids using higher pixel spacing. The problem of optical flow is modified and made hierarchical to appear as linear as possible. Large scale motions are used to warp the image and linearize the problem of the next finer level.

M_n should contain the same gradient information during the warping procedure and thus is not affected. Whereas, $\mathbf{b}_n$ contains the inter-frame information and therefore has to be recomputed to take warping $\mathcal{T}_{\mathbf{v}_n}$ into account: $\mathbf{b}_n = \mathbf{b}_n - M_n\mathbf{v}_n$.

Pyramidal approaches are the most widely used techniques in optical flow. They allow to capture **large motions** that are recurring in image sequences. By processing each scale separately, they don't only provide a general framework for the analysis of multi-scale motion, but also reduce the computational burden by processing coarser grids.

Algorithm 2 Calculate the optical flow solution $\mathbf{v}^\star$ with multi-resolution approach

Define N the number of grid levels
Initialize $\mathbf{v}_N = 0$
for $n = 2$ **to** N **do**
  $I1_n = I1_{n-1}\downarrow$
  $I2_n = I2_{n-1}\downarrow$
  Compute M_n
  Compute $\mathbf{b}_n$
end for
for $n = N$ **to** 2 **do**
  Solve $M_n(\mathbf{v}_n + \mathbf{u}) = \mathbf{b}_n$ for $\mathbf{u}$
  $\mathbf{v}_{n-1} = 2(\mathbf{v}_n + \mathbf{u})\uparrow$
  $n = n - 1$
end for
Solve $M_1(\mathbf{v}_1 + \mathbf{u}) = \mathbf{b}_1$ for $\mathbf{u}$

2.6 The capture range

As soon as the object stays within the FoV, one could believe that optical flow computation is possible, regardless of the motion magnitude. This is not exactly true. In practice, the displacement magnitude should not exceed the size of the object to be tracked. If so, ambiguous matches can occur with other objects of the scene. This issue is particularly obvious in the case of periodic image patterns. Let us consider a simple cosine function describing a 1D image texture:

$$I(x,t) = cos(k_0(x - vt)) \tag{2.30}$$

with $k_0 = \frac{2\pi}{\lambda_0}$ the spatial frequency of the pattern, and λ_0 the wavelength.

If a large motion $vt = \lambda$ occurs between $t_1 = 0$ and t_2, we get:

$$I(x,t_2) = cos(k_0(x - \lambda)) = cos(k_0 x - 2\pi) = cos(k_0 x) = I(x,t_1) \tag{2.31}$$

Solving the optical flow equation would lead to $v = 0$, which is obviously untrue. A point of the image is erroneously matched with a point of the same intensity but from a different period. This reasoning can be extended to every other displacement v being a multiple of λ, showing the misleading effect of image periodicity. As a matter of fact, every displacement exceeding a certain limit, called the **capture range**, will disable optical flow recovery.

In the case of periodic function, we generally resort to the **spatial phase** to determine the capture range. As an example, the technique of MR tagging use a spatial modulation to track the myocardium deformation during heartbeat. The spatial *Fourier* domain is exploited to extract the **harmonic phase** (HARP). The first paper

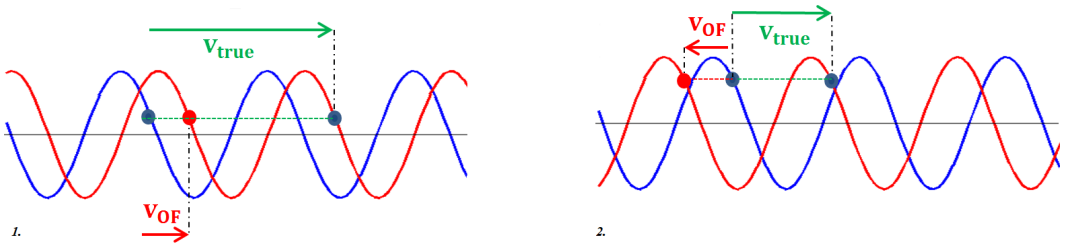

Figure 2.9: *Illustration of the capture range problem when dealing with periodic signal/images. The reference signal is displayed in blue, and the target signal in red. When the displacement exceeds the capture range, other phases of the cosine function carrying the same intensity will occlude the true target and a mismatch will occur. In 1., the displacement is greater than the wavelength λ_0. Hence, the reference point will be paired with the closer target, belonging to the previous spatial period. In 2., the situation is even worse since the sign of the time difference signal is inverted. The displacement vector points in the opposite direction and another target point is found.*

dedicated to HARP tracking [Osman et al., 1999] points out the problem of **phase warping** and demonstrates that the assessment of cardiac motion is possible when:

$$|\Delta\phi| < \pi \tag{2.32}$$

where $\Delta\phi$ is the shift of the spatial phase at point x during the time lapse $\Delta t = t_2 - t_1$. If this condition is satisfied, the tracking of cardiac wall motion can be performed.

From equation (2.30) and (2.32), we deduce:

$$\begin{aligned} &|\Delta\phi| < \pi \\ \Longrightarrow &k_0 v \Delta t < \pi \end{aligned} \tag{2.33}$$

Knowing the relations $\Delta x = v\Delta t$ and $k_0 = \frac{2\pi}{\lambda}$ lead to expression of the capture range:

$$\boxed{\Delta x_{max} = \frac{\lambda}{2}} \tag{2.34}$$

On the other hand, a temporal resolution that guarantees a displacement within the capture range reads:

$$\boxed{\Delta t < \frac{T}{2}} \tag{2.35}$$

Here we see the importance of **time sampling** in the tracking of periodic image sequence. For the signal not to alias in the temporal domain, one should use a sufficiently small time resolution. Without a fine time sampling, the displacements tend to be larger, and the problem of capture range starts to appear. The capture range can

be generalized to non periodic images, but is less easy to formalize. In this thesis, we will deal with pseudo-periodic image sequences. Hence, further mentions to capture range will refer to the formula (2.34).

2.7 Brightness changes during sequence

A frequent problem that arises in image sequence analysis is the breaking of intensity conservation assumption. There are two main reasons responsible for this, namely the brightness changes, and the occlusion phenomenons.

In natural video scenes, illumination changes may introduce intensity changes which are not directly related to the motion of an object. More in the scope of this thesis, intensity changes in DSA image sequences may be related to variation due to different factors including uncontrolled changes in X-ray source intensity. In order to address this problem, some authors choose to estimate the physical parameters of the brightness change model. *Negahdaripour et al.* integrate radiometric and geometric cues into the optical flow solver [Negahdaripour and Yu, 1993, Negahdaripour, 1998], while *Haussecker et al.* [Haussecker and Fleet, 2001] makes use of an extended version of the LMSE employed by *Lucas-Kanade* [Lucas and Kanade, 1981] (see section 2.3.1) to estimate brightness variation parameters. In the latter, the brightness constancy assumption (2.1) is replaced by:

$$I(\mathbf{x} + d\mathbf{x}, t + dt) = \alpha(\mathbf{x})I(\mathbf{x}, t) + \beta(\mathbf{x}) \tag{2.36}$$

in order to account for temporal changes in brightness values, with α and β locally constant in the image.

The unknown vector to be estimated is then $t = [\mathbf{v}\ \alpha\ \beta]^T$, and the LMSE described in section 2.3.1 minimizes now:

$$E_{\mathbf{x}}(\mathbf{v}, \alpha, \beta) = \sum_{\mathbf{p}\in\mathcal{W}} W(\mathbf{p}) \left[\nabla I1(\mathbf{p}) \cdot \mathbf{v} + I2(\mathbf{p}) - \alpha I1(\mathbf{p}) - \beta\right]^2 \tag{2.37}$$

The system to be inverted for each $\mathbf{x}$ is now:

$$\begin{pmatrix} \sum W \nabla I1 \nabla I1^T & -\sum W \nabla I1 \, [I1\ 1] \\ -\sum W \nabla I1 \, [I2\ 1] & \sum W \, [I1\ 1]^T \, [I1\ 1] \end{pmatrix} \begin{pmatrix} \mathbf{u} \\ [\alpha\ \beta]^T \end{pmatrix} = \begin{pmatrix} -\sum W I2 \nabla I1 \\ \sum W I2 \, [I1\ 1]^T \end{pmatrix} \tag{2.38}$$

This full rank system is invertible, but can be nonetheless subject to ill-conditioning, and high sensitivity to computation of image gradient is also reported in [Negahdaripour and Yu, 1993]. Moreover, multiple interpretations of motion and illuminance can be made by the system inversion. Typically the discontinuities at motion boundaries or occlusion can lead to erroneous estimates and large residuals. The main advantage of this method lies in the introduction of illuminance models.

2.8 Other optical flow techniques

The previous classes of optical flow methods belong to the family of **variational approaches**, using the 1st order expansion of brightness constancy equation(2.1). However, other ways to exploit the constancy assumption exist.

2.8.1 Block-matching methods

The most intuitive one is the **correlation-based method**, also called **block-matching**, that use a similarity measure between the neighborhood of a pixel in an image, and the neighborhood of a candidate pixel in the next image.

The main advantage of this technique is there is no need to compute intensity derivatives and deal with associated inaccuracies. Instead of minimizing an energy, a window surrounding the pixel of interest is translated across the next image. The translation with the best similarity score will be the optical flow candidate. The general formulation of the similarity score reads:

$$\mathcal{S}(\mathbf{x}, \Delta\mathbf{x}) = \sum_{\mathbf{y}\in\mathcal{W}} S(I_1(\mathbf{x}+\mathbf{y}), I_2(\mathbf{x}+\Delta\mathbf{x}+\mathbf{y})) \tag{2.39}$$

The similarity measure is calculated by summing S over the window $\mathcal{W}$ surrounding $\mathbf{x}$ in image I_1 and $\mathbf{x}+\Delta\mathbf{x}$ in image I_2. A common similarity measure is the sum of squared difference (SSD) of the pixel values:

$$\mathcal{S}(\mathbf{x}, \mathbf{x}+\Delta\mathbf{x}) = \sum_{\mathbf{y}\in\mathcal{W}} (I_1(\mathbf{x}+\mathbf{y}) - I_2(\mathbf{x}+\Delta\mathbf{x}+\mathbf{y}))^2 \tag{2.40}$$

The displacement $\Delta\mathbf{x}$ that minimizes the similarity measure gives the flow vector sought. In [Bulthoff et al., 1989], a maximum displacement $\Delta\mathbf{x}_{max}$ is chosen in each direction, with a research window of size n. The smallest value of the SSD similarity measure defines the proper displacement.

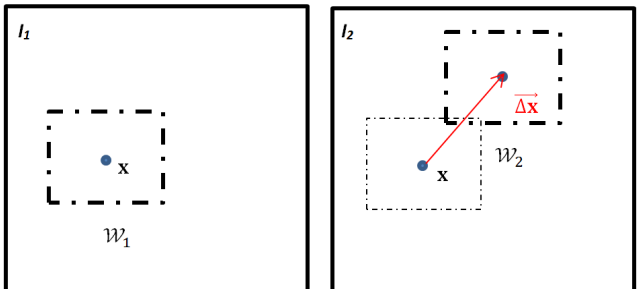

Figure 2.10: *Block-matching based optical flow. The window $\mathcal{W}_2$ is translated in the vicinity of $\mathbf{x}$ as a way to compare the similarity between its pixel intensities with those of window $\mathcal{W}_1$. The best score defines the optical flow $\Delta\mathbf{x}$.*

Other common similarity measure are the sum of absolute differences (2.41), cross-correlation operator (2.42) , or its normalized version (2.43):

$$\mathcal{S}_{abs}(\mathbf{x}, \mathbf{x}+\Delta\mathbf{x}) = \sum_{\mathbf{y}\in\mathcal{W}} |I_1(\mathbf{x}+\mathbf{y}) - I_2(\mathbf{x}+\Delta\mathbf{x}+\mathbf{y})| \tag{2.41}$$

$$\mathcal{S}_{cross}(\mathbf{x}, \mathbf{x}+\Delta\mathbf{x}) = \sum_{\mathbf{y}\in\mathcal{W}} I_1(\mathbf{x}+\mathbf{y}) I_2(\mathbf{x}+\Delta\mathbf{x}+\mathbf{y}) \tag{2.42}$$

$$\mathcal{S}_{ncross}(\mathbf{x}, \mathbf{x}+\Delta\mathbf{x}) = \frac{\sum_{\mathbf{y}\in\mathcal{W}} (I_1(\mathbf{x}+\mathbf{y}) - \bar{I}_1)(I_2(\mathbf{x}+\Delta\mathbf{x}+\mathbf{y}) - \bar{I}_2)}{\sqrt{\sum (I_1(\mathbf{x}+\mathbf{y}) - \bar{I}_1)^2} \sqrt{\sum (I_2(\mathbf{x}+\Delta\mathbf{x}+\mathbf{y}) - \bar{I}_2)}} \tag{2.43}$$

Cross-correlation might be more suited in case of slight illumination change between two images. It does not penalize the exact difference of intensity, but rather the dissimilarity of the intensity profiles. More generally, two signal being proportional can be matched by the correlation measures.

The drawback of block-matching methods is the expense incurred by having to test different windows at each pixel. A displacement can range from few pixels to the size of the entire image, so that the number of windows to be evaluated can be very large. Some methods such as in [Ogata and Sato, 1992] first evaluate a rough estimate of the optical flow, before refining with correlation methods.
Another issue is the selection of the window size for the similarity measure. The window must be large enough to contain a sufficient amount of details, so that local noise is not taken as a real texture. The size should not be too large either as ambiguous match could occur with other objects within the window. The window size is thus an important parameter of the block-matching methods. In practice, feature-based methods are employed as a first step to identify points of interests. The correlation measures are then used to adjust the flow field in the neighborhood of these key points.

For fluid flow estimation, this technique may be used to correctly estimate the motion of lumen regions or of their walls. It is probably totally inadequate to follow subtle changes in CA isophote changes.

2.8.2 Feature detection methods

As discussed before, the aperture problem is widespread in image sequences. The optical flow regularization and its block matching derived methods only reduce the effect of ill-posedness, but do not provide high accuracy in all the image. The idea of **feature-based** optical flow methods is to give up the quest of dense flow field, while only focusing on a set of points in the image, called features. The features are generally

image locations containing reliable gradient information, i.e **corners** or **edges with high curvature**. Each features are paired independently in the two images to be registered. Two steps are performed: the first is the **feature detection** that attempts to automatically find the corners and the second one is the **pairing** that matches the features with those of the next image.

One of the most common detection method is the *Moravec* operator [Hans and Moravec, 1977]. Directional variance is determined by the minimum of the SSD difference of each pixel in 4 directions (vertical, horizontal, two diagonals). This feature will tend to have a high minimum in corners, where both gradient information can be found. The anisotropy of this approach was reported, but later [Harris and Stephens, 1988] invented the *Plessey*'s operator. In this approach, image gradients are evaluated around the pixel of interest, and weighted by a gaussian function W. From a *Taylor* expansion of the SSD term, a structure tensor M is derived:

$$M = \begin{pmatrix} \sum W I_x^2 & \sum W I_x I_y \\ \sum W I_x Iy & \sum W I_y^2 \end{pmatrix} \tag{2.44}$$

such that the dissimilarity measure at a small shift $\mathbf{x}$ is:

$$E(\mathbf{x}) = \mathbf{x}^T M \mathbf{x} \tag{2.45}$$

As the structure tensor is rotationally invariant, no direction is privileged in the computation of E. One should not the high similarity between matrix used in corner detection (2.44), and the structure tensor used in *Lucas-Kanade* (2.12) where corners provide the best flow estimations.

Other methods as *SUSAN* described by [Smith and Brady, 1997], [Beaudet, 1978] or [Dreschler and Nagel, 1982] address corner detection using more sophisticated features. However, they will not be discussed in this section, since they are beyond the scope of this thesis.

After the corner detection, techniques of local correlation are generally used to assess the displacement between two images. [Barnard and Thompson, 1980], or [Burger and Bhanu, 1990] use the *Moravec* operator [Hans and Moravec, 1977] to determine feature points, before using SSD similarity measure. [Lawton, 1983] prefers to rely on the edges curvature by applying a *Laplacian of Gaussian* (LoG) filter, before threshing high curvatures and apply similarity metrics.

Other authors such as *Ellen Hildreth* propose to estimate flow not only based on corners, but on edges [Hildreth, 1984]. After using an edge detection operator, a classical optical flow method is applied for every point of the contours, with the assumption of rigid body motion. A smoothness regularization is added similarly to [Horn and Schunck, 1981] as a way to insure the flow vector not to deviate to much from its contour neighbors. The irregular sampling of contour points was pointed out, but [Gong

and Brady, 1990] solved the problem using wave-diffusion equation along the edges from high-curvature points to low-curvature points.

2.8.3 Optical flow in frequency domain

Another class of method resort to the frequency domain to solve the optical flow problem. The simplest technique is the **phase correlation** in *Fourier* domain. The pair of image $I1$ and $I2$ are *Fourier*-transformed and the translation $\mathbf{v}$ between the two images gives the following formula:

$$\tilde{I2} = \tilde{I1}e^{-i\mathbf{k}.\mathbf{v}} \tag{2.46}$$

where $\mathbf{k}$ is the spatial frequency vector.

The normalized cross-power spectrum of the complex *Fourier* images is:

$$\frac{\tilde{I2}\tilde{I1}^*}{|\tilde{I2}\tilde{I1}^*|} = e^{-i\mathbf{k}.\mathbf{v}} \tag{2.47}$$

Solving $\mathbf{v}$ can be done by considering the surface of phase correlation,

$$C(\mathbf{v}) = \mathcal{F}^{-1}(\frac{\tilde{I2}\tilde{I1}^*}{|\tilde{I2}\tilde{I1}^*|}) \tag{2.48}$$

and maximizing this quantity:

$$\mathbf{v}^\star = argmax_{\mathbf{v}}(C(\mathbf{v})) \tag{2.49}$$

Yet, this method does not provide dense flow fields but an overall translation of the two images to be registered. Only integer displacements can be calculated and the presence of other peaks in the correlation surface can arise when dealing with periodic images. This straightforward method is suitable for rigid translations between two images, but shows its limits very rapidly.

More sophisticated approaches try to solve the optical flow equation (2.4) in the *Fourier* domain:

$$\tilde{\nabla} I \cdot \mathbf{v} + \tilde{I}_t = 0 \tag{2.50}$$

The idea is to take benefit from a family of *Gabor wavelets* $\mathcal{G}$ that result from the product of a *Gaussian* function and a trigonometric spatiotemporal function:

$$\mathcal{G}_i(\mathbf{x}, t) = \frac{1}{(2\pi)^N \prod \sigma_{i,n}} e^{-\frac{1}{2}\mathbf{x}^T \Sigma \mathbf{x}} \cos(2\pi(\mathbf{k}_i.\mathbf{x} + f_i t)) \tag{2.51}$$

where Σ is the covariance matrix, $\mathbf{k}_i$ and f_i are both the spatial frequency and temporal frequency of the said *Gabor* filter. Once computed in *Fourier* domain, this filter turns to a $(N+1)$ dimensional *Gaussian* filter centered around $(\mathbf{k}_i, f_i)$, with variance $diag(\Sigma)$.

Weber and Malik use these filters with different orientations in such a way that the optical flow system becomes over-determined [Weber and Malik, 1995]. Likewise, [Fleet and Jepson, 1990] propose to extract the phase of the spatio-temporal signal after utilizing a family of *Gabor* wavelet, while [Wu et al., 1998] complement the wavelet approach with a coarse-to-fine technique.

The drawback concerning all these methods is the excessive filtering that tends to erase or distort the original information, especially in the case of small motions. Moreover, the number of wavelet parameters to be tuned (central frequencies, scale, shape...) is problematic for a generic and reproducible assessment of the flow estimation.

*
* *

The recovery of optical flow is an ill-posed problem. It needs to be regularized to overcome the issue of aperture. Many techniques already exist in the literature, almost all use variational approaches. They can be classified as local or global methods. The first class uses the local constancy of the flow vectors, while the second class focusses on the regularity of the whole flow field. Once the problem is reduced to a linear algebraic system of equations, all eigen values of the related linear operator should be positive with a finite condition number. Optical flow is only a first order approximation based on intensity derivatives and therefore suffers from inaccuracies. In case of large displacements, iterations are required to bring more accuracy to the flow estimate, using iterative warping or multi-resolution approaches. The optical flow recovery is also limited by the capture range. Erroneous estimations appear for image with periodic content, and time resolution needs to be properly chosen to avoid temporal aliasing. Other optical flow techniques using brightness models or correlation techniques can be mentioned. Nevertheless, none of them will be exploited. First, no sharp brightness change should occur during contrast sequences. Secondly, the specification of blood flow estimation requires dense velocity estimates, which discards block-matching techniques and feature-based methods. Instead, global variational approaches together with frequency domain methods are more interesting. They provide dense flow estimates that are more suited for fluids, and exploit the signal periodicity existing because of contrast modulation.

Several prerequisites need to be met before an optical flow assessment can be considered. In the case of contrast imaging, the ratio between acquisition frequency (60Hz in DSA, 40Hz in MPI) and heart frequency ($\simeq$ 1Hz) is sufficiently large to insure that the displacements are small compared to the capture range. The rich image gradient

information together with the fine temporal resolution allows the study of optical flow in pulsed contrast sequence. The next chapter will develop the mathematical armamentarium that gives rise to a novel 3D optical flow technique, specific for contrast modalities such as MPI and 3D flow scanners.

Chapter 3

New optical flow algorithm dedicated to bloodflow estimation

Contents

Abstract

This chapter describes the optical flow algorithm developed during this thesis. To the best of our knowledge, this contribution pioneers the problem of 3D optical flow based on contrast imaging. Given the very exploratory nature of this thesis, numerous problems and limitations were encountered. Indeed, 3D contrast flow systems (i.e MPI and 3DRA) are still ahead of their time, and no clinical data have been acquired so far. This work basically tries to foresee and anticipate the advent of these modalities by exploring the potential of 3D flow estimation on virtual images. This chapter presents image and signal processing tools specific to the analysis of modulated contrast sequence in arterial flow. Given the prior knowledge concerning contrast pulsatility, a time processing of the image sequence in *Fourier* domain is proposed. This approach mainly helps to provide a reformulation of optical flow as an instantaneous velocity, as opposed to the displacement described in classical techniques. The principal pitfalls of 3D optical flow estimation are analyzed, particularly in the spatial domain. Spatial regularization schemes are employed to bring more accuracy and more reliability to physics. Then numerical instabilities are pointed out and the importance of boundary conditions is discussed. A new approach for the estimation of wall shear stress is finally presented. As a reminder of the thesis, the chapter 4 will confront the new optical flow method with virtual contrast images. Afterward, tentative flow estimations are described on *in vitro* data and *in vivo* MPI data (chapter 5).

Résumé

Ce chapitre décrit l'algorithme de flot optique développé pendant cette thèse. A notre connaissance, cette contribution est la première à aborder le problème du flot optique 3D basé sur de l'imagerie de contraste. Compte tenu de la nature très exploratoire de cette thèse, de nombreux problèmes et limitations ont été rencontrés. De fait, les imageurs 3D de flux de contraste (comme le MPI et la 3DRA) sont encore d'avant garde, et aucune donnée clinique n'a encore été acquise jusqu'ici. Ce travail essaie principalement de prévoir et anticiper l'avènement de ces modalités en explorant le potentiel de l'estimation de flux 3D sur des images virtuelles. Au cours de ce chapitre théorique sont détaillés des outils de traitement d'image et du signal spécifiques à l'analyse de séquence d'images de contraste modulé dans le flux artériel. En partant d'une connaissance a priori sur la pulsatilité du contraste, un traitement de la séquence d'images dans le domaine de *Fourier* est proposé. Cette approche permet principalement de reformuler le flot optique à partir d'une vitesse instantanée, contrairement au déplacement utilisé dans les techniques classiques. Les principaux écueils de l'estimation du flot optique 3D sont analysés, particulièrement dans le domaine spatial. Des stratégies de régularisation spatiale sont utilisées afin d'apporter plus de précision et de fidélité à la physique. Ensuite, les instabilités numériques ainsi que l'importance de conditions aux limites sont mentionées. Une nouvelle méthode concernant l'estimation de la contrainte de cisaillement sur la paroi est finalement

présentée. Pour rappel, le chapitre 4 confrontera la nouvelle méthode de flot optique proposée avec des images virtuelles de contraste. Ensuite, des resultats d'estimation de flux seront décrites sur des données MPI *in vitro* et *in vivo* (chapitre 5).

3.1 Blood flow estimation in contrast sequences

3.1.1 Short review on fluid flow estimation

The analysis of fluid motion is a longstanding research field in computer vision. A fluid motion is different from any motion in that it follows the laws of fluid mechanics, described in section 1.3.1. The optical flow estimation of fluid displacement is a particular case of optical flow estimation, and requires specific regularization methods. The most used, but also the most restrictive and computationally demanding, is to impose the flow field to verify the *Navier-Stokes* equation (1.5) [Doshi and Bors, 2010, Doshi and Bors,]. Slighter constraints, as the continuity equation (1.4) have been used to impose compliance with fluid mechanics [Wildes et al., 2000] . The variational framework met in 2.3 can be complexified by adding first or second order penalization of the curl and the divergence of the flow field to the usual optical flow penalty [Corpetti et al., 2005, Benz et al., 2014]. *Mémin, Corpetti and Pérez* especially published several works in that respect [Corpetti et al., 2000, Corpetti et al., 2002a, Corpetti et al., 2002b, Papadakis et al., 2007].

$$\mathcal{R} = \int \alpha(\nabla \cdot \mathbf{v})^2 + \beta \|\nabla \wedge \mathbf{v}\|^2 \tag{3.1}$$

or:

$$\mathcal{R} = \int \alpha \|\nabla(\nabla \cdot \mathbf{v})\|^2 + \beta \|\nabla(\nabla \wedge \mathbf{v})\|^2 \tag{3.2}$$

Note that the first regularizer is actually the same than that met in *Horn and Schunck* (2.17) with a *Frobenius* norm on the velocity gradient, but reformulated with the *Helmotlz-Hodge* decomposition [Starn, 2001]. Whereas, the second regularizer is a smoother version that tolerates natural flow discontinuities occurring in non-laminar flows.

3.1.2 State of the art on blood flow estimation

When it comes to blood flow, the subject is even more specific. The fluid motion is **incompressible**, **pulsatile**, with specific **boundary conditions**. In *Rhodes et al.* [Rhode et al., 2005], six categories of blood flow estimation methods are enumerated:

- Indicator dilution techniques ([Hilal, 1966, Korbuly, 1973, Lantz et al., 1980, Mygind et al., 1995, Doriot et al., 1997])

- Time-intensity curve (TIC) analysis ([Rosen and Silverman, 1973,Silverman and Rosen, 1977, Bürsch et al., 1981])
- Distance-time-intensity curve analysis ([Shaw and Plewes, 1986, Guggenheim et al., 1994, Dorsaz et al., 1997, Seifalian et al., 1991, Shpilfoygel et al., 1999])
- First pass analysis (FPA) techniques ([Marinus et al., 1990, Hangiandreou et al., 1991, Ersahin et al., 1995, Molloi et al., 1993])
- Optical flow methods (OFM) ([Efron et al., 1978, Amimi, 1994, Imbert et al., 1997, Huang et al., 1997])
- Inverse advection methods techniques ([Sarry et al., 1997, Sarry et al., 2002])

All these techniques rely on DSA sequences, also called *Roentgen videodensitometry*, but supposedly can be extended to other kind of modalities as CT, MR and 3DRA. A critical review from [Shpilfoygel et al., 2000] described and classified the aforesaid blood flow estimation methods. Among them, distance-time-intensity curves and optical flow methods proved to be the most successful. The first class of method utilizes the intensity information along a profile, often determined as the centerline of the vessel. This is a very convenient way to study flow in a particular path of the bloodstream, but unfortunately does not yield accurate estimates of the flow patterns. In OFM, the same centerline analysis is often achieved, also by averaging the intensity, and evaluating spatio-temporal statistics of the estimated velocities.

3.1.3 Motivations

By delving into the state of the art of blood flow estimation, a natural conclusion comes that very few works exist in vector field estimation of blood velocity. While 2D flow field estimation is rare in DSA sequence analysis, not a single study, to the best of the author knowledge, has ever been conducted with 3D time resolved contrast imaging until now.

Yet, if we consider the recent advances of angiography modalities, as MPI or 3DRA, we can suspect that the achievement of **3D flow fields** will become a major feature in the forthcoming 3D flow acquisition systems. For the moment, we can just envision **3D optical flow based estimation** for the future. Nevertheless, new paths can be explored in the meantime, with the support of virtual images, and *in vitro* acquisitions.

First let us recall the definition of a **3D contrast sequence** $I(\mathbf{x}, t)$ and its corresponding **3D+T flow field sequence** $\mathbf{v}(\mathbf{x}, t)$:

$$I : \begin{cases} \mathbb{R}^3 \times \mathbb{R}^+ \longrightarrow \mathbb{R} \\ (\mathbf{x}, t) \longmapsto I(\mathbf{x}, t) \end{cases} \qquad \mathbf{v} : \begin{cases} \mathbb{R}^3 \times \mathbb{R}^+ \longrightarrow \mathbb{R}^3 \\ (\mathbf{x}, t) \longmapsto \mathbf{v}(\mathbf{x}, t) \end{cases}$$

The real or virtual 3D pulsed contrast sequence should respect several specifications, described in table 3.1.

Contrast sequence specifications		
	Sequence properties	Mathematical expression
pulsatility assumption	(**1**) I is **pseudo-periodic**: it can be decomposed in the *Fourier* domain with narrowband components $\tilde{I}(f)$ around the fundamental cardiac frequency and the first harmonics. Other frequency components should be close to 0.	$I(t) = \int_{-\infty}^{+\infty} \tilde{I}(f) e^{-2\pi j f t} df$,$\tilde{I}(f) \simeq 0$ outside narrowbands
physical properties	(**2**) I should be kept constant along a flow line according to the **brightness constancy assumption**.	$\mathbf{v} \cdot \nabla I + \frac{\partial I}{\partial t} = 0$
	(**3**) $\mathbf{v}$ should be a **smooth** flow field to account for blood viscosity.	$\|\nabla \mathbf{v}\|$ as small as possible
	(**4**) $\mathbf{v}$ should be an **incompressible** flow field.	$\nabla \cdot \mathbf{v} = 0$
boundary conditions	(**5**) Flow should be **enclosed** in the vessel **lumen** $\mathcal{L}$ and should be tangent to the vessel boundary $\mathcal{B}$ of outward normal $\mathbf{n}$.	$\mathbf{v}(\mathbf{x} \notin \mathcal{L}) = 0$ and $\mathbf{v}(\mathbf{x} \in \mathcal{B}) \cdot \mathbf{n} = 0$

Table 3.1: *Synthetic table of the blood flow estimation framework*

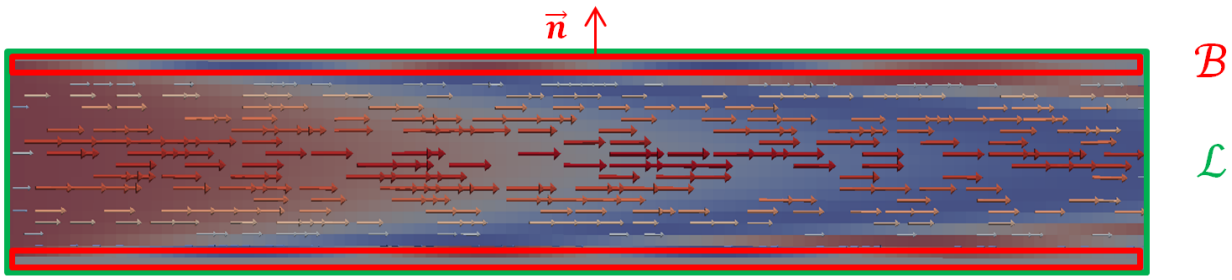

Figure 3.1: *Overall appearance of a modulated contrast sequence with the corresponding velocity field. The color coded image intensity I corresponds to the contrast concentration, while the vector field corresponds to the contrast velocity vectors* $\mathbf{v}$ *that also represents blood velocity vectors. The magnitude of the velocity vectors is visualized with both length and color of the vectors.* $\mathcal{L}$ *and* $\mathcal{B}$ *correspond to the vessel lumen and boundary areas.*

3.2 New optical flow method for pseudo-periodic time signals

3.2.1 Time signal processing in Fourier domain

In section 1.3.2, the assumption of contrast periodicity was put forward. However, it appears that the time intensity curves (TICs) observed in DSA are not exactly periodic. A slow variation of the **signal envelop** can be noticed. The curve of the contrast flow rate at the injection point evolves slowly during the acquisition, resulting in a **pseudo-periodic** behavior.

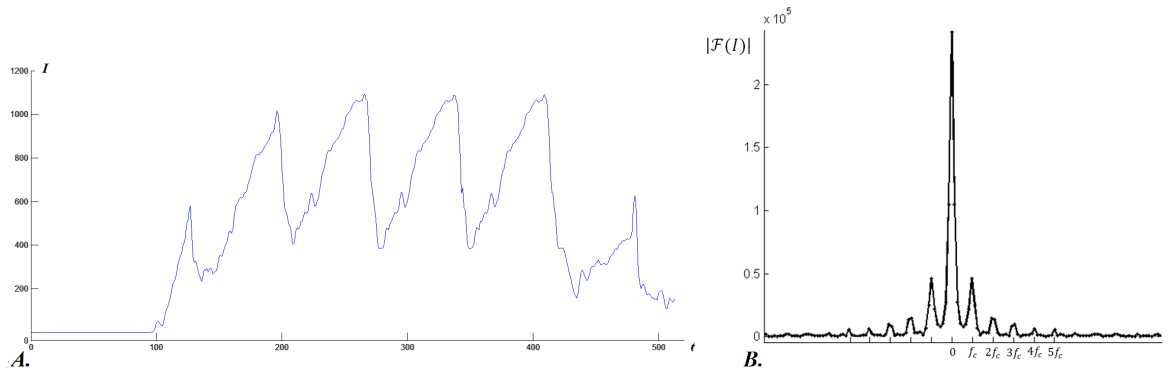

Figure 3.2: *A. TIC of a single pixel in DSA sequence with pseudo-periodicity. B. Spectral density of the Fourier transform* $|\mathcal{F}[I]|$*, where several peaks including cardiac frequency* f_c *and four other harmonics can be distinguished.*

Hence, the main spectral information of the time sequence is contained in narrow bands around the fundamental cardiac frequency and several harmonics.

Now, let us consider the **discrete** *Fourier* transform of a numerical signal $\tilde{I}(\mathbf{x}, n) = \mathcal{F}[I(\mathbf{x}, i)]$:

$$\forall n \in [0 \quad n_{max}], \quad \tilde{I}(\mathbf{x}, n) = \sum_{i=0}^{n_{max}-1} I(\mathbf{x}, i) e^{-2j\pi \frac{n}{n_{max}} i} \tag{3.3}$$

where n and i are respectively the discrete frequency and time samples, and n_{max} both the number of time and frequency samples.

Given the narrow bandwiths of the spectral information, one can make the assumption that only some frequency components $\tilde{I}(\mathbf{x}, n)$ are significant to represent the contrast sequence. Therefore, one can choose to filter out the other components of the spectral content. Three options are considered:

1. A filter that simply cuts the frequencies outside the harmonic bandwiths. Let us call $\mathbf{F}_{narrowbands}$ the set of frequencies within the narrowbands of cardiac harmonics. The corresponding bandpass filter will read:

$$\boxed{\tilde{I}_{BP}(\mathbf{x}, n) = \mathbf{1}_{\mathbf{F}_{narrowbands}}(n) \tilde{I}(\mathbf{x}, n)} \tag{3.4}$$

   with $\mathbf{1}_{\mathbf{F}_{narrowbands}}$ the indicator function:

$$\mathbf{1}_{\mathbf{F}_{narrowbands}} : \begin{cases} 1 & if \quad n \in \mathbf{F}_{narrowbands} \\ 0 & otherwise \end{cases}$$

2. A smoother filtering that windows the harmonics with *gaussian* functions. The bandpass filtered spectrum $\tilde{I}_{BP}(\mathbf{x}, n)$ will read:

$$\boxed{\tilde{I}_{BP}(\mathbf{x}, n) = \left[\prod_{h}^{N_h} e^{-2\pi^2 \sigma^2 (n - h n_c)^2} \right] \tilde{I}(\mathbf{x}, n)} \tag{3.5}$$

   with σ the standard deviation of the gaussian frequency filters, n_c the frequency sample corresponding to the cardiac frequency and N_h the number of selected harmonics. The windows are centered around each harmonic component hn_c and will then damp the frequency components in a neighborhood controlled by σ. This windowing helps to avoid ringings artifacts when coming back to temporal domain. However, the narrowbands are already damped naturally around the harmonic frequencies (see figure 3.2), which makes this filtering not necessarily better than the indicator filter.

   After the discrete inversion of the *Fourier* filter, the bandpass signal $S(\mathbf{x}, i)$ in the temporal domain will read:

$$S(\mathbf{x}, i) = \mathcal{F}^{-1}(\tilde{I}_{BP}) = \frac{1}{n_{max}} \sum_{n=0}^{n_{max}-1} \tilde{I}_{BP}(\mathbf{x}, n) e^{2j\pi \frac{n}{n_{max}} i} \tag{3.6}$$

3. A filter equivalent to (3.5) exists in the temporal domain. It belongs to the family of **wavelets**, and was evoked in section 2.8.3: the *Gabor* filter. The convolution of this filter with the temporal signal equals to the *gaussian* windowing in the frequency domain. The advantage with this filter is the absence of computation in the *Fourier* domain. It only performs a convolution with the temporal signal as follows:

$$\boxed{S(\mathbf{x}, i) = \sum_{h=0}^{N_h} \sum_{k=0}^{n_{max}-1} I(\mathbf{x}, k) w_h(i-k)} \tag{3.7}$$

with

$$w_h(i) = \frac{1}{h\sigma\sqrt{2\pi}} e^{-\frac{i^2}{2(h\sigma)^2}} e^{-2j\pi h \frac{n_c}{n_{max}} i}$$

The *Gabor* wavelet filters the components of I that oscillate at the frequency of the h-th harmonic. The *gaussian* time window locally captures the spectral content of the signal, thus allowing to account for slow changes of the low frequency envelop. Note that the *Fourier* transform of a *gaussian* function is still *gaussian*, but with a different σ (actually the inverse of the time σ). In addition, the cosine functions shift the *gaussian* windows to the harmonic frequencies in the *Fourier* domain.

Basically, the three above bandpass filters will extract the pulsatility of the contrast information by removing the constant component $C(\mathbf{x}, 0)$ and the high frequency noise that potentially hinders the flow analysis. This signal processing approach can also be considered as a **compression** of the spectral information, leading to a simpler representation of the contrast sequence that only contains few *Fourier* components.

The main advantage of this approach is that knowing the narrowband frequency components of the sequence, the bandpass signal can be derived for any time instant $t \in \mathbb{R}$, and not only for the discrete time samples $i \in [0\, n_{max}]$:

$$S(\mathbf{x}, t) = \frac{1}{n_{max}} \sum_{n=0}^{n_{max}-1} \tilde{I}_{BP}(\mathbf{x}, n) e^{2j\pi \frac{n}{n_{max}} f_s t} \tag{3.8}$$

where $t = \frac{i}{f_s}$ is the actual time (in seconds) and f_s the actual sampling frequency (in Hertz). The discrete representation of time i is replaced by a more intuitive and physical time t.

The contrast sequence is **approximated semi-analytically** in a continuous fashion, by assuming that only few frequency component can describe its time-evolution. In fact, the continuity of the temporal signal will be enforced, while the *Fourier* signal will stay discretized. Evaluating the bandpass contrast sequence S for any time t amounts to interpolate the signal with a *Fourier* decomposition. This interpolation is more or less accurate according to the number of frequency component selected. One could choose to utilize all the *Fourier* component so as to avoid frequency leaks. However, the bandwiths are very narrow. Using all the *Fourier* coefficients is not required in practice and would lead to an unnecessary computational burden.

Essentially, the key point of this signal processing lies in the evaluation of the **time derivative** of the bandpass signal:

$$\frac{\partial S(\mathbf{x},t)}{\partial t} = \frac{1}{n_{max}} \sum_{n=0}^{n_{max}-1} j\omega(n)\tilde{I}_{BP}(\mathbf{x},n)e^{j\omega(n)t} \tag{3.9}$$

where $\omega(n) = 2\pi\frac{n}{n_{max}}f_s$ is the real angular pulsation corresponding to the frequency sample n.

The continuous time representation enables the exact computation of the time derivative. This is particularly interesting in optical flow, since it allows to avoid the problem of large displacements met in section 2.4, and more importantly to use the instantaneous optical flow equation (2.4):

$$\boxed{\nabla S(\mathbf{x},t)\cdot\mathbf{v} + \frac{\partial S(\mathbf{x},t)}{\partial t} = 0} \tag{3.10}$$

Thus, no iterative warping is required, and the unknown variable of the equation becomes an **instantaneous velocity**, instead of a displacement vector. **A straightforward solving of the instantaneous optical flow equation becomes possible thanks to the *Fourier* decomposition.**

However a problem remains, the bandpass signal S can exhibit several extrema and as such its derivative can vanish during a fundamental period. The same issue arises with the spatial gradient ∇S, when the signal is on crest or trough of a spatial wave. In this case, the equation (3.10) cannot be solved.

3.2.2 The Hilbert transform

To circumvent the pitfall of spatio-temporal extrema, one can resort to a powerful mathematical tool known as the *Hilbert* transform. The *Hilbert* transform basically creates a **quadrature** signal, *i.e.* a time-shifted signal of the original sequence I that undergoes a phase shift of $\frac{\pi}{2}$. It can be defined in the temporal domain by:

$$\boxed{\forall\, t \in \mathbb{R}^{\star}, \quad h(t) = \frac{1}{\pi} v.p \frac{1}{t}} \tag{3.11}$$

An analytic signal $\hat{I}$ is created by convolving the real time sequence I with a quadrature filter $\mathcal{Q}$:

$$\hat{I}(t) = \mathcal{Q}(t) * I(t) = (\delta(t) + jh(t)) * I(t) \tag{3.12}$$

Unfortunately h is not causal and has an infinite support. As such, suitable precautions should be taken when filtering the discrete time sequence I. The main requirement for the contrast sequence is to be **band-limited**, *i.e.* to have few *Fourier* components, excluding the DC term and the high frequencies. If the original signal I does not meet this requirement, the bandpass signal S obtained from ((3.4) or (3.5)) particularly suits for the quadrature processing:

$$\hat{S}(t) = \mathcal{Q}(t) * S(t) = (\delta(t) + jh(t)) * S(t) \tag{3.13}$$

Rather than convolving h with a temporal signal, which is computationally expensive, we prefer to resort, once again, to a *Fourier* transform:

$$\mathcal{F}\left[\hat{S}\right](f) = (1 + jH(f))\hat{I_{BP}}(f) \tag{3.14}$$

with

$$H(f) = -j\text{sign}(f)$$

where $sign(f)$ is the sign function described by:

$$\text{sign}(f) = \begin{cases} 1 & \text{for } f > 0 \\ 0 & \text{for } f = 0 \\ -1, & \text{for } f < 0 \end{cases}$$

Basically, the filter H performs a rotation of $-\frac{\pi}{2}$ on the frequency components with positive frequencies, and $\frac{\pi}{2}$ for those with negative frequencies. The main effect will be to cancel out the negative frequencies, and amplify the positive frequencies by a factor of 2:

$$\mathcal{F}\left[\hat{S}\right](f) = (1 + \text{sign}(f))\hat{I_{BP}}(f) \tag{3.15}$$

Hence, by breaking the conjugation of positive and negative frequencies, an imaginary part appears when coming back to the temporal domain. The real part will be the original bandpass signal S while the imaginary part will be the sought quadrature term Q:

$$\boxed{\hat{S}(t) = S(t) + jQ(t)} \tag{3.16}$$

where Q and S have the same envelop M -also called modulus - but a phase shift of $\frac{\pi}{2}$.

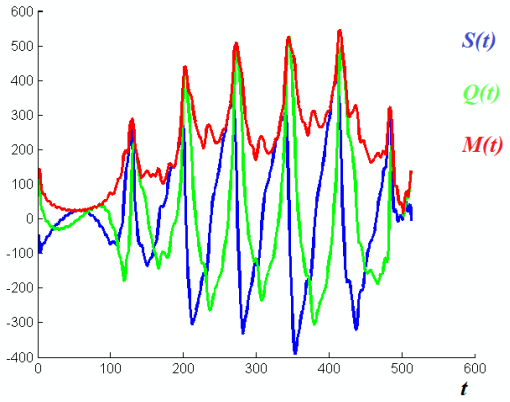

Figure 3.3: *Bandpass signal of the DSA TIC (figure 3.2)colored in blue, and its quadrature in green. The quadrature is shifted by an angle of $\frac{\pi}{2}$ with respect to the bandpass signal. The modulus $M = |\hat{S}|$ in red represents the envelop of the complex signal oscillations.*

The quadrature term prevents the spatial and temporal derivative of the analytic signal $\hat{S}$ to cancel. Figure 3.3 shows that when the signal derivative gets to 0, the quadrature derivative is maximal, and the other way around. The same phenomenon occurs for the spatial gradient ∇S and ∇Q. As a result, $|\frac{\partial \hat{S}}{\partial t}|$ and $\|\nabla \hat{S}\|$ never vanish (excepted if $\|\hat{S}\|$ is constant). The quadrature filter removes the uncertainties on the extrema of the spatio-temporal signal S. The analytic optical flow equation therefore reads:

$$\boxed{\nabla \hat{S}(\mathbf{x},t) \cdot \mathbf{v} + \frac{\partial \hat{S}(\mathbf{x},t)}{\partial t} = 0} \tag{3.17}$$

The above equation can be rewritten as a system:

$$\begin{cases} \nabla S(\mathbf{x},t) \cdot \mathbf{v} + \frac{\partial S(\mathbf{x},t)}{\partial t} = 0 \\ \nabla Q(\mathbf{x},t) \cdot \mathbf{v} + \frac{\partial Q(\mathbf{x},t)}{\partial t} = 0 \end{cases} \tag{3.18}$$

One could believe that this improves the underdetermination of the optical flow constraint. In fact, the above system is similar to one optical flow equation, excepted a rotation matrix was pre-multiplied (see appendix A). The two spatial gradients ∇S and ∇Q have the same directions, and the aperture problem is kept unsolved.

Nonetheless, exploiting both information at the same time is crucial to remove the issue of derivatives vanishing in time and space. In order to minimize the local optical flow error, one can use the conjugate product of the analytic optical flow equation (3.17). Thus, the set of possible solutions $\mathbf{v}^\star$, denoted $\mathcal{V}$ will minimize the following energy:

$$\mathcal{V} = argmin_{\mathbf{v}} \quad (\nabla \hat{S}(\mathbf{x},t) \cdot \mathbf{v} + \frac{\partial \hat{S}(\mathbf{x},t)}{\partial t})(\nabla \hat{S}(\mathbf{x},t) \cdot \mathbf{v} + \frac{\partial \hat{S}(\mathbf{x},t)}{\partial t})^* \tag{3.19}$$

which yields after some algebra:

$$\boxed{\mathcal{V} = argmin_{\mathbf{v}} \quad (\nabla S(\mathbf{x},t) \cdot \mathbf{v} + \frac{\partial S(\mathbf{x},t)}{\partial t})^2 + (\nabla Q(\mathbf{x},t) \cdot \mathbf{v} + \frac{\partial Q(\mathbf{x},t)}{\partial t})^2} \tag{3.20}$$

where $\mathcal{V}$ contains all possible velocity vector $\mathbf{v}$ within the aperture space.

3.2.3 Phase-based optical flow algorithm

Our optical flow based method fully relies on the oscillation of the contrast product concentration. Therefore, any change of oscillation amplitude is likely to disturb the optical flow estimation. When the contrast bolus arrives in the FoV, the envelop of the oscillation slowly increases until it reaches a stable level, and then decreases to zero a few second after the end of injection (see figure 3.3, previous subsection). Other causes of envelop variation can appear when different phases of the product mix in the same location, or when the contrast gets diluted over time.

To get rid of the envelop variations, we resort to the **phase of the complex signal** $\phi = Arg(\hat{S})$. The signal phase can be defined for each time t of the sequence by the angle between the analytic signal and the real axis:

$$\phi(t) = arg(S(t), Q(t)) = atan2(Q, S). \tag{3.21}$$

The main advantage of the phase, is the absence of envelop. The values constantly oscillate between $-\pi$ and π, resulting in periodic discontinuities (see figure 3.4).

The phase can be interpreted as the angular time elapsed since the last maxima of the real signal occurred. Hence, the zero-crossings correspond to a peak of the real signal, while the discontinuity corresponds to a trough.

The phase is a very convenient tool to enforce the **envelop constancy**, and get freed from the slow signal variation due to the effect of the traveling contrast bolus. The phase based optical flow (PBOF) equation describing the phase constancy reads:

$$\boxed{\nabla \phi \cdot \mathbf{v} + \frac{\partial \phi}{\partial t} = 0} \tag{3.22}$$

The numerous phase discontinuities bring an issue concerning the evaluation of the phase derivatives. To avoid these discontinuities, one can add an integer multiple of

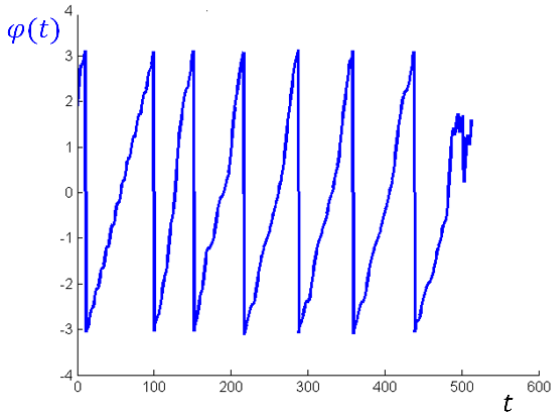

Figure 3.4: *Phase of the bandlimited signal (showed in figure 3.3) exhibiting periodic discontinuities.*

2π, what is called **phase unwrapping**. This work can be tedious, fortunately another elegant and efficient way to deal with this problem exists: both spatial and temporal phase derivatives can be related to those of the real and imaginary part, according to:

$$\begin{cases} \frac{\partial \phi}{\partial t} = \frac{1}{S^2+Q^2}(S\frac{\partial Q}{\partial t} - Q\frac{\partial S}{\partial t}) \\ \\ \nabla\phi = \frac{1}{S^2+Q^2}(S\nabla Q - Q\nabla S) \end{cases} \tag{3.23}$$

Rewriting the phase derivatives with continuous quantities, such as S and Q circumvents the discontinuity pitfall, and stabilizes the derivative evaluation.

Additionally, it should be noted that solving the PBOF amounts to solve the normalized analytic bandlimited signal $\hat{S}_n = \frac{\hat{S}}{|\hat{S}|}$. Indeed, the normalized analytic signal $\hat{S}_n$ does not undergo envelop variations as well. This complex number oscillates around the complex unity circle:

$$\hat{S}_n = \frac{1}{|\hat{S}|}(|\hat{S}|(\cos(\phi) + j\sin(\phi))) = \cos(\phi) + j\sin(\phi) \tag{3.24}$$

It can be demonstrated (see appendix A) that the PBOF energy:

$$E_{\mathbf{v}}(\mathbf{x}) = (\nabla\phi \cdot \mathbf{v} + \frac{\partial \phi}{\partial t})^2 \tag{3.25}$$

is equivalent to:

$$E_{\mathbf{v}}(\mathbf{x}) = (\nabla\hat{S}_n(\mathbf{x},t) \cdot \mathbf{v} + \frac{\partial \hat{S}_n(\mathbf{x},t)}{\partial t})(\nabla\hat{S}_n(\mathbf{x},t) \cdot \mathbf{v} + \frac{\partial \hat{S}_n(\mathbf{x},t)}{\partial t})^* \tag{3.26}$$

A simple and natural way to solve this optical flow equation would be the *Lucas-Kanade* approach [Lucas and Kanade, 1981], pointed out in 2.3.1. The corresponding local equation system would read:

$$M\mathbf{v} = \mathbf{b} \tag{3.27}$$

where M is the phase gradient tensor, such that:

$$M = \begin{pmatrix} \sum W\phi_x^2 & \sum W\phi_x\phi_y & \sum W\phi_x\phi_z \\ \sum W\phi_x\phi_y & \sum W\phi_y^2 & \sum W\phi_y\phi_z \\ \sum W\phi_x\phi_z & \sum W\phi_y\phi_z & \sum W\phi_z^2 \end{pmatrix} \tag{3.28}$$

and $\mathbf{b} = -\sum W\frac{\partial\phi}{\partial t}\nabla\phi$ is the right hand side term.

The PBOF approach is particularly interesting in our case, since it excludes the undesirable spectral information (DC component and high frequency noise) and is not sensitive to envelop variations, *i.e.* verifies the brightness assumption (2.1) throughout the sequence. As a result, we can interpret phase displacement as the **pure expression of flow motion**. We will use henceforth the phase ϕ and its derivatives as the suitable feature for representing contrast propagation.

Unfortunately, a straightforward application of *Lucas-Kanade* does not yield good results in contrast sequences. The spatial behavior of the contrast phase ϕ inside the arterial lumen, which is the main responsible for failure, will be detailed in the next subsection.

3.2.4 Image gradient based optical flow and its pitfalls

Now that we settled the technical background for temporal processing, we may focus on what happens on the spatial side. In order to further understand the spatial behavior of phase, and have insightful overview of the associated pitfalls, we resort here to the simplified model of artery described in chapter 1 1.3.1.

A *Poiseuille* fluid velocity pattern within a cylinder of radius R with axis coinciding with z-axis and a velocity v_0 on the z-axis can be written in the form:

$$\mathbf{v} = (1 - \frac{r^2}{R^2}) \begin{pmatrix} 0 \\ 0 \\ u_0 \end{pmatrix} \tag{3.29}$$

where $\mathbf{v} = (v_r\, v_\theta\, v_z)^T$ is defined here with cylindrical coordinates.

Let the CA density have a complex harmonic time dependence with frequency $\omega = 2\pi f$. In the cylinder cross-section at $z = 0$, the concentration is assumed to be independent with respect to $r = \sqrt{x^2 + y^2}$ so that the propagating CA density $\hat{S}(r, z, t)$ can be expressed as:

$$\boxed{\hat{S}(r, z, t) = Ae^{j(\omega t - \frac{\omega z}{u_0(1-(\frac{r}{R})^2)} + \phi_0)} = Ae^{j\phi(r,z,t)}} \tag{3.30}$$

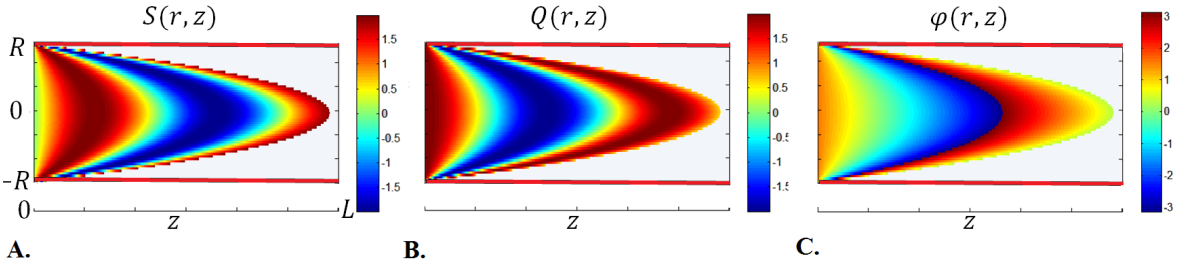

Figure 3.5: *Poiseuille flow simulation in a cylindrical tube with complex contrast quantities. A cut plane is represented at ($x = 0$), and the vessel wall is shown as red lines. A. shows the real part of the analytic signal S. B. shows the imaginary part Q. C. represents the phase ϕ. The simulation was carried out using equation* (3.30) *with the following parameters:* $A = 2$, $t = 800\,(in\ frames)$, $R = 30\,pixel$, $u_0 = 4\,pix.frame^{-1}$, $f = 1.5\,10^{-3}\,frame^{-1}$, $\phi_0 = \frac{\pi}{2}$.

As expected, the contrast isovalues follow the parabolic velocity profile. The flow slows down near the wall, in a so-called **limit layer**, where the contrast moves slowly. Analytically, the phase at $r = \pm R$ stays still at the injection point $z = 0$, while phase at profile peak ($r = 0$) rapidly gets away from the injection point at the velocity v_0. As a result, the **isophase profile** forms a very elongated shape in direction of the flow, and gets even more elongated as we progress on the z axis.

The phase gradient can be written:

$$\nabla\phi = \frac{-2R^2\omega z}{u_0(R^2 - r^2)^2} \begin{pmatrix} x \\ y \\ \frac{(R^2-r^2)}{2z} \end{pmatrix} \tag{3.31}$$

We can easily see the singularity that occurs at $r = R$:

$$\boxed{\lim_{r\to R} \quad \|\nabla\phi_r\| = +\infty}$$

Moreover, the dependency of ϕ_x and ϕ_y with respect to z tends to accentuate this divergence as we get further from the injection point. This singularity cannot be directly observed in discrete images indeed, but instead, one gets very high values near the rim of the cylinder. The norm of the spatial gradient $\|\nabla\phi\|$ will increase dramatically around $r = \pm R$, as illustrated in figure 3.6.

On top of that, the ratio between the radial component, for instance ϕ_r and the longitudinal component ϕ_z also diverges when r approaches R:

$$\boxed{\lim_{r\to R} \quad \frac{\phi_r}{\phi_z} = \lim_{r\to R} \quad \frac{2zr}{(R^2 - r^2)} = +\infty} \tag{3.32}$$

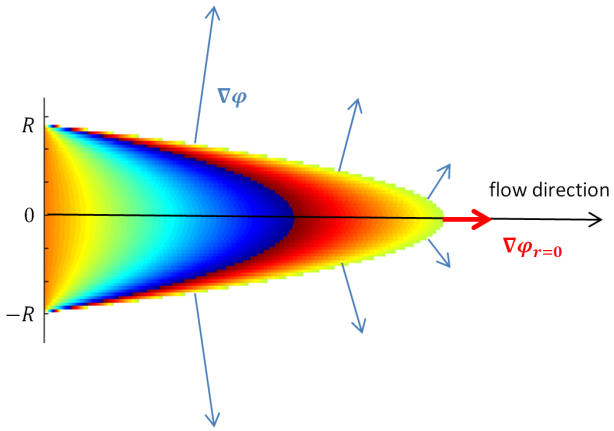

Figure 3.6: *Phase gradient in a Poiseuille tube. The phase gradient direction is aligned with z-axis at $r = 0$, but drifts strongly as r gets closer to the cylinder boundary ($r = R$ or $r = -R$).*

This proves that the phase gradient $\nabla\phi$ has a tendency for a **radial orientation** in the neighborhood of the vessel wall. In the boundary layer, where the **viscosity is dominant**, slow traveling lamina adjacent to the wall and fast traveling lamina coexist. The velocity component parallel to the wall has a large gradient component in the radial direction. As a result, the phase profile is almost **tangent** to the wall in the boundary layer, so that its normal, or gradient is pointing completely outwards. The following figure describes the behavior of the phase gradient components throughout the cylindrical model.

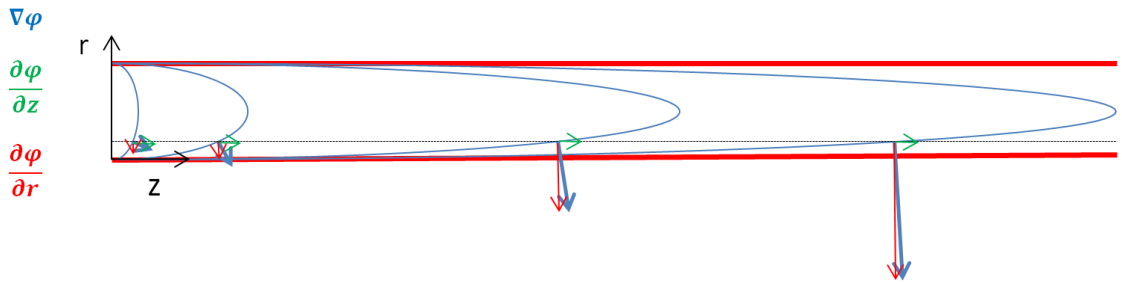

Figure 3.7: *The further we move away from the injection point, the sharper the isophases behave. This tends to dramatically increase the radial component of the phase gradient. In the above figure, the blue arrows represent the phase gradient vector. The green arrow is the longitudinal component (z-axis), only this information is needed to recover the velocity magnitude. Its value is kept constant alongside the Poiseuille tube. The red arrow is the 'error component' that does not play a role in the contrast transport. Due to the important elongation of the contrat profile, this component grows linearly along the z-axis.*

Because optical flow estimation is based on the direction of $\nabla\phi$, one can expect **misestimations** of the flow direction in areas close to the vessel wall. The aperture

problem is strongly present in the limit layer where the image gradient is irrelevant for the computation of flow propagating in an orthogonal direction. When using the *Lucas-Kanade* approach, the large aperture scale will create high instabilities in the recovery of the unknown velocity (see section 2.3.1).

The numerical example of *Poiseuille* flow does not represent all the sorts of flows existing in arteries indeed. However, it highlights the phenomenon occurring in the **boundary layer**, where the phase gradient $\nabla\phi$ inevitably points in the radial direction. According to the size of the limit layer, this issue is more or less bothersome. To deal with aperture problem in contrast phase sequences, we propose a global optical flow regularization, including physical priors.

3.3 On the integration of physical constraints

For all imaging modalities, optical flow literature often indicates the necessity of using a suitable regularization scheme to obtain a reliable flow estimation. In this section, several priors concerning blood flow will be integrated in the PBOF framework. Some of them are already used in state-of-the art OFM, while one of them is original and specific to fluid flow.

3.3.1 Bringing a physical meaning to the optical flow

As pointed out in section 3.1 (see table 3.1), blood flow should respect the three following constraints:

1. **Flow smoothness**
2. **Flow incompressibility**
3. **Flow tangency to arterial wall**

A suitable framework for the enforcement of **global properties** is a global variational approach:

$$\mathbf{v}^\star = argmin_{\mathbf{v}} \int_\Omega (\nabla\phi \cdot \mathbf{v} + \frac{\partial\phi}{\partial t})^2 + \mathcal{R}(\mathbf{v}, \partial\mathbf{v}, \ldots, \partial^n\mathbf{v}) \tag{3.33}$$

The three enumerated constraints can be translated in a variational framework. In our formulation, the constraints are expressed as quadratic penalties in the objective function to minimize:

$$\boxed{\begin{aligned} \mathcal{R}_1(\mathbf{v}) &= \int_\Omega \mu \|\nabla\mathbf{v}\|_F^2 \\ \mathcal{R}_2(\mathbf{v}) &= \int_\Omega \lambda(\nabla\cdot\mathbf{v})^2 \\ \mathcal{R}_3(\mathbf{v}) &= \int_\Omega \nu B(\mathbf{n}^T\cdot\mathbf{v})^2 \end{aligned}}$$

where μ, λ and ν are three regularization factors, and $\mathbf{n}$ is the outward normal vector of the lumen boundary, referred to as $\mathcal{B}$. The mask $B(\mathbf{x})$ of $\mathcal{B}$ reads:

$$B = \begin{cases} 1 \text{ if } \mathbf{x} \in \mathcal{B} \\ \\ 0 \text{ otherwise} \end{cases} \tag{3.34}$$

Those three quadratic terms should be summed up to the data fidelity energy to give:

$$\boxed{E = \int_{\Omega} \left[(\nabla\phi \cdot \mathbf{v} + \frac{\partial \phi}{\partial t})^2 + \mu \|\nabla \mathbf{v}\|_F^2 + \lambda (\nabla \cdot \mathbf{v})^2 + \nu B (\mathbf{n}^T \cdot \mathbf{v})^2 \right]} \tag{3.35}$$

This energy groups four quadratic terms that penalize a flow field which would violate phase constancy assumption (3.22) or fluid mechanics laws. Nevertheless, this setting allows for some flexibility in the solution. The three constraints should be respected in an ideal case, but numerical issues arise when dealing with discrete images. As a consequence, only a best compromise between each constraint is sought. One should not that the first term corresponds to the one used in *Horn and Schunk* [Horn and Schunck, 1981], while the divergence term is found several times in optical flow literature [Corpetti et al., 2005, Benz et al., 2014, Corpetti et al., 2000, Corpetti et al., 2002a, Corpetti et al., 2002b, Papadakis et al., 2007]. **What makes the originality of our approach is essentially the third regularization term $\mathcal{R}_3$. The flow tangency penalty $\mathcal{R}_3(\mathbf{v})$ replace the usual hard constraint $\mathbf{n}^T \cdot \mathbf{v}$ at the lumen wall. In our view, this is more convenient with our cartesian image representation which would introduce unpleasant pixelization effects**.

On top of that, the originality of the approach lies in the way to minimize the global energy E: the use of a conjugate gradient algorithm. The algorithmic framework is presented in the following section.

3.3.2 Minimization of a global functional: the preconditioned conjugate gradient algorithm

The previous energy 3.35 can be minimized using lots of different optimization algorithms. When dealing with very large systems, as in our present problem, straightforward matrix inversion is not possible. Instead, **iterative algorithms** are employed, especially with **sparse systems** as ours. Large sparse systems often arise when numerically solving partial differential equations or optimization problems.

The **conjugate gradient** method (CGM) is well known to solve unconstrained optimization problem such as **energy minimization**. It was mainly developed by *Magnus Hestenes and Eduard Stiefel* [Straeter, 1971, Hestenes and Stiefel, 1952], in order to solve a linear system:

$$\boxed{A\mathbf{v} = \mathbf{b}} \tag{3.36}$$

with A **symmetric** ($A^T = A$), **positive definite** ($\forall \mathbf{v} \in \mathbb{R}^{3*}, \mathbf{v}^T A \mathbf{v} > 0$), and **real**. The solution $\mathbf{v}^\star$ is unique and can be reached in $n = rg(A)$ iterations.

The energy (3.35) is minimized using the *Euler-Lagrange* equations. The solution flow field $\mathbf{v}$ is found when:

$$\frac{\partial E}{\partial \mathbf{v}} - \frac{\partial \left(\frac{\partial E}{\frac{\partial \mathbf{v}}{\partial \mathbf{x}}} \right)}{\partial \mathbf{x}} = 0 \tag{3.37}$$

The *Euler-Lagrange* equation simplifies when canceling the second term. After several developments (see appendix A), the derivation of E with respect to $\mathbf{v}$ yields:

$$\boxed{M\mathbf{v} - \mathbf{b} - \mu\Delta\mathbf{v} - \lambda\nabla(\nabla \cdot \mathbf{v}) + \nu B\mathbf{n}\mathbf{n}^T\mathbf{v} = 0} \tag{3.38}$$

where $M = \begin{pmatrix} \phi_x^2 & \phi_x\phi_y & \phi_x\phi_z \\ \phi_x\phi_y & \phi_y^2 & \phi_y\phi_z \\ \phi_x\phi_z & \phi_y\phi_z & \phi_z^2 \end{pmatrix}$ is the phase gradient tensor and $b = -\frac{\partial\phi}{\partial t}\nabla\phi$ the right hand side term.

This equation can be rewritten $A\mathbf{v} = \mathbf{b}$, by using a new system matrix:

$$A = M + \nu B\mathbf{n}\mathbf{n}^T - \mu\Delta - \lambda\nabla(\nabla\cdot) \tag{3.39}$$

This system function is symmetric and non negative definite, as each term comes from a quadratic expression. In our preferred framework, A should be rather used as an **operator**, than as a matrix. Indeed, the differential operators Δ and $\nabla(\nabla\cdot)$ are more convenient to use as a function of space than a matrix. The overall matrix product $A\mathbf{v}$ is painful to write, or even to think:

$$\left[\begin{pmatrix} M_{\mathbf{x}_1} & & & & \\ & M_{\mathbf{x}_2} & & 0 & \\ & & \dots & & \\ & 0 & & \dots & \\ & & & & M_{\mathbf{x}_{Card(\Omega)}} \end{pmatrix} - \mu\mathcal{R}_1 - \lambda\mathcal{R}_2 + \alpha\mathcal{R}_3 \right] \begin{pmatrix} \mathbf{v}(\mathbf{x}_1) \\ \mathbf{v}(\mathbf{x}_2) \\ \dots \\ \dots \\ \mathbf{v}(\mathbf{x}_{Card(\Omega)}) \end{pmatrix}$$

where $\mathcal{R}_1, \mathcal{R}_2$ and $\mathcal{R}_3$ are the global regularity matrices corresponding to respectively $\Delta\mathbf{v}$, $\nabla(\nabla\cdot\mathbf{v})$ and $B\mathbf{n}\mathbf{n}^T$.

Luckily, the conjugate gradient or similar solver only require to perform a linear application instead of a matrix product:

$$A\mathbf{v}(\mathbf{x}) = A(\mathbf{v}(\mathbf{x})) = M_{\mathbf{x}}\mathbf{v}(\mathbf{x}) - \mu\Delta\mathbf{v}(\mathbf{x}) - \lambda\nabla(\nabla\cdot\mathbf{v}(\mathbf{x})) + \nu B(\mathbf{x})\mathbf{n}\mathbf{n}^T\mathbf{v}(\mathbf{x}) \tag{3.40}$$

Now, let us recall the basic principle of conjugate gradient. We aim to solve the linear system $A\mathbf{v} = \mathbf{b}$ by starting from an initial guest, $\mathbf{v} = 0_\Omega$, and using specific conjugate directions to gradually make the energy E decrease. Conjugate flow vectors $\mathbf{d}$ are computed to orient the flow field $\mathbf{v}$ toward the solution field $\mathbf{v}^\star$, by using a *Krylov* orthogonality condition. Any pair of conjugate directions $\mathbf{d}_i$ and $\mathbf{d}_j$ verify:

$$\mathbf{d}_i A \mathbf{d}_j = 0 \tag{3.41}$$

At each iteration, $\mathbf{v}_i$ gets closer to the solution vector $\mathbf{v}^\star$ by performing a step in direction $\mathbf{d}_i$:

$$\mathbf{v}_{i+1} = \mathbf{v}_i + \alpha \mathbf{d}_i \tag{3.42}$$

The conjugation of descent vectors speed up the convergence of $\mathbf{v}$, by using the inner properties of the system matrix A [Shewchuk, 1994]. The direction $\mathbf{d}_{i+1}$ is built based on the current **residual** $\mathbf{r} = \mathbf{b} - A\mathbf{v}$ and all the previous conjugate directions $\mathbf{d}_k$ ($k \in [0\, i]$):

$$\mathbf{d}_{i+1} = \mathbf{r}_i + \beta \mathbf{d}_i \tag{3.43}$$

An important property of the CGM is its ability to converge in n iterations, n being the rank of the system matrix A. Here, n is the number of elements in Ω, which can be rather large in 3D images. Luckily, much fewer iterations are generally required. In order to improve the convergence of the CGM, it is always of great help to use a **preconditioning**. In a review, *Shewchuck* details the different CGM, including preconditioning [Shewchuk, 1994], and explains that pre-multiplying the equation (3.36) with a preconditioner P will help improving the conditioning of A, thereby accelerating the CGM convergence. P shall be symmetric, positive-definite and approximating A, but should be easier to invert so that equation (3.36) becomes:

$$P^{-1} A \mathbf{v} = P^{-1} \mathbf{b} \tag{3.44}$$

where $C(P^{-1}A) \ll C(A)$.

The algorithm for preconditioned conjugate gradient (PCG) is described in the next page. Note that the CGM can be retrieved when setting $P = I$, the identity matrix.

Both fields $\mathbf{v}$ and descent direction $\mathbf{d}$ are iterated until the overall residual norm δ_{new} goes below a tolerance threshold. δ_{new} is the sum of the squared residuals in Ω, it represents a distance between the current flow field $\mathbf{v}$ and the sought solution $\mathbf{v}^\star$:

$$\begin{aligned}
\delta_{new} &= \sum_\Omega (\mathbf{b}(\mathbf{x}) - A(\mathbf{x})\mathbf{v}(\mathbf{x}))^T (\mathbf{b}(\mathbf{x}) - A(\mathbf{x})\mathbf{v}(\mathbf{x})) \\
&= \sum_\Omega (\mathbf{v}(\mathbf{x}) - \mathbf{v}^\star(\mathbf{x}))^T A(\mathbf{x})^T A(\mathbf{x}) (\mathbf{v}(\mathbf{x}) - \mathbf{v}^\star(\mathbf{x}))
\end{aligned}$$

Algorithm 3 Preconditioned conjugate gradient algorithm for flow recovery $\mathbf{v}^\star$

Define i_{max} the maximal number of iterations and ϵ the stop criterion
Initialize $i = 0$ and the residual $\mathbf{r}_0 = \mathbf{b} - A\mathbf{v}_0$
Initialize the first direction $\mathbf{d}_0 = P^{-1}\mathbf{r}_0$, $\delta_0 = \mathbf{r}_0^T\mathbf{d}_0$, and $\delta_{new} = \delta_0$
while $i < i_{max}$ **and** $\delta_{new} > \epsilon^2\delta_0$ **do**
  $\mathbf{q} = A\mathbf{d}_i$
  $\alpha = \frac{\delta_{new}}{\mathbf{d}^T\mathbf{q}}$
  $\mathbf{v}_{i+1} = \mathbf{v}_i + \alpha\mathbf{d}_i$
  if i is divisible by 50 **then**
    $\mathbf{r}_{i+1} = \mathbf{b} - A\mathbf{v}_{i+1}$
  else
    $\mathbf{r}_{i+1} = \mathbf{r}_i - \alpha\mathbf{q}$
  end if
  $\delta_{old} = \delta_{new}$
  $\delta_{new} = \mathbf{r}_{i+1}^T P^{-1}\mathbf{r}_{i+1}$
  $\beta = \frac{\delta_{new}}{\delta_{old}}$
  $\mathbf{d}_{i+1} = P^{-1}\mathbf{r}_{i+1} + \beta\mathbf{d}_i$
  $i = i + 1$
end while

3.3.3 Effect of the different constraints

Now the variational framework is set up, let us shed some light on the different regularization terms.

Flow tangency to arterial wall

The regularization term $\mathcal{R}_3$ is necessary to ensure the conservation of flow rate. It was proven in section 1.3.1, that no flow leaks should occur alongside the arterial wall (equation (1.12)), so as to insure flow conservation. Furthermore, the previous section 3.2.4 showed how phase gradients badly influence the velocity direction near the wall boundary. Since the term $\mathcal{R}_3$ is **local**, we simply add it to the tensor matrix of the phase gradient near the lumen wall $\mathcal{B}$:

$$M_{\mathcal{B}} = M + \nu\mathbf{n}\mathbf{n}^T \tag{3.45}$$

where $\mathbf{n}\mathbf{n}^T$ is a symmetric matrix with $Tr(\mathbf{n}\mathbf{n}^T) = 1$. The product of this matrix with the velocity $\mathbf{v}(\mathbf{x})$ should be the smallest possible, meaning that $\mathbf{v}(\mathbf{x})$ should not have any component in the direction of $\mathbf{n}$. Since M has only one eigenvector with non-zero eigenvalues ($\nabla\phi$) and $\mathbf{n}\mathbf{n}^T$ only $\mathbf{n}$, the addition of both tensors improves the conditioning of $M_{\mathcal{B}}$, and reduce the underdetermination of flow direction to only one line (see figure 3.8).

In practice, the aperture inside the boundary layer is fully solved thanks to the

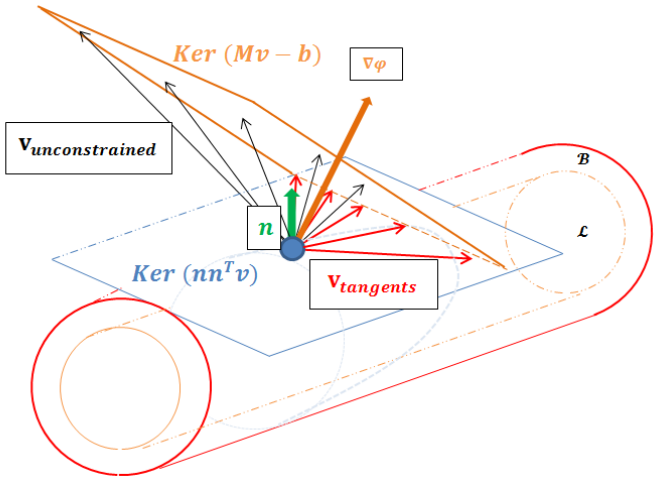

Figure 3.8: *Flow tangency constraint along the arterial wall.* $\nabla\phi$ *is pointing outwards, which misleads the flow direction* $\mathbf{v}$*. The tangency constraint reduces the aperture to one line, which is the intersection between the optical flow constraint plane* $Ker(M\mathbf{v}-\mathbf{b})$ *and the flow tangency constraint plane* $Ker(\mathbf{n}\mathbf{n}^T\mathbf{v})$*.*

other regularization terms. Typically, the neighborhood will transmit the third missing component, in such a way that $\mathbf{v}$ smoothly follows its neighbors.

Gradient penalization

The smoothness term has already been investigated with the *Horn and Schunck* algorithm [Horn and Schunck, 1981]. It **diffuses** the reliable gradient information in the areas with almost no spatial gradients. The parameter μ has to be chosen according to the image **fidelity**, *i.e.* the strength of the tensor matrix $M = \nabla\phi\nabla\phi^T$. In order to understand this, let us simplify the *Euler-Lagrange* equation with only the smoothness term:

$$M\mathbf{v} - \mu\Delta\mathbf{v} = \mathbf{b} \tag{3.46}$$

Let us approximate M as a scalar with $M\mathbf{v} \simeq \frac{Tr(M)}{3}\mathbf{v}$ and $m = \frac{1}{Card(\mathcal{L})}\int_{\mathcal{L}}\frac{Tr(M)}{3}$ the average fidelity in the lumen $\mathcal{L}$. *Fourier*-transforming the equation in the spatial domain yields:

$$m\tilde{\mathbf{v}} + \mu\mathbf{k}^T\mathbf{k}\tilde{\mathbf{v}} = \tilde{\mathbf{b}} \tag{3.47}$$

where $\mathbf{k}$ is the spatial frequency vector. Isolate $\tilde{\mathbf{v}}$, we get:

$$\tilde{\mathbf{v}} = \frac{\frac{\tilde{\mathbf{b}}}{\mu}}{\frac{m}{\mu} + \mathbf{k}^T\mathbf{k}} \tag{3.48}$$

This *Lorentzian* function is well-known to be a *bi-exponential* function after inverse *Fourier* transform:

$$\mathbf{v}(\mathbf{x}) = \frac{1}{2\sqrt{(m\mu)}}\mathbf{b}(\mathbf{x}) * e^{-\sqrt{\frac{m}{\mu}}\|\mathbf{x}\|} \tag{3.49}$$

which means that $\mathbf{v}$ will be **blurred** because of the gradient penalty, with an exponential function of pseudo standard deviation $\sigma = \sqrt{\frac{\mu}{\tilde{m}}}$. This approximation of the solution $\mathbf{v}$ shows the strong influence of the ratio $\frac{\mu}{\tilde{m}}$ on the **flow field diffusion range**. The higher μ compared to M, the more important the diffusion effect. In practice, μ and $\tilde{m}$ should be the same order of magnitude in order to avoid excessive smoothing.

Divergence penalization

The divergence term is uneasy to interpret directly. It can be related to the incompressibility term intervening in fluid mechanics with *Lamé* equations, with λ the *Lamé* factor. However, the analogy cannot go any further, since the equation corresponds to a penalization scheme, and not a true constraint. There is not so much to say about this excepted one has to be very careful when choosing λ. Once derived with the *Euler-Lagrange* equation, this term -$\nabla(\nabla \cdot \mathbf{v})$ - has second order derivatives of the velocity and as such is very sensitive to sharp variations of the flow fields. This factor should be set small enough to correct for the flow divergence, as illustrated in figure 3.9:

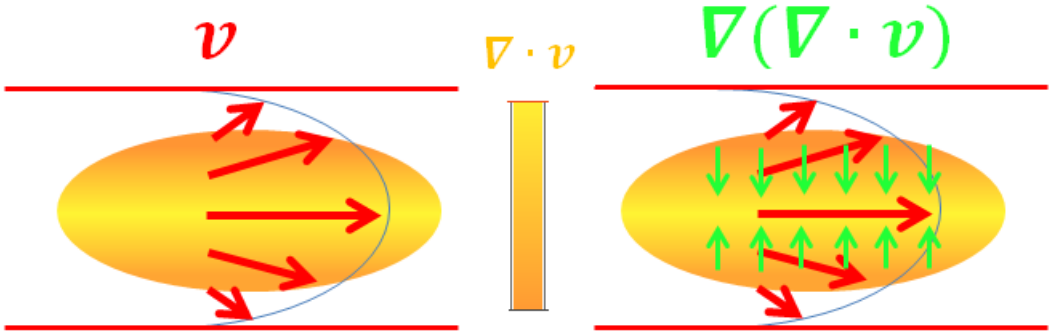

Figure 3.9: *Effect of divergence penalization. The velocity field* $\mathbf{v}$ *is divergent, which is the result of the limit layer on the phase gradient* $\nabla\phi$*. The correction term* $\lambda\nabla(\nabla \cdot \mathbf{v})$ *reduces the divergence by adding inwards vectors. The* λ *factor should be small so that little corrections are performed at each iterations. If the regularization factors is pushed more than necessary, an opposite phenomenon of flow convergence may occur. Subsequently will follow a skyrocketing oscillation behavior of the flow field between local convergent and divergent patterns. This would reflect the inner instability of the second order derivative correction term.*

The divergence correction vector appears when considering the residual of E at iteration i, the new descent direction:

$$\mathbf{r}_i = \mathbf{b} - A\mathbf{v}_i = \mathbf{b} - M\mathbf{v}_i + \lambda\nabla(\nabla \cdot \mathbf{v}_i) + \dots \tag{3.50}$$

In practice, λ is set as the half of μ, as it appears in *Lamé* equations. This choice is arbitrary, but seems to lead to reasonable convergence of the CGM. The flow field corrector $\lambda\nabla(\nabla \cdot \mathbf{v}_i)$ slowly decreasing $\nabla \cdot \mathbf{v}_i$ over iterations is the ideal case.

The weight of optical flow fidelity

Finally, let us investigate the fidelity term of the overall energy E, and how it behaves compared to the others. Recall the expression of the phase gradient tensor:

$$M = \begin{pmatrix} \phi_x^2 & \phi_x\phi_y & \phi_x\phi_z \\ \phi_x\phi_y & \phi_y^2 & \phi_y\phi_z \\ \phi_x\phi_z & \phi_y\phi_z & \phi_z^2 \end{pmatrix} \tag{3.51}$$

Use the previous simplification $M\mathbf{v} \simeq Tr(\frac{M}{3})\mathbf{v}$, and the expression of the phase tensor M, we get:

$$M\mathbf{v} \simeq \frac{1}{3}\|\nabla\phi\|^2\mathbf{v} \tag{3.52}$$

This means that the fidelity to brightness conservation is weighted with the factor $\|\nabla\phi\|^2$. Considering the *Euler-Lagrange* equation, we then see clearly the contribution of each term:

$$\frac{1}{3}\|\nabla\phi\|^2\mathbf{v} - \mathbf{b} - \mu\Delta\mathbf{v} - \lambda\nabla(\nabla \cdot \mathbf{v}) + \nu B\mathbf{n}\mathbf{n}^T\mathbf{v} = 0 \tag{3.53}$$

Where $\|\nabla\phi\|^2$,μ,λ and ν compete with each other. Unfortunately, it was demonstrated in section 3.2.4 that $\|\nabla\phi\|$ is highly unreliable in the boundary layer $\mathcal{B}$ and increases to very large values. In other words, the weighting of optical flow fidelity is the strongest in areas where its reliability is the lowest. As a result, **the bad gradient information in the boundary layer will diffuse inside the lumen**, which is not desirable indeed.

3.3.4 Weighting of optical flow fidelity

In order to circumvent the issue of improper fidelity weight distribution, one can resort to a **normalization** of the optical flow equation. Under the assumption that $\|\nabla\phi\|$ does not cancel, the optical flow equation (3.22) turns to:

$$\frac{\nabla\phi}{\|\nabla\phi\|} \cdot \mathbf{v} + \frac{1}{\|\nabla\phi\|}\frac{\partial\phi}{\partial t} = 0 \tag{3.54}$$

Let $\mathbf{q} = \frac{\nabla\phi}{\|\nabla\phi\|}$ be the normalized phase gradient and $v_q = -\frac{\frac{\partial\phi}{\partial t}}{\|\nabla\phi\|}$ be the unregularized optical flow magnitude. Hence, we get the normalized optical flow equation:

$$\boxed{\mathbf{q}\cdot\mathbf{v} - v_q = 0} \tag{3.55}$$

From this we can derive the normalized matrix tensor:

$$\boxed{M = \mathbf{q}\mathbf{q}^T} \tag{3.56}$$

and the normalized right hand side vector:

$$\boxed{b = -v_q\mathbf{q}} \tag{3.57}$$

This normalization reduces the pollution of boundary layer during the fidelity diffusion. Every pixel in the lumen carries the same fidelity weight $Tr(\mathbf{q}\mathbf{q}^T) = 1$, which homogenizes the diffusion of phase gradient. As illustrated in figure 3.10, the large phase gradient vectors will be reduced to the same size of those in the lumen center, where the velocity is maximal.

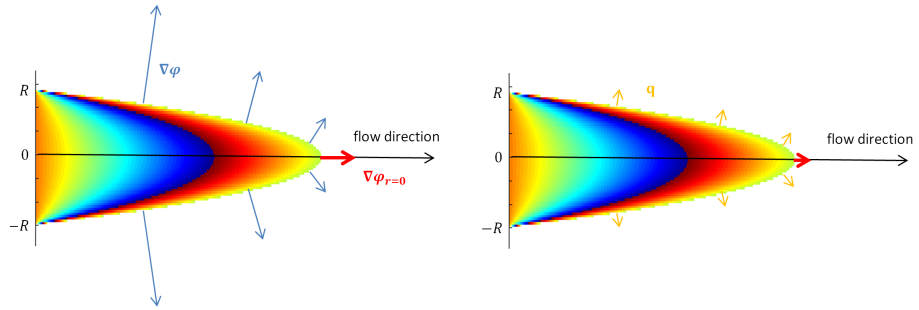

Figure 3.10: *Phase gradient normalization in the vessel lumen with* $\mathbf{q} = \frac{\nabla\phi}{\|\nabla\phi\|}$.

The vanishing phase gradients can finally be dealt with by using a specific weighting depending on a threshold parameter γ:

$$M_{weighted} = \frac{\|\nabla\phi\|^2}{\|\nabla\phi\|^2 + \gamma^2} M$$
$$\mathbf{b}_{weighted} = \frac{\|\nabla\phi\|^2}{\|\nabla\phi\|^2 + \gamma^2} \mathbf{b}$$

Now that every terms of the energy have been thoroughly explained, we read here our final *Euler-Lagrange* equation:

$$\boxed{M_{weighted}\mathbf{v} - \mathbf{b}_{weighted} - \mu\Delta\mathbf{v} - \lambda\nabla(\nabla\cdot\mathbf{v}) + \nu B\mathbf{n}\mathbf{n}^T\mathbf{v} = 0} \tag{3.58}$$

Yet this equation has to be solved in a very large domain Ω with 3D velocity vectors, which is extremely costly in term of computations. In order to speed up the convergence of the CGM, we take benefit from a multi-grid approach, described in the next subsection.

3.3.5 A multi-grid algorithm for the resolution of scaling issue

Over the last decades, the efficiency of *Multigrid* techniques have been proven on a wide variety of numerical problems, especially elliptic partial differential equations (PDEs), parabolic and hyperbolic PDEs, integral equations, evolution problems and geodesic problems. *Multigrid* is of great interest because of its scalability to many physical problems as fluid mechanics [Brandt and Livne, 2011], its efficiency and its rigorous mathematical basis. In the late 1980s, *William L. Briggs* published a very educational tutorial on *Multigrid* [Briggs, 1987], with an improved edition with a larger spectrum of applications in 2000 [Briggs et al., 2000]. *Multigrid* essentially provides a generalization of the *coarse-to-fine* approach discussed in section 2.5.

In our present case, a pyramid of 3D cartesian grids is built. A CGM aims to solve the system (3.36):

$$\boxed{A\mathbf{v} = \mathbf{b}}$$

with A a full-rank matrix system, $\mathbf{v}$ the flow field to be solved, and $\mathbf{b}$ the right hand side field, which can also be written $\mathbf{b} = A\mathbf{v}^\star$, with $\mathbf{v}^\star$ the solution flow field.

The overall flow field error $\mathbf{e}$ can be written:

$$\boxed{\mathbf{e} = \mathbf{v}^\star - \mathbf{v}} \tag{3.59}$$

It measures how far $\mathbf{v}$ is from the solution. However, since we do not know directly the solution flow field $\mathbf{v}^\star$, we cannot have access to the error $\mathbf{e}$. Instead, we resort to the **energy residual**:

$$\begin{aligned}\mathbf{r} &= \mathbf{b} - A\mathbf{v} \\ &= A(\mathbf{v}^\star - \mathbf{v}) \\ &= A\mathbf{e}\end{aligned}$$

Unfortunately, we see above that when $\mathbf{r}$ is small in norm, $\mathbf{e}$ is not necessary small. The flow field $\mathbf{v}$ can stagnate in a state without reaching the global minimum. *Briggs* pointed out in his book the **very slow error convergence at low spatial frequencies**, compared to those with high frequency. Moreover, the **damping of error magnitude** during CG iterations is uneven in the spatial spectrum. High frequency components are efficiently corrected, while low frequency components are left undamped. The core idea in *Multigrid* is that the error $\mathbf{e}$ can be decomposed in a **frequency space** $\mathbf{e} = \sum_h c_h \mathbf{w}_h$, with $\mathbf{w}_h$ the frequency mode, and c_h the associated mode magnitude. The different grid levels h represent different **bandwidths** of the error e, in which the associated error e_h can be efficiently minimized:

$$\boxed{\mathbf{e}_h = \mathbf{v}_h^\star - \mathbf{v}_h} \tag{3.60}$$

This is typically what motivates a *Multigrid* scheme in our problem where both low and high spatial frequency coexist. Phase ϕ exhibits high and low spatial frequencies - *i.e.* short and long waves - while physical constraints should be respected in coarse scales.

Now, let us explain the basic implementation of a *Multigrid* algorithm. First, a **restriction operator** is used with suitable anti-aliasing pre-smoothing to inject the values of the finer grid A_h and $\mathbf{b}_h$ into the coarser grid A_{2h} and $\mathbf{b}_{2h}$:

$$A_{2h} = A_h \downarrow \quad \text{and} \quad \mathbf{b}_{2h} = \mathbf{b}_h \downarrow \tag{3.61}$$

with $\downarrow$ the restriction operator. This operation is repeated for A and $\mathbf{b}$ until the coarsest level H is reached.

Dealing with coarse grids shifts the error spectrum in higher frequencies, therefore improving the attenuation of low frequencies. This way, coarsening the spatial domain leverages the premature steadiness of $\mathbf{e}$. The reader is invited to delve into *Briggs*'s tutorial to further understand how error $\mathbf{e}_h$ behaves according to the grid level.

Thereafter, the linear system $A\mathbf{v} = \mathbf{b}$ is relaxed in every grid, starting from the coarsest, to the finest. After a small number of iterations, chosen by the user, a flow field error $\mathbf{e}_{2h}$ is extracted and added to the finer flow field error by the use of a **prolongation operator** (also known as interpolation operator):

$$\mathbf{e}_h = \mathbf{e}_{2h} \uparrow \tag{3.62}$$

with $\uparrow$ the prolongation operator that generally also uses binomial weights.

Usually, a *coarse-to-fine* approach does not suffice to fully eliminate the error $\mathbf{e}$. *Briggs* explains that the bandwidth components $\mathbf{e}_h$ cannot be eradicated by a single relaxation. Instead, one has to travel back and forth within the different grids to completely get rid of the resistant error residuals. This can be explained algebraically, as prolongation and restriction operators slightly differ from bandpass filtering, which create a small 'angle' between their image and kernel spaces (see [Briggs, 1987]). The bandwith component c_h is in some way distributed in every grid level but with a strong predominance at grid level h. Consequently, multiple go and backs are desired through the *Multigrid* structure.

V-cycle and Full Multigrid

Several *Multigrid* schemes are proposed in [Briggs et al., 2000], including V-cycles, W-cycles or *Full-MultiGrid* (FMG). A V-cycle is rather simple to describe, it is made of a **descending phase**, and an **ascending phase**

In descent, each is grid is relaxed with few CG iterations n_d, and transmits its residual $\mathbf{r}_h$ to the right hand side term $\mathbf{b}$ of the coarser grid. Then, the energy component c_h corresponding to its specific bandwidth is minimized, and the minimization of the overall error $\mathbf{e}$ in evenly distributed in the *Multigrid* structure.

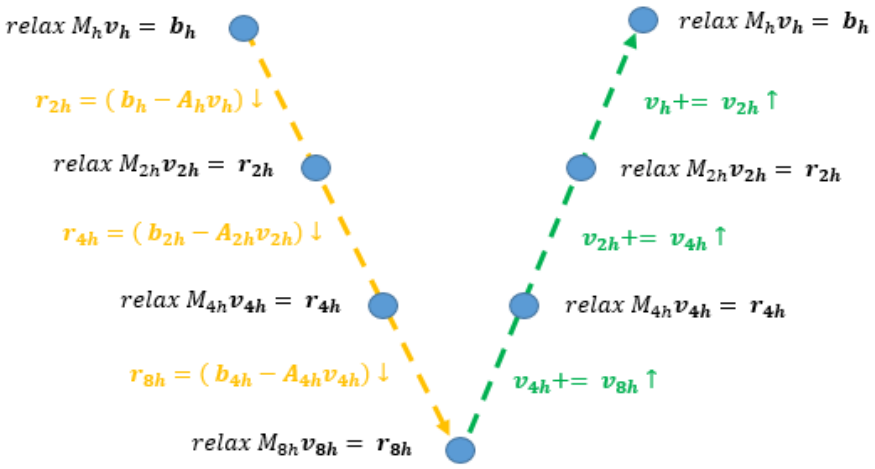

Figure 3.11: *V cycle with four grid levels in Multigrid algorithm.*

Algorithm 4 Vcycle scheme of conjugate gradient relaxations

Define H the number of grid levels, n_d and n_a the number of iterations in descent and ascent.
Restrict M and $\mathbf{b}$ to the coarsest level H
for $h = 0$ **to** $h = H - 1$ **do**
  Relax $A_h \mathbf{v}_h = \mathbf{b}_h$ for $\mathbf{v}_h$ with n_d iterations
  Restrict the residual $\mathbf{b}_{h+1} = (\mathbf{b}_h - A_h \mathbf{v}_h) \downarrow$
end for
Solve $A_H \mathbf{v}_H = \mathbf{b}_H$ for $\mathbf{v}_H$
for $h = H - 1$ **to** $h = 1$ **do**
  Prolong the velocity increment $\mathbf{v}_h += \mathbf{e}_{h+1} \uparrow$
  Relax $A_h \mathbf{v}_h = \mathbf{b}_h$ for $\mathbf{v}_h$ with n_a iterations
end for
Relax $A_0 \mathbf{v}_0 = \mathbf{b}_0$ for $\mathbf{v}_0$ with n_a iterations

The number of voxels $Card(\Omega)$ is divided by $2^3 = 8$ at each grid restriction, *i.e.* 8 for the second grid, 64 for the third grid, and 512 for the fourth grid, which turns to very fast CG iterations in smallest grid. In order to take benefit from this efficiency and time gain, the number of iteration is set higher at coarse levels. Finally, the ascent consists in a simple *coarse-to-fine* inheritance of the velocity **increments** $\mathbf{e}_h$. Again, each grid is relaxed during the ascent with n_a CG iterations.

In our preferred setting, a FMG algorithm is implemented, which is the combination between V-cycles and *coarse-to-fine* approaches. FMG attempts to solve the equation at coarse resolutions as much as possible. Multiples upward and downward inheritances are carried out on the lowest resolutions so as to efficiently get rid of low frequency errors. Basically a small V-cycle is used at the coarsest resolution H, before gradually increasing in size, until a full V-cycle is achieved.

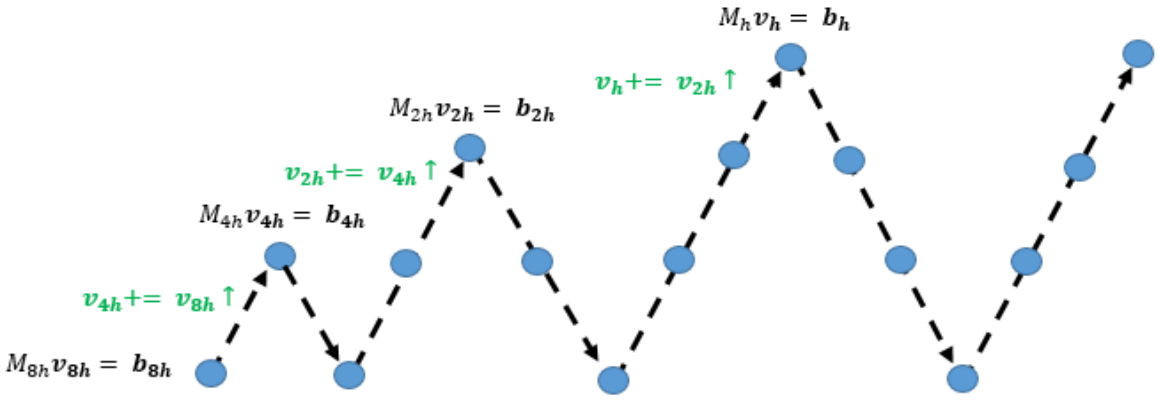

Figure 3.12: *Full-Multigrid scheme with grid levels.*

What basically comes out of a *Full Multi-grid* utilization is an efficient elimination of the low frequency errors, with an acceleration of the CG convergence. For instance, a global smoothness constraint, or an incompressibility constraint are much easier to enforce when using small and coarse grids, where they play an important role. Conversely, the fidelity term is smoothed in coarse scales, where it gets inaccurate. This local term is more relevant in fine resolutions, it delivers the high frequency patterns of the flow field $\mathbf{v}$. The **physical constraints** requiring lots of iterations are then minimized within **coarse scales**, while **optical flow fidelity** term requiring a few iterations is relaxed within **finer scales**.

Algorithm 5 Full-Multigrid method

Define H the number of grid levels, $n_{d,h}$ and $n_{d,h}$ the number of iterations in descent and ascent, for each grid level
Restrict M and $\mathbf{b}$ to the coarsest level H
Relax $A_H \mathbf{v}_H = \mathbf{b}_H$ for $\mathbf{v}_H$ with $n_{a,H}$ iterations
for $h = H - 1$ **to** $h = 0$ **do**
  Prolong the velocity increment $\mathbf{v}_h += \mathbf{v}_{h+1} \uparrow$
  Execute V cycle with h the finest level
end for

3.3.6 Boundary conditions

Multigrid methods were originally created for solving **boundary value problems**, that arise in many physical problem. Without boundary conditions, a partial differential equation cannot be solved. In our problem, we can define two kinds of boundary conditions.

First, there should be no contrast displacement outside the vessel lumen, as stipulated in section 3.1, which means for the velocity to cancel outside $\mathcal{L}$:

$$\mathbf{v}(\mathbf{x} \notin \mathcal{L}) = 0 \tag{3.63}$$

If this condition is suitable outside the vessel lumen, it cannot be used at the interface between vessel lumen and FoV edges. Obviously, angiography acquisitions focus on a particular segment of the cardiovascular system. At some point, the FoV cuts the extremities of the vasculature of interest, where flow occurs. Besides, in many image processing settings, a region of interest (ROI) is previously defined inside the FoV, wherein the image analysis is desired. As the ROI is often smaller than the FoV, it inevitably **intersects the lumen** $\mathcal{L}$. The intersections will be denoted $\mathcal{C}$.

In $\mathcal{C}$, we wish the flow rate to be conserved. In practice, this condition is hard to implement, but a lighter constraint can be imposed **in the vicinity of the intersection** by setting to 0 the velocity gradient component orthogonal to $\mathcal{C}$:

$$\nabla \mathbf{v}(\mathbf{x}) \cdot \mathbf{c} = 0 \tag{3.64}$$

where $\mathbf{c}$ is a unit vector normal to $\mathcal{C}$.

If such a condition is not respected, the derivative terms $\Delta \mathbf{v}$ and $\nabla(\nabla \cdot \mathbf{v})$ will undergo sharp transitions nearby $\mathcal{C}$, and eventually will lead to skyrocketing oscillations, that will propagate through the lumen $\mathcal{L}$. On the contrary, imposing the $\mathbf{v}$ derivative to cancel in the direction of $\mathbf{c}$ will stabilize the minimization process, and insure flow continuity.

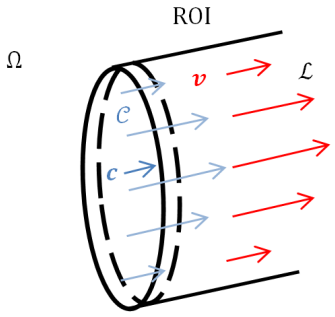

Figure 3.13: *Boundary conditions at the vessel extremity $\mathcal{C}$: the velocity gradient $\nabla \mathbf{v}$ should have no component in direction of flow, so that flow is conserved in that direction.*

The next section will describe how we divide the image domain Ω in several regions, and how we implement the boundary conditions.

3.4 A multi-region description of the flow object

In our preferred flow estimation method, the spatial domain of an input contrast image I can be divided in five regions, as illustrated in the following figure:

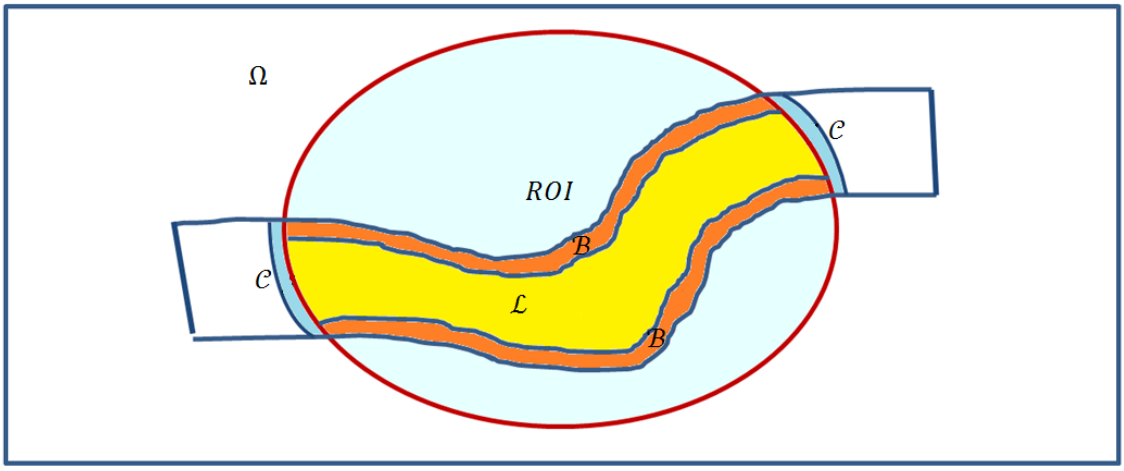

Figure 3.14: *Multi-region flow object.*

- Region Ω refers to the whole spatial extent of the image data, only a small proportion of it contains signal
- ROI is specified by the user in the application input. The rest of the domain $\bar{ROI}$ is ignored in the algorithm execution, ideally no signal is present in it, excepted in the neighborhood of the vessel extremities. It allows to focus on a

small portion of the vasculature and also to avoid the vessel extremities to disturb the flow estimation. The user selects ROI in such a way that it intersects the inlet and outlet of a vessel segment. This way, the interface between signal area, and no-signal area corresponds only to the lumen wall, and no spurious gradient information as $\nabla\phi$ is picked up at the vessel cuts.

- Region $\mathcal{L}$ corresponds to the vessel lumen, wherein flow estimation is performed. This area contains usual optical flow fidelity, as well as regularization terms on smoothness and incompressibility.

- Region $\mathcal{B}$ corresponds to the vessel walls. In this area, the spurious phase gradient information pollutes the overall flow estimation. A specific regularization is employed to enforce the velocity vector lying in a plane tangent to the wall.

- Region $\mathcal{C}$ refers to the band of pixel adjacent to the vessel extremities. These points are needed to compute spatial differentiation operators in the vessel extremities. As $\bar{ROI}$ contains no signal, we need to fill $\mathcal{C}$ with relevant information that prevents the differential on extremities to skyrocket. A boundary condition is set in this region to keep the spatial derivatives of the velocity relatively small and stabilize the algorithm.

It should be noted that those five regions have to be downsampled for every pyramid level, in view of a *Multigrid* implementation. For each region, a different condition has to be fulfilled.

Region based constraint implementation	
Region of the flow object	Mathematical expression
$ROI \cap (\mathcal{L} \cup \mathcal{B})$	$\mathbf{v} = 0$
Lumen $\mathcal{L}$	$M_{weighted}\mathbf{v} - \mathbf{b_{weighted}} - \mu\Delta\mathbf{v} - \lambda\nabla(\nabla \cdot \mathbf{v}) = 0$
Vessel boundary $\mathcal{B}$	$M_{weighted}\mathbf{v} - \mathbf{b_{weighted}} - \mu\Delta\mathbf{v} - \lambda\nabla(\nabla \cdot \mathbf{v}) + \nu\mathbf{n}\mathbf{n}^T\mathbf{v} = 0$
Vessel cuts $\mathcal{C}$	$\nabla\mathbf{v} \cdot \mathbf{c} = 0 \Rightarrow \mathbf{v} = \sum_{\mathbf{p}\in\mathcal{W}\cap(\mathcal{L}\cup\mathcal{B})} W(\mathbf{p})\mathbf{v}(\mathbf{p})$

Table 3.2: *Region based implementation of the conjugate gradient*

In $\mathcal{C}$, the velocity inside each pixel is **mirrored** with respect to the lumen neighborhood W, a binomial window that weights each neighbor belonging to window $\mathcal{W} \cap (\mathcal{L} \cup \mathcal{B})$ (see figure 3.15). Note that the mirroring is performed at each CG iteration so as to preserve flow continuity.

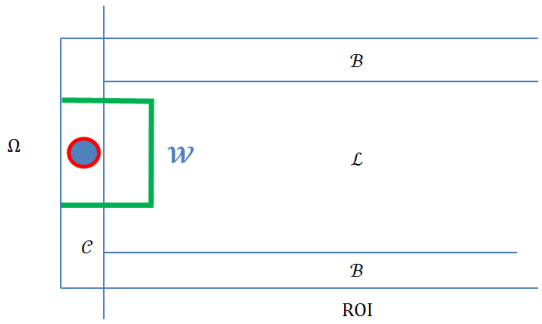

Figure 3.15: *Boundary condition on the velocity gradient* -$\nabla\mathbf{v}(\mathbf{x})\cdot\mathbf{c} = 0$ - *is smoothly imposed by a mirroring operation of the region* $\mathcal{C}$ *with respect to the lumen region* $\mathcal{L}$*, and wall region* $\mathcal{B}$*.*

General discussion

In the previous sections of this chapter, an original optical flow formulation applied to blood flow estimation was detailed. It can be divided into two independent sub-methods. A first processing on the **temporal domain** that uses the knowledge of contrast **pulsatility**. Then a second processing on the **spatial domain** that uses the knowledge of **smoothness**, **incompressibility**, and **boundary conditions** of the **blood flow field**. The basic **input** of the whole image processing technique is a **3D+T pulsed contrast sequence** $I(\mathbf{x}, t)$, with the **contrast lumen segmentation**, and the basic **output** is the **3D+T velocity flow field** of the contrast product $\mathbf{v}(\mathbf{x}, t)$, equivalent to **3D+T blood flow field**.

From a blood flow field $\mathbf{v}$, a very large number of features can be extracted. Nowadays, only a few of them are clinically exploited:

- The **blood flow**: $Q = \int_S \mathbf{v} \cdot \mathbf{dS}$
- The **average velocity** along a centerline: $\hat{\mathbf{v}}(s) = \frac{1}{S}\int_S \mathbf{v}(\mathbf{s}) \cdot \mathbf{dS}$
- The **maximum velocity** along a centerline: $\mathbf{v_{max}}(s) = max_S(\mathbf{v}(\mathbf{s}))$
- The **velocity distribution** along a profile: $\mathbf{v}(r)$ (radial profile) is the most common
- The **wall shear stress**

The last feature is particularly meaningful for physicians, it gives an idea of how bad blood flow forces can harm the vessel wall. Computing the WSS necessitate a fine evaluation of **flow patterns** in the vicinity of the vessel wall, since it requires the evaluation of **spatial derivatives of the velocity**. Therefore, only **flow field imaging** has the ability to achieve a WSS estimation. The next and last section will propose a novel optical flow based approach for the WSS estimation.

3.5 On the estimation of wall shear stress

The influence of wall shear stress on the development of atherosclerosis and aneurysm was investigated in section 1.1.4. CFD simulations [Jung et al., 2006, Morales, 2012], and cine-MRI acquisitions [Marshall et al., 2004,Petersson et al., 2012,Isoda et al., 2010, Geers et al., 2011] have widely studied how WSS gets distributed in the arterial walls, with different hemodynamic conditions. However, no optical flow based evaluation of WSS has been reported until now.

First, let us recall the general definition of shear stress. A **shear stress**, denoted τ is defined as the component of stress **coplanar** with a material cross section. Any real fluid moving along a solid boundary, *i.e.* a vessel wall, will incur a wall shear stress on that boundary. The no-slip condition dictates that the speed of the fluid at the boundary should be 0, while at some distance from the boundary should be the flow velocity. Generally, the region between those two points is referred to as the **boundary layer**. At a distance r from the boundary, the shear stress is in direction of the flow, and equals to the product between the dynamic viscosity of the fluid μ and the **strain rate**:

$$\tau(\mathbf{r}) = \mu \frac{\partial \mathbf{v}}{\partial r}(r) \tag{3.65}$$

The wall shear stress, however, is defined at the contact of the wall, at $r = R$:

$$\boxed{\mathbf{WSS} = \mu \frac{\partial \mathbf{v}}{\partial r}(r = R)} \tag{3.66}$$

Obviously, the accuracy of wall shear stress estimation depends on the spatial resolution, according to which discretized evaluation of strain rate is more or less accurate.

Now, let us develop our WSS estimation method. The first assumption that is made is the **quadratic behavior** of the velocity with respect to the wall distance d. A quadratic distance map $\zeta(\mathbf{x})$ is built based on quadratic morphology with:

$$\forall\, \mathbf{x} \in \mathcal{B},\ \zeta(\mathbf{x}) = \|\mathbf{x}_m\|^2 - \|\mathbf{x} - \mathbf{x}_m\|^2 \tag{3.67}$$

with $\mathbf{x}_m$ the lumen center, and $\mathbf{x}_b$ the nearest point on the vessel wall, as shown in figure 3.16.

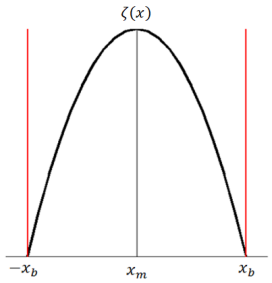

Figure 3.16: *Quadratic distance map ζ, defined as a negative quadratic function with respect to radial component. The maximum is at the lumen center, while the lowest value is reached on the boundary point $\mathbf{x}_b$.*

A window $\mathcal{W}$ is defined about $\mathbf{x}_b$, within which the velocity field can be expressed as:

$$\boxed{\mathbf{v}(\mathbf{x}) = \zeta(\mathbf{x})\mathbf{u}(\mathbf{x})} \tag{3.68}$$

where $\mathbf{u}$ is a vector normal to outward normal $\mathbf{n}$, which does not vary within the window. The outward normal can be defined by $\mathbf{n} = -\frac{\nabla\zeta}{\|\nabla\zeta\|}$.

For flow in the iso-ζ surfaces, we must have $\mathbf{v} = \mathbf{v} - \mathbf{v}(\mathbf{n}^T\mathbf{v}) = (I - \mathbf{n}\mathbf{n}^T)\mathbf{v}$, where $(I - \mathbf{n}\mathbf{n}^T)$ is the projection matrix in the plane normal to $\mathbf{n}$. With this in mind, the optical flow penalty within the boundary layer is written as:

$$E_{OF}(\mathbf{x}) = (\mathbf{v}^T \cdot \nabla\phi + \frac{\partial\phi}{\partial t})^2 = (\mathbf{v}^T(I - \mathbf{n}\mathbf{n}^T) \cdot \nabla\phi + \frac{\partial\phi}{\partial t})^2 = (\mathbf{v}^T \cdot \mathbf{g} + \frac{\partial\phi}{\partial t})^2 \tag{3.69}$$

with $\mathbf{g} = (I - \mathbf{n}\mathbf{n}^T)\nabla\phi$ the projected phase gradient.

The local penalty to minimize within a window $\mathcal{W}$ around wall point $\mathbf{x}_b$ therefore reads:

$$E_{\mathcal{W}}(\mathbf{x}_b) = \sum_{\mathbf{x}\in\mathcal{W}} W(\mathbf{x} - \mathbf{x}_b)(\frac{\beta}{2}(\zeta\mathbf{u}^T\mathbf{g} + \frac{\partial\phi}{\partial t})^2 + \frac{\alpha}{2}(\zeta\mathbf{u}^T\mathbf{n})^2) \tag{3.70}$$

where W is a gaussian weighting window.

Let us write $\gamma = \alpha\sum_{\mathcal{W}} W(\mathbf{x} - \mathbf{x}_b)\zeta^2$ and $C = \frac{\beta}{2}\sum_{\mathcal{W}} W(\mathbf{x} - \mathbf{x}_b)\frac{\partial\phi}{\partial t}^2$.

This energy can be reformulated $E_{\mathcal{W}} = \frac{1}{2}\mathbf{u}^T M\mathbf{u} - \mathbf{u}^T\mathbf{b} + C$, with $M = \gamma\mathbf{n}\mathbf{n}^T + \beta\sum_{\mathcal{W}} W(\mathbf{x} - \mathbf{x}_b)\zeta^2\mathbf{g}\mathbf{g}^T$ and $\mathbf{b} = -\beta\sum_{\mathcal{W}} W(\mathbf{x} - \mathbf{x}_b)\zeta\mathbf{g}\frac{\partial\phi}{\partial t}$.

By construction, it is clear that matrix M has an eigenvector $\mathbf{n}$ with eigenvalue γ and two eigenvectors in the tangential plane whose sum of eigenvalues is $Tr(\beta\sum_{\mathcal{W}} W(\mathbf{x} - \mathbf{x}_b)\zeta^2\mathbf{g}\mathbf{g}^T)$. We can now evaluate the wall shear vector $\mathbf{u}$ as a minimizer of $E_{\mathcal{W}}$ as

$\mathbf{u} = (M + \epsilon I)^{-1}\mathbf{b}$ in which we make use of *Tikhonov* regularization. The estimation of the local **strain rate** in the window finally reads:

$$\boxed{\mathbf{S} = \nabla\mathbf{v} \cdot \mathbf{n} = -(\mathbf{n}^T \nabla\zeta)\mathbf{u} = \|\nabla\zeta\|\mathbf{u}} \tag{3.71}$$

However, the estimate of the tangential strain rate is valid only if the laminar projection of the gradient is not erratic. One way to evaluate this is to note that $\sum_{\mathcal{W}} W(\mathbf{x} - \mathbf{x}_b)\zeta^2 \mathbf{g}\mathbf{g}^T$ is a second order moments matrix of the $\mathbf{g}$ vectors with weights given by $W(\mathbf{x} - \mathbf{x}_b)\zeta^2$. To get the corresponding covariance matrix, we first need to divide by the sum of weights yielding matrix Σ:

$$\Sigma = \frac{\sum_{\mathcal{W}} W(\mathbf{x} - \mathbf{x}_b)\zeta^2 \mathbf{g}\mathbf{g}^T}{\sum_{\mathcal{W}} W(\mathbf{x} - \mathbf{x}_b)\zeta^2} \tag{3.72}$$

With the same weights, we can also compute a weighted average $\mathbf{G}$ for the gradient $\mathbf{g}$:

$$\mathbf{G} = \frac{\sum_{\mathcal{W}} W(\mathbf{x} - \mathbf{x}_b)\zeta^2 \mathbf{g}}{\sum_{\mathcal{W}} W(\mathbf{x} - \mathbf{x}_b)\zeta^2} \tag{3.73}$$

The centered covariance matrix about the mean reads: $\Sigma_c = \Sigma - \mathbf{G}\mathbf{G}^T$. A reasonable estimation of the data is obtained by comparing $\sigma_c^2 = Tr(\Sigma_c)$ with $\|\mathbf{G}\|^2 = Tr(\mathbf{G}\mathbf{G}^T)$. Thus, if σ_c is comparable or larger than $\|\mathbf{G}\|^2$, the above strain estimation cannot be relied upon nor be used for the definition of wall shear stress. In the favorable case:

$$\boxed{\mathbf{WSS}(\mathbf{x}_b) = \mu\mathbf{S}(\mathbf{x}_b)} \tag{3.74}$$

3.6 Additional fidelity terms: jet fidelity and wall fidelity

In our first trials for solving the flow field PDE (partial differential equations), we noted two different phenomenons:

- The estimated normal velocity gradient $|\mathbf{n} \cdot \nabla\mathbf{v}|$ near the lumen wall is generally considerably smaller than the ground truth.
- The velocity $\mathbf{v}_{jet}$ at the peak of the contrast profile in the lumen center is always in the direction of the phase gradient $\nabla\phi$.

Consequently, the two following ideas were implemented.

3.6.1 The wall fidelity

The boundary penalty $(\mathbf{v}^T \cdot \mathbf{n})^2$ is effective in reducing the near wall velocity but the velocity parallel to the wall changes much more slowly along the normal $\mathbf{n}$ than ground truth predicts. To resolve this issue, we introduce a method specially aimed to improve estimation in a thin layer $\mathcal{B}$ near wall boundary.

We now focus on the optical flow penalty term $\frac{1}{2}(\mathbf{v}\nabla\phi + \frac{\partial\phi}{\partial t})^2$. For points very near the wall boundaries, we know that $\mathbf{v}$ should be nearly orthogonal to the wall normal unit vector $\mathbf{n}$ so that the optical flow penalty can be rewritten as $\frac{1}{2}(\mathbf{v}_\parallel\nabla\phi + \frac{\partial\phi}{\partial t})^2$ where $\mathbf{v}_\parallel$ is the projection of $\mathbf{v}$ parallel to the wall $\mathbf{v}_\parallel = \mathbf{v} - (\mathbf{v}^T \cdot \mathbf{n})\mathbf{n}$. Making use of associativity of matrix algebra, we have:

$$\mathbf{v}_\parallel = \mathbf{v} - (\mathbf{v}^T \cdot \mathbf{n})\mathbf{n} = \mathbf{v} - \mathbf{n}(\mathbf{n}^T \cdot \mathbf{v}) = (I - \mathbf{n}\mathbf{n}^T)\mathbf{v} \tag{3.75}$$

resulting in $\mathbf{v}_\parallel^T\nabla\phi = \mathbf{v}^T(I-\mathbf{n}\mathbf{n}^T)\nabla\phi$ and $\frac{1}{2}(\mathbf{v}_\parallel\nabla\phi+\frac{\partial\phi}{\partial t})^2 = \frac{1}{2}\|(I-\mathbf{n}\mathbf{n}^T)\nabla\phi\|^2(\mathbf{v}^T\mathbf{q}-v_q)^2$ where $v_q = -\frac{\frac{\partial\phi}{\partial t}}{\|(I-\mathbf{n}\mathbf{n}^T)\nabla\phi\|}$ and $\mathbf{q} = \frac{(I-\mathbf{n}\mathbf{n}^T)\nabla\phi}{\|(I-\mathbf{n}\mathbf{n}^T)\nabla\phi\|}$.

We now add the penalty term $\frac{1}{2}\|(I-\mathbf{n}\mathbf{n}^T)\nabla\phi\|^2(\mathbf{v}^T\cdot\mathbf{n})^2$ resulting in $\|(I-\mathbf{n}\mathbf{n}^T)\nabla\phi\|^2 Q$ where $Q = \frac{1}{2}(\mathbf{v}^T\mathbf{q} - v_q)^2 + \frac{1}{2}(\mathbf{v}^T\mathbf{n})^2$. After some matrix algebra manipulations:

$$Q = \frac{1}{2}\mathbf{v}^T(\mathbf{q}\mathbf{q}^T + \mathbf{n}\mathbf{n}^T)\mathbf{v} - v_q\mathbf{v}^T\mathbf{q} + \frac{1}{2}v_q^2 = \frac{1}{2}\mathbf{v}M_{wall}\mathbf{v} - \mathbf{v}^T\mathbf{b}_{wall} + \frac{1}{2}v_q^2 \tag{3.76}$$

where $M_{wall} = \mathbf{q}\mathbf{q}^T + \mathbf{n}\mathbf{n}^T$ and $\mathbf{b}_{wall} = v_q\mathbf{q}$.

Matrix M_{wall} has now clearly two well defined eigenvectors, namely $\mathbf{q}$ and $\mathbf{n}$ with unit eigenvalues. In 3D, the third eigenvector is just normal to the two others with zero eigenvalue whereas $\mathbf{b}_{wall}$ has only one component v_{of} in the direction of $\mathbf{q}$. Taking the fidelity terms alone and adding a small *Tikhonov* term ϵI to M_{wall}, *i.e.* $M_{wall} = \mathbf{q}\mathbf{q}^T + \mathbf{n}\mathbf{n}^T + \epsilon I$, this procedure clearly leads to a full rank (non-singular) fidelity matrix M_{wall}. We now have to solve the system:

$$M_{wall}\mathbf{v}_{wall} = \mathbf{b}_{wall} \Longrightarrow \mathbf{v}_{wall} = M_{wall}^{-1}\mathbf{b}_{wall} \tag{3.77}$$

This estimation can serve as a **soft boundary condition** for the regularized flow velocity further away from the wall. To do so, we add an extra penalty $\int_{mathcalB}\frac{1}{2}WallFid\|\mathbf{v}-\mathbf{v}_{wall}\|^2$. This amounts to replacing the fidelity matrix M and vector $\mathbf{b}$ in layer $\mathcal{B}$ by $M^\star$ and $\mathbf{b}^\star$ with:

$$M^\star = M + WallFid.I \qquad\qquad \mathbf{b}^\star = \mathbf{b} + WallFid.\mathbf{v}_{wall} \tag{3.78}$$

where I stands for the identity matrix. The weight **WallFid** and the thickness of the layer $\mathcal{B}$, called **LayerDepth** are considered as adjustable parameters which we shall empirically determine in the next chapter.

3.6.2 The jet fidelity

In the previous section, we made use of prior knowledge on the direction of flow velocity in a near wall layer $\mathcal{B}$ to alleviate the optical flow window issue and to allow a local estimation of the flow velocity. There is another situation where knowledge of the local flow velocity direction can be assessed. Consider a tracer particle $\mathbf{p}_t$ having velocity $\mathbf{v}_t$ for which neighboring particles in the plane Π_t containing $\mathbf{p}_t$ and normal to the direction of $\mathbf{v}_t$ have smaller velocities than $\mathbf{v}_t$. We refer the streamlines defined by such particles as **jets**. These may occur within tubular flow but also within vortices. An instance of such a situation is provided by the *Poiseuille* flow example presented in section 3.2.4. It can be seen that, in this case, all points on the cylinder center line have this property. As can be observed in the figures, the curvature of the iso-intensity contrast density surface is maximal in the transverse plane Π_t. In 3D, we may use the iso-intensity mean curvature defined as in [Rieger et al., 2004] by:

$$\kappa_m = \nabla \cdot \frac{\nabla\phi}{\|\nabla\phi\|} \tag{3.79}$$

In the given example where κ_m can be evaluated analytically, it is easily seen that for any point along the z-axis, $|\kappa_m|$ has a maximum at the centerline (*i.e.* at $x = 0, y = 0$). Furthermore, the evaluated $|\kappa_m|$ at centerline increases linearly with the distance z from coordinate while a transverse (x, y) plane is taken perpendicular to the jet line with origin on the centerline. The transport time $\tau(x, y, z, t)$ from injection point will be minimal at $x = 0, y = 0$ with an associated isophote curvature κ_m expected to increase roughly proportionally with $\tau(x, y, z, t)$ when distance from injection point increases. In the example given this can be seen in figure 3.17.

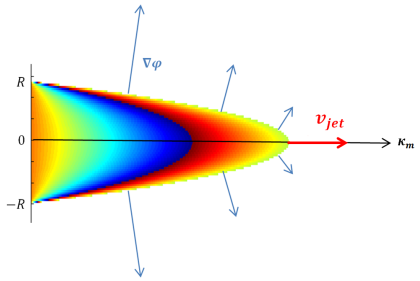

Figure 3.17: *Jet velocity in a Poiseuille flow. The black line is the set of point* $\mathbf{p}_t$ *with the highest local curvature* κ_m *of the phase gradient* $\nabla\phi$*. At these locations, the jet velocity* $\mathbf{v}_{jet}$ *is parallel to the phase gradient* $\nabla\phi(\mathbf{p}_t)$*.*

Points of the jet lines are detected by computing the κ_m map and localizing the points p_t for which $|\kappa_m|$ is maximum in the transverse plane through p_t and normal to $\nabla\phi$. Since the flow velocity is expected to be in the direction of $\nabla\phi$, we just take the local flow velocity as:

$$\mathbf{v}_{jet} = -\frac{\frac{\partial\phi}{\partial t}}{\|\nabla\phi\|^2}\nabla\phi \tag{3.80}$$

For each such detected jet points, we modify again the fidelity matrix M and vector $\mathbf{b}$ by $M^\star$ and $\mathbf{b}^\star$ with:

$$M^\star = M + JetFid.I \qquad \mathbf{b}^\star = \mathbf{b} + JetFid.\mathbf{v}_{jet} \tag{3.81}$$

The weight **JetFid** is an adjustable parameter which we shall empirically determine in the next chapter.

Overall, the two new boundary conditions can be brought up to the table 3.3 as follows:

Region based constraint implementation	
Region of the flow object	Mathematical expression
$ROI \cap (\mathcal{L} \cup \mathcal{B})$	$\mathbf{v} = 0$
Jet points $\mathbf{p}_t$	$(M_{weighted} + I)\mathbf{v} - \mathbf{b}_{\mathbf{weighted}} - JetFid\mathbf{v}_{jet} - \mu\Delta\mathbf{v} - \lambda\nabla(\nabla \cdot \mathbf{v}) = 0$
Lumen $\mathcal{L}$	$M_{weighted}\mathbf{v} - \mathbf{b}_{\mathbf{weighted}} - \mu\Delta\mathbf{v} - \lambda\nabla(\nabla \cdot \mathbf{v}) = 0$
Vessel boundary $\mathcal{B}$	$(M_{weighted} + I)\mathbf{v} - \mathbf{b}_{\mathbf{weighted}} - WallFid\mathbf{v}_{wall} - \mu\Delta\mathbf{v} - \lambda\nabla(\nabla \cdot \mathbf{v}) = 0$
Vessel cuts $\mathcal{C}$	$\nabla\mathbf{v} \cdot \mathbf{c} = 0 \Rightarrow \mathbf{v} = \sum_{\mathbf{p}\in\mathcal{W}\cap(\mathcal{L}\cup\mathcal{B})} W(\mathbf{p})\mathbf{v}(\mathbf{p})$

Table 3.3: *Region based implementation of the conjugate gradient with wall and jet fidelity terms*

*
* *

This methodological chapter presented a collection of signal and image processing tools meant for the assessment of blood flow in pulsed contrast sequences. It should be considered as a whole framework, each brick aiming to solve a particular issue or to model a particular property of the contrast sequence. It does not pretend to cover all the range of possible flow estimation techniques, neither to overcome all the potential issues pending to **optical flow based blood flow estimation**. As the state of the art is very narrow -almost inexistent-, the workstream is fully opened, and will certainly grow in the forthcoming years. The current difficulty is the absence of 3D+T contrast imaging systems providing clinical flow data. Nevertheless, *X-Ray* DSA and its related 2D flow estimation techniques paved the way for the achievement of future 3D flow estimation methods. It teaches that contrast **pulsatility** is the first property to exploit. It allows to compress the signal in the **Fourier domain**, and

to derive a **semi-analytic** expression of the time signal. Ultimately, it abolishes the time discretization and leverages the approximate nature of optical flow. The phase of the analytic signal can then be employed to emancipate from the low frequency envelop of the bandwidth signal. Secondly, the spatial behavior of the velocity has to be addressed. If no regularization is carried out, basic numerical simulations predict that the flow field will tend to orientate radially in a boundary layer. Physical cues as **smoothness**, **incompressibility**, and **wall tangency** can be exploited to correct for the spurious flow behavior. Furthermore, local feature of the flow field such as the wall and jet velocity can serve as boundary conditions to the partial differential equation. This scientific endeavour would not have any relevance without a proper evaluation of the methodology. The following chapter proposes to challenge the optical flow method developed in this chapter with virtual angiography. As a reminder of this thesis, the last chapter will present the first optical flow results on MPI flow data.

Chapter 4

In-silico evaluation of the optical flow method

Contents

Abstract

Nowadays, a lot of tools exist in modeling and reproducing physical phenomenons. **Computational Fluid Dynamics**, among them, is specialized in fluid mechanics and widely used in medical physics and biomechanics. This branch of fluid mechanics is especially useful in modeling and studying blood flow in the circulatory system. In medical flow imaging, the role of CFD is mainly to provide realistic digital imaging data when ground truth is missing, which is almost always the case in DSA, MRI and MPI. In this chapter, CFD is used for the generation of virtual angiography test and validation data. With the use of appropriate tools, this may be done with a very good accuracy and reliability. Several CFD models of angiography sequences and their corresponding flow field ground truth will be confronted to the optical flow algorithm developed in the previous chapter. The influence of optical flow parameters will be pointed out, together with the flow rate and geometry parameters. Finally, the potential of the optical flow algorithm will be discussed.

Résumé

De nos jours, de nombreux outils existent dans la modélisation et la reproduction de phénomènes physiques. La **Mécanique des Fluides Numérique**, parmi ceux-ci, est spécialisée en mécanique des fluides et largement utilisée en physique médicale et en biomécanique. Cette branche de la mécanique des fluides est particulièrement utile dans la modélisation et l'étude du flux sanguin dans le système circulatoire. En imagerie de flux, le rôle de la MFN est principalement de fournir des images réalistes d'angiographie lorsque les vérités terrains sont inaccessibles, ce qui est presque toujours le cas en ASD (angiographie par soustraction digitale), IRM et MPI. Dans ce chapitre, la MFN sera présentée, et comment elle permet de générer des images virtuelles d'angiographie avec une très bonne précision et fiabilité. Par la suite, différents modèles MFN de séquences angiographiques ainsi que la vérité terrain de leurs champs de vitesses correspondant seront confrontés à l'algorithme de flot optique développé dans le chapitre précédent. L'influence des paramètres de flot optique sera mise en avant, ainsi que celle du débit sanguin et de la géométrie des artères. Enfin, une discussion sur le potentiel de l'algorithme de flot optique concluera le chapitre.

4.1 Presentation of CFD

CFD is a branch of fluid mechanics that reproduces physical experiments and compute meaningful features such as fluid pressure, velocity, shear stress, strain, or even a scalar quantity transported by the fluid, such as a CA. *Navier-Stokes* equations are solved in the studied system by using numerical analysis and algorithms, which are applied in a discretized version of the regions of interest. CFD models need boundary conditions to solve the partial differential equations governing the studied system. Additionally, CFD software is generally complemented with computed graphics tools that help tremendously the representation and evaluation of 3D scalar and vector fields.

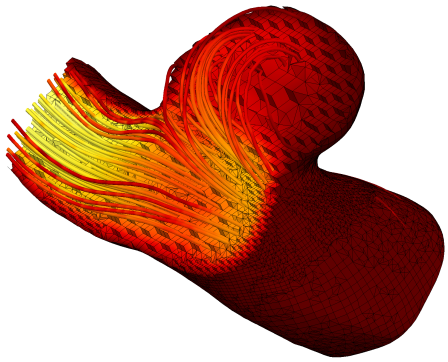

Figure 4.1: *Examples of CFD simulation for arterial flow. Fluid flows from right to left. Part of the arterial flow penetrates the aneurysm cavity, forming a recirculating vortex, as shown with colored streamlines.*

CFD provides a third approach to understand the physics of flow dynamics after pure theory and experiments. In medical imaging, the multiple assets of using CFD are the following: the **predictive performance** of therapeutic devices (*i.e.* endovascular coiling [Morales, 2012]), the **non-invasiveness**, the **full control** on the simulation parameter, the countless possibilities of **data visualization** at infinite time and space resolution, and the very **low cost** of CFD compared to in vitro and in vivo experiments.

4.2 Virtual angiography

Virtual angiography can be used as an alternate solution to clinical data, as it satisfies the same requirements, *i.e.* time resolved contrast information, and provides in addition the true velocity field. **Virtual angiography** can be achieved trough CFD simulation, using specific **boundary conditions** adapted to blood flow and arteries, with a reliable physical framework and a high accuracy. **The goal is to estimate**

velocity vectors in the contrast map sequence, based on the OFM described in chapter 3, and compare the output with the ground truth flow field.

Ideally, the boundary conditions should be extracted, or inspired from true clinical data. In 2005, an image-based model pipeline using medical data for simulating hemodynamics was defined [Cebral et al., 2005], and later extended with morphological, morphodynamics and structural analysis, providing patient specific models with diagnosis and prognosis descriptors [Villa-Uriol et al., 2010].
The preparatory work before generating the CFD model consists in the **segmentation** of the vasculature of interest. A 3DRA image is generally used in order to extract the arterial tree, and remove the background. Hence, a precise delineation of the lumen and the vessel wall can be performed, with any state of the art segmentation tools. The second phase is the **volumetric mesh generation**, where the regular and cartesian mesh extracted from the image segmentation is made into an **unstructured** mesh, often conformed by tetrahedral elements. Finally, the CFD solves the *Navier-Stokes* equations on the volumetric mesh, often assuming blood to be an incompressible fluid in a transient laminar flow regime and adiabatic. The equation (1.6) and (1.5) describing blood flow are then enforced throughout the CFD model. Boundary conditions concerning physical quantities can be derived from studies that measure the physiological blood flow [Cebral et al., 2008], one-dimensional models [Reymond et al., 2009], or even from OFMs [Bonnefous et al., 2012].

The pipeline for CFD model generation and simulation is presented in figure 4.2.

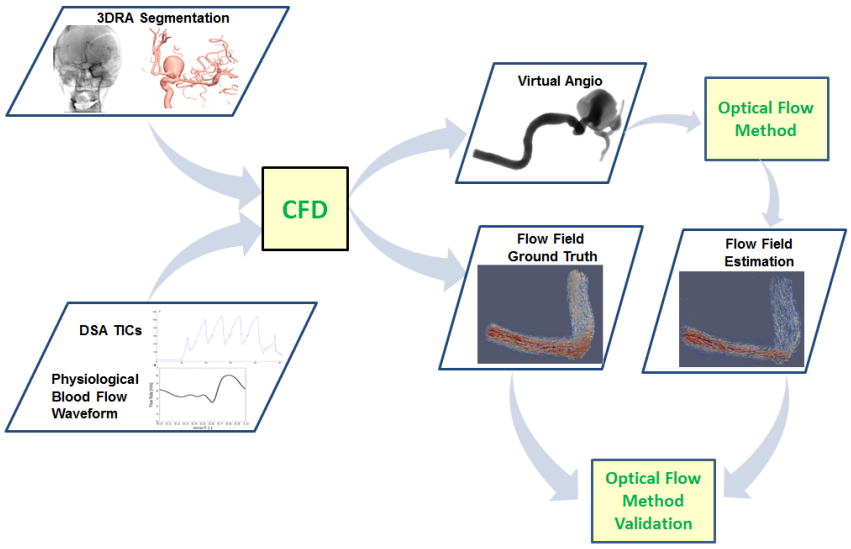

Figure 4.2: *Pipeline of the OFM validation with CFD simulations*

Eventually, the **contrast map sequence** can be extracted from the virtual angio, as well as the corresponding **velocity field**.

Materials

For the evaluation of the optical flow algorithm, five different models of virtual angiography were used. The vessel lumen were extracted from 3DRA data by means of a state of the art segmentation tool used internally in Medisys Research Lab. Each model contained an aneurysm with different degrees of severity, as illustrated in figure 4.3:

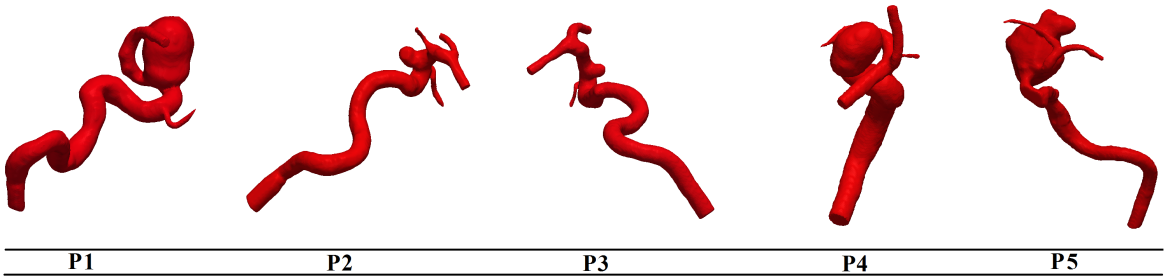

Figure 4.3: *Illustration of five CFD models used for the in-silico evaluation of the optical flow algorithm. Several morphological features can be observed from these models, including straight vessel portion, multiple bends, degrees of tortuosity and aneurysms as well.*

The continuity and Navier–Stokes equations of an incompressible Newtonian fluid were numerically solved with OpenFOAM (2013, v2.2.1). Blood density and viscosity were 1060 kg/m3 and 0.0035 Pa s, respectively, knowing that viscosity changes are negligible inside cerebral aneurysms [Morales et al., 2013]. A physiological bloodflow waveform was extracted from a DSA sequence using OFM [Bonnefous et al., 2012], and post-processed in order to fit our current CFD models. A period was extracted from the bloodflow waveform, scaled in the time domain to match the working time resolution, and **periodized** over several cardiac cycles (see example figure 4.4). A thorough explanation of how these waveforms were derived can be found in [Morales and Bonnefous, 2015] and [Morales and Bonnefous, 2014]. The scaling preserves the shape of the generic waveform but varies Q among the generated waveforms. Finally, a **parabolic profile was imposed at the model inlet**. This velocity profile changes over time, following a generic pulsatile waveform.

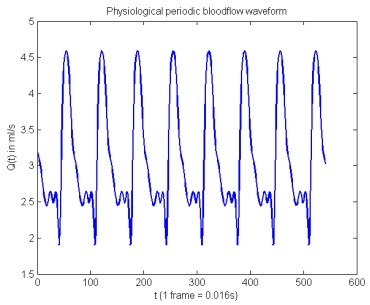

Figure 4.4: *Example of blood flow waveform with a periodic pattern (average flow rate:* $3ml.s^{-1}$*).*

In order to model the contrast propagation, TICs were extracted from DSA sequences - corresponding to the 3DRA routine- **at the model inlet**. A scalar field of the contrast concentration was solved from a transport equation. The TIC at the inlet region of the DSA images was imposed as boundary condition for the contrast concentration at the inlet of the CFD model with a homogeneous distribution [Morales et al., 2011]. The CFD simulations were performed with OpenFOAM©(version 2.2.1) and the visualizations presented throughout this chapter are made with ParaView©(version 4.1.0 , 64 bit).

4.3 Optical flow evaluation with CFD

Finally, the optical flow algorithm was implemented in C++ by means of a Microsoft Visual Studio 2010©environment. The optical flow software was run on a hp ©machine, with an operating system Windows 7©64 bits (processor Intel(R) Core(TM) i7-2820 QM, CPU 2.30 GHz, 8 Go RAM, graphic card Nvidia Quadro 1000M 96 @ 700 MHz 128 Bit @ 900 MHz).

For the evaluation of the OFM, three main experiments were conducted.

- **Parameter sensitivity analysis**: Analysis on the optical flow parameters for one model (section 4.3.1).
- **Flow rate analysis**: Analysis on the arterial flow rate on the same model with the optimal parameters from the previous study (section 4.3.2).
- **Geometry sensitivity analysis**: Analysis of the arterial morphology with five models (section 4.3.3).

4.3.1 Parameter sensitivity analysis

To understand the impact of the most relevant parameters of the developed OFM (chapter 3), a sensitivity analysis was performed. A non-exhaustive list of parameters that intervene upstream or downstream the algorithm is presented in table 4.1. In order to cover as much as possible the parameter space (formed by all possible combinations), an educated approach was followed by identifying the most critical and relevant parameters and their values/range. The varied parameters were μ, *WallFid* and *JetFid* while the rest were fixed with the values shown in 4.1.

The compressibility penalty was set to $\lambda = \frac{\mu}{2}$, as suggested in the corresponding subsection 3.3.3. The reason for selecting these three parameters is only experimental: the other parameter were found poorly significant in the optical flow result. Only the bandpass filter proved to have an important role in optical flow accuracy, a point which would require a deeper analysis in the future. The working bandpass ($[0.25Hz\ 5Hz]$) simply provided correct results compared to other possible filters.

Optical flow parameters and their corresponding values		
Parameter	Description	Value
$\tilde{\mathbf{I}}_{\mathbf{BP}}$	Bandpass filter for frequency filtering, comprising number of frequency components and weights of each component (section 3.2.1)	$\mathbf{1}_{\mathbf{F}_{[0.255]}}$: indicator filter between 0.25 Hz and 5 Hz (cardiac frequency $\simeq 1Hz$)
γ	Thresh parameter for phase gradient fidelity (section 3.3.4)	0.00001
μ and λ	Regularity *Lamé* factors (section 3.3.3)	not fixed
WallFid ***JetFid*** ***LayerDepth***	Weighting factors for wall fidelity, jet fidelity, and pseudo boundary layer depth (sections 3.6)	not fixed (excepted ***LayerDepth*** = 3mm)
ϵ	Tolerance threshold for the CG residue (section 3.3.5)	10^{-8}: CG stops if the current residue is inferior than 10^{-8} the initial residue
$\mathbf{L}$, $\mathbf{n_a}$, $\mathbf{n_d}$	Parameters of the Multigrid structure: number of pyramid levels, number of iterations in ascent and descent of the V-cycles (section 3.3.5)	$L = 4$, $n(l) = n_a(l) = n_d(l)$ at each level l with $n(1) = 20$, $n(2) = 30$, $n(3) = 50$ and $n(4) = 150$ (4 for the coarsest level)

Table 4.1: *List of optical flow parameters.*

Finally, case **P3** is selected for the sensitivity analysis (see figure 4.5). 480 frames of contrast and bloodflow information are available from the CFD. A particular cardiac period is selected, when the model is fully injected with CA. 15 frames are used for the optical flow evaluation, from frame 350 to 420 with a time interval of 5 frames (one cardiac period corresponds to 67 frames approximately).

Flow rate evaluation

The flow rate was measured in several different cross sections of the CFD model for both optical flow estimation and ground truth velocity field. A set of cross sections was extracted from the vessel model starting from the inlet with a regular spacing of 2 mm. The flow rate is given by a cross section $\mathcal{S}$:

$$Q_{\mathcal{S}} = \iint_{\mathcal{S}} \mathbf{v} \cdot \mathbf{n} dS \tag{4.1}$$

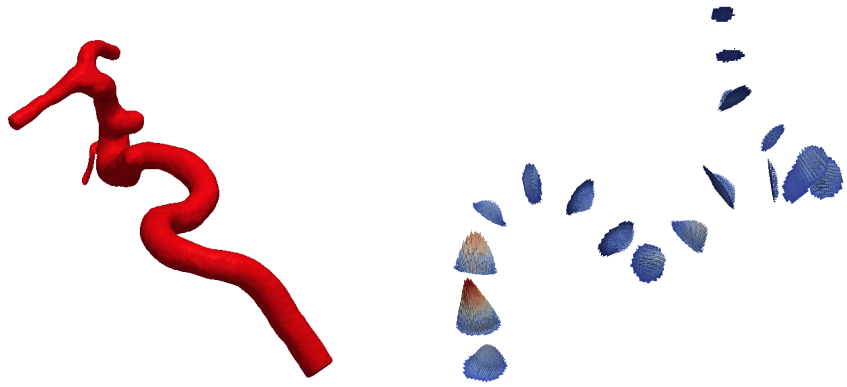

Figure 4.5: Model P3 with flow field evaluation on different cross sections

with $\mathbf{n}$ the outward unit normal to the cross section $\mathcal{S}$. Note that the flow rate ground truth did not have to be computed at each cross section, since this value has to be constant along a vessel segment (see section 1.3.1). The figure 4.5 illustrates an example of optical flow estimation and associated 3D flow field on several cross sections.

For the sensitivity analysis, the flow rate was averaged over one cardiac period, and over several cross sections. 15 frames were selected from 350 to 420, in order to limit the memory storage. First, only the first cross section was considered ($n_s = 1$), then the first three ($n_s = 3$) and first five ($n_s = 5$) cross sections and their corresponding flow rate were averaged. Finally, the whole model was evaluated (excluding aneurysms and bifurcations), which yielded a spatio-temporal average flow rate ($n_s = N_s$). The parameters μ, *JetFid* and *WallFid* were independently changed while other sensitivity parameters were kept constant. Hence, three different parameter analyses were carried out about a fixed 3D point in the parameter space (*JetFid*=5, *WallFid*=5, $\mu_{PREFAC} = 100$). The illustration hereafter shows the three axis of parameter space.

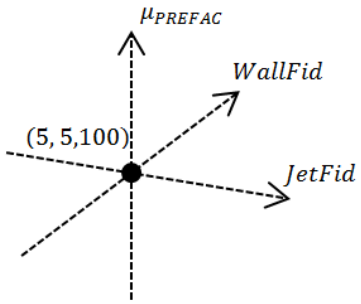

Figure 4.6: *Parameter space and its three axis. For the sensitivity analysis, each parameter is changed along its corresponding axis, about a centered position (5,5,100). The parameters are evaluated for different values, respectively JetFid* = [0 0.1 1 3 5 7 9 20 100], *WallFid* = [0 0.1 1 3 5 7 9 20 100], *and* μ_{PREFAC} = [40 70 100 130 160].

One should note that μ_{PREFAC} is not the actual regularization weight used in the optical flow algorithm but only a **pre-multiplying factor**. μ should be chosen according to the average gradient fidelity m (see section 3.3.3). Hence, μ_{PREFAC} determines the factor between the smoothness penalty and the average fidelity m. Moreover, μ is scaled to the system resolution, since the term $\mu\Delta\mathbf{v}$ in (3.38) numerically depends on $\frac{1}{res^2}$, with res the system resolution. Overall, the relation between regularity prefactor, gradient fidelity and resolution reads:

$$\boxed{\mu = m\, res^2\, \mu_{PREFAC}} \tag{4.2}$$

In our setting, **a resolution of res = 0.2923 mm was used**, as inspired from Philips DSA systems. This way, the term $res^2\mu_{PREFAC}$ ranges between 1 and 10, so m and μ have the same order of magnitude.

Two different ways to evaluate the flow rate estimation are employed: the normalized error of the time averaged flow rate estimation compared to CFD ground truth e_{flow}, and the ratio between time averaged flow rate estimation and CFD, ρ_{flow}. The first one gives a very precise idea of the accuracy of the optical flow estimation, while the second one allows to know whether the flow rate is overestimated or underestimated (see figure 4.7).

We denote the time average flow rate percentage error as:

$$\boxed{e_{flow} = \frac{1}{N_{frame} * n_s} \sum_{\mathcal{S}=1}^{n_s} \sum_{frame=350}^{420} \frac{|Q_{\mathcal{S}}(frame) - Q_{GT}(frame)|}{Q_{GT}(frame)}} \tag{4.3}$$

The time average flow normalized with ground truth flow rate is:

$$\boxed{\rho_{flow} = \frac{1}{N_{frame} * n_s} \sum_{\mathcal{S}=1}^{n_s} \sum_{frame=350}^{420} \frac{Q_{\mathcal{S}}(frame)}{Q_{GT}(frame)}} \tag{4.4}$$

Influence of WallFid and JetFid

Figure 4.7 shows the local one-dimensional minima of e_{flow} for each parameter *JetFid*, *WallFid* and μ_{PREFAC}. When the parameter *WallFid* is small (0, 0.1, and 1) compared to the parameter *JetFid* (graph A, blue curves),e_{flow} is high (from 300% error at *WallFid*=0 to 50% error at *WallFid*=3). At *WallFid*=5 and *JetFid*=5, e_{flow} goes through a minimum at 3% error in the inlet, 15% for three sections, 35% for five cross sections, and 65% when considering the whole model. At this minimum we can see **the decreasing of flow estimation accuracy as we get further from the**

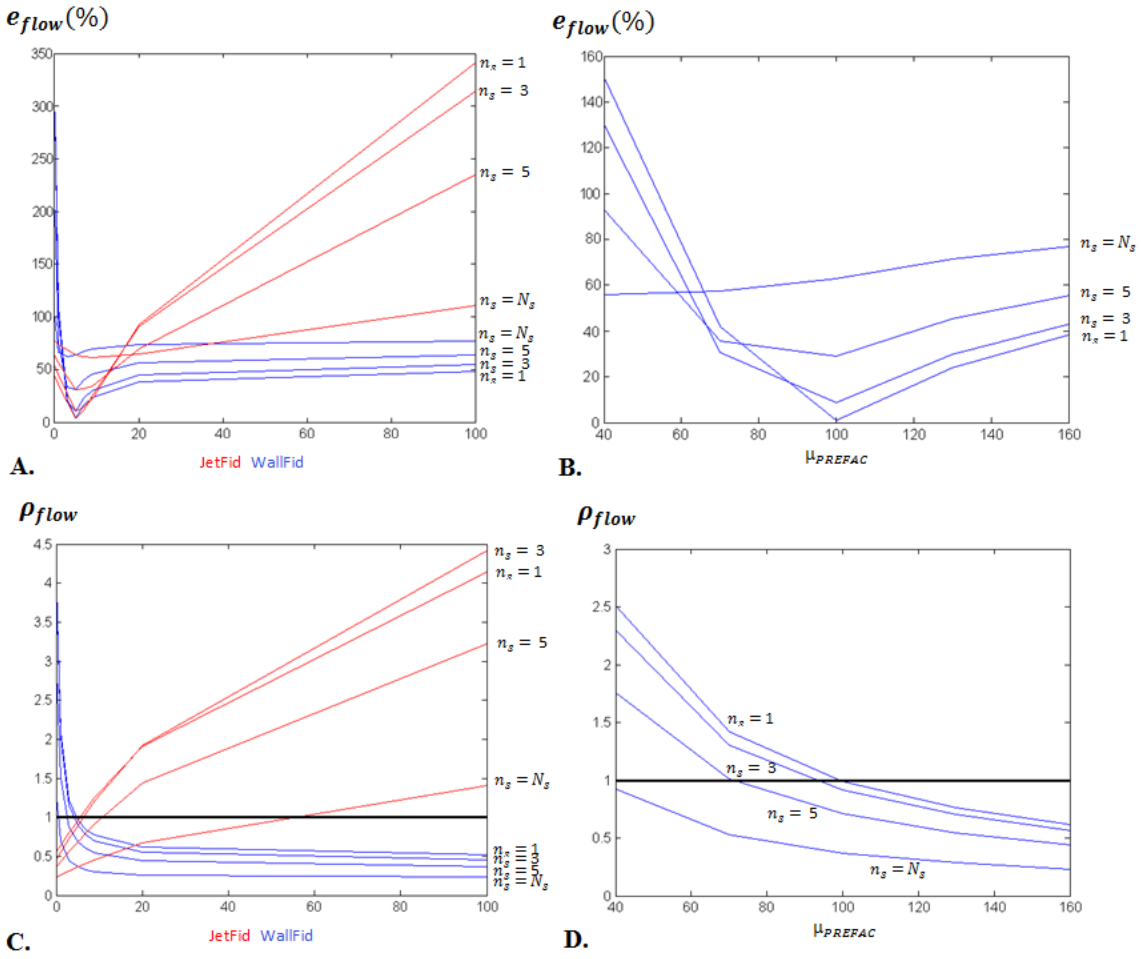

Figure 4.7: *Parameter sensitivity analysis. For each error curve, the other parameters are fixed with the following values: JetFid=5, WallFid=5, and* $\mu_{PREFAC} = 100$. ***A*** e_{flow} *(in %), when the JetFid and WallFid parameters vary. A local minimum is observed for both curves at JetFid = 5, WallFid = 5.* ***B*** e_{flow} *when* μ_{PREFAC} *varies. A local minimum is found when* $\mu_{PREFAC} = 100$. ***C*** ρ_{flow} *when JetFid and WallFid vary,* ***D*** *The same ratio for different values of* μ_{PREFAC}. *For each parameter sensitivity analysis, four different error curves are displayed: one when only considering the first cross-section (the inlet,* $n_s = 1$*), one with the three first cross-section averaged (*$n_s = 3$*), one with the five first cross-sections (*$n_s = 5$*) and one considering the whole model (*$n_s = N_s$*).*

inlet. This point will be further discussed in this chapter. Finally, when *WallFid* increases (7, 9, 20 and 100) with respect to *JetFid*, e_{flow} slowly increases. This can be explained by the **over-regularization** of the flow field when *WallFid* dominates *JetFid* and the parabolic fitting is misestimated. Section 3.6 demonstrated how the shape of the fitted parabola depends on the spatial resolution, and particularly near the wall. When the spatial resolution is not fine enough to estimate properly a parabolic profile, which is often the case, the latter is underestimated. Graph C (blue curves) show this underestimation as we increase the wall parameter. Because of this inaccuracy, and the fact that **the true profile is not always parabolic**, the *WallFid* parameter shouldn't be pushed more than necessary. **The wall fidelity is of great help for boosting the flow field near the wall, but should be balanced with the jet fidelity**.

The red curves of graph A slightly exhibit the same behavior. When the parameter *WallFid* is fixed at 5, the parameter *JetFid* widely influence e_{flow}. For values smaller than 5, the flow rate is underestimated (figure 4.7, Graph C, red curves) which can be explained by the aforementioned effect of the dominant wall fidelity. When changing *JetFid*, e_{flow} reaches a minimum at *JetFid*=5 (for $n_s = 1, n_s = 3, n_s = 5$), the error increases to high values (350% at the inlet and 100% for the whole model). This effect could be related to the very weak value of the phase gradient in the profile peak. Because the CA propagation is very fast in this area, the phase gradient gets close to zero. During the inversion of the phase gradient tensor, any numerical inaccuracy can have an impact on the jet estimation.

As can be seen in graph C (figure 4.7), the wall parameter tends to underestimate the flow rate while the jet parameter tends to overestimate the flow rate. As a result, **a proper balance between the two contributions should be respected in order to reduce e_{flow} as much as possible**. **In the next tests, the values of both *WallFid* and *JetFid* will be fixed to 5, as they provide to our knowledge the lowest flow estimation error.**

Influence of the smoothness factor

Graphs B and D (figure 4.7) show the influence of the smoothness factor μ_{PREFAC}. A local minimum of e_{flow} can be observed at $\mu_{PREFAC} = 100$ (graph B), for *JetFid* and *WallFid* fixed at 5. For lower values (40 and 70), the flow field is overestimated, while higher values (130 and 170) lead to an underestimation. One should note that ρ_{flow} is based on a temporal average of 15 frames. Therefore a ratio crossing 1 is not necessarily an indicator of good flow estimation. **One should only resort to e_{flow} for evaluating the flow accuracy, while ρ_{flow} yields an overall information on the overestimation or the underestimation of the flow rate.**

The analysis on the cross-section number n_s shows that the flow estimation at the inlet tends to be over-estimated for small values of μ_{PREFAC}, while it reaches a very

small error (3%) at $\mu_{PREFAC} = 100$, before increasing again as μ_{PREFAC} increases. The two curves for $n_s = 3$ and $n_s = 5$ exhibit the same behavior though the local minimum at $\mu_{PREFAC} = 100$ is higher (10% for $n_s = 3$ and 30% for $n_s = 5$). This can be explained in the same way as the previous parameter analysis, as **the flow estimation accuracy decreases when we get further from the model inlet.** When $n_s = N_s$ (18 for this model), e_{flow} behaves differently as no local minimum shows up. However, graph D seems to show a coherent behavior with the other curves, as we notice a gradual underestimation of the flow rate when increasing n_s.

Finally the influence of μ_{PREFAC} is predictable as this term corresponds to the smoothness factor met in *Horn and Schunck* [Horn and Schunck, 1981]. **Pushing too much this factor leads to over-smoothing of the flow field and underestimation of the flow rate, while not pushing it enough encourages the outliers of the phase gradient to ruin the flow estimate, and to cause overestimation. In the next tests, the value of μ_{PREFAC} will be fixed to 100, as it provides to our knowledge the lowest flow estimation error.**

This sensitivity analysis helped us to understand the influence of the key parameters. This analysis was based on an educated guess of combination and for this case, the optimal combination was:

$$JetFid = 5,\ \ WallFid = 5,\ \ \mu_{PREFAC} = 100 \tag{4.5}$$

Among the different combination tested previously, these parameters provide the lowest flow error e_{flow}, as illustrated in table 4.2.

Flow error with chosen parameters (4.5)	
Number of cross-sections	e_{flow}
$n_s = 1$ (inlet)	3%
$n_s = 3$	10%
$n_s = 5$	30%
$n_s = N_s$ (whole model)	60%

Table 4.2: Flow estimation error for optimal parameters after sensitivity analysis

The next sections are to analyze how this set of parameters can provide different results when changing the flow rates or the morphology.

4.3.2 Flow rate errors versus time and slice number

This section presents a sensitivity analysis on the flow rate that was done for case P3. The same bloodflow waveform used in figure 4.4 is imposed at the inlet of the model P3, with **five different average flow rates:** $< Q1 >= 1ml.s^{-1}, < Q2 >= 2ml.s^{-1}, < Q3 >= 3ml.s^{-1}, < Q4 >= 4ml.s^{-1}, and < Q5 >= 5ml.s^{-1}$**.** The parameters used for those optical flow estimation were mentioned in the previous section ($JetFid$=$WallFid$=5, $\mu_{PREFAC} = 100$). The temporal evolution of the flow rate within one heart cycle (frame 350 to 420, timestep of 5 frames) is displayed in the following figure, for the five different flow rates.

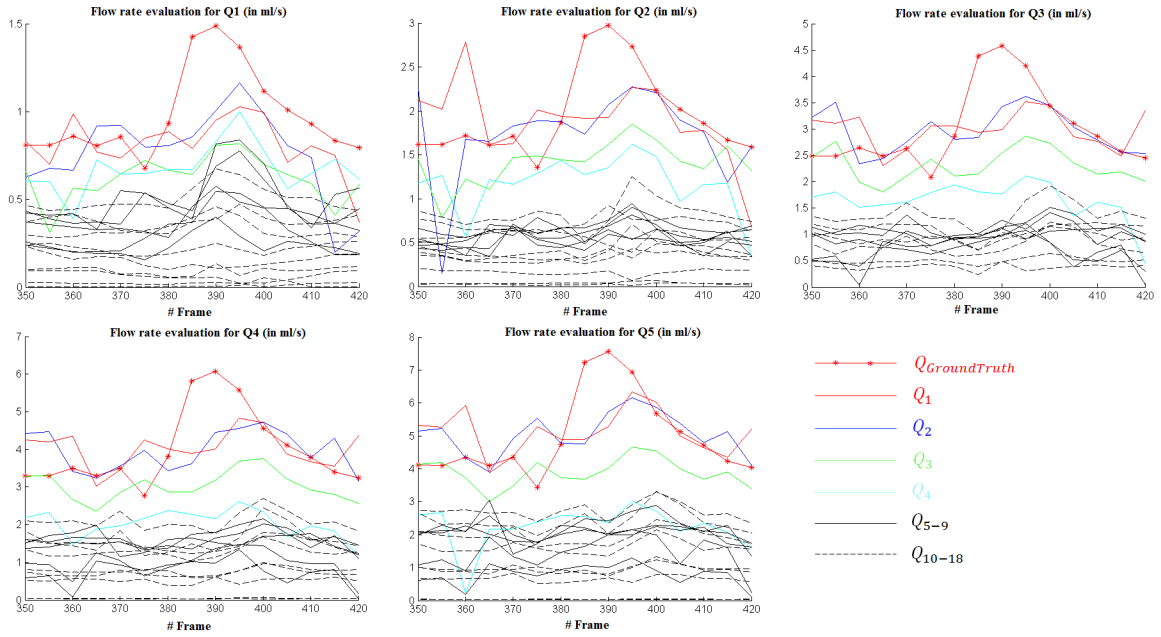

Figure 4.8: *Time evolution of flow estimation for different ground truth flow rates. Each flow curve corresponds to one cross-section $\mathcal{S}$ of the model P3. 18 cross-sections are evaluated for 15 different frames, and 5 different flow rates.*

From these five graphs, one can observe a fast deterioration of optical flow accuracy with increasing distance from the inlet (black curves). **The four first colored curves better match the average ground truth, even though the systolic peak is not fully captured.** After five cross-sections, that is $1cm$ away from the inlet, the estimated flow rate halves, which is the direct result of aperture dominance of the phase information in these locations. Taking the time-average flow rate $< Q_{\mathcal{S}} >$ better helps to figure out this phenomenon, as illustrated in figure 4.9.

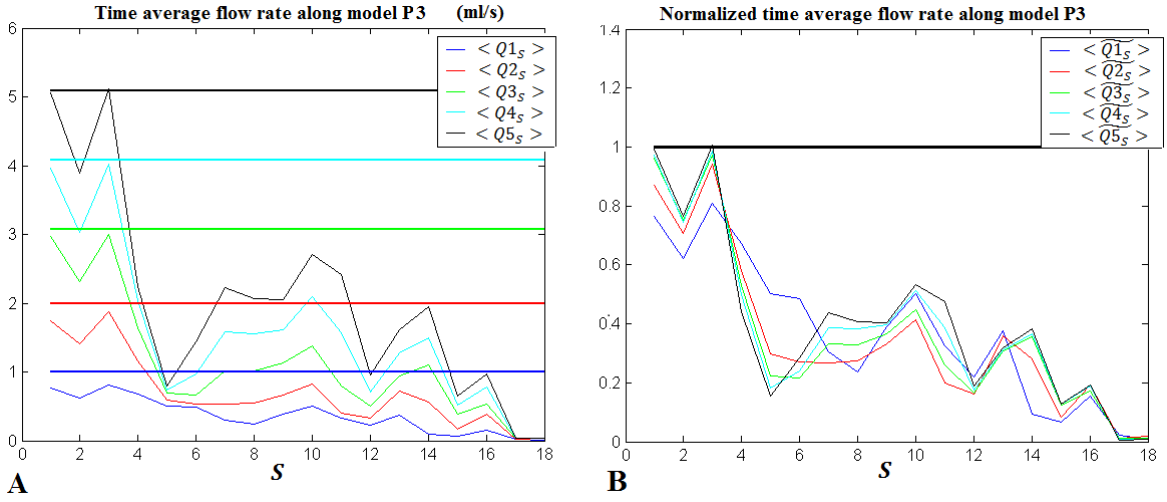

Figure 4.9: *Time average flow estimation with respect to* $\mathcal{S}$ *and ground truth flow rate for P3. Each color corresponds to the flow rate imposed in the CFD model as boundary conditions:* $< Q1 >= 1ml.s^{-1}, < Q2 >= 2ml.s^{-1}, < Q3 >= 3ml.s^{-1}, < Q4 >= 4ml.s^{-1}, and < Q5 >= 5ml.s^{-1}$. *For each one is compared the flow estimation and its evolution along the model, with the CFD ground truth (thicker lines). In B, the ratio between flow estimation and ground truth* $< \tilde{Q}_{\mathcal{S}} >= \frac{<Q_S>}{Q}$ *is displayed as to normalize the flow rate and better compare the curves. The black line of value* 1 *corresponds to the normalized ground truth.*

It can be clearly seen from figure 4.9 that flow rate gets underestimated after five cross sections, for $Q1, Q2, Q3, Q4$ and $Q5$. On the other side, the **the optical flow estimation exhibits the same behavior for the different flow rates imposed in the CFD model** (graph A). When normalizing the flow rate estimates with their corresponding ground truth (graph B), the curves of each flow rates are roughly overlaid. This shows that flow rate does not seem to play a role in the distribution of optical flow accuracy along the model. **A strong correlation can therefore be found between flow estimation and ground truth as the flow rate increases.** Figure 4.10 shows this correlation when different set of cross-sections were selected: at the inlet ($n_s = 1$), close to the inlet ($n_s = 3$ and $n_s = 5$) and for the whole model excluding aneurysm ($n_s = N_s$).

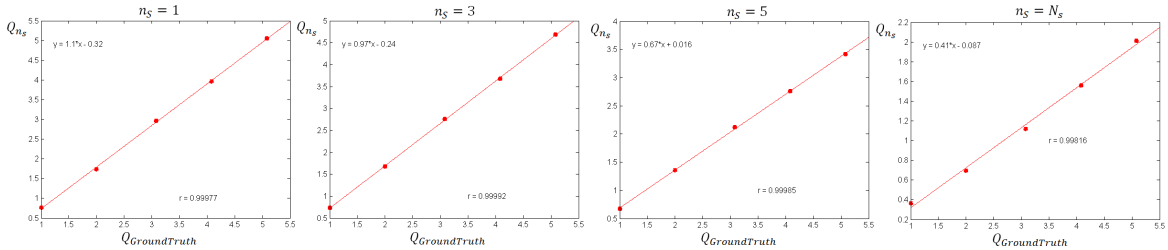

Figure 4.10: *Correlation between flow rate estimation and ground truth flow rate. Different cases are shown: inlet ($n_s = 1$), close to the inlet ($n_s = 3$ and $n_s = 5$) and whole model ($n_s = N_s$). A strong linear correlation ($r > 0.998$) can be observed in each case. The proportionality factor is close to 1 at the inlet, while it decreases for longer portion of the model.*

Local evaluation of the flow field

The optical flow estimation can be evaluated globally by considering the flow rate, but can also be evaluated locally by considering the blood flow velocities. Because, to our knowledge, optical flow estimation in virtual angiography is new, we essential focus on the most essential feature: flow rate. Indeed, our optical flow algorithm is not accurate enough to motivate a deep analysis of flow field patterns. However, the accuracy is better at the model inlet as was pointed out previously. The sequence of images below shows how the flow field weakens far from the inlet (figure 4.11). This occurs mostly because of the sharpening and elongation of contrast profile (see section 3.2.4), which misleads the evaluation of the longitudinal phase gradient component.

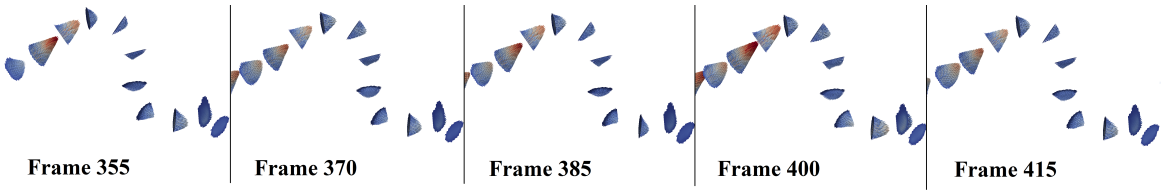

Figure 4.11: *Color-coded velocity field of model P055 (a full cardiac cycle is represented from frame 355 to frame 415, with a timestep of 15 frames). The flow field is weakening after five cross-sections, which is the effect of the elongated contrast profiles.*

Since the inlet is less subject to aperture problems, the flow field at this location is more reliably estimated by the optical flow algorithm.

Figure 4.12 shows similar results between optical flow reconstruction and ground truth for the third cross section $\mathcal{S}_3$. One can still notice a slight difference in the velocity profile where the optical flow exhibits a behavior that is closer to a linear function. This can be explained by the ambiguous information of the contrast phase gradient near the lumen wall. However, the peak of the parabola in the optical flow reconstruction is faithful to the ground truth (excepted for the systolic peak at frame 385).

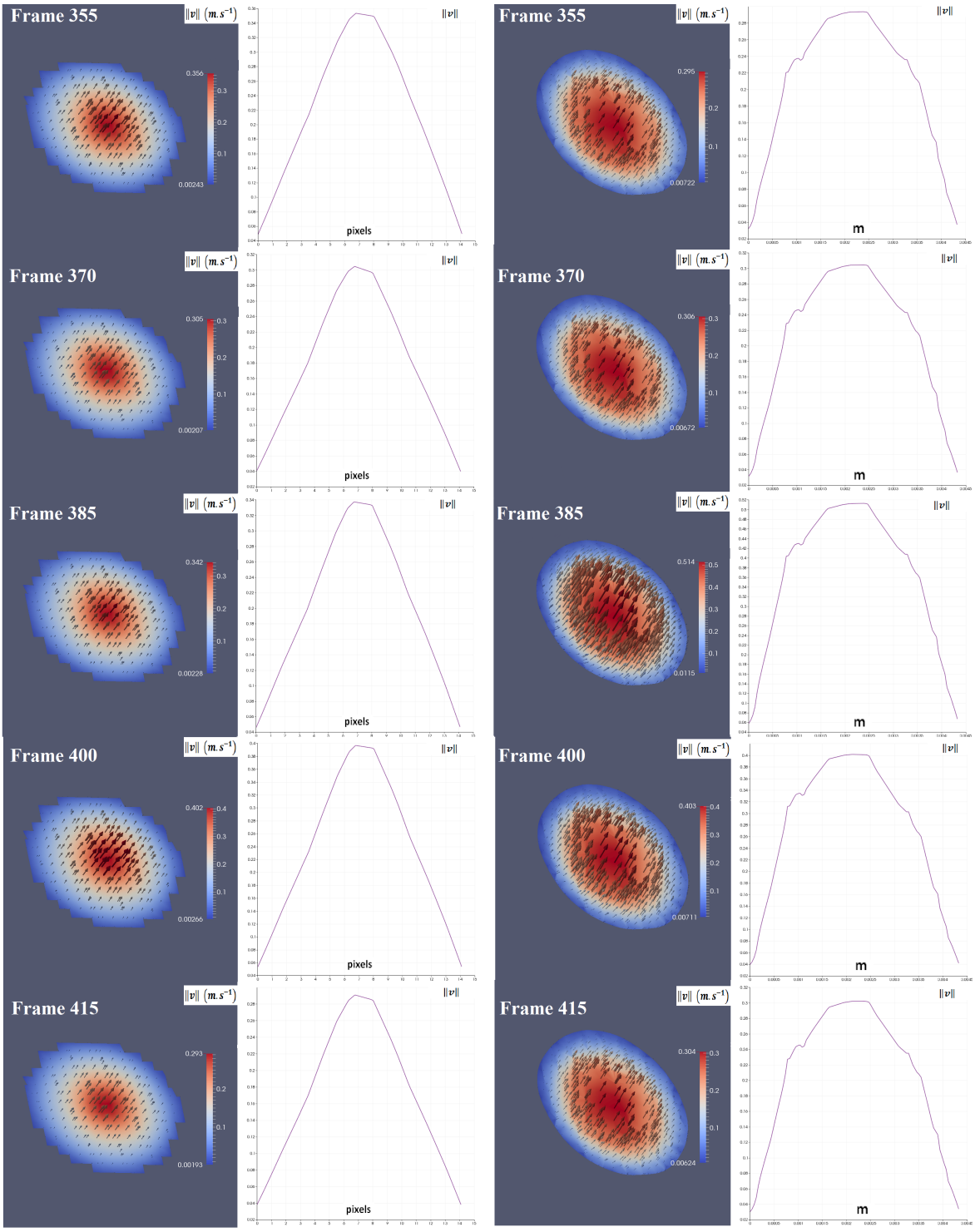

Figure 4.12: *Local flow field evaluation of P3, at $\mathcal{S}_3$. Five time steps are displayed, for both flow field reconstruction and ground truth. The first column depicts the reconstructed flow field from optical flow, with a 3D arrow representation and its corresponding color coded magnitude map. Second column contains graphs representing the velocity magnitude along a profile selected in the cross section. Both third and fourth column represent the ground truth.*

Those results are an overview of what our optical flow algorithm is capable of. The optical flow method proves to have to potential to achieve 3D velocity patterns with relatively low estimation error.

4.3.3 Geometry sensitivity analysis

This section presents the results of the optical flow method to four other models. For each model, illustrations and results of optical flow estimation are displayed. Similarly to the figure 4.9, the time average flow rate $< Q_{\mathcal{S}} >$ is compared with the ground truth $< Q >$ for different flow rates. Subsequently, correlation curves between flow estimation and ground truths for different flow rates are shown (as illustrates figure 4.10).

Model 1

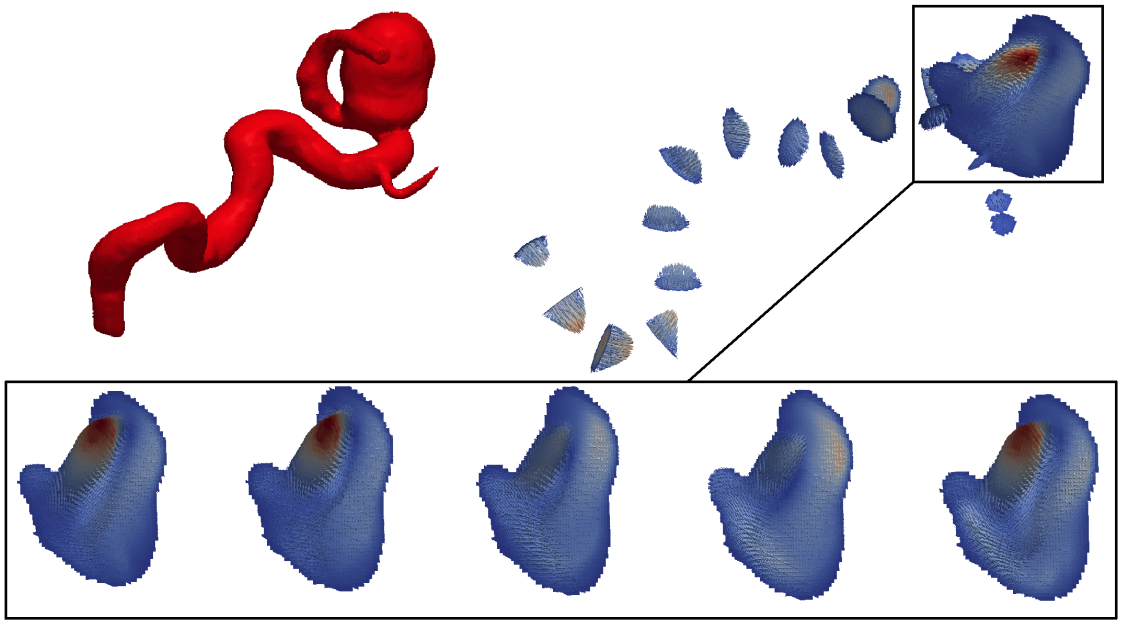

Figure 4.13: *Model P1 with flow field example of the time sequence. The flow pattern within the aneurysm are zoomed at for five different timesteps.*

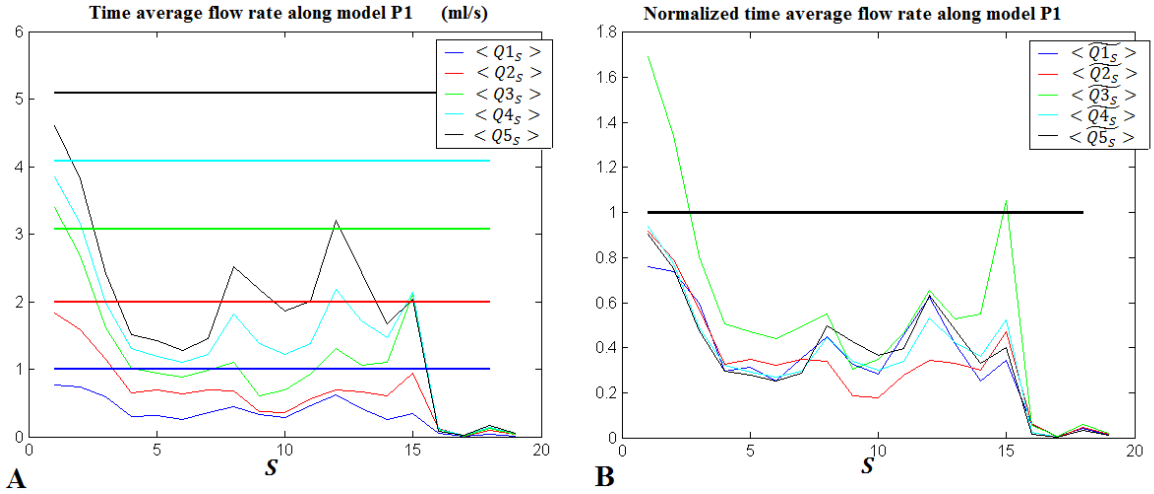

Figure 4.14: *Time average flow estimation versus section number $\mathcal{S}$ and ground truth flow rate for P1. In B is displayed the ratio between flow estimation and ground truth* $< \tilde{Q_S} >= \frac{<Q_S>}{Q}$.

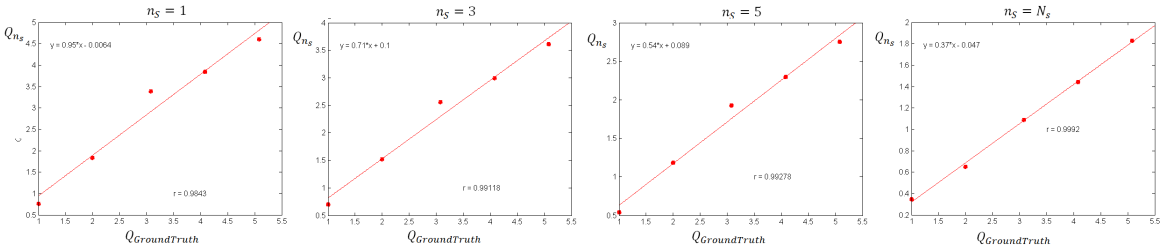

Figure 4.15: *Correlation between flow rate estimation and ground truth flow rate for model P1. Different cases are shown: inlet ($n_s = 1$), close to the inlet ($n_s = 3$ and $n_s = 5$) and whole model ($n_s = N_s$).*

Aneurysm evaluation

In addition to the flow rate evaluation, a close-up view of the flow patterns for different cardiac phases is provided in the figure 4.16. Our optical flow estimation can provide coherent flow patterns, especially in a location such as aneurysm, where the flow information is much more complex.

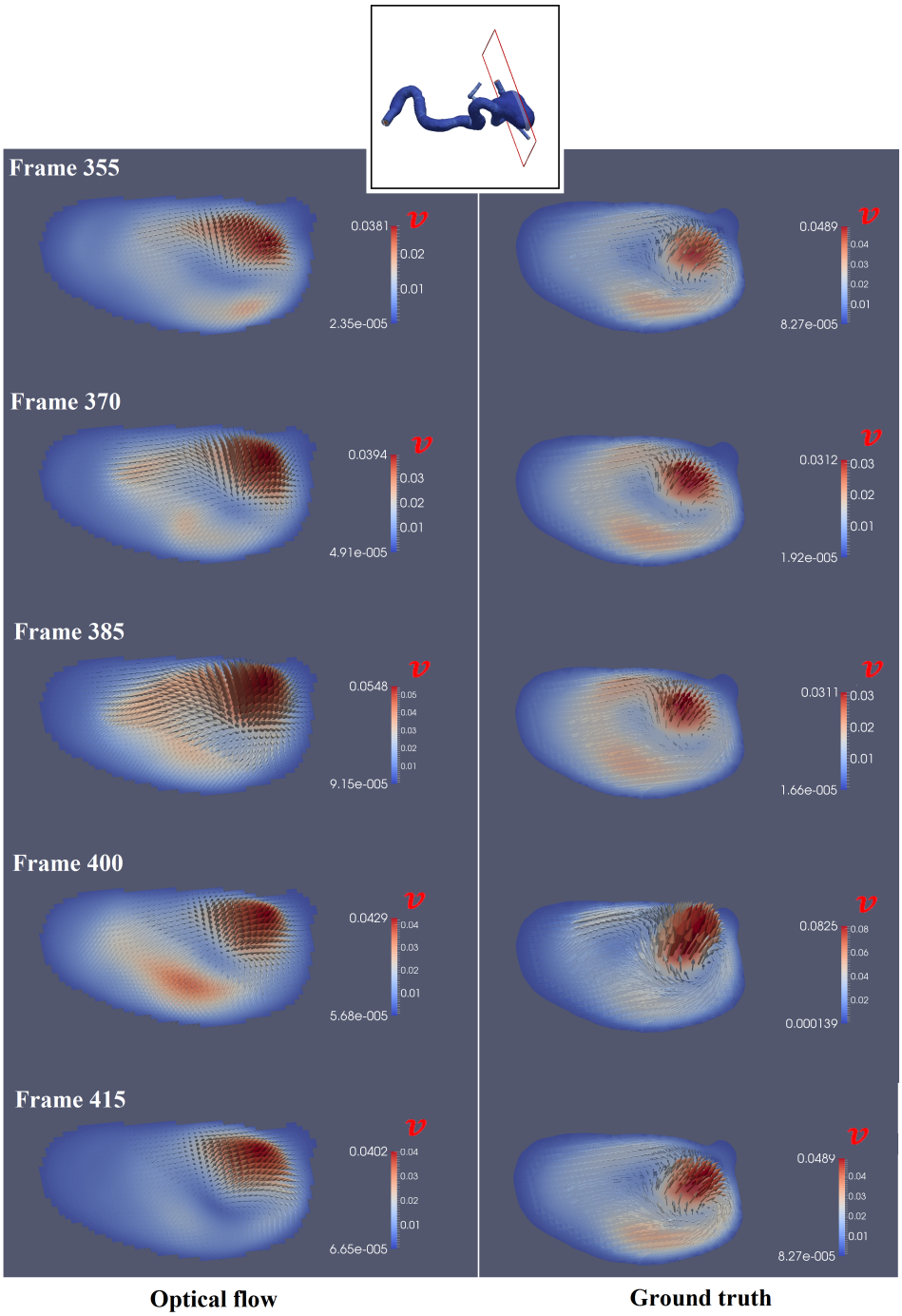

Figure 4.16: *Flow patterns inside an aneurysm of the model P1, with flow rate Q1. Both optical flow reconstruction (left column) and ground truth (right column) are displayed. The map of the velocity magnitude* $\|\mathbf{v}\|$ *and the velocity vectors* $\mathbf{v}$ *show similar distribution and orientation. However, the systolic peak (frame 400) is more prevalent in the ground truth. The optical flow field reconstruction is also smoother than the ground truth, which can be explained by the existence of the smoothness penalty.*

Model 2

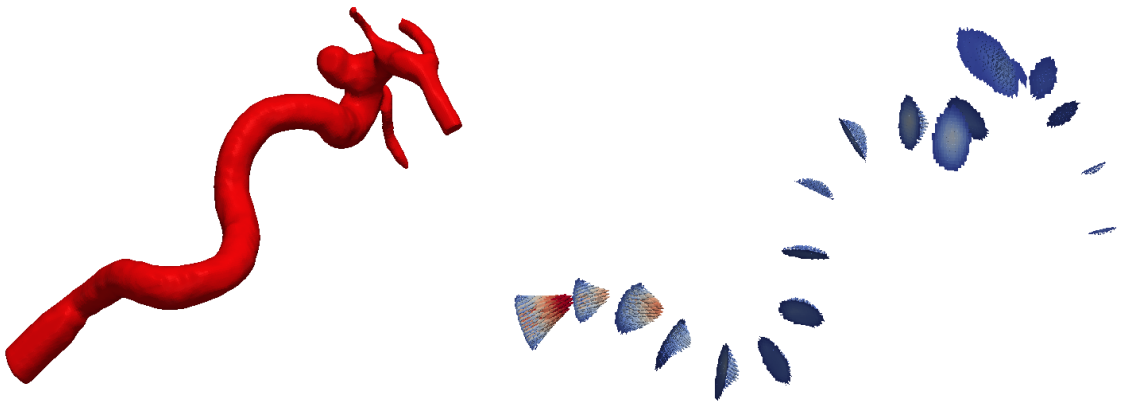

Figure 4.17: *Model P2 with flow field example of the time sequence.*

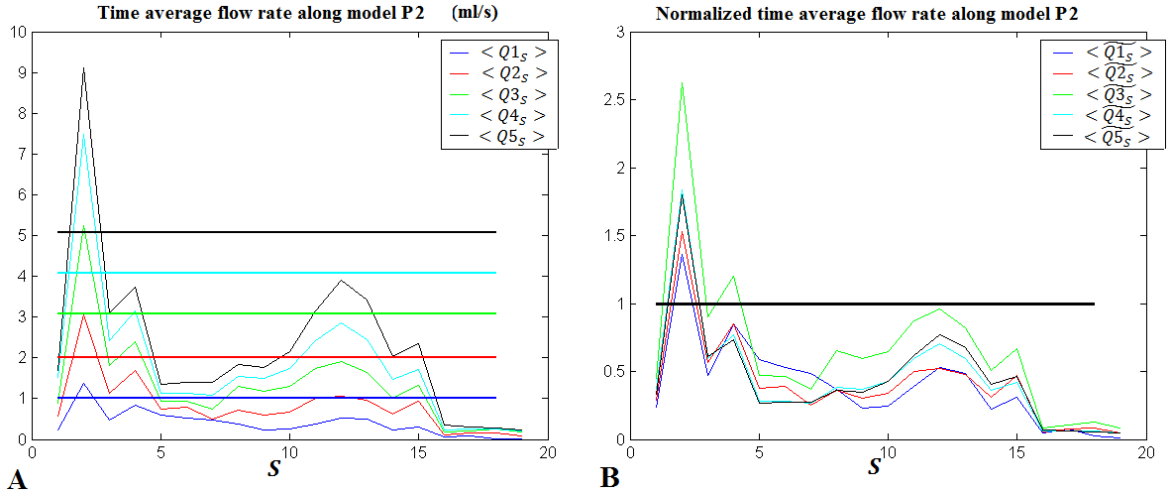

Figure 4.18: *Time average flow estimation versus section number $\mathcal{S}$ and ground truth flow rate for P2. In B is displayed the ratio between flow estimation and ground truth* $< \tilde{Q_S} >= \frac{<Q_S>}{Q}$.

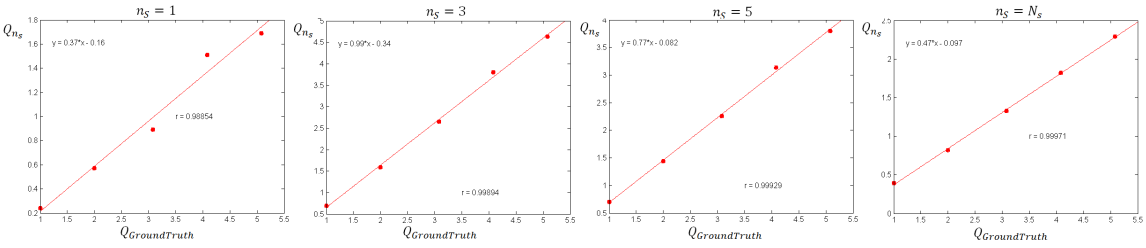

Figure 4.19: *Correlation between flow rate estimation and ground truth flow rate for model P2. Different cases are shown: inlet ($n_s = 1$), close to the inlet ($n_s = 3$ and $n_s = 5$) and whole model ($n_s = N_s$).*

Model 4

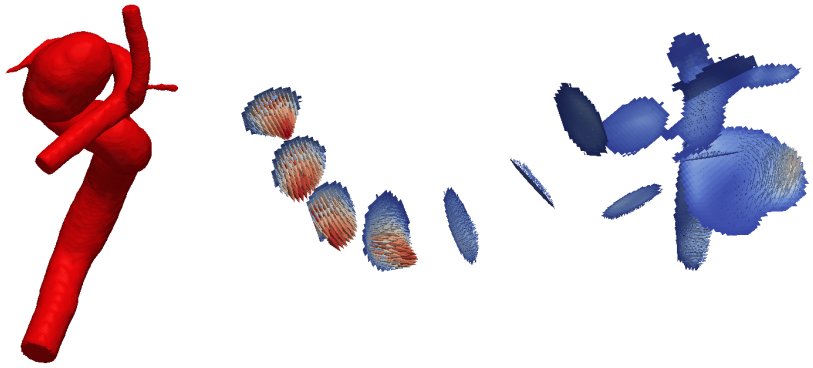

Figure 4.20: *Model P4 with flow field example of the time sequence.*

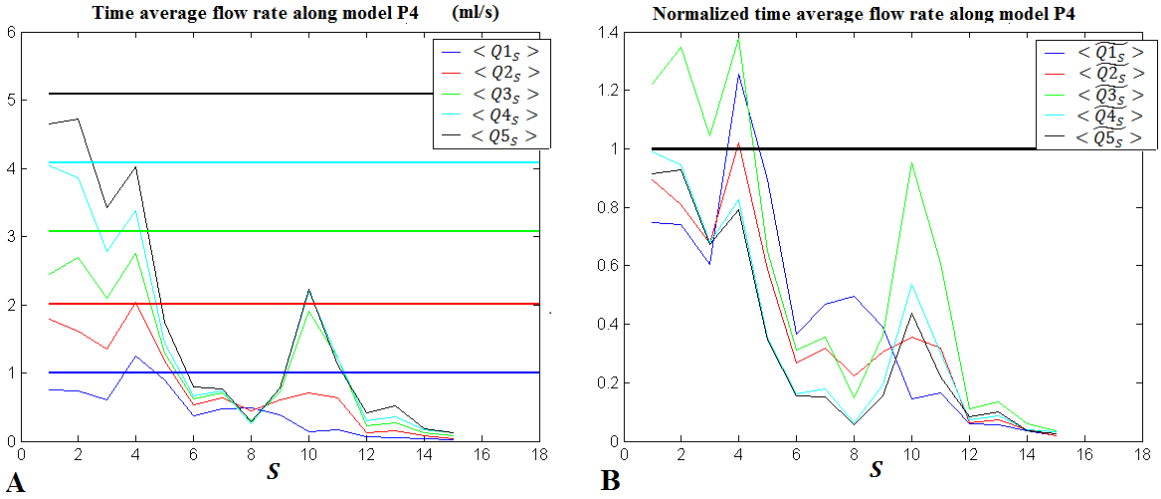

Figure 4.21: *Time average flow estimation versus section number $\mathcal{S}$ and ground truth flow rate for P4. In B is displayed the ratio between flow estimation and ground truth* $< \tilde{Q}_{\mathcal{S}} >= \frac{<Q_{\mathcal{S}}>}{Q}$.

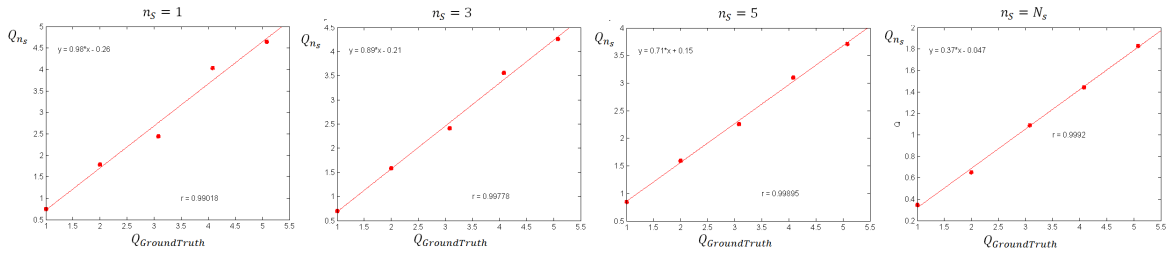

Figure 4.22: *Correlation between flow rate estimation and ground truth flow rate for model P085. Different cases are shown: inlet ($n_s = 1$), close to the inlet ($n_s = 3$ and $n_s = 5$) and whole model ($n_s = N_s$).*

Model 5

Figure 4.23: *Model P5 with flow field example of the time sequence.*

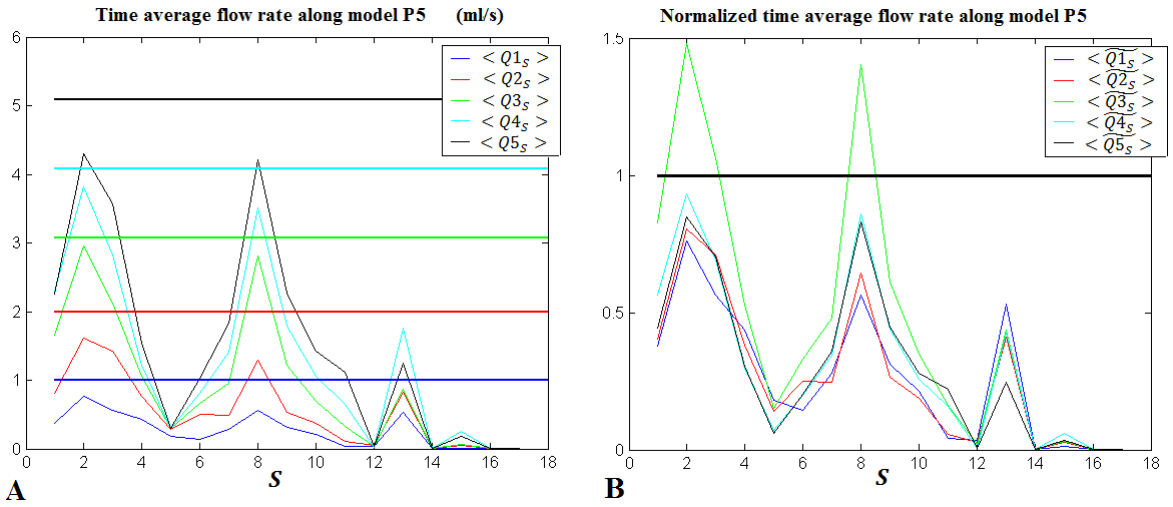

Figure 4.24: *Time average flow estimation versus section number $\mathcal{S}$ and ground truth flow rate for P5. In B is displayed the ratio between flow estimation and ground truth* $< \tilde{Q}_{\mathcal{S}} >= \frac{<Q_{\mathcal{S}}>}{Q}$.

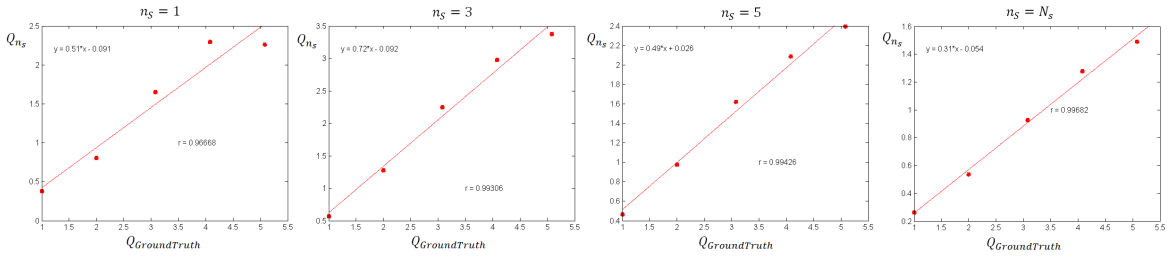

Figure 4.25: *Correlation between flow rate estimation and ground truth flow rate for model P5. Different cases are shown: inlet ($n_s = 1$), close to the inlet ($n_s = 3$ and $n_s = 5$) and whole model ($n_s = N_s$).*

4.4 Discussion

In this section, special attention was paid to the arterial flow rate. The reason is because it is the most basic and generic measurement that can be obtained from medical images. Flow rate can be of reference to understand the physiological hemodynamic condition in an artery [Pereira et al., 2014, Bonnefous, 2001]. To complement the arterial flow measurement, flow patterns and other hemodynamic quantities, like velocity, WSS and pressure can be also obtained [Ebbers and Farnebäck, 2009, Isoda et al., 2010, Petersson et al., 2012, Berg et al., 2014]. These quantities are related to the biological reaction of the endothelial cells due to the hemodynamic stimuli [Wootton and Ku, 1999a]. Therefore, an effort to obtain velocity field was aimed (see figure 4.12 and 4.16). However, those quantities are more challenging to extract because they depends on the accuracy of the technique at pixel level.

In the analysis of models P1, P2, P3, P4 and P5, **the flow rate estimated from the optical flow method provides a better accuracy in the three first sections**. For each imposed flow rate, the estimated flow rate roughly provides an accuracy within 40% error. Then, the behavior of the estimated flow rate depend on the model. **For P1, P2 and P3, the flow rate decreases and stabilizes to low values with shallow peaks (figures 4.14, 4.18 and 4.9), while for P4 and P5 the flow rate exhibits higher rebounds (figures 4.21 and 4.24)**. The influence of bends of the CFD model can be an explanation to these phenomenon, since the secondary flow spreads the CA towards the walls. As a results, the sharpening of contrast profile is interrupted, and phase gradients with more favorable directions (smaller aperture effect) can appear. Nevertheless, more effects can intervene in the distribution of flow rate along the model, and a deeper investigation should be carried out in the future.

Even if the flow rate shows a disadvantageous behavior after sever cross sections - sharp diminution -, one can notice an interesting correlation between the estimated flow rate, and the ideal flow rate. First, the figures 4.14, 4.18, 4.9, 4.21 and 4.24 show that the estimated flow rate behaves similarly for each ground truth flow rate $Q1, Q2, Q3, Q4, Q5$. Secondly, the correlation curves for each model, figure 4.15, 4.19,4.10,4.22 and 4.25 show an excellent linear correlation coefficient ($0.996 < r < 1$) when considering the spatio-temporal average of the whole model ($n_s = N_s$). The flow rate is better estimated at the inlet (the slope of this correlation surrounds 1: 0.95 for P1, 1.1 for P3, 0.98 for P4, and for three cross sections, 0.99 for P2 and 0.72 for P5), but the correlation coefficient tends to be lower than those observed for the whole model. Conversely, **the flow estimation is worst when considering the whole model (the linear factor is** 0.37 **for P1,** 0.47 **for P2,** 0.41 **for P3,** 0.37 **for P4 and** 0.31 **for P5), but the correlation coefficient converges to** 1. As a result, these linear correlation factors lie within a narrow interval (0.31 to 0.47) and, in the future, could be taken into account to further adjust the flow rate estimation.

Yet, the main difficulty encountered in this study is that **the blood flow rate**

constancy is not verified. Although a penalty term dedicated to the diminution of divergence is used (section 3.3.3), it appears that blood flow incompressibility is not sufficiently enforced. A common observation comes for every model that flow estimation accuracy decreases after the model inlet (after 1 cm approximately) and the decrease of the estimated flow rate cause the breaking of incompressibility constraint. This phenomenon is widely due to the accentuation of the aperture problem when the contrast profile gets elongated in direction of flow. As was pointed out in section 3.2.4, the phase gradient becomes more and more orthogonal to the direction of flow as we progress downstream. **The attempts to deal with this difficulty, as the divergence regularization (section 3.3.3) and the wall term (section 3.6) might not suffice to recover the velocity component in direction of flow.** Besides, the accuracy of the CFD model can also be questioned. While CFD software provides very precise contrast density and flow fields within tetrahedral elements, **the CFD data gets slightly less accurate when exported into a cartesian grid**. **Since the optical flow algorithm outcome fully relies on the contrast phase ϕ, any loss of information during the cartesian mesh exportation can dramatically affect the flow recovery (especially nearby the model boundaries where tetrahedral elements are much smaller than in the lumen center). Because our optical flow algorithm uses finite difference approximations and cartesian coordinates, the evaluation of phase gradient or any other derivative can mislead the flow estimation.** Henceforth, a more suited framework for the resolution of the CGM could be the utilization of finite elements methods within more complex meshes. More accurate evaluation of the phase gradient $\nabla\phi$, among other, could provide better flow estimates.

Lastly, one could object that the PBOF (Phase Based Optical Flow) equation (3.22) that attempts to cancel **the material derivative of the phase** ϕ does not fully correspond to the original optical flow equation $\nabla I \cdot \mathbf{v} + \frac{\partial I}{\partial t} = 0$ that wishes to cancel **the material derivative of the contrast density** I**.** Basically, ϕ and I are not the same features to track. Because a temporal filtering has been carried out on the original signal (see section 3.2.1 with bandpass and *Hilbert* filtering), so the velocity $\mathbf{v}$ implicitly undergoes a time filtering. Therefore, unless the velocity $\mathbf{v}(\mathbf{x}, t)$ is stationary, the velocity of the contrast density I and the velocity of the phase ϕ are not exactly equal. This said, one can propose an explanation for the systolic peaks being missed in figure 4.8. If the blood flow quickly varies within a heart cycle, the phase information may not capture this sharp variation and **the optical flow of the phase may differ from the optical flow of the contrast density.**

*
* *

CFD is a very powerful tool to study contrast propagation in the bloodflow, especially in the absence of in vivo and in vitro data. With its high flexibility and

reliability, it allows to simulate a wide variety of flow experiment, with different geometries and different flow rates, both inspired from clinical data. Moreover, CFD -or virtual angiography- provides accurate information on contrast propagation, blood flow, and as such can serve as a ground truth for the evaluation and the improvement of an OFM (Optical Flow Method). The OFM developed in chapter 3 was confronted to virtual angiography and provided 3D estimates of the blood flow field.

A large number of parameters intervene in the optical flow algorithm, but three of them are the most sensitive: the jet fidelity, the wall fidelity and the smoothness penalty. While an exhaustive optimization of the parameters is theoretically possible, a small amount of parameter combinations was used and yielded local minimums of the flow estimation error. When changing the boundary conditions, the OFM shows stable results. The flow rate imposed at the model inlet and the model geometry do not significantly change the accuracy of the flow rate estimation. While the OFM provides satisfactory estimates of the flow rate at the inlet, the flow rate accuracy decreases downstream. Several reasons have been identified:

- The dominance of aperture problem far from the model inlet (phase gradient $\nabla\phi$ gets orthogonal to the flow direction).
- The precision or resolution of the CFD contrast map after export in a cartesian mesh.
- The approximation of the PBOF framework where the velocity $\mathbf{v}$ is supposed to slowly vary over time.

The workstream is fully opened, and the topic is new. Though the first results are very promising, many improvements can be brought to the current OFM. As a reminder, the next chapter tests the PBOF method on early MPI data, and the conclusion presents several prospects and possible upgrades of the current OFM.

Chapter 5

Optical flow application on in vitro and in vivo MPI data

Contents

Abstract

Estimating and assessing blood flow from 3D+T MPI angiography were among the objective of this thesis. This chapter describes some preliminary work using this modality. Unfortunately, we only had access to a small amount of MPI data. The current MPI hardware is still on progress, which limits the development of dedicated image processing tools. Nonetheless, hopes can be raised concerning the future of MPI in clinical applications. Flow-phantom MPI experiments will be presented and the possibility to capture blood flow will be exposed. Secondly, in-vivo evaluation describing contrast propagation in mice heart will be presented. A tentative approach to extract the cardiac dynamics will finally be proposed and discussed before concluding this chapter.

Résumé

L'estimation et l'évaluation du flux sanguin en angiographie MPI 3D+T était un des principaux objectifs de cette thèse. Ce chapitre décrit un travail préliminaire sur cette modalité. Malencontreusement, une quantité très limitée de données MPI fut accessible. Le système MPI actuel est toujours en cours de développement, ce qui limite le dévelopement d'outils de traitement d'image dédiés. Néanmoins, quelques espoirs peuvent être permis concernant le futur du MPI dans les applications cliniques. Des expériences de flux MPI sur fantôme sont présentées ainsi que la possibilité de capturer le flot sanguin. Dans un deuxième temps, des acquisitions in vivo décrivant la propagation de contraste dans le coeur de souris seront exposées. Une première approche pour extraire la dynamique cardiaque sera finalement proposée et discutée avant de conclure ce chapitre.

5.1 In-vitro MPI acquisition

The number of in-vivo data is growing rather slowly since the 2008 evaluation, which hampers substantial studies on MPI in vivo flow assessment. Until then, phantom experiments are the only alternative to explore the potential of MPI for flow assessment. This section proposes one of the first MPI flow-phantom experiments dedicated to flow estimation. For that, we described the method used for the injection of contrast agent in the phantom inlet, and how a velocity map was derived from the acquired data.

5.1.1 The flow-phantoms

The first step of this experiment was to select the shape of the phantom and the injection mode. A static tubular phantom was chosen. In in vivo mice data [Weizenecker et al., 2009], the sizes of heart chambers were just above the spatial resolution, which resulted in partial volume effects and made difficult the distinction between wall motion and contrast propagation. Subsequently, a flow free of wall motion was reached with the use of simple geometries making use of tubular structures (figure 5.1).

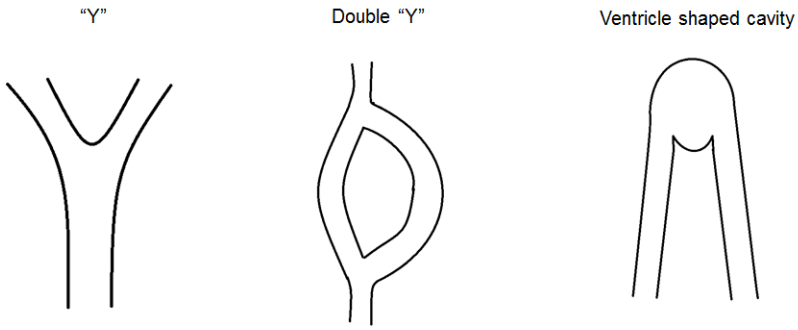

Figure 5.1: *Different possible shapes of flow phantoms.*

The second phantom was selected: a single inlet and outlet, and the possibility to study the flow in bifurcations. Finally, the injection mode had to be considered. In DSA, the mixability between blood and contrast is exploited to study bloodflow [Lieber et al., 2009]. Tracer density is spatially and temporally modulated along the vessels, due to the periodic bolus dilution that the heart pumping generates. This modulation is what allows accurate blood flow estimation in angiography sequences. In the same idea, we wanted to build an experimental set-up that created an alternate flow of water and MPI contrast agent inside the physical phantom.

5.1.2 Toward an acquisition protocol of pulsated contrast flow

Flow experiments were performed in the preclinical MPI demonstrator available at the Philips Research facilities in Hamburg. The flow system consisted of two reservoirs (60ml syringes), placed above the Faraday cage, one with 1/20 diluted Resovist©and

the other with water. The reservoirs were connected to two tubes which flow rates were controlled by a straightway diaphragm valve system, namely a Lego Mindstorm©unit. Then, the tubes entered the MPI scanner, and were brought together via a Y-junction for mixing. The water-contrast mixture finally flowed inside a phantom placed at the scanner isocenter (see figure 5.2).

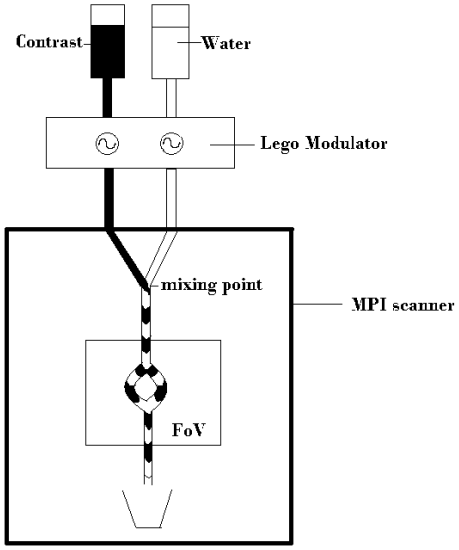

Figure 5.2: *Experimental set-up*

The outlet discharged the mixed fluid into a bucket. The total height difference between the reservoirs and the outlet was approximately 1.5 m. Note that the Lego unit was kept away from the MPI room in order to avoid electromagnetic interferences of its metal components. Concerning the modulation device, the Lego motor drove two connecting rods back and forth which compressed both tubes alternately with a frequency of 2.3 Hz. This set up allows a periodic release of contrast agent inside the phantom, with an approximately constant flow (the two feeding tube were squeezed alternately in perfect phase opposition).

To calibrate the total flow rate, the syringes graduations were used. After releasing the contrast-water mixture for 5 seconds, the drop of volume in each syringe was recorded, and the experiment was repeated 3 times. An average flow rate $Q_{total} = 4ml.s^{-1}$ was found for both syringes combined. The average velocity in the phantom inlet can be directly derived from the flow rate, knowing the inner diameter of the PVC tubes, d=4 mm. The average inlet velocity of the mixture in the phantom was $V_{inlet} = 32cm.s^{-1}$ and for each branch $V_{branch} = 16cm.s^{-1}$ (the whole circuit was tubed with the same diameter).

Figure 5.3: *Lego unit modeling the contrast pump. Left: Oscillatory tube compressor allowing the modulation of the volumetric flow ratio between contrast and saline solution. Right: Lego unit on top of the MPI Faraday cage, during the flow experiment.*

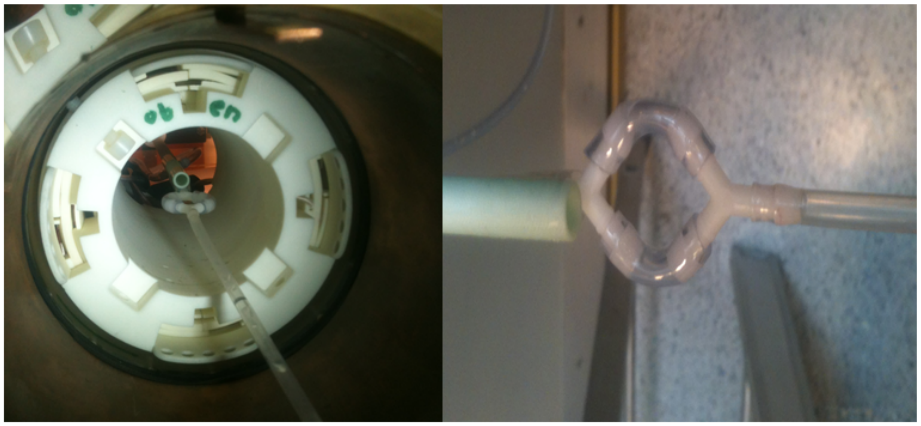

Figure 5.4: *Phantom in the MPI bore (left) and out of the scanner (right).*

From the modulation frequency f of the Lego and the velocity inside the branches, the spatial wavelength of the contrast wave was derived as:

$$\lambda = \frac{V_{branch}}{f} = 7cm \tag{5.1}$$

This wave can be tracked with a temporal resolution of $21.5ms$ and a spatial resolution of $1mm$. With such resolutions, a velocity of $16cm.s^{-1}$ corresponds to a displacement of 3.44 voxel, which is less than 10 times the capture range ($CaptureRange = 0.5\lambda = 35voxels$). The capture range, as explained in section 2.6 with equation (2.34), is the maximum distance between two phasefronts that allows a proper registration. This condition can be more easily understood by considering the time resolution (equation (2.35)):

$$\Delta t_{max} = \frac{T}{2}$$

which works here since the resolution Δt is $21.5ms$ and the modulation period approximately $435ms$ ($\frac{T}{2} \simeq 218ms$).

In this way, the modulation frequency and velocity range were selected for suitable flow quantification. Moreover, the working Reynolds number matches state-of-the art values for arterial flow [Ku, 1997] (Re=640 in the branches). Finally, single-volume acquisitions were performed. Volume sequences of approximately $20 * 36 * 36mm3$ (that is $20 * 36 * 36$ voxels) were recorded during 2.5 minutes. MPI dynamic data were exported on the standard image processing software MATLAB R2010a ©. The behavior of the CA inside the phantom, and TICs were analyzed.

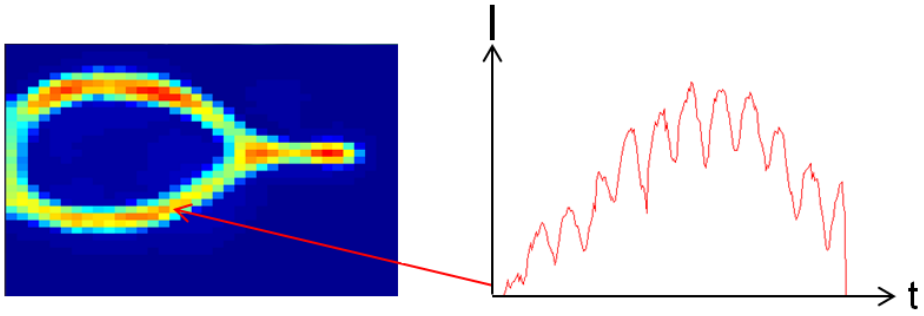

Figure 5.5: *MPI phantom slice (left) and TIC of one voxel (right).*

A temporal modulation was visible inside each voxel belonging to the phantom lumen. However, the spatial modulation was still hidden in the baseline component of the signal. To remove the baseline component and extract the frequency components (narrowband components around fundamental and harmonics), a temporal filtering was performed for each pixel inside the phantom, as described in section 3.2.1 with $\hat{S}$. One should note that the narrowband frequency extraction allows to retrieve the low frequency envelop of oscillations, while discarding the baseline. With a FoV of 20*36*36 voxels, half of a wavelength could be visible ($\frac{\lambda}{2} \approx 35$ voxels is approximately the extent on z axis, the axis along which the product propagates). In figure 5.6 is displayed the real part of $\hat{S}$, its TIC in a voxel and its quadrature.

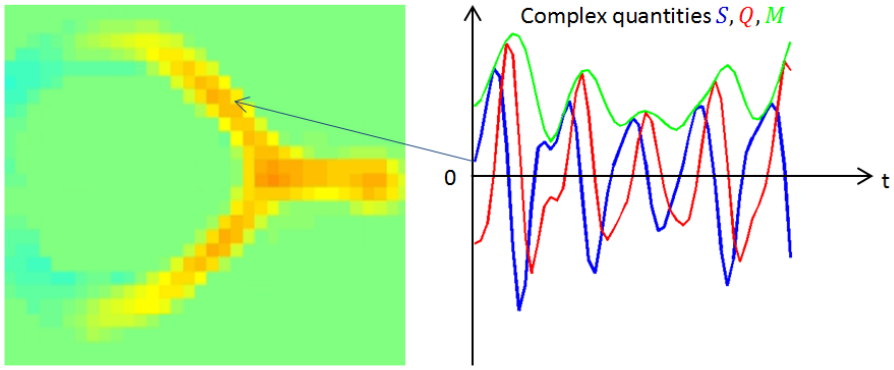

Figure 5.6: *Slice of the filtered signal S (left), TIC inside a voxel and its quadrature Q (right).*

5.1.3 The results

Under the approximation that concentration does not change along a flowline, the signal $\hat{S}(\mathbf{x},t)$ should follow the analytic optical flow equation (3.17) met in section 3.2.2:

$$\frac{\partial \hat{S}(\mathbf{x},t)}{\partial t} + \mathbf{v}(\mathbf{x},t) \cdot \nabla \hat{S}(\mathbf{x},t) = 0$$

where $\mathbf{v}(\mathbf{x},t)$ is the instantaneous velocity vector for every couple $(\mathbf{x},t)$ of the spatial-temporal sequence. Here, $\frac{\partial \hat{S}(\mathbf{x},t)}{\partial t}$ is very easy to compute: the semi-analytic representation of the signal with Fourier series described in section 3.2.1 allows a straightforward calculation of the time derivative. This is a way to cope with numerical approximation of finite differences and also long iteration procedures often arising in Lucas-Kanade algorithm [Lucas and Kanade, 1981]. Such system is well-known to be solved with the minimization of the LMSE (equation (3.19), section 3.2.2):

$$E = \sum_{\mathbf{x}\in\mathcal{W}} W(\mathbf{x})(\frac{\partial \hat{S}(\mathbf{x},t)}{\partial t} + \mathbf{v}(\mathbf{x},t) \cdot \nabla \hat{S}(\mathbf{x},t))(\frac{\partial \hat{S}(\mathbf{x},t)}{\partial t} + \mathbf{v}(\mathbf{x},t) \cdot \nabla \hat{S}(\mathbf{x},t))^*$$

where W is a Gaussian low-pass filter of scale σ in a small window $\mathcal{W}$.

Furthermore, temporal robustness is brought by considering the quadrature signal $Q(\mathbf{x},t) = \Im(\hat{S}(\mathbf{x},t))$. This component always prevents the temporal derivatives to cancel out. Figure 5.6 shows that when the signal derivative gets to 0, the quadrature derivatives is maximal, and the other way around. As a result, the same thing occurs for the spatial gradients.

The resolution of the LMSE minimization leads to the linear system (2.11):

$$M\mathbf{v} = \mathbf{b}$$

where $M = \Re(\sum W(\frac{\partial \hat{S}}{\partial x_i}\frac{\partial \hat{S}}{\partial x_j}^*))$ is a tensor matrix containing spatial gradients, and which conditioning has been strongly improved by the quadrature term (diagonal elements never reach zero) . $\mathbf{b} = -\Re(L_\sigma(\frac{\partial \hat{S}}{\partial t}\nabla \hat{S}^*))$ is the right hand side vector containing temporal derivatives. The matrix inversion becomes very simple with classic linear system resolutions as Gauss-Siedel. This first method was tried on the in-vitro phantom and yielded very promising results in figure 5.7.

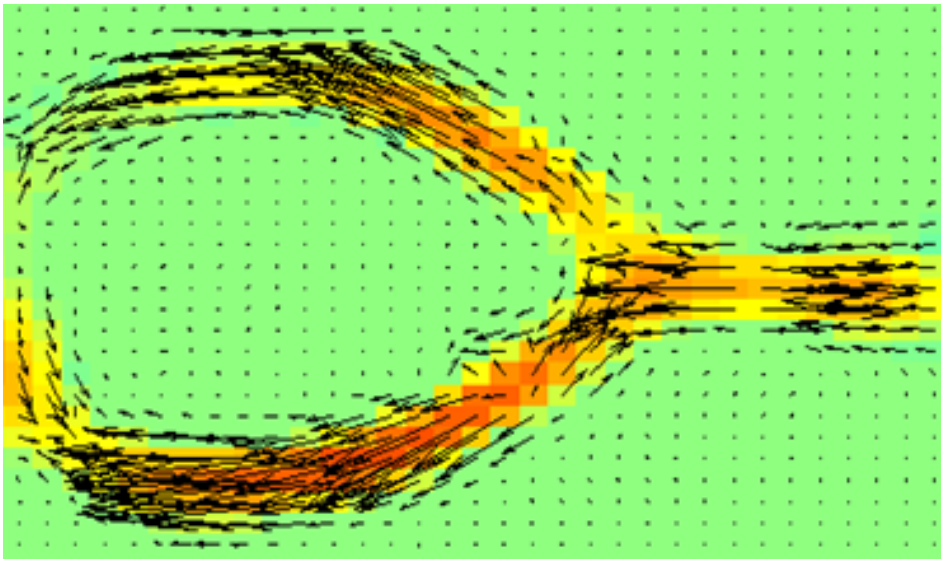

Figure 5.7: *Optical flow estimation in a Y-shape phantom. Arrows represent estimated velocity vectors and jet map is the contrast intensity.*

To evaluate the optical flow estimation, the flow calibration was relied upon. The mean values of velocity magnitude were compared: a mean velocity of $16cm.s^{-1}$ was derived for the calibration, and $14.5cm.s^{-1}$ average for the optical flow estimation. This 10% error is acceptable enough for a first trial and enough to carry on with MPI in-vitro flow assessment. These early results were presented during the conference dedicated to MPI [Lacroix et al., 2014].

One could object that the global multigrid techniques developed in chapter 3 (section 3.3.1 and 3.3.5) was not used for the in vitro flow experiment. The main reason for this is the size of the MPI FoV and the acquired phantom lumen (few voxels diameter in figure 5.7). A multigrid technique cannot be suited for such small lumen, and the aperture problem is less predominant at this scale which is why local techniques suffice. **However, with future MPI data with larger FoV and larger lumen, the overall optical flow approach presented in chapter 3 would be certainly useful.**

Tentative aneurysm phantom experiment

Some acquisitions were performed on the MPI scanner later during this thesis. A physical phantom was tailored to look like an aneursym, with a thicker diameter of

1cm (figure 5.8). The modulated injection protocol was repeated on this phantom but failed. The scanner was being repaired for months and its calibration was not properly done. As a result, a periodic signal was gathered by the MPI system, but the reconstruction yielded a deformed image, where accurate flow estimation was not achievable (figure 5.9). The system has only recently been repaired, but too late to be used in this thesis work.

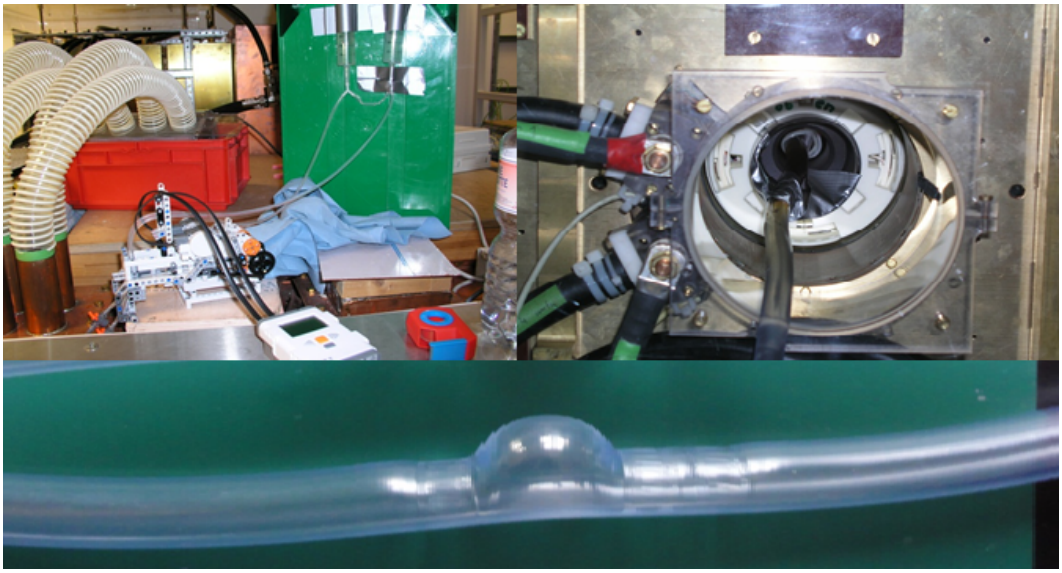

Figure 5.8: *Flow acquisition with aneurysm phantom and pulsed contrast injection. The dynamic data was reconstructed with a 2D system function.*

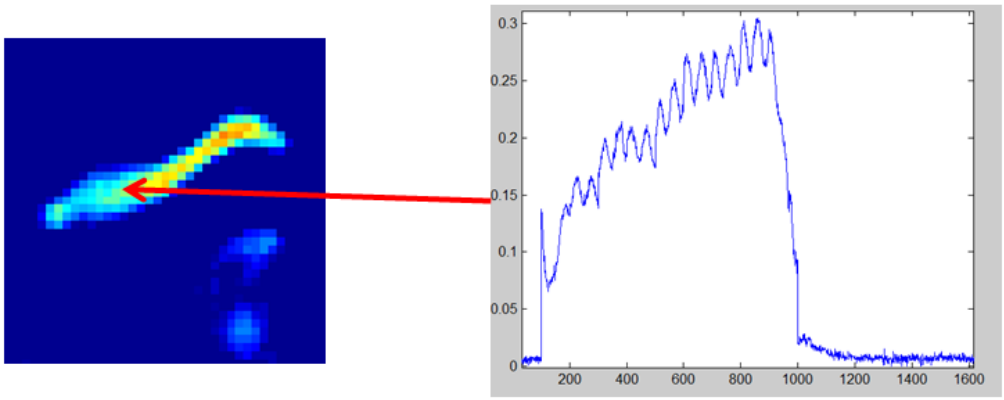

Figure 5.9: *Reconstructed data from the aneurysm phantom. The deformed shape makes the data unexploitable. However, a good temporal modulation is observed in the bright areas.*

However, it can be hoped in the future that images with better quality will resolve a vorticity within the aneurysm-shaped phantom. First phantom acquisitions exhibited very promising results with MPI, this experimental section can form the basis of many other MPI flow experiments.

5.2 In-vivo MPI acquisition

5.2.1 The first in-vivo MPI evaluation

The feasibility of in vivo cardiovascular MPI was demonstrated by the three-dimensional visualization of a beating mouse heart by *Weizenecker et al* in 2008 [Weizenecker et al., 2009]. In this experiment, a small FoV 3D+T MPI scan was performed, and a bolus of magnetic particles was injected into the tail vein of the living animal. For tracer concentration in the range between 8 and 45 $\mu mol(Fe).l^{-1}$, a sufficiently high sensitivity was reached to image clinically approved iron-oxide-based MRI contrast agents (Resovist, Bayer Schering Pharma) at allowed concentrations (below 40 $\mu mol(Fe).l^{-1}$).

Before the animal experiments, the system was calibrated by acquiring a *system function* (see Appendix B). It was measured on a grid of $34 * 20 * 28$ with a voxel size of $(0.6\,mm)^3$ using a small reference sample of undiluted ($500\,mmol\,(Fe).l^{-1}$) Resovist ©. Finally, mice were placed on a cylindrical animal support with an inner diameter of $29\,mm$ so that the heart was within the FoV after insertion into the scanner bore. The raw data acquired after bolus injection were reconstructed to 1800 volumes.

The diffusion and propagation of the contrast product through the blood stream is captured as a 3D+T signal by the MPI imaging system. The bloodstream drives the tracer steadily through the vena cava to the right atrium of the heart. Then the contrast penetrates the heart chambers gradually, first in the right atrium and right ventricle, and comes back in the left atrium and right ventricle after a short pass in the pulmonary vessels. Though the propagation of the bolus is slow (several seconds), the contrast also undergoes the fast wall motion during the different cardiac phases (240 beats per minutes, i.e 250ms for a cardiac period). Subsequently, a signal is observed on the vessel and the heart chambers and shows a deep modulation at the cardiac frequency (see figure 5.11).

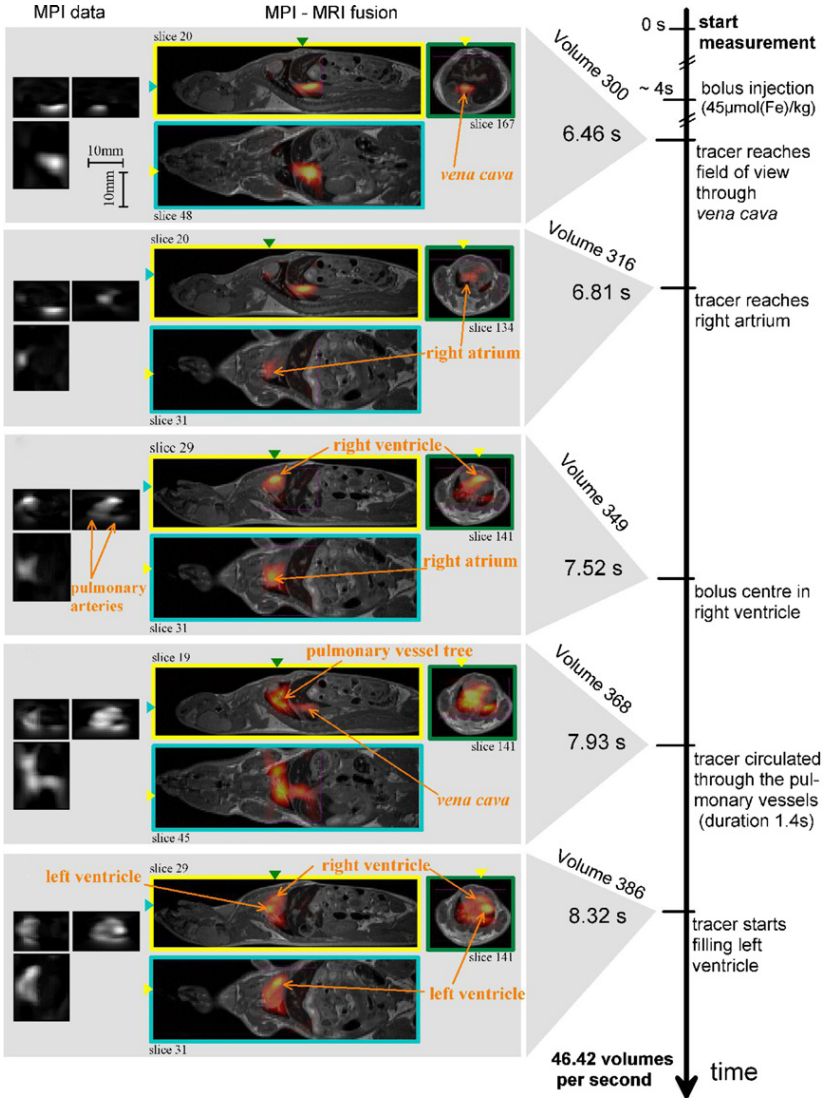

Figure 5.10: *MPI sequence with overlay of static MRI image in three orthogonal views at different times. The frame rate was 21.5 ms per volume and the acquisition lasted 23 min. A ferromagnetic tracer (Resovist) was injected in the tail vein few second after the acquisition started. The colored triangles indicate the position of the orthogonal slices in the corresponding frame. The position of MRI slices is depicted by three numbers at the corner of the frames. The different phases of the bolus passage are represented by the time axis. The spatio-temporal resolution allowed to resolve heart chambers and great arteries. This image was reproduced from [Weizenecker et al., 2009] (doi: 10. 1088/ 0031-9155/ 54/ 5/ L01) by permission of IOP Publishing (©Institute of Physics and Engineering in Medicine, all rights reserved).*

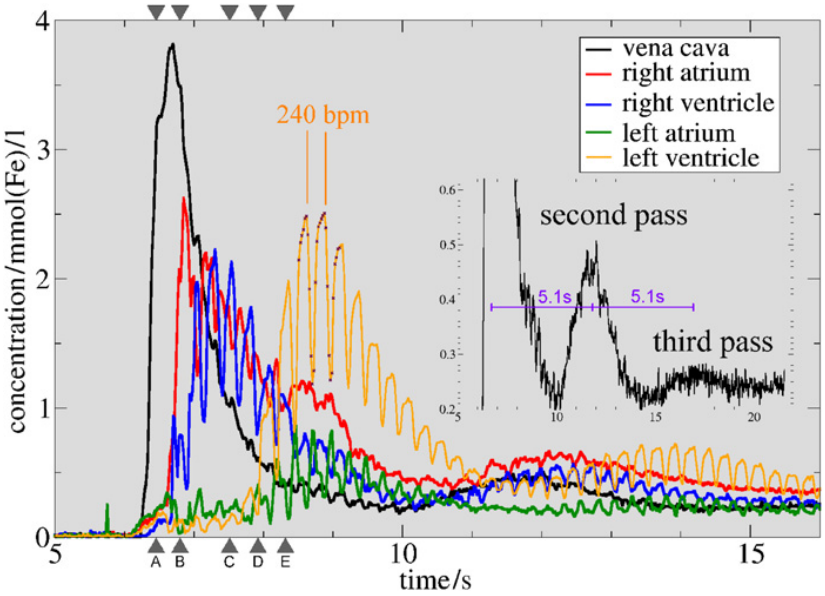

Figure 5.11: *Time intensity curves of the tracer concentration for different location of the heart. After the injection, the ferroparticles first arrived in the vena cava, before filling the right atrium and then right ventricle. A contraction behavior can be noticed, with a phase opposition between atrium and ventricle. After 1.4 s in the pulmonary circulation, the tracer comes back in the left atrium and then left ventricle. A phase opposition can be noticed again between these two chambers, while atria and ventricles are beating in phase. From the TICs can be derived a heart periodicity of 240 beats per minute. The small crosses on the curves of the left ventricle illustrate the sampling points. Eventually, the tracer makes a second and a third pass in the whole circulatory system with delays of approximately 5.1 s, with shallow concentration peaks. This image was reproduced from [Weizenecker et al., 2009] (doi: 10. 1088/ 0031-9155/ 54/ 5/ L01) by permission of IOP Publishing (©Institute of Physics and Engineering in Medicine, all rights reserved).*

5.2.2 Harmonic time-processing of cardiac dynamics

In this subsection is described the first contribution and also the starting point of this thesis which was the analysis of in-vivo data illustrated in the previous sub-section. From these first results, signal and image processing techniques were employed to reconstruct and interpret the cardiac dynamics, e.g, by calculating streamlines describing the direction of propagation of the tracer at a given moment. Given the natural periodicity of the contrast density, the idea was to extract from the TICs the narrowband frequency components around the heart frequency and its harmonics. Let $I(\mathbf{x}, t)$ be the signal intensity, for $\mathbf{x}$ covering the whole FoV, and $t \in \{0\,1800\}$ covering the whole time sequence. Then the bandpass filtered signal $\hat{S}(\mathbf{x}, t)$ can be obtained by convolution with the wavelet filter (3.7) met in section 3.2.1:

$$\hat{S}^n(\mathbf{x}, t) = \sum_{t=0}^{t_{max}} I(\mathbf{x}, \tau) w_n(t - \tau) d\tau$$

where $w_n(t) = \frac{1}{n\sigma\sqrt{2\pi}} e^{-\frac{t^2}{2(n\sigma)^2}} e^{-2j\pi n \frac{f_c}{f_s} t}$ is a complex Gabor wavelet corresponding to the n^{th} harmonic component.

Here, f_c denotes the cardiac frequency (4Hz), f_s the sampling frequency (46.51 Hz) and σ the wavelet scale. The different Gabor filters are finally summed up to recover the full filtered signal:

$$\hat{S}(\mathbf{x}, t) = \sum_n \hat{S}^n(\mathbf{x}, t) \tag{5.2}$$

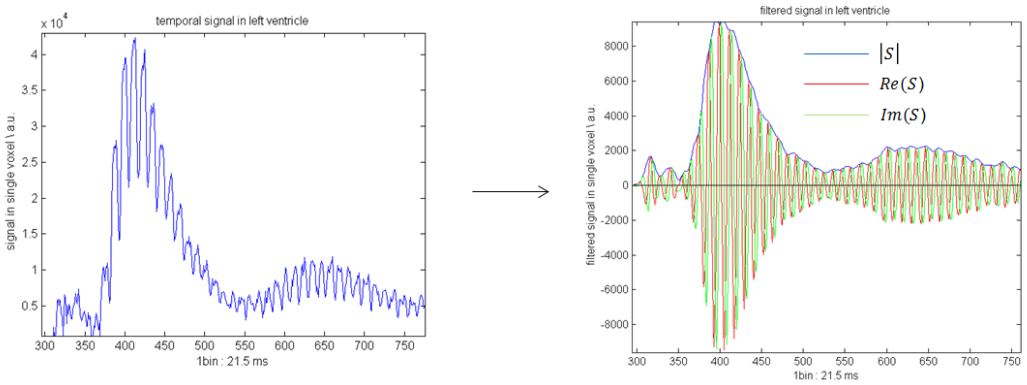

Figure 5.12: *Frequency filtering of a TIC in a pixel inside the left ventricle. The original TIC (to the left) was filtered with wavelets corresponding to the fundamental cardiac frequency and three harmonic components. The three filtered signals (to the right) corresponds to the real part (in red), the imaginary part (in green) and the instantaneous modulus (in blue). The phase of the filtered signal represents the angle between the real and imaginary part.*

This time-frequency signal processing suppresses the baseline signal and the high frequency noise while capturing the spectral components reflecting the cardiac dynamics. Most importantly, it allows to represent the signal at every point $\mathbf{x}$ of the FoV by a time dependent instantaneous phase $\phi(\mathbf{x}, t) = \arg(\hat{S}(\mathbf{x}, t))$. Analyzing the evolution of $\phi(\mathbf{x}, t)$ over one heart period amounts to observe the time elapsed since the last intensity maximum occurs at $\mathbf{x}$ (actually, elapsed time from the diastole).

One should note that this frequency filtering can be performed as well in Fourier domain by selecting narrowband components and computing the Hilbert transform $\mathcal{H}(\mathcal{F}(I))$ of the bandpassed spectrum. This returns an analytic signal after inverse Fourier transform, which is similar to the Gabor filtering:

$$\hat{S}^n(\mathbf{x}, t) = \mathcal{F}^{-1}\left[\mathcal{K}_\sigma^{fn} \mathcal{H}(\mathcal{F}(I))\right] \tag{5.3}$$

where $\mathcal{K}_\sigma^{fn}$ is a spectral gaussian kernel of scale σ and centered on harmonic component fn, and $\mathcal{F}(I)$ is the Fourier transform of I. The Hilbert transform $\mathcal{H}$ can be defined as $\mathcal{H}(\mathcal{F}(f)) = \mathcal{F}(f)(1 - jsign(f))$ (see section 3.2.2).

To avoid the so-called *bolus effect* (the signal delay caused by the slow contrast traveling), further techniques have been employed to compress and simplify the TIC into one cardiac period. Indeed, the signal envelop reaches its peaks at different time in the left or right ventricle. Because the bolus length is short compared to the circulatory system, the first pass only allows to image one half-heart at a time. For this problem to be tackled, the whole time sequence is fused into one cardiac period, which can be compared to a **gating technique**. This can easily be done by adding up all the contributions of the many heart cycles into one fundamental cardiac period:

$$\boxed{I_T(\mathbf{x},\beta) = \frac{1}{N}\sum_{p=0}^{N} \|\hat{S}\|\hat{S}(\mathbf{x},\beta + p.T)} \tag{5.4}$$

where $I_T(\mathbf{x},\beta)$ is the synthetic signal of length T, N the number of cardiac cycles in the TIC, and β the cardiac phase of the reconstructed period ($\beta \in \{0\,T\}$).

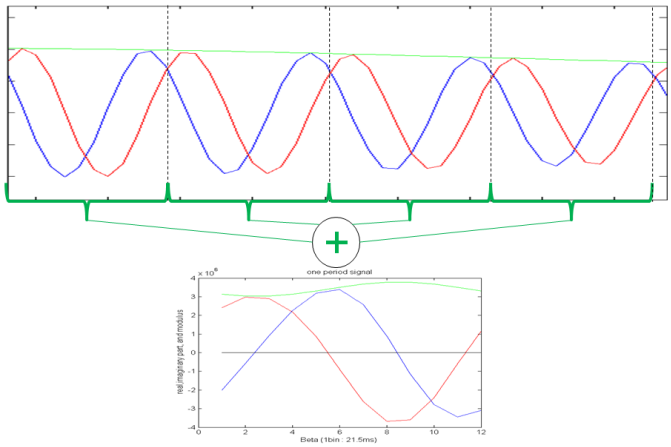

Figure 5.13: *The filtered signal $\hat{S}$ is cut in consecutive intervals of length T, before being summed phase-wise. Given the periodic behavior of the TICs, the real part (red) and imaginary part (blue) of $\hat{S}$ keep the same shape. However, the reconstructed modulus (in green) is directly computed from I_T.*

This can be visualized with a surface rendering to bring more intuition to the contrast behavior. In figure 5.14, we clearly see two iso-surfaces of I_T (the real part).

The *Fourier* compression together with gating strategy deliver a synthetic representation of the 3D+T signal over one standard heartbeat, but also allow to segment atria and ventricles, *i.e.* areas in phase opposition.

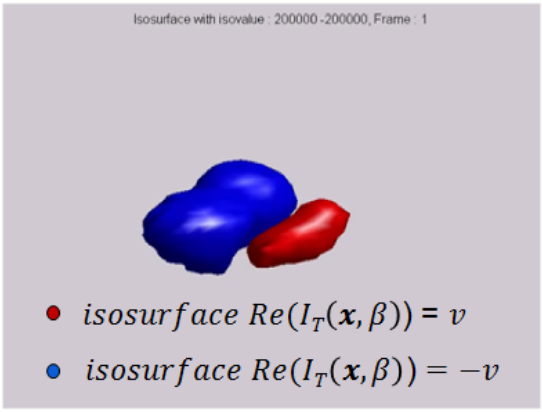

Figure 5.14: *The surface mesh corresponds to an iso-surface of I_T (real part), with a color coding. The red surface is displayed for the iso-surface value v, while the blue iso-surface corresponds to the negative iso-value $-v$. The contrast density is maximum in the atrium (red), while it is minimum in the ventricles (blue). This shows the phase opposition between atrium and ventricle signal: the ventricles are contracted and devoid of contrast, while the atria are filled and full of nanoparticles (systolic peak).*

5.2.3 Tentative flow estimation inside a mouse heart

The last step consists in extracting the nanoparticle flow and deriving the velocity of the contrast product. For this purpose, a lot of tools exist in the literature, especially on the optical flow estimation (see chapter 2). Different features are possible to track (contrast intensity, real part, imaginary part, phase,..), but the phase $\phi(\mathbf{x}, t)$ is the most relevant, since it does not depend on the intensity magnitude and its motion is explained only by the periodic contrast flow. Again, the PBOF framework (section 3.2.3) was chosen instead of the Multigrid approach (chapter 3). With the small size of the in vivo data, and the **connectivity between heart chambers**, the Multigrid technique would fail to take into account the walls between each heart chambers and smooth out the overall flow field. In this regard, **a preliminary heart chambers segmentation with larger data would be required for the Multigrid technique to work properly**.

The local PBOF estimation yielded very interesting results [Lacroix et al., 2013], with meaningful tracer streamlines beneath the heart chambers (figure 5.15).

Though these first results look very promising, it is still impossible to validate either flowlines direction and contrast velocity. Up to now, MPI lacks data, and lacks reproducibility to allow any consistent validation study. Unfortunately, the amount of exploitable in-vivo evaluation is very poor and the acquisition campaigns are progressing at a very slow rate. Other in vivo acquisitions were carried out with red blood cells (RBCs) encapsulation [Rahmer et al., 2013], but not any possibility to extract flow pattern was found. The nanoparticles were already diluted in the blood stream because of their long stay inside the circulatory system (several days), resulting in no spatial modulation. Furthermore, the limited FoV makes only possible the acquisition

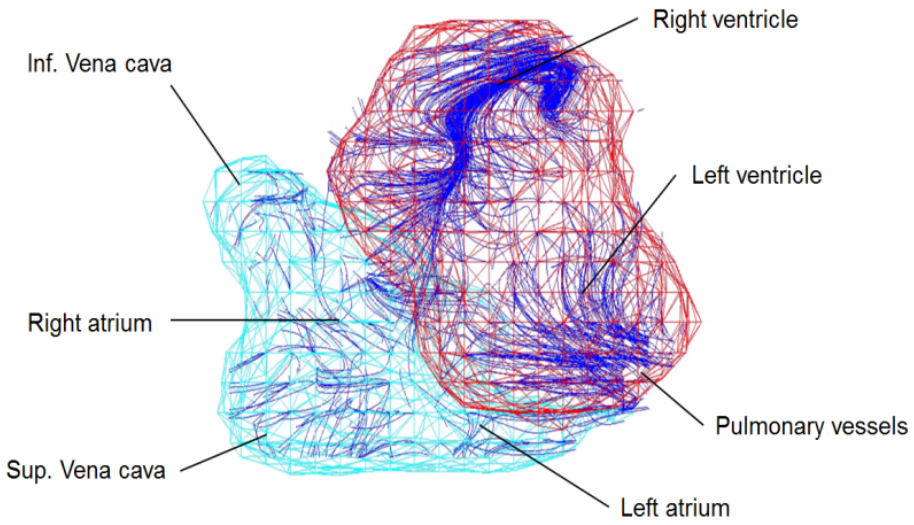

Figure 5.15: *In this picture is represented a mesh of the mouse heart. As in the figure 5.14, the red mesh corresponds to a positive iso-value of the real part, and the blue light describe the negative iso-value. Those meshes roughly represent the heart chambers wall (ventricles for the red mesh and atria for the light blue mesh). Inside these meshes can be distinguished dark blue streamlines which correspond to the tangents to the phase gradient* $\nabla\phi(\mathbf{x}, t)$*. It shows that during the diastole the contrast fills the ventricles: the nanoparticles flow from the atria and follow the volume expansion of the ventricles.*

of small anatomies such as mice heart, which hardly exceed the system resolution. As a consequence, partial volume effects and blurring hamper the analysis of current MPI data.

After further improvements of MPI hardware, experiment will be conducted on larger animals (rat, rabbits), and finally human beings. By this time, the aforementioned tools of temporal filtering and streamlines extraction might become useful to reconstruct and analyze the cardiac dynamic in clinical MPI.

*
* *

MPI is a promising tracer imaging modality combining fast 3D acquisition with fine resolution. Theoretically, it solves several issues met in angiography routines: the accessibility in Doppler US, the acquisition time in flow MRI, and the toxicity in DSA. However, its slow developing hardware is currently an obstacle to the realization of dedicated image processing tools, such as blood flow analysis algorithms. In order to investigate deeper MPI capabilities in the future, data with larger FoV and finer resolution will be desirable. Nonetheless, early experiments on in-vitro and in-vivo data brought a short overview of the potential of MPI flow data, and associated image processing tools. The modulation of contrast density in a silicon phantom proved to be a successful technique in view of a blood flow estimation. The implementation of the time signal processing described in section 3.2 with PBOF yielded a reasonable estimate of the average flow rate. The same technique applied on in-vivo data produced meaningful phase gradient streamlines, with the possibility to compress the sequence over one cardiac cycle and filter out the bolus effect. Further acquisition and flow experiment are needed to confirm the relevance and the efficiency of flow estimation tools developed during this thesis.

Conclusion

This thesis was dedicated to the blood flow estimation in 3D+T contrast sequences, as acquired by 3DRA and MPI systems. A mathematical framework for the estimation of blood flow was presented, and evaluated on in silico, in vitro and in vivo data. This conclusion summarizes the technical and clinical contributions of this thesis, and discusses potential future work.

Summary of the contributions

The technical contributions presented throughout this thesis can be enumerated as follows:

- Using the **spatiotemporal modulation of the CA** in the arterial blood flow to estimate the **velocity field of the blood** as well as the blood flow rate. This idea was already approached in few works addressing DSA image analysis, but was extended and generalized to future 3D contrast flow modalities (3DRA, MPI). Chapter 1 formulates the physical and mathematical background for contrast flow acquisition, while the theory of optical flow and related articles is presented in chapter 2.

- Developing a new variational framework for the estimation of blood flow in 3D contrast flow modalities. Based on the prior art of DSA techniques (see [Efron et al., 1978, Amimi, 1994, Imbert et al., 1997, Huang et al., 1997, Bonnefous et al., 2012]) and fluid flow estimation (see [Corpetti et al., 2000, Corpetti et al., 2002a, Corpetti et al., 2002b, Papadakis et al., 2007]), **physical constraints are brought up to the optical flow estimator**, imposing the strong pulsatility of the CA, and the compliance of the flow field with fluid mechanics. The main contribution, developed in chapter 3, lies in the use of the **conjugate gradient algorithm** [Straeter, 1971, Hestenes and Stiefel, 1952] on **the multigrid technique** [Briggs et al., 2000] **to estimate a 3D blood flow field**. In addition, new features such as **jet** and **wall** flow fidelity are integrated to the optical flow framework to further constrain the flow field.

- Evaluating the optical flow algorithm developed in chapter 3 with **virtual angiography** on several CFD models. **Accurate flow rate estimation is achieved**

at the injection point of the arterial model. The optical flow algorithm proves to be stable to different model geometry and flow rates. This contribution can be found in chapter 4.

- Demonstrating the **feasibility of flow estimation on in vitro 3D+T MPI data**. Given the very small size and FoV of the current MPI settings, only the pulsatility constraint was imposed to the optical flow estimator. Larger MPI data with bigger vessel lumen will hopefully benefit the optical flow approach developed in chapter 3. This contribution was presented in chapter 5 and presented to the MPI conference [Lacroix et al., 2014].

- **Achieving blood flow patterns in 3D+T in vivo MPI data**. The PBOF framework using only the pulsatility constraint provides meaningful results inside the heart chamber of the mouse data. Though MPI ground truths are still a missing element of flow estimation assessment, this promising contribution paves the way to **the first preclinical or clinical real time blood flow estimation methods**. This work as detailed in chapter 5 was also published in the IWMPI conference proceedings [Lacroix et al., 2013].

On the clinical side, this thesis offers the potential to acquire, estimate, and evaluate 3D blood flow patterns. A clinical routine aiming at performing a blood flow estimation should follow the steps hereafter:

- A blood flow acquisition procedure that uses a contrast agent in the arterial bloodstream, and takes benefit from the sharp blood pulsatility to obtain a spatio-temporal modulation. This acquisition procedure suits real-time tracer modalities such as MPI, DSA and 3DRA.

- An optical flow algorithm tracks the propagation of the contrast agent to assess 3D blood flow patterns and/or blood flow rate.

- A simulation tool such as a CFD software mimics the flow experiment with appropriate boundary conditions (vessel boundaries, flow rate, time intensity curves at the inlet, and other features extracted by previous acquisition tools) and finally evaluates the reliability of the optical flow estimation.

Given the small amount of data available, this thesis lacks clinical validation. However, **it provides valuable guidelines for the future MPI or 3DRA systems aiming at acquiring 3D flow data**.

Future work

Many improvements can be brought to this thesis. This research work in 3D blood flow estimation has to be upgraded, since none (to our knowledge) has addressed

this problem before. The most important questions to be answered in the future are described below.

- **Can we optimize the optical flow parameters?**

  As was pointed out in section 4.3.1, a large number of parameters intervene in the optical flow algorithm. Since only a year was dedicated in developing and testing the optical flow method, not all the possible combinations were evaluated. As a result, a thorougher investigation of parameter sensitivity should be carried out. Even if the wall fidelity, jet fidelity and smoothness factor were found the most sensitive, the frequency filter also proved to have an important effect on the optical flow results. Indeed, the low frequency and high frequency variations of the contrast density carry different information on the spatial gradients. Therefore, choosing to cut off certain frequencies will enable or disable some of the gradient patterns of the contrast product. Finally, the influence of parameters should be demonstrated on other patient geometries in order to assess the reproducibility of optical flow results with respect to the parameters.

- **Can we benefit from a temporal regularization of the flow field behavior?**

  The property of contrast pulsatility has been used for the PBOF frawework, but pulsatility is also a strong property of the blood flow. In the CFD simulations in particular, the blood flow patterns were set as periodic, an important property that can be enforced in the optical flow framework. Hence, a temporal regularization, implying temporal smoothness, or temporal periodicity is to be thought in future developments of the optical flow algorithm. This approach was tried especially in gated cardiac sequences with the assumption of motion periodicity [Li and Yang, 2010].

- **Can we bring more physics into the bloodflow estimation?**

  Undoubtedly, the physical constraints developed in chapter 3 were of great help in reducing the undesirable effects of phase gradients in the boundary layer. However, they were not sufficient to ensure the incompressibility of the blood flow field. A more radical way to deal with the fluid mechanics unfaithfulness is to use directly the *Navier-Stokes* equation in the flow estimation. This can be done in an iterative manner by coupling *Navier-Stokes* equation and the continuity equation (1.4) and is widely used in CFD solvers. As an example the SIMPLE algorithm [Caretto et al., 1973] use this algorithmic scheme to ensure the *Navier-Stokes* equation compliance and a divergence free fluid motion. The next challenge would be to integrate this CFD derived idea with the optical flow framework, while staying real-time compatible as much as possibly can. Hence, a best compromise between the *image forces* (optical flow or advection equation) and the *physical forces* (incompressibility and momentum conservation) should be sought.

- **Can we complement CFD with other simulation tools?**

  CFD is a very valuable tool for the simulation of arterial flow. Unfortunately, it does not take into account the acquisition procedure and the imperfections of the imaging systems that sometimes bring artifacts and blurring to the acquired data. This is the case especially in MPI, where blurring occurs because of the limited PSF, or because of other acquisition artifacts (see appendix B). MPI simulators already exist in MPI research facilities and could be greatly beneficial to virtual angiography. Introducing the MPI acquisition process and its imperfections to the tracer concentration map in the CFD could mainly improve the data reliability and further challenge the optical flow method with clinically compatible data.

- **Can we accurately measure the Wall Shear Stress?**

  In chapter 1, the clinical importance of Wall Shear Stress was mentioned as a strong indicator of the generation, evolution and rupture of arterial plaques and aneurysms. In chapter 3, a method for the Wall Shear Stress estimation was proposed, based on its strong relation with the velocity component normal to the wall. Early estimations were carried out during this thesis but did not provide accurate results compared to the CFD ground truth. As we explained in chapter 4, the resolution of the cartesian mesh might not be sufficient to achieve precise evaluation of the spatial gradient nearby the wall. Since Wall Shear Stress is, by essence, strongly sensitive to the spatial resolution, the cartesian grid might not be the best suited. Instead, the original tetrahedral mesh, with a reformulation of the Wall Shear Stress estimator (section 3.5) should be tested. Finally, one can also choose to investigate new flow field features, such as vorticity, turbulence, and jet, among others.

The MPI and 3DRA flow systems still have a long road before becoming clinically relevant. In the meantime, many flow estimation tools can be developed or engineered based on CFD simulation. It can be hoped that this thesis will be a starting point, and will provide a possible basis for the future researchers wishing to develop 3D blood flow estimation tools.

Publications and patents

The work done during this Ph.D. lead to the following publications and patents.

Conference papers

- R. Lacroix, J. Rahmer, J. Borgert, O. Bonnefous, S. Makram-Ebeid. "Visualization and quantification of blood flow patterns in small FoV MPI mouse scan". *Medical Imaging Philips Workshop* (MIP 2012, Suresnes - France)
- R. Lacroix, J. Rahmer, J. Borgert, O. Bonnefous, S. Makram-Ebeid. "Early results on image and signal processing for characterization of blood flow in 4D MPI images". *International Workshop on Magnetic Particle Imaging* (IWMPI 2013, Berkeley - California)
- R. Lacroix, J. Rahmer, O. Weber, H. Morales, S. Makram-Ebeid. "Flow assessment from in vitro and in silico dynamic MPI data". *International Workshop on Magnetic Particle Imaging* (IWMPI 2014, Berlin - Germany)

Patents

- S. Makram-Ebeid, O. Bonnefous, H. Morales, R. Lacroix. "Device and method for imaging of blood flow through a vascular system". *European Application 2014P00798EP, 2014.*
- R. Lacroix, S. Makram-Ebeid, R. Florent. "Corrected flow field estimation". *European Application 2014PF01673, 2015.*

AppendixA

This appendix details several calculus evoked throughout this thesis.

Underdetermination of the complex optical flow system

Recall the the complex optical flow equation (3.18) met in section 3.2.2:

$$\begin{cases} \nabla S(\mathbf{x},t)\cdot\mathbf{v} + \frac{\partial S(\mathbf{x},t)}{\partial t} = 0 \\ \nabla Q(\mathbf{x},t)\cdot\mathbf{v} + \frac{\partial Q(\mathbf{x},t)}{\partial t} = 0 \end{cases}$$

We can rewrite the complex quantities according to $S = real(\hat{S}) = M\cos(\phi)$ and $Q = imag(\hat{S}) = M\sin(\phi)$. We can approximate the modulus M of the complex signal $\hat{S}$ as constant (or we use the normalized version $\hat{S}_n$). Using the previous system in a matrix form, we get:

$$M\begin{pmatrix} -\phi_x\sin(\phi) & -\phi_y\sin(\phi) & -\phi_z\sin(\phi) \\ \phi_x\cos(\phi) & \phi_y\cos(\phi) & \phi_z\cos(\phi) \end{pmatrix}\begin{pmatrix} v_x \\ v_y \\ v_z \end{pmatrix} = -M\phi_t\begin{pmatrix} -\sin(\phi) \\ \cos(\phi) \end{pmatrix}$$

which can be rewritten with a rotation matrix:

$$\begin{pmatrix} -\sin(\phi) & -\cos(\phi) \\ \cos(\phi) & -\sin(\phi) \end{pmatrix}\begin{pmatrix} \phi_x & \phi_y & \phi_z \\ 0 & 0 & 0 \end{pmatrix}\begin{pmatrix} v_x \\ v_y \\ v_z \end{pmatrix} = -\phi_t\begin{pmatrix} -\sin(\phi) & -\cos(\phi) \\ \cos(\phi) & -\sin(\phi) \end{pmatrix}\begin{pmatrix} 1 \\ 0 \end{pmatrix}$$

Which turns to the simple Phase Based Optical Flow constraint:

$$\nabla\phi\cdot\mathbf{v} = -\frac{\partial\phi}{\partial t}$$

Here we notice that the previous complex optical flow system is actually one equation rewritten as a system and pre-multiplied by rotation matrix $R(\phi + \frac{\pi}{2})$ with $R = \begin{pmatrix} \cos(\phi) & -\sin(\phi) \\ \sin(\phi) & \cos(\phi) \end{pmatrix}$. Therefore, we prove that complex optical flow system is underdetermined.

Equivalence between PBOF and normalized optical flow equation

The energy of complex optical flow (section 3.2.2) is:

$$E_{\mathbf{v}}(\mathbf{x}) = (\nabla \hat{S}_n(\mathbf{x},t)\cdot\mathbf{v} + \frac{\partial \hat{S}_n(\mathbf{x},t)}{\partial t})(\nabla \hat{S}_n(\mathbf{x},t)\cdot\mathbf{v} + \frac{\partial \hat{S}_n(\mathbf{x},t)}{\partial t})^*$$

With $\hat{S}_n = \cos(\phi) + j\sin(\phi)$, it comes:

$$\begin{aligned} E_{\mathbf{v}}(\mathbf{x}) = {} & \mathbf{v}^T\nabla(\cos(\phi)+j\sin(\phi))\nabla(\cos(\phi)-j\sin(\phi))^T\mathbf{v} + \\ & \frac{\partial(\cos(\phi)+j\sin(\phi))}{\partial t}\nabla(\cos(\phi)-j\sin(\phi)) + \frac{\partial(\cos(\phi)-j\sin(\phi))}{\partial t}\nabla(\cos(\phi)+j\sin(\phi)) + \\ & \underline{\frac{\partial(\cos(\phi)+j\sin(\phi))}{\partial t}}\,\underline{\frac{\partial(\cos(\phi)-j\sin(\phi))}{\partial t}} \end{aligned}$$

That is:

$$\begin{aligned} E_{\mathbf{v}}(\mathbf{x}) &= (-\sin(\phi)+j\cos(\phi))(\mathbf{v}^T\nabla\phi^T\nabla\phi\mathbf{v} + 2\nabla\phi\frac{\partial\phi}{\partial t} + \frac{\partial\phi}{\partial t}^2)(-\sin(\phi)-j\cos(\phi)) \\ &= \mathbf{v}^T\nabla\phi^T\nabla\phi\mathbf{v} + 2\frac{\partial\phi}{\partial t}\nabla\phi + \frac{\partial\phi}{\partial t}^2 \\ &= (\mathbf{v}^T\cdot\nabla\phi + \frac{\partial\phi}{\partial t})^2 \end{aligned}$$

Here we see that the normalized complex optical flow equation is equivalent to the PBOF and can be implemented in the same way.

Gradient equation for the energy minimization

Recall the global flow field energy (3.35) described in section 3.3.1:

$$E(\mathbf{v}(\mathbf{x},t)) = \int_\Omega \left[(\nabla\phi\cdot\mathbf{v} + \frac{\partial\phi}{\partial t})^2 + \mu\|\nabla\mathbf{v}\|_F^2 + \lambda(\nabla\cdot\mathbf{v})^2 + \nu B(\mathbf{n}^T\cdot\mathbf{v})^2\right] d\Omega$$

The first and last term can be easily derived with respect to $\mathbf{v}$ as a quadratic function of $\mathbf{v}$ itself:

$$\frac{\partial((\nabla\phi\cdot\mathbf{v} + \frac{\partial\phi}{\partial t})^2 + \nu B(\mathbf{n}^T\cdot\mathbf{v})^2)}{\partial\mathbf{v}} = 2(M + \nu B\mathbf{n}\mathbf{n}^T)\mathbf{v} - 2\mathbf{b}$$

with M, B and $\mathbf{b}$ defined in the corresponding section.

Concerning the differential term, however, the derivation is not straightforward. Let us develop the gradient equation for each term, respectively $\mu\|\nabla\mathbf{v}\|^2$ and $\lambda(\nabla\cdot\mathbf{v})^2$.

- *Dirichlet* energy variations: $J(\mathbf{v}) = \int_\Omega \sum_{i=1}^3\sum_{j=1}^3(\frac{\partial v_i}{\partial x_j})^2$

Let $\mathbf{v} \to \mathbf{v}+\mathbf{u}$ be a small variation of flow field $\mathbf{v}$ with $\mathbf{u}$ small. The corresponding *Dirichlet* energy reads:

$$J(\mathbf{v}+\mathbf{u}) = \int_\Omega \|\nabla(\mathbf{v}+\mathbf{u})\|^2 = \int_\Omega \sum_{i=1}^{3}\sum_{j=1}^{3} (\frac{\partial v_i}{\partial x_j})^2 + 2\frac{\partial v_i}{\partial x_j}\frac{\partial u_i}{\partial x_j} + (\frac{\partial u_i}{\partial x_j})^2$$

Note that $\frac{\partial v_i}{\partial x_j}\frac{\partial u_i}{\partial x_j} = \frac{\partial}{\partial x_j}(v_i\frac{\partial u_i}{\partial x_j}) - v_i\frac{\partial^2 u_i}{\partial x_j^2}$, integrating by parts and imposing $\mathbf{u}=0$ on the domain edges $\partial\Omega$. We get then:

$$J(\mathbf{v}+\mathbf{u}) = \int_\Omega \|\nabla\mathbf{v}\|^2 - 2\mathbf{u}\cdot\Delta\mathbf{v} + \|\nabla\mathbf{u}\|^2$$

First variation of J is defined by the *Gâteaux derivative* in the direction of $\mathbf{u}$:

$$\delta J(\mathbf{v},\mathbf{u}) = lim_{\tau\to 0}\frac{J(\mathbf{v}+\tau\mathbf{u}) - J(\mathbf{v})}{\tau} = -2\int_\Omega \mathbf{u}\cdot\Delta\mathbf{v}$$

Hence, the *Euler-Lagrange* gradient equation can be obtained when J is an extremum for the vector field $\mathbf{v}$ and for any $\mathbf{u}$:

$$\frac{\partial J}{\partial \mathbf{u}} = -2\int_\Omega \Delta\mathbf{v}$$

- Divergence square energy: $J(\mathbf{v}) = \int_\Omega (\nabla\cdot\mathbf{v})^2$

Let $\mathbf{v} \to \mathbf{v}+\mathbf{u}$ be a small variation of flow field $\mathbf{v}$ with $\mathbf{u}$ small. The corresponding divergence energy reads:

$$J(\mathbf{v}+\mathbf{u}) = \int_\Omega (\nabla\cdot\mathbf{v})^2 + 2(\nabla\cdot\mathbf{v})(\nabla\cdot\mathbf{u}) + (\nabla\cdot\mathbf{u})^2 \tag{5}$$

Note that $(\nabla\cdot\mathbf{v})\frac{\partial u_i}{\partial x_j} = \frac{\partial(\nabla\cdot\mathbf{v})u_i}{\partial x_i} - v_i\frac{\partial(\nabla\cdot\mathbf{v})}{\partial x_i}$, integrating by parts and imposing $\mathbf{u}=0$ on the domain edges $\partial\Omega$. We get then:

$$J(\mathbf{v}+\mathbf{u}) = \int_\Omega (\nabla\cdot\mathbf{v})^2 - 2\mathbf{u}\cdot\nabla(\nabla\cdot\mathbf{v}) + (\nabla\cdot\mathbf{u})^2$$

First variation of J is defined by the *Gâteaux derivative* in the direction of $\mathbf{u}$:

$$\delta J(\mathbf{v},\mathbf{u}) = lim_{\tau\to 0}\frac{J(\mathbf{v}+\tau\mathbf{u}) - J(\mathbf{v})}{\tau} = -2\int_\Omega \mathbf{u}\cdot\nabla(\nabla\cdot\mathbf{v})$$

Hence, the *Euler-Lagrange* gradient equation can be obtained when J is an extremum for the vector field $\mathbf{v}$ and for any $\mathbf{u}$:

$$\frac{\partial J}{\partial \mathbf{u}} = -2\int_\Omega \nabla(\nabla\cdot\mathbf{v})$$

As a consequence, the overall gradient equation developed in chapter 3 reads:

$$\int_{\Omega} \left[(M + \nu \mathbf{n}\mathbf{n}^T)\mathbf{v} - \mu \Delta \mathbf{v} - \lambda \nabla (\nabla \cdot \mathbf{v}) \right] d\Omega = \int_{\Omega} \mathbf{b} d\Omega \tag{6}$$

AppendixB

This Appendix presents further details about MPI acquisition, MPI encoding, but also the MPI scanner set up.

General MPI background

MPI is a novel imaging modality that uses the non-linear magnetization of SPIO injected into the body. The physics differs substantially from MRI, but it employs hardware and imaging concepts that are familiar to MRI researchers: magnetic excitation and detection, pulse sequences, relaxation effects and reciprocity principle [Saritas et al., 2013]. One compelling reason for MRI specialists to delve into Magnetic Particle Imaging is the *enormous* boost of magnetization. The nuclear paramagnetic susceptibility of water in MRI is only 3.8 parts-per-billon at 37 °C [John, 1996], which translates to a weak NMR magnetization ($\mu_0 M_0 = 27$nT at 7T). The magnetization detected by MPI at 7T -which is electronic superparamagnetism- can reach about 600mT in intensity [R., 1985], that is 22 millions time stronger than MRI. This enormous boost in magnetization enables MPI to compete with MRI angiograms, even when using kidney-safe tracers at extremely low concentration, with an excellent contrast-to-noise ratio.

MPI acquisition

In MPI, the method of acquisition is rather different from MRI. A sensitive point is rapidly rastered across the sample to produce a tomographic image. To produce the sensitive point, called *Field Free Point* (FFP), MPI takes advantage of the nonlinear magnetization response of SPIOs to applied magnetic field. As shown in figure 16, the magnetization of SPIOs is nonlinear with the applied field and converges to saturation above a certain threshold. Hence, in the presence of a strong magnetic field gradient, the SPIOs are considered to be saturated at every point except for at the FFP, where the magnetic field nullifies geometrically. When we apply a time-varying excitation field, the FFP is shifted rapidly across the Field-of-View (FoV). The SPIOs lying within the FFP respond to this rapid change in magnetic field by flipping their magnetization 180°, whereas particles elsewhere remain saturated. Since the receiver coil detects time-varying magnetization, only the SPIOs at the FFP produce an induced MPI signal.

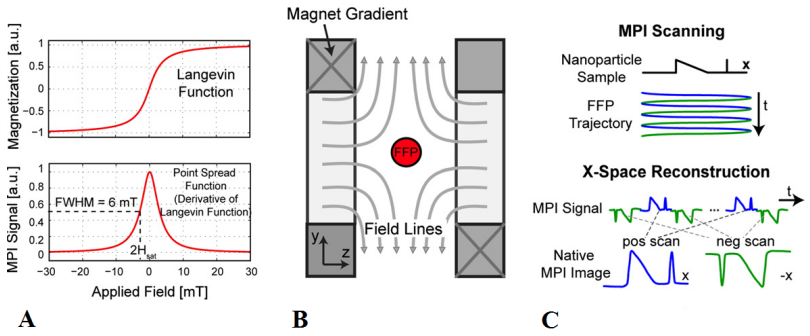

Figure 16: *A. SPIO magnetization characterized by a Langevin function, is non linear with applied magnetic field with a saturation behavior. This non linear magnetization response determines the PSF in MPI. For a 6T/m gradient field, the Full Width at Half Maximum (FWHM) corresponds to 1 mm resolution. B. Two permanents magnets create a strong magnetic gradient field and a sensitive point, the FFP. Only the SPIOs in the instantaneous location of the FFP create a MPI signal. C. To cover the imaging field of view, the FFP is moved rapidly in a trajectory across the imaged volume. The MPI signal is grided to the instantaneous position of the FFP to form a native MPI image. Reprinted from [Saritas et al., 2013], with permission from Elsevier (*`doi:10.1016/j.jmr.2012.11.029`*).*

X-space encoding

2D (or 3D) image encoding can be achieved with a very fast acquisition rate. By sweeping the FFP over the FoV in a 2D or 3D dense Lissajous trajectory, one can relate the time intensity curve of the induced signal to the position where a particle was magnetized. This is the basic principle of x-space encoding [Goodwill and Conolly, 2011, W and M, 2010, Lu et al., 2013], illustrated in figure 17.

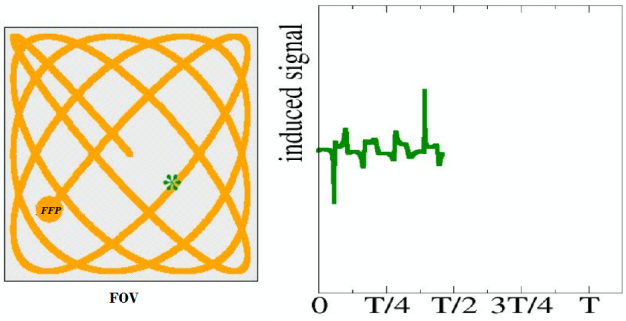

Figure 17: *FFP (yellow circle) following a 2D Lissajous trajectory, enables a fast encoding of the nanoparticle concentration (a single particle represented here by a green star) inside the FoV. The intensity of the induced voltage is directly proportional to the nanoparticle concentration at the corresponding FFP position. Outside a range delimited by the PSF, the induced signals of the other particles are negligible.*

The induced signal is gathered inside two or three pairs of receive coils, before being filtered and converted numerically. Just as MRI, one of the foremost issue is the suppression of the direct feedthrough produced by the magnetic excitation. The

particles get magnetized periodically by the FFP, but their signal is embedded in the powerful excitation induced signal. Fortunately, SPIOs do not only generate a voltage in the narrowband fundamental excitation frequency. Thanks to their non linear behavior described in figure 18, the inducted magnetization curve holds harmonic components. After performing a Fourier transform on the temporal signal, one can distinguish clearly the presence of several peaks in the spectral Fourier density. Those harmonics are the fingerprints of SPIOs in MPI acquisition.

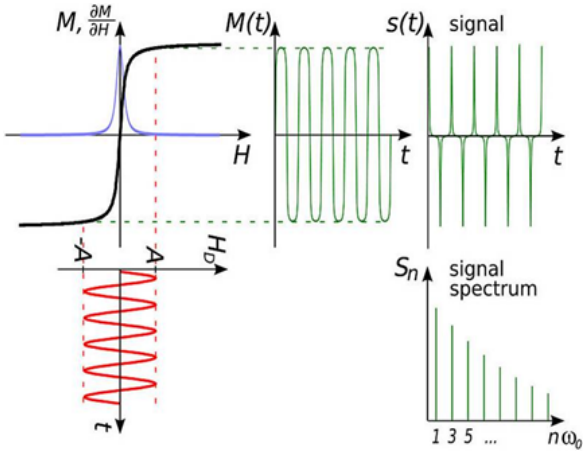

Figure 18: *The nanoparticles subject to a magnetic field respond non linearly to a periodic excitation $H_D(t)$. The Langevin function $M(H_D)$ describes how the particle magnetization gets saturated when the excitation field amplitude increases. When it is sufficiently high, the magnetization stands out of its linear range, and starts to generate harmonic components to the fundamental excitation frequency. This can be visualized in the time-magnetization curve $M(t)$ where the shape of the signal drifts from a perfect sine. The induced signal $s(t)$, which is the magnetization time-derivative holds harmonic components that can be revealed when looking at its Fourier Transform S_n.*

Spectral encoding

The spectrum of the time-induction MPI signal can be exploited for another important class of MPI image reconstruction method called spectro-spatial reconstruction or *system matrix* reconstruction. In this framework, the Fourier transform $\mathbf{S_n}$ can map a concentration vector image, by using a linear relationship between every frequency component of the spectral domain, and every pixel of the image domain [Lampe et al., 2012]. In practice, a tedious calibration step is performed by measuring the spectral answer of a tracer sample in each single voxel position. A robot moves the sample gradually in a 3D grid covering the whole FoV. This is a very long process (several hours), but eventually yields a permanent setting of the MPI reconstruction scheme. This produces a so-called *system matrix*, or *system function* $\mathcal{S}_f$ that maps the MPI frequency vector $\mathbf{S_n}$ to the concentration vector C:

$$\mathcal{S}_f \mathbf{C} = \mathbf{S_n} \tag{7}$$

The huge size of the *system matrix* makes the problem not so easy to solve. For the system to be inverted, a regularized LMSE is minimized:

$$\boxed{\mathbf{C}^* = \|\mathbf{S_n} - \mathcal{S}_f \mathbf{C}\|^2 + \|\mathbf{C}\|^2} \tag{8}$$

During this thesis, images were only reconstructed with system matrices. This reconstruction approach is not the fastest (especially for the calibration part), but up to now, the results in term of image quality (SNR) and resolution outperform the other reconstruction methods (especially x-space imaging).

MPI scanner

The figure 19 schematically shows the basic setup of the 3D scanner. The scanner has an effective bore size of 32 mm. A pair of permanent magnets and a pair of coils produce the selection field gradient. The permanent magnets contribute $3\,T\mu_0^{-1}m^{-1}$ and the coils $2.5\,T\mu_0^{-1}m^{-1}$ to the magnetic field gradient, respectively. The scanner uses three sets of drive field coils to enable 3D imaging. The drive field H_D with an amplitude of $18\,mT\mu_0^{-1}$ in the vertical direction is produced by the selection field coils. The drive fields in the two orthogonal directions are produced by dedicated coils which are driven at the same amplitude. Three drive field frequencies are chosen to move the FFP along a 3D Lissajous trajectory. The frequencies for the three directions are 25.25 kHz, 26.04 kHz and 24.51 Hz, respectively. The Lissajous trajectory has a repetition time of 21.5 ms, corresponding to encoding 46.42 volumes per second, and covers a volume of about $20.4 * 12 * 16.8\,mm^3$. Two saddle-type receive coil pairs are aligned approximately perpendicular to the bore. In the axial direction, the solenoid drive field coil is also used for receiving the signal. The voxel size is independent from the true resolution, which is determined by the particle properties, selection field gradient strength and the level of regularization used in image reconstruction. Furthermore, the image resolution and SNR is not completely homogeneous over the entire FoV, because the FFP speed is lower at the edges of the FoV, thereby stimulating only a weaker particle response and leading to a signal fade-out at the rim.

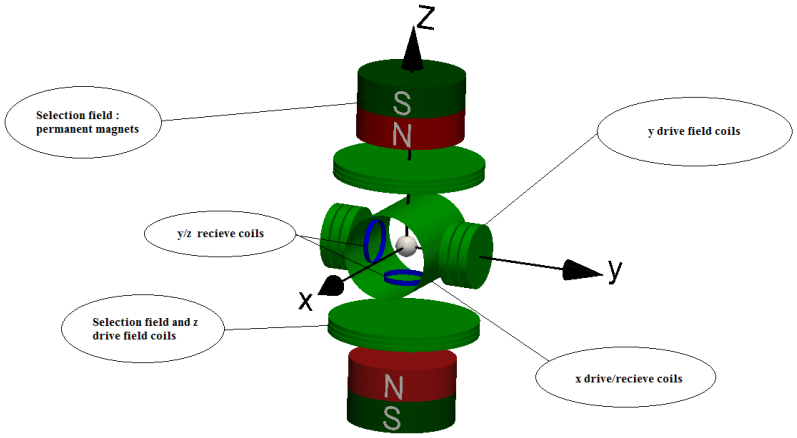

Figure 19: *Schematic scanner setup. For the in vivo experiment, the mouse was inserted into the x drive/receive coil cylinder using an animal support. The bore diameter is 32 mm. The selection field is generated by both the permanent magnets and the coil pair in the z direction. The drive field coils can move the FFP in all three spatial directions. For signal reception, each spatial component of the magnetization is detected by a respective receive coil. In the x direction, the drive field coil is also used for signal reception.*

Bibliography

[Wei, 2001] (2001). Variational optic flow computation with a spatio-temporal smoothness constraint. *Journal of Mathematical Imaging and Vision*, 14(3):245–255.

[Raj, 2013] (2013). The vascular endothelium and human diseases.

[AHA, 2014] AHA (2014). Atherosclerosis.

[Aires et al., 2008] Aires, K. R. T., Santana, A. M., and Medeiros, A. A. D. (2008). Optical flow using color information: preliminary results. *Proceedings of the 2008 ACM symposium on Applied computing*, pages 1607–1611.

[Alvarez et al., 1999] Alvarez, L., Esclarin, J., Lefebure, M., and Sanchez, J. (1999). A PDE for computing optical flow. In *CEDYA XVI*.

[Amimi, 1994] Amimi, A. A. (1994). Computational techniques for determining non-rigid motion of blood from medical images. In *Medical Imaging 1994*, pages 403–412. International Society for Optics and Photonics.

[Anandan, 1989] Anandan, P. (1989). A computational framework and an algorithm for the measurement of visual motion. *International Journal of Computer Vision*, 2(3):283–310.

[AP Dhawan, 2008] AP Dhawan, HK Huang, D. K. (2008). *Principles and advanced methods in medical imaging and image analysis*. World Scientific.

[Aubert et al., 1999] Aubert, G., Deriche, R., and Kornprobst, P. (1999). Computing Optical Flow via Variational Techniques.

[Barnard and Thompson, 1980] Barnard, S. T. and Thompson, W. B. (1980). Disparity analysis of images. *IEEE transactions on pattern analysis and machine intelligence*, 2(4):333–340.

[Barron et al., 1994] Barron, J. L., Fleet, D. J., and Beauchemin, S. S. (1994). Performance of optical flow techniques. *International Journal of Computer Vision*, 12(1):43–77.

[Beauchemin and Barron, 1995] Beauchemin, S. S. and Barron, J. L. (1995). The computation of optical flow.

[Beaudet, 1978] Beaudet, P. R. (1978). Rotationally invariant image operators. In *Proceedings of the 4th International Joint Conference on Pattern Recognition*, pages 579–583.

[Benz et al., 2014] Benz, T., Kowarschik, M., Endres, J., Maday, P., Redel, T., and Navab, N. (2014). *XIII Mediterranean Conference on Medical and Biological Engineering and Computing 2013*, volume 41 of *IFMBE Proceedings*. Springer International Publishing.

[Berg et al., 2014] Berg, P., Baumgarten, K., Geist, S., Stucht, D., and Speck, O. (2014). RELATIVE PRESSURE FIELD COMPUTATION IN HUMAN ARTERIES BASED ON 4D PC-MRI VELOCITIES. In *ISBI 2014*, pages 417–420.

[Bertero et al., 1988] Bertero, M., Poggio, T., and Torre, V. (1988). Ill-posed problems in early vision.

[Bigun et al., 1991] Bigun, J., Granlund, G., and Wiklund, J. (1991). Multidimensional orientation estimation with applications to texture analysis and optical flow. *Pattern Analysis and ...*, 13(8):775 – 790.

[Bigun and Granlund, 1988] Bigun, J. and Granlund, G. H. (1988). Optical flow based on the inertia matrix of the frequency domain. In *Proceedings from SSAB Symposium on Picture Processing: Lund University, Sweden*, pages 132–135.

[Black and Anandan, 1991] Black, M. and Anandan, P. (1991). Robust dynamic motion estimation over time. *Proceedings. 1991 IEEE Computer Society Conference on Computer Vision and Pattern Recognition.*

[Black and Anandan, 1996] Black, M. J. and Anandan, P. (1996). The Robust Estimation of Multiple Motions: Parametric and Piecewise-Smooth Flow Fields. *Computer Vision and Image Understanding*, 63(1):75–104.

[Bock et al., 2010] Bock, J., Frydrychowicz, A., Stalder, A. F., Bley, T. A., Burkhardt, H., Hennig, J., and Markl, M. (2010). 4D phase contrast MRI at 3 T: Effect of standard and blood-pool contrast agents on SNR, PC-MRA, and blood flow visualization. *Magnetic Resonance in Medicine*, 63(2):330–338.

[Bogunović and Loncarić, 2006] Bogunović, H. and Loncarić, S. (2006). Blood flow and velocity estimation based on vessel transit time by combining 2D and 3D X-ray angiography. *Medical image computing and computer-assisted intervention : MICCAI ... International Conference on Medical Image Computing and Computer-Assisted Intervention*, 9(Pt 2):117–124.

[Bonnefous, 2001] Bonnefous, O. (2001). Blood flow and tissue motion with ultrasound for vascular applications. *Comptes Rendus de l'Academie des Sciences - Series IV: Physics, Astrophysics*, 2(8):1161–1178.

[Bonnefous et al., 2012] Bonnefous, O., Pereira, V. M., Ouared, R., Brina, O., Aerts, H., Hermans, R., van Nijnatten, F., Stawiaski, J., and Ruijters, D. (2012). Quantification of arterial flow using digital subtraction angiography.

[Brandt and Livne, 2011] Brandt, A. and Livne, O. E. (2011). *Multigrid techniques: 1984 guide with applications to fluid dynamics*, volume 67. SIAM.

[Briggs, 1987] Briggs, W. L. (1987). Multigrid Tutorial By. *Solutions*, 3(3):78.

[Briggs et al., 2000] Briggs, W. L., Henson, V. E., and McCormick, S. F. (2000). *A Multigrid Tutorial*, volume 37 of *Miscellaneous Bks*. SIAM.

[Brisman et al., 2006] Brisman, J. L., Song, J. K., and Newell, D. W. (2006). Cerebral aneurysms. *The New England journal of medicine*, 355(9):928–939.

[Bruhn et al., 2005] Bruhn, A., Weickert, J., and Schnörr, C. (2005). Lucas/Kanade meets Horn/Schunck: Combining local and global optic flow methods. *International Journal of Computer Vision*, 61(3):1–21.

[Bulthoff et al., 1989] Bulthoff, H., Little, J., and Poggio, T. (1989). A parallel algorithm for real-time computation of optical flow. *Nature*, 337(6207):549–555.

[Burger and Bhanu, 1990] Burger, W. and Bhanu, B. (1990). Estimating 3-D egomotion from perspective image sequences. *IEEE Transactions on Pattern Analysis and Machine Intelligence*, 12(11):1040–1058.

[Bürsch et al., 1981] Bürsch, J., Hahne, H. J., Brennecke, R., Grönemeier, D., and Heintzen, P. H. (1981). Assessment of arterial blood flow measurements by digital angiography. *Radiology*, 141(1):39–47.

[Buzug et al., 2012] Buzug, T. M., Bringout, G., Erbe, M., Gräfe, K., Graeser, M., Grüttner, M., Halkola, A., Sattel, T. F., Tenner, W., Wojtczyk, H., Haegele, J., Vogt, F. M., Barkhausen, J., and Lüdtke-Buzug, K. (2012). Magnetic Particle Imaging: Introduction to imaging and hardware realization. *Zeitschrift fur Medizinische Physik*, 22(4):323–334.

[Caretto et al., 1973] Caretto, L., Gosman, A., Patankar, S., and Spalding, D. (1973). Two calculation procedures for steady, three-dimensional flows with recirculation. In *Proceedings of the third international conference on numerical methods in fluid mechanics*, pages 60–68. Springer.

[Cebral et al., 2008] Cebral, J., Castro, M., Putman, C., and Alperin, N. (2008). Flow–area relationship in internal carotid and vertebral arteries. *Physiological measurement*, 29(5):585.

[Cebral et al., 2005] Cebral, J. R., Castro, M. A., Appanaboyina, S., Putman, C. M., Millan, D., and Frangi, A. F. (2005). Efficient pipeline for image-based patient-specific analysis of cerebral aneurysm hemodynamics: technique and sensitivity. *Medical Imaging, IEEE Transactions on*, 24(4):457–467.

[Cebral et al., 2009] Cebral, J. R., Hendrickson, S., and Putman, C. M. (2009). Hemodynamics in a lethal basilar artery aneurysm just before its rupture. *AJNR. American journal of neuroradiology*, 30(1):95–8.

[Cebral et al., 2011] Cebral, J. R., Mut, F., Weir, J., and Putman, C. M. (2011). Association of hemodynamic characteristics and cerebral aneurysm rupture. *AJNR. American journal of neuroradiology*, 32(2):264–70.

[Cito et al., 2013] Cito, S., Mazzeo, M. D., and Badimon, L. (2013). A review of macroscopic thrombus modeling methods. *Thrombosis research*, 131(2):116–24.

[Cohen, 1993] Cohen, I. (1993). Nonlinear Variational Method for Optical Flow Computation. In *Proc. SCIA*, pages 523–530.

[Conti et al., 2011] Conti, A., Pontoriero, A., Farag, G., Midili, F., Siragusa, C., Granata, F., Pitrone, A., De Renzis, C., Longo, M., and Tomasello, F. (2011). Integration of three-dimensional rotational angiography in radiosurgical treatment planning of cerebral arteriovenous malformations. *International Journal of Radiation Oncology Biology Physics*, 81(3).

[Corpetti et al., 2005] Corpetti, T., Heitz, D., Arroyo, G., Mémin, E., and Santa-Cruz, a. (2005). Fluid experimental flow estimation based on an optical-flow scheme. *Experiments in Fluids*, 40(1):80–97.

[Corpetti et al., 2000] Corpetti, T., Mémin, E., and Pérez, P. (2000). Estimating fluid optical flow. In *Pattern Recognition, 2000. Proceedings. 15th International Conference on*, volume 3, pages 1033–1036. IEEE.

[Corpetti et al., 2002a] Corpetti, T., Mémin, É., and Pérez, P. (2002a). Dense estimation of fluid flows. *Pattern Analysis and Machine Intelligence, IEEE Transactions on*, 24(3):365–380.

[Corpetti et al., 2002b] Corpetti, T., Mémin, É., and Pérez, P. (2002b). Dense motion analysis in fluid imagery. In *Computer Vision—ECCV 2002*, pages 676–691. Springer.

[Dolan et al., 2012] Dolan, J. M., Kolega, J., and Meng, H. (2012). High Wall Shear Stress and Spatial Gradients in Vascular Pathology: A Review. *Annals of Biomedical Engineering*.

[Dolan et al., 2011] Dolan, J. M., Meng, H., Singh, S., Paluch, R., and Kolega, J. (2011). High fluid shear stress and spatial shear stress gradients affect endothelial proliferation, survival, and alignment. *Annals of Biomedical Engineering*, 39(6):1620–31.

[Doriot et al., 1997] Doriot, P.-A., Dorsaz, P.-A., Dorsaz, L., and Rutishauser, W. (1997). Is the indicator dilution theory really the adequate base of many blood flow measurement techniques? *Medical physics*, 24(12):1889–1898.

[Dorsaz et al., 1997] Dorsaz, P.-A., Doriot, P.-A., Dorsaz, L., Chatelain, P., and Rutishauser, W. (1997). A new densitometric approach to the assessment of mean coronary flow. *Investigative radiology*, 32(4):198–204.

[Doshi and Bors,] Doshi, A. and Bors, A. G. Navier-stokes formulation for modelling turbulent optical flow.

[Doshi and Bors, 2010] Doshi, A. and Bors, A. G. (2010). Robust processing of optical flow of fluids. *IEEE Transactions on Image Processing*, 19(9):2332–2344.

[Dreschler and Nagel, 1982] Dreschler, L. and Nagel, H.-H. (1982). Volumetric model and 3d trajectory of a moving car derived from monocular tv frame sequences of a street scene. *Computer Graphics and Image Processing*, 20(3):199–228.

[Dumoulin, 1995] Dumoulin, C. L. (1995). Phase contrast MR angiography techniques. *Magnetic resonance imaging clinics of North America*, 3(3):399–411.

[Duschka et al., 2013] Duschka, R. L., Haegele, J., Panagiotopoulos, N., Wojtczyk, H., Barkhausen, J., Vogt, F. M., Buzug, T. M., and Lüdtke-Buzug, K. (2013). Fundamentals and Potential of Magnetic Particle Imaging. *Current Cardiovascular Imaging Reports*.

[Dyverfeldt, 2010] Dyverfeldt, P. (2010). *Extending MRI to the Quantification of Turbulence Intensity*. Number 1297.

[Ebbers and Farnebäck, 2009] Ebbers, T. and Farnebäck, G. (2009). Improving computation of cardiovascular relative pressure fields from velocity MRI. *Journal of magnetic resonance imaging : JMRI*, 30(1):54–61.

[Efron et al., 1978] Efron, U., Price, R., Smith, C., and Brill, A. (1978). A method to determine the instantaneous blood-flow using cine-or video-densitometric data. In *1978 Technical Symposium East*, pages 154–161. International Society for Optics and Photonics.

[Ersahin et al., 1995] Ersahin, A., Molloi, S. Y., and Hicks, J. W. (1995). Absolute phasic blood row measurement in the brain using digital subtraction angiography. *Investigative radiology*, 30(4):244–253.

[Evans et al., 2011] Evans, D. H., Jensen, J. r. A., and Nielsen, M. B. (2011). Ultrasonic colour Doppler imaging. *Interface focus*, 1(4):490–502.

[Firmin et al.,] Firmin, D. N., Nayler, G. L., Kilner, P. J., and Longmore, D. B. *Magnetic resonance in medicine : official journal of the Society of Magnetic Resonance in Medicine / Society of Magnetic Resonance in Medicine*, (2):230–241.

[Fleet and Jepson, 1990] Fleet, D. J. and Jepson, A. D. (1990). Computation of component image velocity from local phase information. *International Journal of Computer Vision*, 5(1):77–104.

[Galvin et al., 1998] Galvin, B., McCane, B., Novins, K., Mason, D., and Mills, S. (1998). Recovering Motion Fields: An Evaluation of Eight Optical Flow Algorithms. *Procedings of the British Machine Vision Conference 1998*, pages 20.1–20.10.

[Gao et al., 2008] Gao, L., Hoi, Y., Swartz, D. D., Kolega, J., Siddiqui, A., and Meng, H. (2008). Nascent aneurysm formation at the basilar terminus induced by hemodynamics. *Stroke; a journal of cerebral circulation*, 39(7):2085–90.

[Geers et al., 2011] Geers, A. J., Larrabide, I., Radaelli, A. G., Bogunović, H., Kim, M., Gratama van Andel, H. A. F., Majoie, C. B. L. M., VanBavel, E., and Frangi, A. F. (2011). Patient-specific computational hemodynamics of intracranial aneurysms from 3D rotational angiography and CT angiography: an in vivo reproducibility study. *AJNR. American journal of neuroradiology*, 32(3):581–6.

[Girerd et al., 1996] Girerd, X., London, G., Boutouyrie, P., Mourad, J. J., Safar, M., and Laurent, S. (1996). Remodeling of the radial artery in response to a chronic increase in shear stress. *Hypertension*, 27(3 Pt 2):799–803.

[Gleich and Weizenecker, 2005] Gleich, B. and Weizenecker, J. (2005). Tomographic imaging using the nonlinear response of magnetic particles. *Nature*, 435(7046):1214–1217.

[Gómez, 2013] Gómez, A. (2013). *Full 3D Blood Velocity Mapping and Flow Quantification from Doppler Echocardiographic Images*. PhD thesis, King's College London.

[Gong and Brady, 1990] Gong, S. and Brady, M. (1990). Parallel computation of optic flow. In *Computer Vision—ECCV 90*, pages 124–133. Springer.

[Goodwill and Conolly, 2011] Goodwill, P. W. and Conolly, S. M. (2011). Multidimensional x-space magnetic particle imaging. *IEEE transactions on medical imaging, Vol. 30, N. 9*.

[Goodwill et al., 2012] Goodwill, P. W., Saritas, E. U., Croft, L. R., Kim, T. N., Krishnan, K. M., Schaffer, D. V., and Conolly, S. M. (2012). X-Space MPI: Magnetic nanoparticles for safe medical imaging. *Advanced Materials*, 24(28):3870–3877.

[Guggenheim et al., 1994] Guggenheim, N., Dorsaz, P., Doriot, P., Suilen, C., Chappuis, F., and Rutishauser, W. (1994). 3d determination of the intravascular volume and flow of coronary arteries. *International journal of bio-medical computing*, 35(1):13–23.

[Hadamard, 1902] Hadamard, J. (1902). Sur les problèmes aux dérivées partielles et leur signification physique. *Princeton Uni. Bull. (1902)*, 13:49–52.

[Hangiandreou et al., 1991] Hangiandreou, N. J., Folts, J. D., Peppler, W. W., and Mistretta, C. A. (1991). Coronary blood flow measurement using an angiographic first pass distribution technique: a feasibility study. *Medical physics*, 18(5):947–954.

[Hans and Moravec, 1977] Hans, P. and Moravec, H. P. (1977). Towards automatic visual obstacle avoidance. *IJCAI'77 Proceedings of the 5th international joint conference on Artificial intelligence*, 2:584–584.

[Harloff et al., 2009] Harloff, A., Albrecht, F., Spreer, J., Stalder, A. F., Bock, J., Frydrychowicz, A., Schollhorn, J., Hetzel, A., Schumacher, M., Hennig, J., and Markl, M. (2009). 3D blood flow characteristics in the carotid artery bifurcation assessed by flow-sensitive 4D MRI at 3T. *Magnetic Resonance in Medicine*, 61(1):65–74.

[Harris and Stephens, 1988] Harris, C. and Stephens, M. (1988). A Combined Corner and Edge Detector. *Procedings of the Alvey Vision Conference 1988*, pages 147–151.

[Haussecker and Fleet, 2001] Haussecker, H. W. and Fleet, D. J. (2001). Computing optical flow with physical models of brightness variation. *IEEE Transactions on Pattern Analysis and Machine Intelligence*, 23(6):661–673.

[Heitz and Bouthemy, 1993] Heitz, F. and Bouthemy, P. (1993). Multimodal estimation of discontinuous optical flow using Markov random fields. *IEEE Transactions on Pattern Analysis and Machine Intelligence*, 15(12).

[Hestenes and Stiefel, 1952] Hestenes, M. R. and Stiefel, E. (1952). Methods of Conjugate Gradients for Solving Linear Systems. *Journal of Research of the National Bureau of Standards*, 49:409–436.

[Hilal, 1966] Hilal, S. K. (1966). Human carotid artery flow determination using a radiographic technique. *Investigative radiology*, 1(2):113–122.

[Hildreth, 1984] Hildreth, E. C. (1984). Computations underlying the measurement of visual motion.

[Hope et al., 2010] Hope, M. D., Hope, T. A., Meadows, A. K., Ordovas, K. G., Urbania, T. H., Alley, M. T., and Higgins, C. B. (2010). Bicuspid aortic valve: four-dimensional MR evaluation of ascending aortic systolic flow patterns. *Radiology*, 255(1):53–61.

[Horn and Schunck, 1981] Horn, B. K. and Schunck, B. G. (1981). Determining optical flow.

[Huang et al., 1997] Huang, S. P., Decker, R. J., Goodrich, K. C., Parker, D. J., Muhlestein, J. B., Blatter, D. D., and Parker, D. L. (1997). Velocity measurement based on bolus tracking with the aid of three-dimensional reconstruction from digital subtraction angiography. *Medical physics*, 24(5):677–686.

[Imbert et al., 1997] Imbert, B., Meunier, J., Mongrain, R., Hudon, G., and Bertrand, M. J. (1997). Stenosis parameter assessment from contrast medium tracking in cineangiography with an optical flow method. In *Medical Imaging 1997*, pages 631–640. International Society for Optics and Photonics.

[Ishida et al., 1997] Ishida, T., Takahashi, M., Corson, M. A., and Berk, B. C. (1997). Fluid shear stress-mediated signal transduction: how do endothelial cells transduce mechanical force into biological responses? *Annals of the New York Academy of Sciences*, 811:12–23; discussion 23–24.

[Isoda et al., 2010] Isoda, H., Ohkura, Y., Kosugi, T., Hirano, M., Alley, M. T., Bammer, R., Pelc, N. J., Namba, H., and Sakahara, H. (2010). Comparison of hemodynamics of intracranial aneurysms between MR fluid dynamics using 3D cine phase-contrast MRI and MR-based computational fluid dynamics. *Neuroradiology*, 52(10):913–20.

[John, 1996] John, S. F. (1996). The role of magnetic susceptibility in magnetic resonance imaging: Mri magnetic compatibility of the first and second kinds. *Journal of Medical Physics : 1997)*, pages 815–850.

[Jung et al., 2006] Jung, J., Lyczkowski, R. W., Panchal, C. B., and Hassanein, A. (2006). Multiphase hemodynamic simulation of pulsatile flow in a coronary artery. *Journal of Biomechanics*, 39(11):2064–73.

[Korbuly, 1973] Korbuly, D. E. (1973). Determination of the pulsatile blood flow by a radiographic method. *Investigative radiology*, 8(4):255–258.

[Kremkau, 1990] Kremkau, F. W. (1990). *Doppler ultrasound: principles and instruments*. WB Saunders Co.

[Ku, 1997] Ku, D. N. (1997). Blood flow in arteries. *Annual Review of Fluid Mechanics*, 29:399–434.

[Kumar et al., 1996] Kumar, A., Tannenbaum, A. R., and Balas, G. J. (1996). Optical flow: A curve evolution approach. *IEEE Transactions on Image Processing*, 5(4):598–610.

[Lacroix et al., 2013] Lacroix, R., Rahmer, J., Borgert, J., Bonnefous, O., and Makram-Ebeid, S. (2013). Early results on image and signal processing for characterization of blood flow in 4D MPI images. In *2013 International Workshop on Magnetic Particle Imaging, IWMPI 2013*. Ieee.

[Lacroix et al., 2014] Lacroix, R., Rahmer, J., Weber M., O., Morales G., H., and Makram-Ebeid, S. (2014). Flow assessment from in vitro and in silico dynamic MPI data. In *2014 International Workshop on Magnetic Particle Imaging, IWMPI 2014*.

[Lampe et al., 2012] Lampe, J., Bassoy, C., Rahmer, J., Weizenecker, J., Voss, J., Gleich, B., and Borgert, J. (2012). Fast reconstruction in magnetic particle imaging. *Phys. Med. Biol. 2012*.

[Lantz et al., 1980] Lantz, B., Foerster, J., Link, D., and Holcroft, J. (1980). Determination of relative blood flow in single arteries: new video dilution technique. *American Journal of Roentgenology*, 134(6):1161–1168.

[Lawton, 1983] Lawton, D. T. (1983). Processing translational motion sequences. *Computer Vision, Graphics, and Image Processing*, 22(1):116–144.

[Li and Yang, 2010] Li, L. and Yang, Y. (2010). Optical flow estimation for a periodic image sequence. *Image Processing, IEEE Transactions on*, 19(1):1–10.

[Lieber et al., 2009] Lieber, B. B., Sadasivan, C., Hao, Q., Seong, J., and Cesar, L. (2009). The mixability of angiographic contrast with arterial blood. *Medical Physics*, 36(11):5064.

[Lu et al., 2013] Lu, K., Goodwill, P., Saritas, W., Emine, U., Zheng, B., and Conolly Steven, M. (2013). Linearity and shift invariance for quantitative magnetic particle imaging. *IEEE transactions on medical imaging, Vol. 32, N. 9*.

[Lucas and Kanade, 1981] Lucas, B. D. and Kanade, T. (1981). An Iterative Image Registration Technique with an Application to Stereo Vision. *Imaging*, 130(x):674–679.

[Malek, 1999] Malek, A. M. (1999). Hemodynamic Shear Stress and Its Role in Atherosclerosis. *JAMA: The Journal of the American Medical Association*, 282(21):2035–2042.

[Marinus et al., 1990] Marinus, H., Buis, B., and van Benthem, A. (1990). Pulsatile coronary flow determination by digital angiography. *The International Journal of Cardiac Imaging*, 5(2-3):173–182.

[Markl et al., 2007] Markl, M., Harloff, A., Bley, T. A., Zaitsev, M., Jung, B., Weigang, E., Langer, M., Hennig, J., and Frydrychowicz, A. (2007). Time-resolved 3D MR velocity mapping at 3T: Improved navigator-gated assessment of vascular anatomy and blood flow. *Journal of Magnetic Resonance Imaging*, 25(4):824–831.

[Marshall et al., 2004] Marshall, I., Zhao, S., Papathanasopoulou, P., Hoskins, P., and Xu, Y. (2004). MRI and CFD studies of pulsatile flow in healthy and stenosed carotid bifurcation models. *Journal of biomechanics*, 37(5):679–87.

[Memin and Perez, 1998] Memin, E. and Perez, P. (1998). A multigrid approach for hierarchical motion estimation. *Sixth International Conference on Computer Vision (IEEE Cat. No.98CH36271)*.

[Mémin and Pérez, 2002] Mémin, E. and Pérez, P. (2002). Hierarchical estimation and segmentation of dense motion fields. *International Journal of Computer Vision*, 46(2):129–155.

[Meng et al., 2014] Meng, H., Tutino, V. M., Xiang, J., and Siddiqui, A. H. (2014). High WSS or low WSS? Complex interactions of hemodynamics with intracranial aneurysm initiation, growth, and rupture: toward a unifying hypothesis. *AJNR. American journal of neuroradiology*, 35(7):1254–62.

[Molloi et al., 1993] Molloi, S., Qian, Y.-J., and Ersahin, A. (1993). Absolute volumetric blood flow measurements using dual-energy digital subtraction angiography. *Medical physics*, 20(1):85–91.

[Moore et al., 1994] Moore, J. E., Xu, C., Glagov, S., Zarins, C. K., and Ku, D. N. (1994). Fluid wall shear stress measurements in a model of the human abdominal aorta: oscillatory behavior and relationship to atherosclerosis. *Atherosclerosis*, 110(2):225–240.

[Morales, 2012] Morales, H. G. (2012). *Endovascular Coiling and its Influence on Intra-aneurysmal Hemodynamics by Image-based Modeling*. PhD thesis, Pompeu Fabra.

[Morales and Bonnefous, 2014] Morales, H. G. and Bonnefous, O. (2014). *Peak systolic or maximum intra-aneurysmal hemodynamic condition? Implications on normalized flow variables. *Journal of biomechanics*, 47(10):2362–70.

[Morales and Bonnefous, 2015] Morales, H. G. and Bonnefous, O. (2015). *Unraveling the Relationship between Arterial Flow and Intra-aneurysmal Hemodynamics. *Journal of Biomechanics*, 48:585–591.

[Morales et al., 2013] Morales, H. G., Larrabide, I., Geers, A. J., Aguilar, M. L., and Frangi, A. F. (2013). Newtonian and non-newtonian blood flow in coiled cerebral aneurysms. *Journal of biomechanics*, 46(13):2158–2164.

[Morales et al., 2011] Morales, H. G., Larrabide, I., Villa-Uriol, M.-C., Geers, A. J., and Frangi, A. F. (2011). Towards the validation of a virtual coiling technique using a real versus a simulated bolus injection. In *Proceedings of the 2nd International Conference on Mathematical and Computational Biomedical Engineering (CMBE'11)*, pages 512–515.

[Mygind et al., 1995] Mygind, M., Engell, L., and Mygind, T. (1995). Flow measurements with digital subtraction densitometry in a steady flow experimental model. *Acta Radiologica*, 36(4):402–409.

[Nagel, 1983] Nagel, H.-h. (1983). Constraints for the estimation of displacement vector fields from image sequences. In *In International Joint Conference on Artificial Intelligence*.

[Negahdaripour, 1998] Negahdaripour, S. (1998). Revised definition of optical flow: integration of radiometrie and geometric cues for dynamic scene analysis. *IEEE Transactions on Pattern Analysis and Machine Intelligence*, 20(9):961–979.

[Negahdaripour and Yu, 1993] Negahdaripour, S. and Yu, C.-H. (1993). A generalized brightness change model for computing optical flow. *1993 (4th) International Conference on Computer Vision*.

[Ogata and Sato, 1992] Ogata, M. and Sato, T. (1992). Motion-detection model with two stages: Spatiotemporal filtering and feature matching. *JOSA A*, 9(3):377–387.

[Osman et al., 1999] Osman, N. F., Kerwin, W. S., McVeigh, E. R., and Prince, J. L. (1999). Cardiac motion tracking using CINE harmonic phase (HARP) magnetic resonance imaging. *Magnetic Resonance in Medicine*, 42(6):1048–1060.

[Papadakis et al., 2007] Papadakis, N., Corpetti, T., and Mémin, E. (2007). Dynamically consistent optical flow estimation. In *Computer Vision, 2007. ICCV 2007. IEEE 11th International Conference on*, pages 1–7. IEEE.

[Pelc et al., 1991] Pelc, N. J., Herfkens, R. J., Shimakawa, A., and Enzmann, D. R. (1991). Phase contrast cine magnetic resonance imaging. *Magnetic resonance quarterly*, 7(4):229–254.

[Pereira et al., 2013] Pereira, V. M., Bonnefous, O., Ouared, R., Brina, O., Stawiaski, J., Aerts, H., Ruijters, D., Narata, A. P., Bijlenga, P., Schaller, K., and Lovblad, K.-O. (2013). A DSA-based method using contrast-motion estimation for the assessment of the intra-aneurysmal flow changes induced by flow-diverter stents. *AJNR. American journal of neuroradiology*, 34(4):808–15.

[Pereira et al., 2014] Pereira, V. M., Ouared, R., Brina, O., Bonnefous, O., Satwiaski, J., Aerts, H., Ruijters, D., van Nijnatten, F., Perren, F., Bijlenga, P., Schaller, K., and Lovblad, K.-O. (2014). Quantification of internal carotid artery flow with digital subtraction angiography: validation of an optical flow approach with Doppler ultrasound. *AJNR. American journal of neuroradiology*, 35(1):156–63.

[Petersson et al., 2012] Petersson, S., Dyverfeldt, P., and Ebbers, T. (2012). Assessment of the accuracy of MRI wall shear stress estimation using numerical simulations. *Journal of magnetic resonance imaging : JMRI*, 36(1):128–38.

[Poggio and Yuille, 1986] Poggio, T. A. and Yuille, a. L. (1986). Scaling theorems for zero crossings. *IEEE transactions on pattern analysis and machine intelligence*, 8(1):15–25.

[Proesmans et al., 1994] Proesmans, M., Gool, L. V., Pauwels, E., and Oosterlinck, A. (1994). Determination of optical flow and its discontinuities using non-linear diffusion. In *Proceedings of the 3rd ECCV II*, volume 2 of *Lecture Notes in Computer Science*, pages 295–304. Katholieke Universiteit Leuven, Department Elektrotechniek, Afdeling ESAT/MI2, Springer–Verlag.

[R., 1985] R., R. (1985). Ferrohydrodynamics. *Cambridge University Press, Cambridge, New York*.

[Rahmer et al., 2013] Rahmer, J., Antonelli, a., Sfara, C., Tiemann, B., Gleich, B., Magnani, M., Weizenecker, J., and Borgert, J. (2013). Nanoparticle encapsulation in red blood cells enables blood-pool magnetic particle imaging hours after injection. *Physics in medicine and biology*, 58(12):3965–77.

[Reneman et al., 2006] Reneman, R. S., Arts, T., and Hoeks, A. P. G. (2006). Wall shear stress–an important determinant of endothelial cell function and structure–in the arterial system in vivo. discrepancies with theory. *Journal of vascular research*, 43(3):251–69.

[Reymond et al., 2009] Reymond, P., Merenda, F., Perren, F., Rüfenacht, D., and Stergiopulos, N. (2009). Validation of a one-dimensional model of the systemic arterial tree. *American Journal of Physiology-Heart and Circulatory Physiology*, 297(1):H208–H222.

[Rhode et al., 2005] Rhode, K. S., Lambrou, T., Hawkes, D. J., and Seifalian, A. M. (2005). Novel approaches to the measurement of arterial blood flow from dynamic digital X-ray images. *IEEE Transactions on Medical Imaging*, 24(4):500–513.

[Rieger et al., 2004] Rieger, B., Timmermans, F. J., Van Vliet, L. J., and Verbeek, P. W. (2004). On curvature estimation of iso surfaces in 3d gray-value images and the computation of shape descriptors. *Pattern Analysis and Machine Intelligence, IEEE Transactions on*, 26(8):1088–1094.

[Rinkel et al., 1998] Rinkel, G. J., Djibuti, M., Algra, A., and van Gijn, J. (1998). Prevalence and risk of rupture of intracranial aneurysms: a systematic review. *Stroke; a journal of cerebral circulation*, 29(1):251–256.

[Rosen and Silverman, 1973] Rosen, L. and Silverman, N. R. (1973). Videodensitometric measurements of blood flow using crosscorrelation techniques 1. *Radiology*, 109(2):305–310.

[Saritas et al., 2013] Saritas, E. U., Goodwill, P. W., Croft, L. R., Konkle, J. J., Lu, K., Zheng, B., and Conolly, S. M. (2013). Magnetic particle imaging (MPI) for NMR and MRI researchers. *Journal of magnetic resonance (San Diego, Calif. : 1997)*, 229:116–26.

[Sarry et al., 1997] Sarry, L., Boire, J.-Y., Zanca, M., Lusson, J.-R., and Cassagnes, J. (1997). Assessment of stenosis severity using a novel method to estimate spatial and temporal variations of blood flow velocity in biplane coronarography. *Physics in medicine and biology*, 42(8):1549.

[Sarry et al., 2002] Sarry, L., Peng, Y. J., and Boire, J. Y. (2002). Blood flow velocity estimation from x-ray densitometric data: an efficient numerical scheme for the inverse advection problem. *Physics in medicine and biology*, 47(1):149–162.

[Schnorr, 1994] Schnorr, C. (1994). Segmentation of visual motion by minimizing convex non-quadratic functionals. In *Pattern Recognition, 1994. Vol. 1-Conference A: Computer Vision & Image Processing., Proceedings of the 12th IAPR International Conference on*, volume 1, pages 661–663. IEEE.

[Seifalian et al., 1991] Seifalian, A., Hawkes, D., Hardingham, C., Colchester, A., and Reidy, J. (1991). Validation of a quantitative radiographic technique to estimate pulsatile blood flow waveforms using digital subtraction angiographic data. *Journal of biomedical engineering*, 13(3):225–233.

[Shaw and Plewes, 1986] Shaw, C.-G. and Plewes, D. (1986). Pulsed-injection method for blood flow velocity measurement in intraarterial digital subtraction angiography. *Radiology*, 160(2):556–559.

[Shewchuk, 1994] Shewchuk, J. R. (1994). An introduction to the conjugate gradient method without the agonizing pain.

[Shpilfoygel et al., 2000] Shpilfoygel, S. D., Close, R. A., Valentino, D. J., and Duckwiler, G. R. (2000). X-ray videodensitometric methods for blood flow and velocity measurement: a critical review of literature. *Medical physics*, 27(9):2008–2023.

[Shpilfoygel et al., 1999] Shpilfoygel, S. D., Jahan, R., Close, R. A., Duckwiler, G. R., and Valentino, D. J. (1999). Comparison of methods for instantaneous angiographic blood flow measurement. *Medical physics*, 26(6):862–871.

[Shulman and Herve, 1989] Shulman, D. and Herve, J.-Y. (1989). Regularization of discontinuous flow fields. *[1989] Proceedings. Workshop on Visual Motion.*

[Silverman and Rosen, 1977] Silverman, N. R. and Rosen, L. (1977). Arterial blood flow measurement: assessment of velocity estimation methods. *Investigative radiology*, 12(4):319–324.

[Singh et al., 2009] Singh, P. K., Marzo, A., Coley, S. C., Berti, G., Bijlenga, P., Lawford, P. V., Villa-Uriol, M. C., Rüfenacht, D. A., McCormack, K. M., Frangi, A. F., Patel, U. J., and Hose, D. R. (2009). The role of computational fluid dynamics in the management of unruptured intracranial aneurysms: a clinicians' view. *Computational intelligence and neuroscience*, 2009:760364.

[Smith and Brady, 1997] Smith, S. and Brady, J. (1997). SUSAN—a new approach to low level image processing. *International journal of computer vision*, 23(1):45–78.

[Starn, 2001] Starn, J. (2001). A Simple Fluid Solver Based on the FFT.

[Straeter, 1971] Straeter, T. A. (1971). On the extension of the davidon-broyden class of rank one, quasi-newton minimization methods to an infinite dimensional hilbert space with applications to optimal control problems(quasi-newtonian minimization methods extended to infinite dimensional hilbert space with applications to optimal control problems).

[Tikhonov, 1943] Tikhonov, A. N. (1943). On the stability of inverse problems. *Doklady Akademii Nauk Sssr*, 39(5):195–198.

[Traub and Berk, 1998] Traub, O. and Berk, B. C. (1998). Laminar shear stress: mechanisms by which endothelial cells transduce an atheroprotective force. *Arteriosclerosis, thrombosis, and vascular biology*, 18(5):677–685.

[Tsao et al., 2003] Tsao, J., Boesiger, P., and Pruessmann, K. P. (2003). k-t BLAST and k-t SENSE: Dynamic MRI With High Frame Rate Exploiting Spatiotemporal Correlations. *Magnetic Resonance in Medicine*, 50(5):1031–1042.

[Uribe et al., 2009] Uribe, S., Beerbaum, P., Sø rensen, T. S., Rasmusson, A., Razavi, R., and Schaeffter, T. (2009). Four-dimensional (4D) flow of the whole heart and great vessels using real-time respiratory self-gating. *Magnetic Resonance in Medicine*, 62(4):984–992.

[Villa-Uriol et al., 2010] Villa-Uriol, M.-C., Larrabide, I., Pozo, J., Kim, M., Camara, O., De Craene, M., Zhang, C., Geers, A., Morales, H., Bogunović, H., et al. (2010). Toward integrated management of cerebral aneurysms. *Philosophical Transactions of the Royal Society A: Mathematical, Physical and Engineering Sciences*, 368(1921):2961–2982.

[W and M, 2010] W, G. P. and M, C. S. (2010). The x-space formulation of the magnetic particle imaging process : 1-d signal , resolution , bandwidth ,snr ,sar, and magnetostimulation. *IEEE transactions on medical imaging, Vol. 29, N. 11.*

[Weber and Malik, 1995] Weber, J. and Malik, J. (1995). Robust computation of optical flow in a multi-scale differential framework. *International Journal of Computer Vision*, 14(1):67–81.

[Weizenecker et al., 2009] Weizenecker, J., Gleich, B., Rahmer, J., Dahnke, H., and Borgert, J. (2009). Three-dimensional real-time in vivo magnetic particle imaging.

[Wetzel et al., 2007] Wetzel, S., Meckel, S., Frydrychowicz, A., Bonati, L., Radue, E. W., Scheffler, K., Hennig, J., and Markl, M. (2007). In vivo assessment and visualization of intracranial arterial hemodynamics with flow-sensitized 4D MR imaging at 3T. *American Journal of Neuroradiology*, 28(3):433–438.

[WHO, 2015] WHO (2015). Cardiovascular diseases (cvds).

[Wigström et al., 1996] Wigström, L., Sjöqvist, L., and Wranne, B. (1996). Temporally resolved 3D phase-contrast imaging. *Magnetic Resonance in Medicine*, 36(5):800–803.

[Wildes et al., 2000] Wildes, R. P., Amabile, M. J., Lanzillotto, A.-M., and Leu, T.-S. (2000). Recovering Estimates of Fluid Flow from Image Sequence Data. *Computer Vision and Image Understanding*, 80(2):246–266.

[Wootton and Ku, 1999a] Wootton, D. M. and Ku, D. N. (1999a). Fluid mechanics of vascular systems, diseases, and thrombosis. *Annual review of biomedical engineering*, 1:299–329.

[Wootton and Ku, 1999b] Wootton, D. M. and Ku, D. N. (1999b). Fluid mechanics of vascular systems, diseases, and thrombosis. *Annual review of biomedical engineering*, 1:299–329.

[Wu et al., 1998] Wu, Y.-T. W. Y.-T., Kanade, T., Cohn, J., and Li, C.-C. L. C.-C. (1998). Optical flow estimation using wavelet motion model. *Sixth International Conference on Computer Vision (IEEE Cat. No.98CH36271)*.

[Zarins et al., 1987] Zarins, C. K., Zatina, M. A., Giddens, D. P., Ku, D. N., and Glagov, S. (1987). Shear stress regulation of artery lumen diameter in experimental atherogenesis. *Journal of vascular surgery : official publication, the Society for Vascular Surgery [and] International Society for Cardiovascular Surgery, North American Chapter*, 5(3):413–420.

Résumé

De nos jours, les maladies cardiovasculaires restent un sujet de préoccupation majeur pour la santé et une charge économique importante dans les pays développés. Avec les progrès de la médecine, les systèmes d'imagerie médicale ont permis la détection des pathologies cardiovasculaires `a un stade précoce, et la surveillance de leur évolution `a travers des outils d'analyse de données avancés. La mesure du débit sanguin, en particulier, est une information précieuse pour le médecin. Aujourd'hui, de nombreuses techniques d'acquisition du flux sanguin ont été développées et appliquées dans les routines cliniques et la recherche médicale. L'une d'entre elles recourt `a l'injection d'un produit de contraste dans le sang artériel. La propagation du traceur dans la circulation sanguine et sa modulation spatiotemporelle délivre l'information des motifs du flux sanguin dans des séquences d'images 2D. Cependant, les systèmes d'imagerie de contraste 3D+T n'ont pas encore atteint un stade clinique. Le but de cette thèse est d'apporter un cadre général de l'estimation de flux sanguin pour les futurs systèmes d'imagerie de contraste 3D+T.

Une formulation variationnelle du flot optique est présentée, incluant diverses connaissances a priori sur la concentration du produit de contraste, et les propriétés du flux sanguin inspirées de la mécanique des fluides. Par la suite, le potentiel de l'algorithme d'estimation de flot optique est évalué sur de l'angiographie virtuelle par CFD, avec une analyse de l'influence du débit sanguin et des paramètres de l'algorithme. Enfin, une version simplifiée de l'approche de flot optique est testée sur les toutes premières données MPI 3D+T. Dans un premier temps, une expérience de flux in vitro est proposée `a l'intérieur d'un fantôme avec une injection de contraste modulé, dans un second temps une analyse du flux sanguin est démontrée sur des données in vivo.

Dans son ensemble, cette thèse investigue le sujet original de l'estimation de flux sanguin et l'analyse de ses motifs en 3D. La contribution technique consiste en la création d'un nouvel algorithme de flot optique dédié `a de l'information de contraste temporellement résolue dans le système cardiovasculaire. La contribution clinique sous-jacente consiste en un pipeline complet pour l'estimation du flux sanguin, en partant de la procédure d'acquisition par modulation de contraste, jusqu'au calcul du flot optique et `a sa validation in silico.

Mots-clés : Imagerie médicale, Angiographie, Flux sanguin, Produit de contraste, Flot optique, Méthodes variationnelles, CFD, MPI

Abstract

Nowadays, cardiovascular diseases remain a subject of major concern for healthcare and an important economic burden in developed countries. With the progress of medicine, medical imaging systems have allowed to detect cardiovascular pathologies at an early stage, and to monitor their evolution through advanced data analysis tools. The measurement of blood flow, in particular, is a precious information for a physician. Today, numerous blood flow estimation techniques have been developed and applied in clinical routines and medical research. One of them resorts to the injection of a contrast product in the arterial blood. The propagation of tracer throughout the bloodstream and its spatiotemporal modulation delivers the information of blood flow patterns in 2D image sequences. However, 3D+T contrast systems have not reached a clinical stage yet. The goal of this thesis is to provide the future 3D+T contrast systems with a general framework of blood flow estimation.

A variational formulation of optical flow is presented, including different prior knowledge concerning the contrast concentration, and blood flow properties inspired from fluid mechanics. Subsequently, the fruitfulness of the optical flow estimation algorithm is evaluated on CFD based virtual angiography, with a sensitivity analysis on flow rate and algorithm parameters. Finally, a simplified version of the optical flow approach is tested on 3D+T early MPI evaluation. First, an in vitro flow experiment is proposed with a modulated contrast injection and secondly a blood flow analysis on in vivo data is demonstrated.

All in all, this thesis investigates the original subject of blood flow estimation and the analysis of 3D blood flow patterns. The technical contribution consists in the creation of a new optical flow algorithm dedicated to time-resolved contrast information in the cardiovascular system. The underlying clinical contribution is a full pipeline for blood flow estimation, starting from the acquisition procedure with contrast modulation, to the optical flow computation, and the in silico validation.

Keywords : Medical imaging, Angiography, Blood flow, Contrast agent, Optical flow, Variational methods, CFD, MPI

TELECOM Bretagne

n° d'ordre : 2015telb0364

Télécom Bretagne

Technopôle Brest-Iroise - CS 83818 - 29238 Brest Cedex 3

Tél : + 33(0) 29 00 11 11 - Fax : + 33(0) 29 00 10 00